SUSTAINABLE EXTRACTION AND PROCESSING OF RAW MATERIALS

UNIVERSITY OF MINING AND GEOLOGY "ST. IVAN RILSKI"

Edited by Prof. Dr. Marinela Panayotova

Selected Papers of the Annual International Scientific Conference of the University of Mining and Geology "St. Ivan Rilski", Sofia, Bulgaria

October 16 2026

Volume 7

Sofia 2026



ISSN (on-line): 2738-7151
ISSN (print): 2738-7100

UNIVERSITY OF MINING AND GEOLOGY "ST. IVAN RILSKI"

SUSTAINABLE EXTRACTION AND PROCESSING OF RAW MATERIALS

JOURNAL

Volume 7

Sofia 2026

Editorial board

Prof. Dr. Marinela Panayotova – University of Mining and Geology “St. Ivan Rilski”, Bulgaria - Editor-in-Chief
Academician D.Sc. Vladimir Tsitsishvili - “Ivane Javakhishvili” Tbilisi State University, Georgia
Academician D.Sc. Abel Maharramov - Baku State University, Azerbaijan
Prof. Dr. h.c. Carsten Drebenstedt - TU Bergakademie Freiberg, Germany
Prof. D.Sc. Vladimir Litvinenko - Saint-Petersburg Mining University, Rusia
Prof. D.Sc. Tetiana Oliinyk – Kryvyi Rih National University, Ukraine
Prof. D.Sc. Dmytro Kolosov – Dnipro University of Technology, Ukraine
Prof. Dr. Cyril O’Connor – University of Cape Town, RSA
Prof. Dr. Hao Chen – China University of Mining and Technology, China
Prof. Dr. Gabrijela Popovic - University Business Academy in Novi Sad, Serbia
Prof. Dr. Georgios Anastassakis - National Technical University of Athens, Greece
Prof. Dr. Murat Olgaç Kangal – Istanbul Technical University, Türkiye
Prof. Dr. Roland Moraru - University of Petrosani, Romania
Prof. Dr. Zoran Despodov - University "Goce Delcev", North Macedonia
Assoc. Prof. Dr. Yassen Gorbounov - University of Mining and Geology “St. Ivan Rilski”, Bulgaria
Assoc. Prof. Dr. Simeon Asenovski - University of Mining and Geology “St. Ivan Rilski”, Bulgaria
English Editor: Chief Assist. Prof. Monika Hristova - University of Mining and Geology “St. Ivan Rilski”, Bulgaria
Technical Editor: Chief Assist. Prof. Milena Purvanova - University of Mining and Geology “St. Ivan Rilski”, Bulgaria

University of Mining and Geology “St. Ivan Rilski”,
Prof. Boyan Kamenov Str.,
1700 Sofia, Bulgaria
http://www.mgu.bg

ISSN 2738-7100 (print)
ISSN 2738-7151(online)

www.seprm.com ©
Publishing House “St. Ivan Rilski”, Sofia, 2026

SUSTAINABLE EXTRACTION AND PROCESSING OF RAW MATERIALS JOURNAL, 2026

Dear readers and authors,

It is a great honour for me to present to your attention the seventh volume of the "Sustainable Extraction and Processing of Raw Materials" Journal (SEPRM) published by the University of Mining and Geology "St. Ivan Rilski", Sofia, Bulgaria.

The "Sustainable Extraction and Processing of Raw Materials" Journal is a specialised scientific publication aimed at presenting original and innovative research papers as well as concise reviews on the environmentally friendly and viable provision of resources from primary and secondary sources in order to contribute to the sustainable development of our society. It publishes also selected papers from the Annual International Scientific Conference of the University of Mining and Geology “St. Ivan Rilski”, Sofia, Bulgaria.

The official language of this double-blind, double peer reviewed journal is English. The following fields are covered:

- Geological and geophysical studies related to the assessment of mineral resources and their environmentally friendly extraction;
- Sustainable mining (underground and open pit, geo-technology - chemical, physicochemical, biochemical, and microbiological methods, urban mining, conservation, liquidation and reclamation of mining sites);
- Sustainable processing of primary and secondary raw materials - physical methods (comminution, milling and dewatering), physicochemical separation methods (flotation, bio-, hydro-, and electrometallurgy), mineralogical aspects and analytical techniques to follow the mentioned processes;
- Environmental issues, related to mining and raw materials processing, particularly those related to sustainable development;
- Modelling, control, economics and management of extraction and processing of raw materials.

The journal adheres to the standards of publication ethics recommended by the Committee on Publication Ethics (COPE) Core Practices.

I would like to acknowledge the contribution of all the prominent scientists who agreed to be members of the SEPRM Editorial board!

I am grateful to all authors who have chosen SEPRM Journal to share their research!

I am happy to remind that the previous volumes of the SEPRM are indexed in Google Scholar and included in CrossRef, DOAJ, BASE, OpenAIRE, Academic Resource Index (ResearchBib), ROAD, the Scientific Indexing Services, the Russian Scientific Electronic Library (eLIBRARY) and the National Reference List of Contemporary Bulgarian Scientific Publications with Scientific Review. It is archieved in COBISS and in the Bulgarian Portal for Open Science certified according to CoreTrustSeal standards and Bulgarian National Library.

Editor-in-Chief: Prof. Dr. Marinela Panayotova

GRATITUDE TO REVIEWERS

I would like to express my deep thankfulness to all reviewers for their time and dedicated labour to review all papers submitted to the SEPRM Journal in order to choose the soundest works.
This volume of the journal is available due to the efforts of the volunteer reviewers - colleagues listed below:

Arslan F., Prof. Dr. Eng.
Assenova, M., Prof. Dr. Eng.
Benderev A., Prof. Dr. Eng.
Galabova B., Assoc. Prof. Dr.
Gemishev O., Assist. Prof. Dr.
Gospodinova V., Assoc. Prof. Dr. Eng.
Grigorova I., Prof. DSc. Eng.
Ivanov I., Assoc. Prof. Dr. Eng.
Kamburov A., Assoc. Prof. Dr. Eng.
Mamyrbaeva K., Assoc. Prof. Dr. Eng.
Medvedeva O., Prof. Dr. Eng.
Mirdzveli N., Assoc. Prof. Dr.
Nijaradze M., Prof. Dr.
Nishkov I., Prof. Dr. Eng.
Panayotov V., Correspondent member BAS, Prof. D. Tech. Sc. Eng.
Pathania D., Prof. Dr.
Pathania S., Assoc. Prof. Dr.
Ruskov, K., Assoc. Prof. Dr.
Tzankov H., Assist. Prof. Dr.
Veleva L., Prof. Dr. Eng.
Zdravkov A., Assoc. Prof. Dr. Eng.
Zhukov S., Prof. D. Tech. Sc Eng.

Dear Colleagues,
I am very obliged and thankful to you!
With a hope for further cooperation,

Yours Sincerely,
M. Panayotova, Prof. Dr., Editor-in-Chief - SEPRM Journal

SEPRM Journal applies Creative Commons licensing

Attribution-NonCommercial-ShareAlike 4.0 International (CC BY-NC-SA 4.0)

CONTENTS

Page

Brodt, A. FEATURES OF INTERACTION BETWEEN POTASSIUM SALTS MINING AND THE ENVIRONMENT **6**

Doneva, B., Panov, Z., Stefanovska, R. K., Popovski, R. GEOPHYSICAL INVESTIGATIONS USING SEISMIC REFLECTION METHOD IN THE AREA WITH THE GEOTHERMAL WATERS **13**

Duru, N. U. DEVELOPMENT OF A NON-LINEAR LEAST-SQUARES KINETIC MODEL FOR HEAP LEACH CHEMICAL EXTRACTION USING COLUMN LEACH DATA **20**

Georgiev, P., Nicolova, M., EFFICIENCY AND SELECTIVITY OF COPPER PRECIPITATION AS COPPER OXALATE FROM SOLUTIONS FROM THE MINING INDUSTRY **28**

Georgiev, P., Nicolova, M., Spasova, I. NON-FERROUS METAL BIOLEACHING FROM COPPER SLAG WITH A SPENT MEDIUM OF SPOROSARCINA UREAE **34**

Ivanov, R. INFLUELNCE OF THE CONSTRUCTION OF A BIOSENSOR BASED ON SEDIMENT MICROBIAL FUEL CELLS ON ITS SENSITIVITY TO WATERS CONTAMINATED WITH HEAVY METALS **40**

Korobiichuk, V., Iskov, S., Mamrai V., Shamrai, V., Bilobrov, D. STUDY OF STRENGTH REDUCTION IN NATURAL STONE UNDER REPEATED NON-DESTRUCTIVE DYNAMIC LOADING **45**

Loukanov, A. SUSTAINABLE MATERIALS FOR URANIUM REMOVAL FROM MINE WATER: COMPARATIVE EVALUATION OF ZERO-VALENT IRON NANOPARTICLES, CONVENTIONAL SORBENTS, AND FUNCTIONALISED MAGNETIC NANOMATERIALS **53**

Petrov, P., Stefanova, V., Vasilev, Z., Ivanova, S., Stamenova-Yordanova, I., Georgieva, E. REHABILITATION AND RECONVERSION OF COAL MINING SITES: SUSTAINABLE SOLUTIONS FOR ENERGY TRANSITION IN THE PERNIK REGION **62**

Polischuk, D., Panasiuk, A., Mamrai, V. INVESTIGATION OF FACTORS AFFECTING UAV-BASED MINE SURVEYING ACCURACY **69**

Svietkina, O. Yu., Fedoskina, O. V. INTENSIFICATION OF THE PROCESS OF BENEFICIATION OF MINERALS BY VIBRATION-IMPACT ACTIVATION **75**

Instructions for authors **83**

FEATURES OF INTERACTION BETWEEN POTASSIUM SALTS MINING AND THE ENVIRONMENT

Alexander Brodt

Eco-Safe Mining Corp., 510 Reeves Drive, Grand Forks, ND 58201, USA
Corresponding author: alexander.brodt@gmail.com

ABSTRACT. Unlike the vast majority of minerals, the gangue in all types of halurgic raw materials is represented by a water-soluble material - rock salt, contaminated clay and other impurities insoluble in water. Thus, the storage of water-soluble waste from the enrichment of ground-based sylvinite enrichment plants out in the open air, in addition to the disfigurement of natural landscapes, is accompanied by the dissolution of waste congestions due to atmospheric precipitation, with the formation of gigantic volumes of excess brines, causing soil salinisation and contamination of drinking water sources. This paper proposes prevention of the harmful impact of the potassium salts industry on the environment, achieved by enriching the initial water-soluble raw materials in underground conditions based on new environmentally friendly technologies using fire- and explosion-proof non-aqueous heavy liquids with a given set of physical and physiologically inert properties with a full cycle of their energy-efficient regeneration.

Key words: mining of potash salts; underground processing minerals without harming to environment

Introduction

The Earth's population is growing steadily (Figure 1). According to UN projections, by 2050, more than 9.8 billion people will live on our planet which is an increase by 1.8 billion (United Nations, 2024).

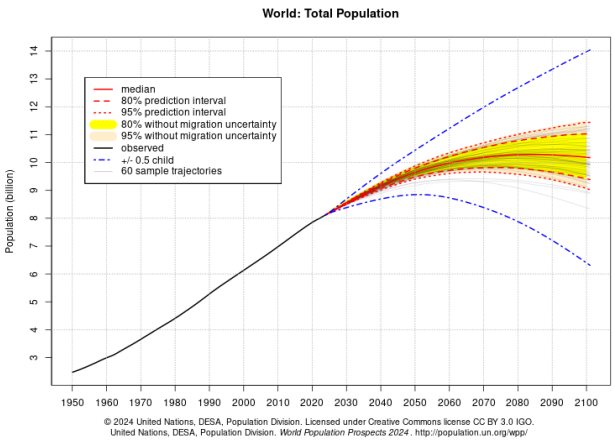


Fig. 1. Total world population grow
(https://population.un.org/wpp/graphs)

The growing global population requires, first and foremost, increased food production. Meanwhile, there is almost no additional available arable land suitable for agriculture in countries with suitable climate. Therefore, increasing crop yields is becoming the primary resource for increasing agricultural production. However, intensifying agricultural production is impossible without the use of mineral fertilizers, including potash.

Most countries in the world lack their own potash reserves, while 25.9% (almost 2 billion people) of the world's population already experience food shortages (United Nations, 2025). Potash fertilizers, along with phosphorus and nitrogen fertilizers, significantly increase the yields of major agricultural crops, leading to enlarged demand for potash products. However, the uneven distribution of potash deposits worldwide means that of the world's total potash fertilizer production 77% (for 2025) is accounted for by just four countries: Canada, Russia, China and Belarus – Figure 2 (Jasinski, 2026).

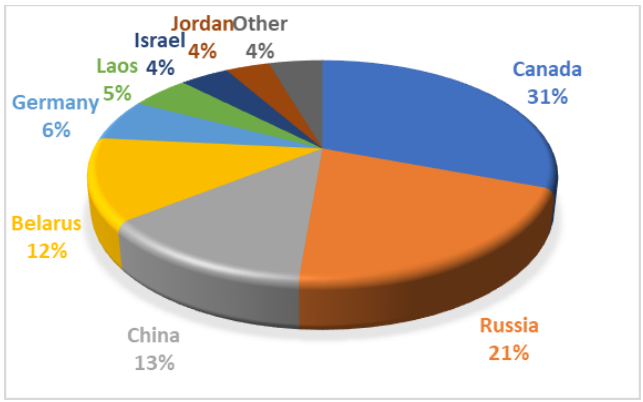


Fig. 2. Major world potash producers in 2025

Unlike most minerals, the waste rock in potash ores is primarily rock salt contaminated with clay impurities. For every ton of potassium salt obtained as a finished product, there are 3...4 tons of rock salt and 0.2...0.5 tons of clay-salt sludge stored on the surface in the form of waste heaps and sludge - Figure 3 (Ushakova et al., 2023).



Fig. 3. "Potash ore processing waste disposal facilities on the Verkhnekamskoe deposit's territory:
(a) potash tailings pile; (b) potash tailing slurry" (Ushakova et al., 2023)

As a result, open-air storage of water-soluble waste from potash ore processing not only consumes vast areas of arable land but also leads to the accumulation of excess brines, which

form as a result of atmospheric precipitation. Halite dumps and clay-salt sludge storage facilities are underlain by polyethylene waterproofing, which is susceptible to chemical destruction, leading to seepage of saltwater into underground horizons (Latipov et al., 2023).

Such anthropogenic processes lead not only to soil salinisation and loss of fertility, but also to the irreversible mineralisation of local drinking water sources.

The accumulation of water-soluble waste as a result of the enrichment of potassium salts is reaching alarming proportions in all major potash-producing countries. Suffice it to say that in the south of Belarus alone, in four waste dumps belonging to the Belaruskali mining company, approximately one billion tons of rock salt, contaminated with clay impurities saturated with the remains of flotation reagents, have already accumulated (Andrejchuk and Rózkowski, 2000; Liskova, 2017). In addition to rock salt, sylvinite contains a high clay content. This clay must be removed from the beneficiation process before potassium chloride (KCl) flotation. Special basins are being constructed to receive clay sludge, which leads to the withdrawal of thousands of hectares of fertile land from agricultural use (Eminov et al., 2026).

The waste rock accounts for 65 to 75% of the ore's mass (Ushakova et al., 2023) making mine hoisting clearly inefficient, as three-quarters of the energy expended is spent transporting the waste rock, not to mention the environmental damage caused by warehousing of waste products on the surface.

Extracting such poor raw materials from the mine, in addition to the obviously inefficient energy consumption for vertical transportation of the ballast component of the extracted ore, leads to the formation of enormous volumes of mined-out empty space in the subsoil.

However, nature abhors a vacuum. Over time, this leads to irreversible, uncontrolled development of geomechanical processes of displacement of the overlying rock mass, which leads to irreparable damage to all natural and anthropogenic surface objects due to soil subsidence, up to the destruction of above-ground buildings and a rupture of the continuity of the earth's surface with the formation of giant sinkholes (Florkowska and Bryt-Nitarska, 2025). In addition, when the occurrence groundwater level is high enough, subsidence of the earth's surface leads to waterlogging of the soil, flooding of basements of houses and salinisation of water in village wells.

The above-described leads to the conclusion that the only radical way out of this situation, capable of resolving this fundamental technological contradiction of the modern potash industry, is to abandon the delivery of the entire volume of mined ore onto the earth's surface, and to process the rock mass underground, with subsequent prompt placement of enrichment waste in the underground mined space.

The current paper aims to present such a technology.

Materials and methods

The underground enrichment of potash salts must be based on the differences in the properties of the minerals that make up sylvinite. The universal parameter for the state of any mineral is its density. Potash ores contain three main components:

- sylvine (KCl, density 1.98 g/cm^3);
- halite (NaCl, density 2.17 g/cm^3);
- clay impurities (Al_2O_3 .2SiO_2.2H_2O, density 2.60 g/cm^3).

Therefore, if we prepare a non-aqueous, fire- and explosion-proof liquid with a density of 2.05 g/cm³, with a given set of all the main physical, chemical, and physiologically inert properties, in which mineral salts are devoid of solubility, then, after immersing a mechanical mixture of the minerals that make up sylvinite in such a natural liquid medium, only KCl will float to the surface of such a liquid medium, while all other components will sink (Wills and Napier-Munn, 2006).

Preliminary laboratory experiments on the stratification of sylvinite ore of varying sizes in a natural heavy liquid yielded results that fully confirm the feasibility of producing beneficiated products of acceptable quality.

However, after hydromechanical separation of such a system into concentrate and waste, the beneficiated products remain wet, carrying residual non-aqueous liquid phase on their surface. To avoid spending thermal energy to remove them in a dry state from such a beneficiation cycle, the liquid impregnating them must have a boiling point lower than the ambient medium mine air temperature. Then, by arranging heat exchange between such a wet material and the surrounding environment, the beneficiated products automatically become dry, and their further use is no longer impeded.

The non-aqueous vapours released from these processes can be compressed, condensed under elevated pressure, and thus the regenerated working heavy fluid can be returned to the head of the process. Consequently, the working fluid cycle is virtually completely closed, eliminating the need for thermal energy to dry the enrichment products.

The lower the boiling point of such a liquid, the easier it is to dry the enrichment products through heat exchange with the surrounding environment. In other words, the challenge of this technological process lies in the problem of loading the feedstock ore into such a low-boiling liquid, as the crushed rock leaves the face hot, not to mention the ambient air temperature. If this heated material is immersed in a liquid whose boiling point is lower than the ambient temperature, it will immediately boil.

To overcome this technological obstacle, an original solution is proposed in this paper. The working fluid must be at least two-component, consisting of a high-boiling and a low-boiling component. Moreover, the regeneration cycle of such a fluid must also include continuous rectification of the mixture into its two original components.

Then, by pre-loading the initial mechanical mixture of minerals into the high-boiling component of the fluid (which has not only a higher boiling point but also a higher density), it is possible to prevent the boiling of this less volatile liquid.

After this, the low-boiling component of the working fluid is added to the resulting suspension, bringing the density of the liquid mixture not only to an intermediate value between the minerals being separated but also lowering its boiling point to a level lower than the ambient mine air temperature.

Moreover, the milling of the feedstock ore can be carried out in the liquid itself, to avoid reducing the finished product's particle size below the threshold required by agricultural consumers.

Three pilot plants in total were used in the experiments.

The majority of the ore being mined from the face is represented by halite (NaCl) in an open form. Some reduction in the harmful impact of potash production on the environment is possible by increasing the selectivity of extracting sylvinite ore from layers of complex structure, separated from each other by a layer of rock salt. By sawing this monolith into blocks, pre-prepared building material is obtained that is ready for the construction of artificial pillars from it, to control rock pressure

instead of supporting the roof on expensive hydraulic supports, which are characterised by increased metal consumption.

These goals are achieved by a cutting machine equipped with a system for an advance preparation of rock salt blocks using saws for longitudinal and transverse cutting of the rock salt layer into monolithic blocks, followed by the assembly of stacks from them (with preliminary assembly of sets of such supports in the receiving unit of the cutting machine), with the subsequent construction of artificial pillars from them. The construction of artificial pillars from blocks of rock salt, prepared by sawing the monolithic balk remaining in the chest of the working face after the removal of the upper and lower layers of sylvinite, can be carried out using a forklift, available in the complex of mining equipment. The cutting machine can be equipped with a screening surface for preliminary removal of coarse halite with the subsequent use of halite tailings discharged as a damping bed during the construction of artificial pillars, thereby imparting a certain flexibility to them for a smoother absorption of rock pressure.

The harmful impact of potash production on the environment can be reduced not only by increasing the selectivity of sylvinite ore extraction from layers of complex structure separated from each other by a layer of rock salt, but also by organising the underground processing of initial raw material, using for this purpose a mobile enrichment plant equipped with a crusher and designed to continue the processing of potassium ore (Figure 4).

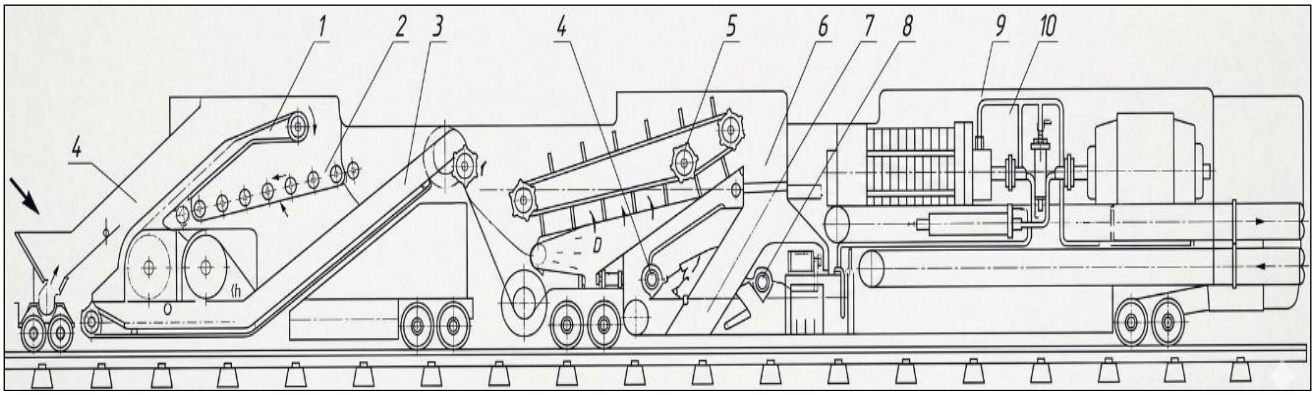


Fig. 4. Mobile pilot plant for separation of sylvinite in the field of gravitational forces:1. Feeder, 2. Classifier, 3. Loader, 4. Heavy liquid tank, 5. Scraper conveyor, 6. Concentrate receiver, 7. Waste product receiver, 8. Cover, 9. Regeneration system shown, 10. A conditional connection of the regeneration system with process pipelines

In this regard, the refined sylvinite coming from the shearer is loaded into the preparatory compartment 4, equipped with a roller crusher, after which, via conveyor 3, this material enters bath 6 for stratification of the mixture of salt minerals in a quiescent liquid medium.

To justify the optimal parameters of such a multi-stage enrichment process, modelling of the separation of sylvinite of various sizes was carried out on a pilot plant equipped with a separator with an internal scraper conveyor, the bath of which was flooded by a heavy liquid (Figure 5). Product of each preceding stage supplies for further processing to the next stage as its size decreases. This multi-stage beneficiation approach is designed to remove waste rock in its largest form, helping to save energy during grinding.

The upper branch of the internal scraper conveyor is designed to unload the floating concentrate, while the lower branch scrapes out the waste rock from the bottom of such a separator. The ore was first crushed in a hammer mill, and three ore classes of varying sizes were separated from it. Sylvinite with initial particles size of -30...+3 mm and KCl content of 25.5 % is used in the experiments.

The process flow diagram of the final stage of finishing the intermediate product to its final state using additional grinding and a centrifugal field is shown in Figure 6 (description of the equipment designation is given in the text). Rough concentrate obtained by enriching sylvinite concentrate with a size of -1...+0 mm in a bath with a stationary heavy liquid of a static separator (Figure 5) is used for the process in Figure 6. This process diagram shows a sylvinite enrichment system using a centrifugal field to separate the finest ore fractions (less than 1 mm) to intensify their stratification.

The material is loaded from bin 1 via feeder 2 through rotary valve 3 into mixer 4, where this material is pre-mixed with the heavy component of the working fluid, dibromo(difluoro)methane - CBr_2F_2 - a colourless non-flammable liquid with density 2.28 g/cm³, boiling point 24.5 degrees Celsius (Morachevskii and Sladkov, 1996) and NIOSH REL of 860 mg/m³ (https://www.cdc.gov/niosh/npg/npgd0214.html).

The resulting suspension is diluted in mixer 5 with the light component of the working fluid, difluorochlorobromomethane $CBrClF_2$ - a colourless non-flammable liquid at low temperatures with density 1.83 g/cm³ and boiling point - 3.4 degrees Celsius (Morachevskii and Sladkov, 1996; https://pubchem.ncbi.nlm.nih.gov/compound/Bromochlorodifluoromethane) until the liquid phase of this system reaches a density of 2.05 g/cm³. This substance is used to extinguish fires because it is not hazardous (the maximum permissible concentration in the atmosphere of the working area is 1000 mg/m³ (Tryon et al., 1969).

Wet milling of the ore is carried out in drum mill 6. The mill drum is half-filled with a liquid medium whose density is between that of the minerals being separated. The opened sylvinite minerals, which do not require grinding, remain afloat, while the intergrown KCl and NaCl crystals sink into the grinding media. As a result, as they are released from the intergrown crystals, the valuable minerals escape the impact of the balls, preventing further unnecessary destruction.

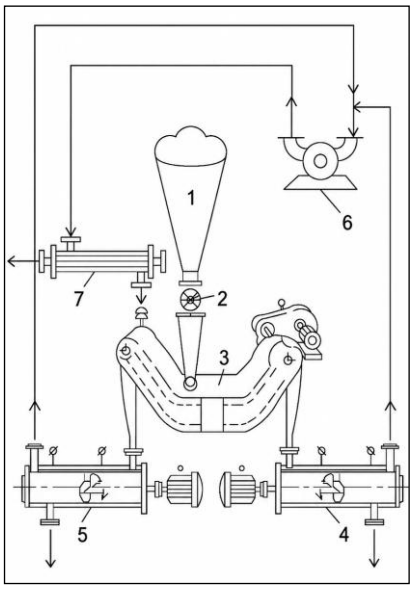
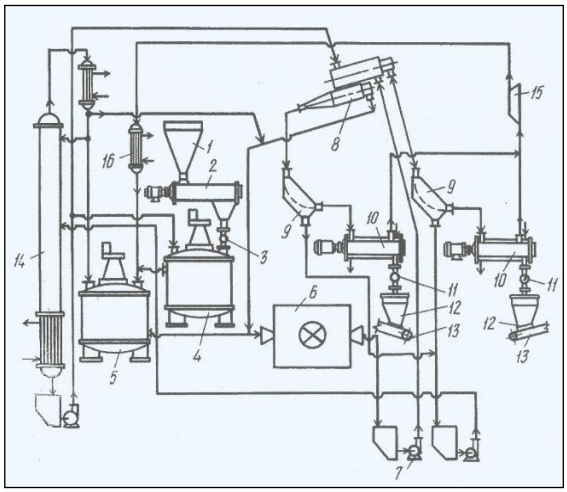




Fig. 5. Separator for separation of sylvinite in a gravitational field (a) Chart of a pilot plant with a bath-type separator: 1. Loading hopper, 2. Rotating shutter, 3. Separator, 4. Concentrate dryer, 5. Gangue minerals dryer, 6. Compressor, 7. Condenser; (b) Photo of the pilot installation working underground

The overflow from mill 6 is directed by pump 7 to centrifugal separation in a three-product hydrocyclone 8. The conditioned products of gravity enrichment, separated by means of a centrifugal field, are wringed from the liquid phase on arc screens 9, after which they are dried in evaporators 10, operating under a vacuum created at the suction of compressor 15. The intermediate product of centrifugal enrichment of sylvinite ore, represented by still under-opened intergrowths, is returned from the three-product hydro cyclone 8 to the mill 6. To intensify the evaporation of the liquid impregnating the enrichment products, warm mine air is blown into the jackets of evaporators 10.

Dry enrichment products are discharged through rotary valves 11, accumulated in storage tanks 12, and then sent for further transportation on belt conveyors 13. A portion of the working fluid, freed from its solid phase, is sent for distillation to the distillation column 14, where it is separated into a heavy component (dibromo(difluoro)methane) and a light component (difluorochlorobromomethane).



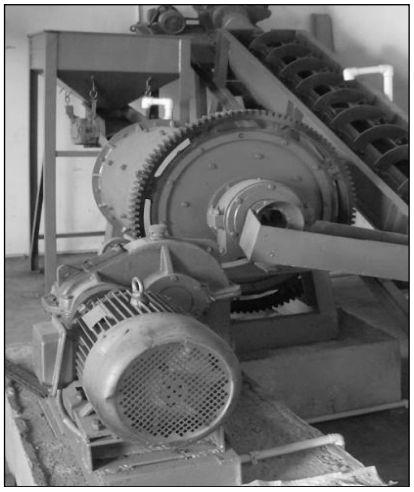


Fig. 6. Process flow diagram (a) and a picture of the pilot plant used in the final series of experiments (b)

Dibromo(difluoro)methane is fed to the feedstock ore and to weight the liquid phase of the system entering the cylindrical-conical section of hydrocyclone 8, while difluorochlorobromomethane is used to dilute the sylvinite suspension to a lower density prior to centrifugal separation of the ore's constituent mineral mixture.

The non-aqueous vapours released from the evaporators are sucked in by compressor 15. They are liquefied in condenser 16, after which the regenerated working fluid returns to mixer 5, thereby completely closing the circuit of its internal circulation.

However, the set of underground mining operations in this case does not end with the receipt of the finished product, since this material must be raised to the earth's surface and loaded into railway cars.

Traditional mine hoisting systems suffer from an inherent technological drawback, such as high cyclic operation and, associated with this circumstance, a sharp drop in the productivity of rope-and-skip hoisting installations with increasing depth of the extracted raw material (Ilin et al., 2019).

This disadvantage is overcome by switching to a continuous process of delivering the finished product by its continuous floating vertically in a stationary liquid with a density exceeding its own. Tests of this process were carried out on a pilot plant, using the same liquid that filled the separator for enriching sylvinite (Figure 7). The purpose of testing the lifting pilot plant shown in Figure 7 was to determine the competitiveness of hydrostatic hoisting by continuously moving product up a vertical

borehole with the cyclic operation of a conventional vertical mine mechanical haulage system using a skip hoist. The experiments were conducted with concentrate sizes of 0.707-0.841 mm and 0.841-1.000 mm. This pilot unit was installed in two configurations, depending on the size of the material being loaded. When handling lower-size material, the loading unit was designed as an auger (position 2). To load larger material, a rotary valve (position 3) was used. The vertical pipeline 4 was made collapsible, which allowed testing such a system with different heights of material floatation (Figure 8).

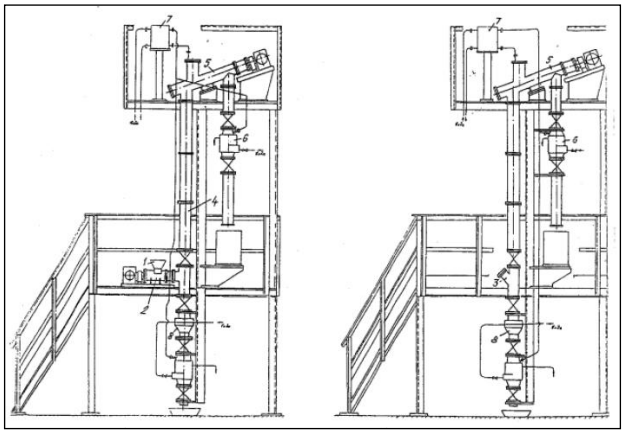


Fig. 7. Installation of hydrostatic lifting of the finished product by its buoyancy: 1. Loading hopper, 2. Screw feeder, 3. Airlock loader, 4. Pipeline, 5. Unloading auger, 6. Dryer with electric heating, 7. Condenser, 8. A trap for substandard products

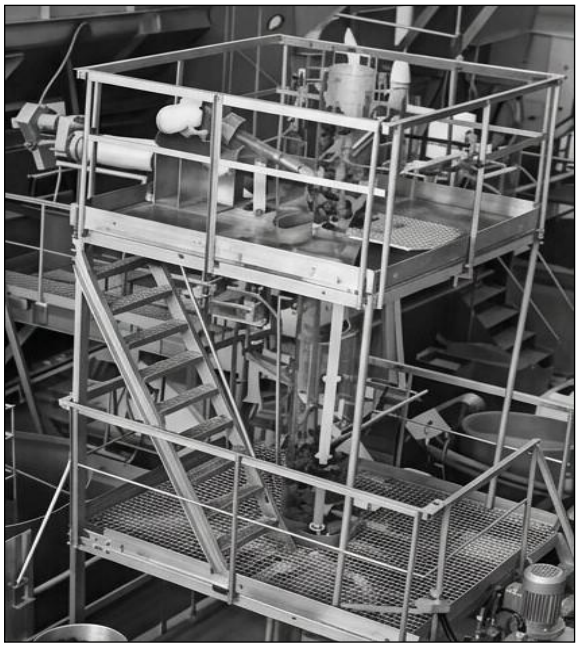


Fig. 8. General view of the pilot hydrostatic lift unit

Results and discussion

The obtained results of testing the step-by-step enrichment process through implementing each stage of such a process in a continuous mode (with a reduction in particle size as it is ground and the majority of the ballast rock salt is removed in the largest possible form) - obtained during testing with the setup shown in Figure 5 - confirmed the full validity of the multi-stage enrichment of potassium salts in underground conditions, since after each stage of separation it is possible to separate the waste rock with the least energy consumption for its grinding. Results are presented in Tables 1 - 3.

Table 1. *Stage 1: Enrichment of sylvinite with a size of -30...+3 mm*

Parameter/ Product name	Yield, %	Content, % KCl	Recovery, % KCl
Initial sylvinite	100	25.5	
Concentrate	34	72.4	96.5
Final tailings	66	1.34	3.5

Table 2. *Stage 2: Enrichment of pre-enriched sylvinite with a size of -3...+ 1 mm*

Parameter/ Product name	Yield, %	Content, % KCl	Recovery, % KCl
Pre-cleaned sylvinite	100	72.4	
Concentrate	78	92.4	99.6
Final tailings	22	1.28	0.4

Table 3. *Stage 3: Refinement of rough concentrate to a final product with a particle size of -1...+0 mm*

Parameter/ Product name	Yield, %	Content, % KCl	Recovery, % KCl
Pre-cleaned sylvinite	100	92.4	
Concentrate	95.8	96.4	99.95
Final tailings	4.2	1.02	0.05

As it can be seen from Tables 1 – 3 decreasing the particles size by additional grinding increases sylvinite recovery and grade.

However, the separation capacity of fine material in a stationary heavy liquid does not allow for high process throughput. Therefore, unlike the three previous enrichment stages, the final refinement of the concentrate to a high-quality end product was carried out in a centrifugal field using hydrocyclones (see Figure 6).

The results of processing rough concentrate in a beneficiation system with additional grinding in a drum mill and the use of a centrifugal field to intensify separation (the equipment shown in Figure 6) are not much different from the beneficiation of such an intermediate product in a stationary heavy liquid – Table 4. However, although separation in a centrifugal field is not as precise as in a bath, in a hydrocyclone the process is incomparably faster than in a stationary liquid. The grade of the product obtained (Table 4) is comparable with that of the market available fertilizers (Wakeel and Ishfaq, 2022).

The success of the entire process of producing the final product with minimal environmental impact is largely determined by the mining technology. Therefore, the higher the selectivity of sylvinite seam extraction without rock salt contamination, the more economical and environmentally friendly the production will be.

Table 4. *Stage 3: Final refinement of rough concentrate to a finished product with a particle size of -1...+0 mm in centrifugal field*

Parameter/ Product name	Yield, %	Content, % KCl	Recovery, % KCl
Pre-cleaned sylvinite	100	92.4	
Concentrate	94.2	97.9	99.78
Final tailings	5.8	3.1	0.22

A mixture of halogenated organic compounds based on dibromomethane is proposed as the working fluid in an attempt to beneficiate high-clay potash ores using continuous heavy liquid concentration (Liles et l., 1973). In this case, a mixture of halogenated organic compounds based on dibromomethane is used as the working fluid. The density of this base liquid is 2.48 g/cm³ while the boiling point is 99 degrees Celsius. Therefore, all components of the sylvinite ore float up within it, and mechanical separation of the mineral mixture does not occur. To reduce the density of such a working fluid, trichloroethylene is used. This solvent has a density of 1.46 g/cm^3 and a boiling point of 86.5 degrees Celsius. Hence, the boiling point of the working mixture of these two liquids is at a level of approximately 95 degrees Celsius.

However, after the separation of the minerals that make up the initial raw material into concentrate and tailings, both of these enrichment products will remain impregnated with such a high-boiling liquid. In order to remove the enriched products from such an enrichment process in dry form, they will have to be heated to high temperatures directly in the mine (in the case of underground enrichment).

On the other hand, as the depth of potash ore increases, the temperature of the atmosphere in the mine also increases in proportion to the size of the geothermal step. Assuming a geothermal gradient of 35 meters per degree Celsius (https://www.icgc.cat/en/Thematic-areas/Territori-sostenible/Potencial-solar-i-geotermic/Geothermics/Geothermics-Gradient-flow-and-propagation), we can determine the depth of a mine where the host rock temperature is at least 100 degrees Celsius. We'll also assume the ground temperature at the Earth's surface is 25 degrees Celsius. A temperature increase of 75 degrees Celsius would occur if we descended to a depth of 75 x 35 = 2625 meters. In this case, if the enrichment products are impregnated by a liquid with a boiling point of 95 degrees Celsius, then such a liquid can be distilled off from them with hot air and the concentrate and waste can be dried directly in the mine.

However, there are no deposits of potassium salts at such great depths, while at a depth of 800 meters the ambient temperature is clearly insufficient to evaporate the remains of the non-aqueous working fluid prepared on the basis of high-boiling brominated organic compounds from the surface of the enrichment products.

The fire- and explosion-proof heavy liquid system proposed here overcomes the shortcomings pointed. Using the natural heat exchange between wet beneficiation streams and the surrounding environment, the beneficiated products automatically become dry in the nowadays potassium salts mines.

When comparing the proposed method with classical flotation, it should be emphasized that before sending the potassium ore to flotation, it must first be completely crushed to a particle size of less than 1 mm, whereas 75% of the composition of such raw material consists of waste rock.

Three-quarters of potash ore is ballast. The energy consumption for lifting ore is directly related to the volume of rock mass lifted (Mine Hoist Equipment Electrical Calculations – 911 Metallurgist). Therefore, energy costs, regardless of the method used to lift the finished concentrate instead of the original ore, will be four times lower.

Unlike lifting installations cyclic action, the level of energy perfection of hydrostatic lifting is several times higher, since it does not require lifting vessels, whose mass is almost equal to the weight of the portion of ore being lifted.

Besides the lack of energy required to lift the skips, the working fluid remains stationary. Therefore, only material that has to be moved vertically moves. Everything else remains stationary. It is also necessary to take into account the absence of dusting during the operation of hydrostatic lifting, while losses of transported cargo due to dust carried away from the delivery of mined ore by mine hoisting units can reach 0.5...1.5%. (Cecala et al., 2019).

From an economic point of view, the costs of constructing a hydrostatic lifting system are incomparably lower. Sinking a large diameter shaft takes several years, while drilling a borehole to the same depth takes several months (Bołoz, 2019).

To illustrate the advantages of hydrostatic lifting over the use of rope-and-skip devices, we present the results of measurements of the floating up to the surface rate of sylvine grains (using the pilot plant shown in Figures 7 and 8) and the calculations of the productivity of this method based on them of delivering finished products to the earth's surface – Table 5:

Table 5. *Productivity of hydrostatic lifting achieved in continuous operation mode*

Concentrate size, mm; Parameter	0.707-0.841	0.841-1.000
Concentrate density, kg/m^3	1980	1980
Density stationary liquid, kg/m^3	2270	2270
Buoyancy rate, m/sec	0.21	0.38
Transverse diameter of the well, m	0.3	0.3
Efficiency, kg/sec	29.1	52.7
Productivity, t/h	104.8	189.6

Potash ore is typically mined at a productivity rate of 350-400 tons per hour. However, no more than a quarter of this mass is extracted from the ore as finished products, or 90-100 tons per hour. Therefore, a hydrostatic lift is fully capable of handling this load.

So, as a result of the tests on delivering the finished products to the surface by floating them up in a vertical well, it was proven that a mine shaft with a diameter of 6...8 m can be replaced by a borehole with a diameter of 250...300 mm, filled with a liquid with a density superior to the floating material, which will ensure the same lifting performance due to the continuity of the transport process.

There is not a single mineral deposit in the world that can be mined indefinitely. The only question is the environmental consequences after the closure of such a mine. Only potash deposits, once their reserves are depleted, will pose a threat to

the environment, since the waste rock remaining on the earth's surface is water-soluble material.

The only way to prevent such a dramatic scenario is to abandon the processing of potash ore on the surface and instead produce the finished product in underground conditions.

Conclusions

The processing of potassium salts in underground conditions based on the use of gravitational enrichment of sylvinite in a fire- and explosion-proof liquid with a given set of physical properties, followed by a full cycle of its energy-efficient regeneration solves the following problems: (i) occupation of arable land by waste heaps of clay-salt sludge, (ii) salinisation of groundwater and (iii) unsuitability of adjacent soils for agricultural use.

The finished product (high-grade sylvine concentrate) can be delivered to the surface by floating it in a vertical well in the proper inflammable liquid with a density that exceeds the concentrate density. This way the productivity of the hoisting systems is increased at decreased energy use.

Laboratory studies and pilot tests have confirmed the direct economic feasibility of applying the enriching of the initial halurgical raw materials in underground conditions by using fire- and explosion-proof non-aqueous heavy liquids with a given set of physical properties.

The proposed technology is environmentally friendly with a full cycle of energy-efficient regeneration of reagents.

References

Andrejchuk, V. & Rózkowski, J. (2000): Hydrogeological conditions and environmental hazard of salt dumps with special reference to potassium salt deposits in Vierchniekamsk, the Middle Ural Mountain, Russia. - Proceedings, 7th International Mine Water Association Congress: 38-48. https://www.imwa.info/imwaconferencesandcongresses/imwa-congresses/152-proceedings-2000.html

Bołoz, Ł. (2019). The analysis of shaft sinking progress as a function of technical and organisational parameters. *Multidisciplinary Aspects of Production Engineering, 2*(1), 203-212. DOI:10.2478/mape-2019-0020

Cecala, A.B., O'Brien, A.D., Schall, J., Colinet, J.F., Franta, R.J., Schultz, M.J., Haas, E.J, Robinson, J., Patts, J., Holen, B.M., Stein, R., Weber, J., Strebel, M., Wilson, L., & Ellis, M. (2019). *Dust control handbook for industrial minerals mining and processing.* 2nd ed. U.S. Department of Health and Human Services, Centers for Disease Control and Prevention, National Institute for Occupational Safety and Health NIOSH, Publication No. 2019–124, RI 9701, Pittsburgh PA.https://doi.org/10.26616/NIOSHPUB2019124

Eminov, E., Mirzakulov, K., Melikulova, G., Arifdjanova, K., Boymatova M. (2026). Reverse flotation for enhanced desliming of low-grade sylvinite ores from the Khojaikon deposit. *International Journal of Advanced Research in Science, Engineering and Technology,13(*5), 25060-25065. chrome-extension://efaidnbmnnnibpcajpcglclefindmkaj/ https://www.ijarset.com/upload/2026/may/29-e_eminov-35.pdf

Florkowska, L., & Bryt-Nitarska, I. (2025). Natural and anthropogenic rock mass deformations as threats to sustainable development, In Sokoła-Szewioła & Jarczyk (Eds.), *Mine Surveying and Mining Area Protection* (1st ed.), CRC Press. DOI: 10.1201/9781003655558-6

Ilin, S., Adorska, L., Samusia, V., Kolosov, D., & Ilina, I. (2019). Conceptual bases of intensification of mining operations in mines of Ukraine based on monitoring and condition management of mine hoisting systems. *E3S Web of Conferences - Essays of Mining Science and Practice 2019, 109,* 00030. https://doi.org/10.1051/e3sconf/201910900030

Jasinski, S.M. (2026) Potash. In *U.S. Geological Survey, 2026, Mineral commodity summaries (ver. 1.3, May 2026).* U.S. Geological Survey, pp. 146-147. https://doi.org/10.3133/mcs2026

Latipov, Z., Uzoqov, Z.Z., & Bobomurodov, A.Yu. (2023). Development of recommendations for chemical fixation of salt waste. *Universum: tekhnicheskie nauki: elektron. nauchn. zhurnal 10*(115). https://7universum.com/ru/tech/archive/item/16103).

Liles, K. J., Brown, J. W., & Sullivan, G. V. (1973). *Continuous heavy liquid concentration of high-clay potash ores.* Washington, U.S. Dept. of the Interior, Bureau of Mines.

Liskova, M. Yu. (2017). Negative impact on the environment caused by companies that mine and process potassium and magnesium salts. *Bulletin of PNRPU. Geology. Oil & Gas Engineering & Mining, 16* (1), 82–88. DOI: 10.15593/2224-9923/2017.1.9

Morachevskii, St. A.G., & Sladkov I.B. (1996). *Fiziko-himicheskie svojstva molekulyarnyh neorganicheskih soedinenii (Physicochemical properties of molecular inorganic compounds)*. Petersburg, Khimiya.

Tryon, G. H., & McKinnon, G. P., (1969). *Fire protection handbook* (13th ed.), Published by National Fire Protection Association.

United Nations (2025). *The Sustainable Development Goals Report 2025 - revision August 2025.* Department of Economic and Social Affairs, New York. chrome-extension://efaidnbmnnnibpcajpcglclefindmkaj/https://unstats.un.org/sdgs/report/2025/The-Sustainable-Development-Goals-Report-2025.pdf

United Nations. (2024). *World population prospects 2024: Summary of Results* (UN DESA/POP/2024/TR/NO. 9). New York, United Nations. https://desapublications.un.org/publications/world-population-prospects-2024-summary-results

Ushakova, E., Perevoshchikova, A., Menshikova, E., Khayrulina, E., Perevoshchikov, R., & Belkin, P. (2023). Environmental aspects of potash mining: a case study of the Verkhnekamskoe potash deposit. *Mining, 3*(2), 176–204. https://doi.org/10.3390/mining3020011

Wakeel, A., & Ishfaq, M. (2022). Potash for quality of agricultural commodities. In *Potash use and dynamics in agriculture*, Springer, Singapore. https://doi.org/10.1007/978-981-16-6883-8_6

Wills, B. A., & Napier-Munn, T. (2006). *Mineral processing technology, an introduction to the practical aspects of ore treatment and mineral recovery* Elsevier Science & Technology Books.

GEOPHYSICAL INVESTIGATIONS USING SEISMIC REFLECTION METHOD IN THE AREA WITH THE GEOTHERMAL WATERS

Blagica Doneva, Zoran Panov, Radmila Karanakova Stefanovska, Risto Popovski

Faculty of Natural and Technical Sciences, Goce Delcev University, Stip, North Macedonia, blagica.doneva@ugd.edu.mk
Corresponding author: blagica.doneva@ugd.edu.mk

ABSTRACT. Reflection seismic investigations in the „Podlog-Banja" geothermal field are the first investigations of this kind planned to perform „pilot" doublet-system for using of geothermal energy in the Republic of Macedonia. The selection of the "Podlog–Banja" geothermal field for the installation of a pilot doublet system was based on its favourable geothermal characteristics and the availability of an established team of qualified experts who could manage, monitor and operate the system effectively. Reflection seismic surveys were conducted within a metamorphic rock complex overlain by sedimentary and volcano-sedimentary formations with a thickness of approximately 300–500 m. Under such geological conditions, the quality of the seismic reflection data is expected to be lower than that typically achieved in geological environments characterised by horizontal layers. The effectiveness of the studies is further limited by the inclined spatial orientation of the geological structures and the low seismic velocity contrasts among the lithological units in the investigated metamorphic complex. These factors reduce the resolution and interpretability of the acquired seismic data. Due to the inclined spatial orientation of the geological units, the litho-spaces identified through reflection seismic investigations have not been adequately documented by previous drilling activities within the "Podlog–Banja" geothermal field. As a result, the litho-physical interpretation of the reflection seismic results should therefore be regarded as "forecasting".

Key words: Podlog - Banja, seismic, reflection, geothermal.

Introduction

Reflection seismic investigations are actual phase of the investigations for performing the pilot-industrial doublet system in geological environment of the "Podlog-Banja" geothermal field.

The feasibility of the proposed location for the doublet wells is evaluated primarily on the basis of the presence of karstified carbonate rocks. With that goal, reflection seismic investigations were realised on 4 profiles at a depth of 1500 m. On the base of the results from the reflection seismic investigations final decisions for micro locations and projecting of the performance of the planned investigational and doublet - system wells was made (Babaei, 2019; Mahbaz, 2021).

Kocani geothermal field is situated within a complex geologic region, structured by the following 3 tectonic units: Vardarian zone, East-Macedonian zone and Kratovo-Zletovo volcanic area between them. The main directions of the tectonic distortions of this geologic region are north-west and north-east. The block of Kocani geothermal field is a lifted structural-tectonic block with an approximate area of 2.5 x 4.0 km, which is bended to the north-east. The depth of bedding in this block varies from 400 m to south-west to 750 m to the north-east.

According to the geological data, the terrain of the Kocani geothermal field is structured from the following litho-straticgraphic units (Rakikevic et al., 1965 – 1968):

- Q - Quaternary (alluvial) sediments – of dust, clay, sand, gravel;
- Ol - Oligocene sediments – predominantly of alevrolites;
- (aω) - Oligocene upflowing magmatism - andesites, andesitic tuffs and breccia;
- E_3 – Upper Eocene sediments - erosion backwards of marble, sandstone limestone;
- Pz_1 - Palaeozoic (and Proterozoic age rocks) - metamorphic basement of the terrain, built from schist and carbonate rock (limestone and dolomites) which are of great importance for the "Podlog-Banja" hydrothermal system.

The metamorphic basement of the terrain is related to the Hercinic orogenesis. The general structural and tectonic framework of the geothermal field can be interpreted as a tectonic, pre-existing anticlinal structure. The strongest tectonic processes are related to the Tertiary, more particularly the Neogen till the beginning of the Quartery.

Hydrogeothermal conditions of the Kocani geothermal field have been studied based on analysis of the drilling results and testing of 19 (nineteen) investigating and operational wells and data on the industrial operation of 4 (four) exploitation and 1 (one) reinjection well. The depth of these wells varies from 86.5 m to 1096 m. As general characteristics of the Kocani geothermal field, we should note the following:

- The distribution of temperature in the area of the geothermal aquifer is unequal. In the central part of the field the temperature is 70 °C – 78 °C, while in the peripheral part it decreases to 50 °C. During the operational period (about 25 years) no changes of temperature have been observed both in the area and in the exploitation well head.
- The circulation of thermal waters within the field is not limited by a particular lithological type of rocks but it relates to porous and cracked permeable zones within the geological environment of the geothermal aquifer. In general, the distribution of these zones is typical for 450-550 m depth.
- The thermal waters are characterised as bicarbonate–sulphate–chloride–sodium type waters, with pH = 7 and water mineralisation of ≈1.0 g/L.

Static heat measurements in the wells show that within the field there is a natural flow of ground water, which flows to the northern direction, i.e., the flow is directed from the central part of the Kocani valley to its peripheral parts.

Although the seismic data were originally acquired during investigations conducted in 2008 for the "Podlog–Banja" geothermal field, the present paper does not represent a simple reproduction of the original technical report. The current study

provides a revised geological and hydrogeological interpretation focused specifically on the suitability of the area for modern geothermal doublet - system applications. In contrast to the original report, this paper integrates the seismic interpretation with contemporary concepts of geothermal reinjection systems, well-doublet spacing optimisation, and sustainable geothermal reservoir management. The study additionally discusses the limitations of seismic reflection investigations in metamorphic environments characterised by inclined structures and low seismic-velocity contrasts, which were not elaborated in detail in the original documentation. The results from 2008 have not been published previously.

Well locations of the doublet system

The selection of the doublet-wells locations was based on the following considerations (Wu, 2021; Wang, 2022):

1. The distance between the reinjection and production wells should ensure the time needed for the temperature front to reach the reinjected cooled down waters, i.e., operation of the production well with constant temperature of the heat carrier at the head for a period of about 30 years.
2. The production well should be located as close to the geothermal heat exchangers as possible to decrease the capital costs for laying down the heat insulated thermal water pipeline.
3. The geological structure, the geothermal and hydrogeological conditions of the section, where the doublet system well will be placed, should comply with the following requirements:

a. The productive collector should be maintained in horizontal and vertical perspective;
b. The filtration parameters of the productive collector within the area of developed section should be relatively the same;
c. The stratum temperature within the whole developed section should be approximately the same;
d. There should be no hydrodynamic interaction of the productive collector with the upper and lower aquifers;
e. The capacity of the productive collector should ensure a high injectivity of the reinjection well;
f. The natural stream of thermal waters, if any in the productive aquifer, should impact the reinjected cooled down thermal waters in a way preventing their movement to the side of operation, within the geothermal field wells.

The spacing between the production and reinjection wells of the doublet system is determined through heat mass transfer calculations within the permeable reservoir formation in which both wells operate. The temperature of the stratum fluid is set to 80°C. The temperature of the cooled down geothermal water is set to 30°C.

Depending on the heat load in a heating season, the reinjection flow varies between max 40 l/s and min 12.5 l/s.

Within the heating season there is a constant production and reinjection flow in the doublet system equal to 22 l/s. In the summer period the doublet system is closed, i.e., the production and reinjection volumes equal to zero (Torres, 2019; Gascuel, 2024).

Using the above assumptions and the thermal physical and filtration parameters of the stratum fluid and rock structure, the set period of 30 years of the doublet system operation is ensured by a production and reinjection volume of 22 l/s. This proves that the distance between the production and reinjection wells ensuring the production of geothermal water with constant temperature at the well head should be at least 800 m. This is the distance between the wells' bottoms but not the distance between drill sites (Satman, 2011; Xia, 2017).

Two drilling sites were selected for the reinjection and production wells in the Kocani valley - two recommended options for dislocation of the production and reinjection wells of the doublet system to be established on the Kocani geothermal field (Figure 1).

The final decision on the location of the production well must be taken during the drilling project design upon completion of additional geophysical works.

The reinjection well is in the northern outskirts of the village D. Podlog close to the thermal water main pipeline (Vardon, 2020; Vižintin, 2024).

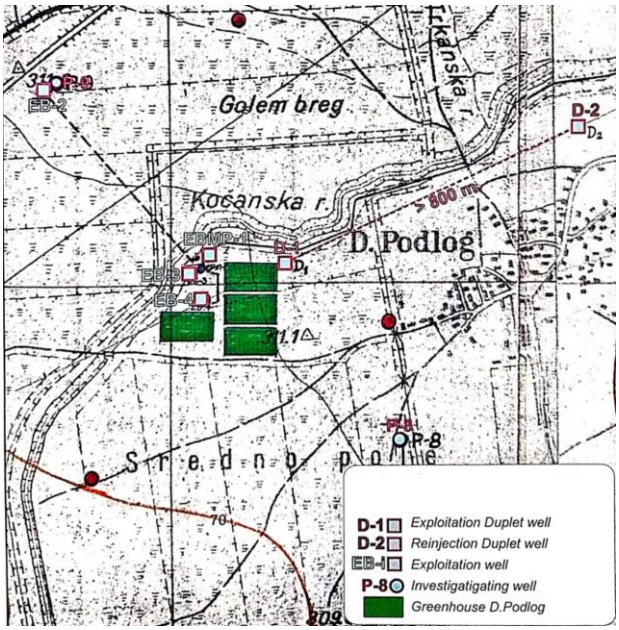


Fig. 1. Topographic map with wells locations
EBMP-1 – exploitational well

The main arguments justifying the selection of drilling sites are given below:

- The doublet system wells should be located close to the designed geothermal heating substation, where geothermal heat exchanges are installed.

- The doublet wells should be located perpendicular to the natural stream of thermal waters in the productive aquifer which ensures drift to the zone of thermal water pumping due to this stream. This zone is in the opposite direction from the production wells EB-1; EB-2; EB-3 and EB-4 (Figure 1). This one is an additional factor ensuring safety of the heat mass transfer calculations.

- Doublet wells are located within the tectonically insulated block of well heated rocks with relatively homogeneous filtration properties and roughly similar, on the block area, stratum temperature.

- Wells have to be located on the flat relief area having nearly horizontal surface which allows elimination of the hydraulic resistance in the pipeline that could happen due to

overcoming difference in the geodesic marks in some sections of the pipeline.

Re-injection and production wells level has shown the following:

- The water level in reinjection well D-2 during operation is expected to remain below ground surface elevation. Consequently, the well is expected to operate in a “pouring-in” reinjection mode.

- Regardless of the water re-injection into well D-2 in the amount of 340 000 m^3/year, the depth of the level in both D-1 and D-2 wells shall continue to decline in time indicating strata energy recharge deficiency by re-injection into D-2.

- The intensity (rate) of the level drop in the doublet wells is different and depends on the total volumes of geothermal water production in Kocani.

- The anticipated depth of geothermal water in the production and the re-injection wells within 30 years of operation: re-injection well about 70 - 90 m, production well - about 80 – 100 m.

Reflection seismic investigation

The reflective seismic investigations were conducted on the following four investigated profiles: Ko-0701, Ko-0702, Ko-0703 and Ko-0704. The investigated profiles were realised with effective length of 1.250 m to 2.600 m, and with a total effective length of 7.815 m (Mirakovski, 2008).

The profile Ko-0701 was carried out with a length of 2.5 km, in parallel with the structural-tectonic direction "Podlog - Banja" (close to the North-South direction). The other investigated profiles were carried out approximately in normal direction of Ko-0701 (East-West), with lengths of 1250 - 2300 m, and their eastern sides were intersected with profile Ko-0701.

Parallel to profile Ko-0702, two shorter parallel profiles, Ko-0702a and Ko-0702b, were surveyed on either side of the facility. Each profile had a length of approximately 320 m and provided an investigation depth of 700–1000 m. These profiles were conducted to improve the understanding of the local hydrogeological conditions in the vicinity of production well D-1 and to support the selection of its optimal microlocation.

Seismic wave generation was achieved using explosive charges placed in boreholes with a depth of 2.5 m, ensuring detonation below the groundwater table. Seismic data acquisition was carried out using 30 Hz geophones and a 24-channel Terraloc Mark-6 seismograph (by ABEM, Sweden). Linear disposition was used for the excitement and geophone positions, with excitement step of 20 m and geophone distance of 10 m.

Investigations were carried out with two excitements for each position, and with two geophone dispositions with 24 channels.

Profile Ko-702 was realised with minimal offset of 40 m. To register better reflections from the metamorphic complex, the minimal offset of the other profiles was enlarged to 160 m.

Results of the reflection seismic explorations

Using 2D - processing, the results of the investigations were finalised in the following reflexive seismic sections:

- Definitive (non-migrated) time section;
- Migrated time section;
- Definitive (non-migrated) depth section;
- Migrated depth section.

To convert the Time-section to Depth-section a “Smoothed RMS- velocity” was used within “time-velocity models" per each of the investigated profiles.

For a series of parallel layers of velocity V_i, where the travel time of the seismic energy perpendicularly through each layer is t_i, the RMS (root-mean square) - velocity is defined using the following expression:

$$V_{RMS} = [\sum V_i^2 \, t_i / \sum t_i]^{0.5}.$$

where is:

V_{RMS} - root mean square seismic velocity

V_i - interval seismic velocity of the i-th layer

t_i - two-way travel time through the i-th layer.

Geological interpretation

The results from the investigation are shown on definitive and migrated (Figures 2 and 4) depth seismic sections of the exploration profiles, in variants with “presented" and “generalised” deposit over metamorphic basement. The following litho-mediums are interpreted in the depth sections:

- ✓Quaternary sediments (Q) - alluvial deposit present at a depth of ≈ 200 m;
- ✓Oligocene sediments (Ol) - alevrolites present at a depth up to 500 m;
- ✓Oligocene up flowing magmatism (aω) - andesites and andesitic tuffs, with presence in the “roof” as well in the basement of the Oligocene sediments;
- ✓Eocene sediments (E_3) - erosion backwards with thickness of up to 50 m;
- ✓Paleozoic basement (Pz_1 - probable Ordovician age) - presents at depths from 280 m up to over 500 m, built from low water-permeable or non-water - permeable schist rock.

The objective of the investigation was to characterise the lithophysical structure of the metamorphic basement underlying the geothermal field. Particular attention was paid to the occurrence and spatial distribution of karstified limestone units within the basement complex, as these formations represent the most favourable reservoir environment for both geothermal water production and the reinjection of spent geothermal fluids through the doublet-well system.

From the "Time-Velocity" models (Figures 3 and 5) of the investigating profiles the following interpretation of the terrain structure is presented:

According to the first half of profile Ko-702 (Figure 3), the increased amplitudes of the seismic sections indicate karstified limestones, but they are not the only factor for this increase. Similar seismic reflection patterns were not identified elsewhere along the surveyed profiles. However, this observation should not be interpreted as evidence for the absence of additional karstified limestone bodies within the investigated area due to the following considerations:

- The limestone rocks in the investigated terrain are among the oldest rocks in the region, and it is realistic to expect to be intensively cracked;

- Cracking of the carbonate rocks is a precondition for their karstification. Taking into account the geological age of this terrain, it is reasonable to assume that karstification processes have been active over extended periods of time.

- With geothermal water above 40 ^{o}C, the karstification processes become more intensive, and dolomites can also be karstified.

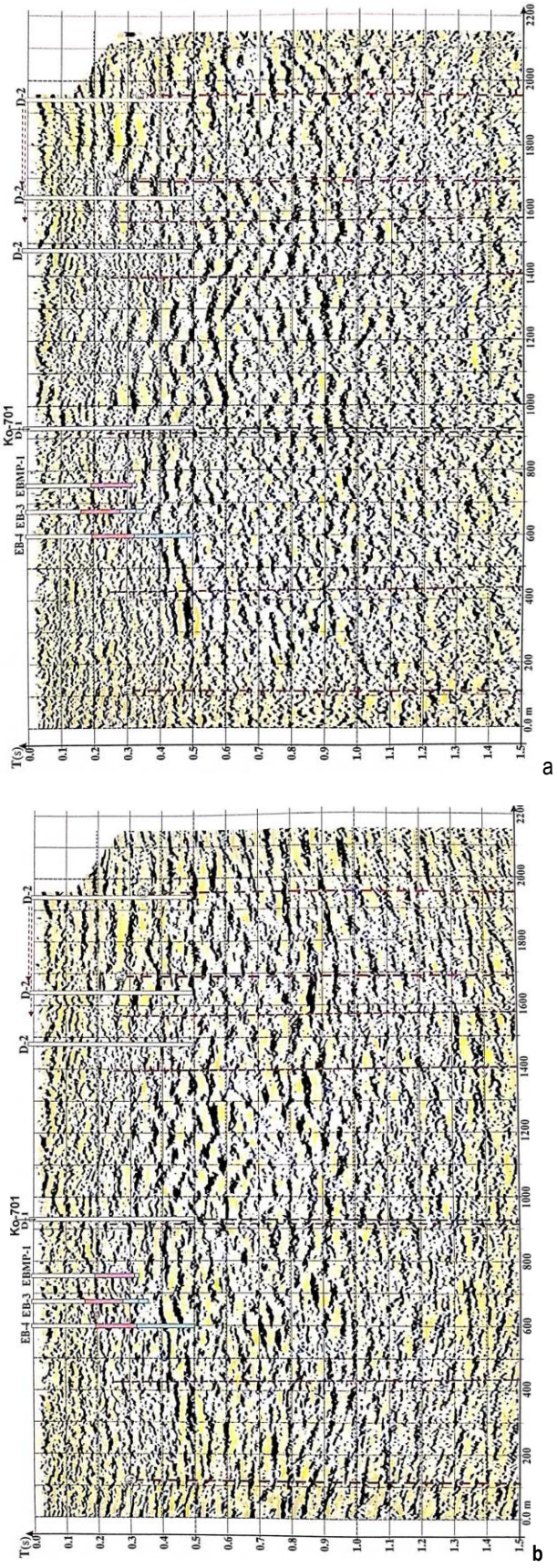


Fig. 2. Profile Ko – 702 Definitive (a) and migrated (b) time section

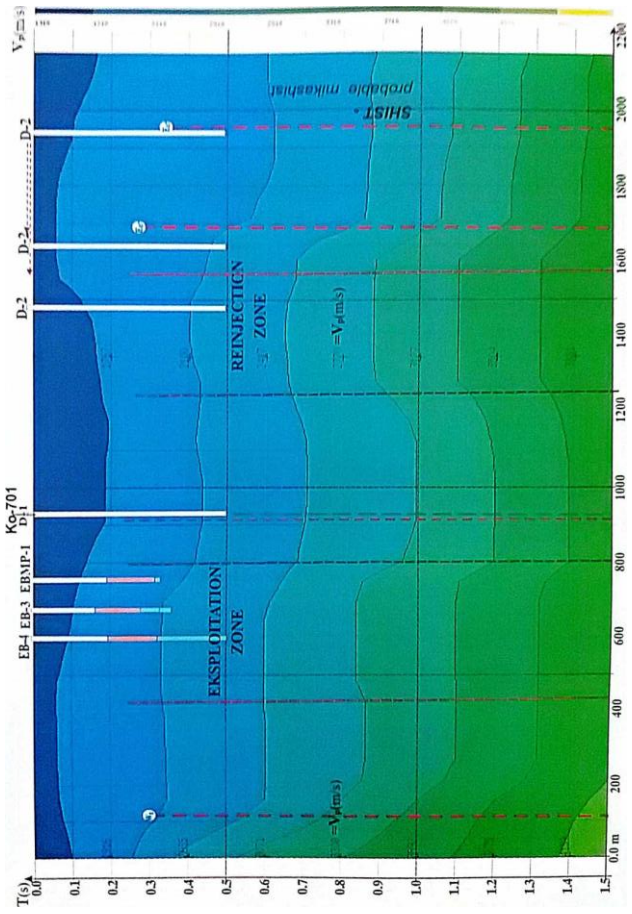
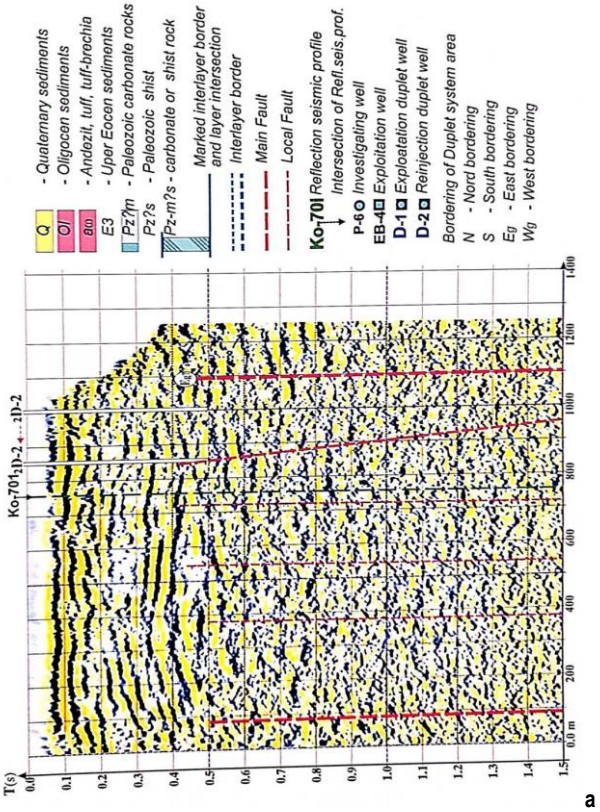
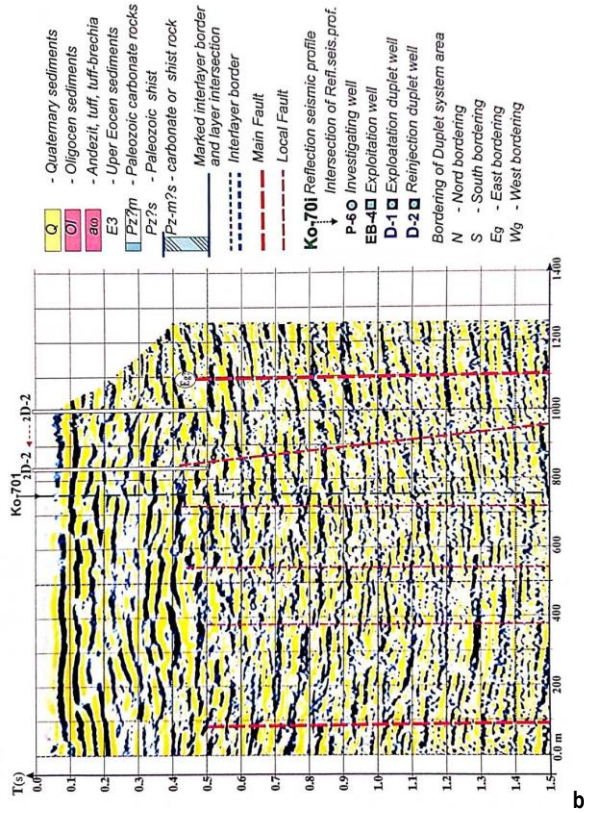


Fig. 3. Profile Ko – 702 – Time – Velocity model



a



b

Fig. 4. Profile Ko – 704 – Definitive (a) and migrated (b) time section

With regard to the above considerations, the presence of karstified carbonate rocks within the limestone units of the metamorphic basement is considered highly probable.

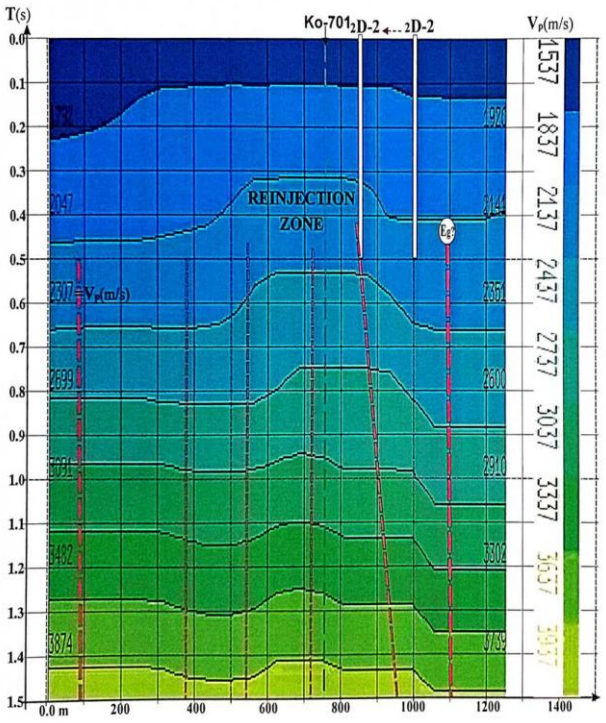


Fig. 5. Profile Ko – 704 – Time – Velocity model

However, it should be taken in consideration the "geological positioning" of the karstification by predestined structures (faults, cracked zones, clear calcite inter-layers, in the lower parts of the carbonate layers when placed over the water non-permeable layers, etc.)

Structure of the investigated terrain

The structure of the investigated terrain was analysed by developing a fault network model of the area (Figure 6).

"Faults net" of the investigated terrain is constructed on the base of interpreted faults in the metamorphic basement of the investigating profiles Ko-0701 to Ko-0704. Seismic investigations were conducted to interpret the faults in a direction normal to the exploration profiles. As a result of that, several mistakes are often made when connection is established between faults indications on different profiles. Also, built-up net of the profiles is not suitable for quality interpretation of fault net (a profiles net for 3D investigation is more appropriate for better quality interpretation of the fault net).

The constructed fault network indicates that the interpreted faults can be grouped into three systems:

a) The system with orientation in the direction of the "Podlog-Banja" structure,
b) The system with orientation East-West,
c) The system with extension North-South, probably formed with horizontal faulting of the terrain.

A fault system with extension North-South is detected as follows:

1. Correlation of similar structure at ≈ 250-500 m length from the Ko-702, at ≈ 200-450 m length from the Ko-703 and ≈1100 m from profile Ko-704, indicates the presence of tectonic zone with a near north-south orientation;

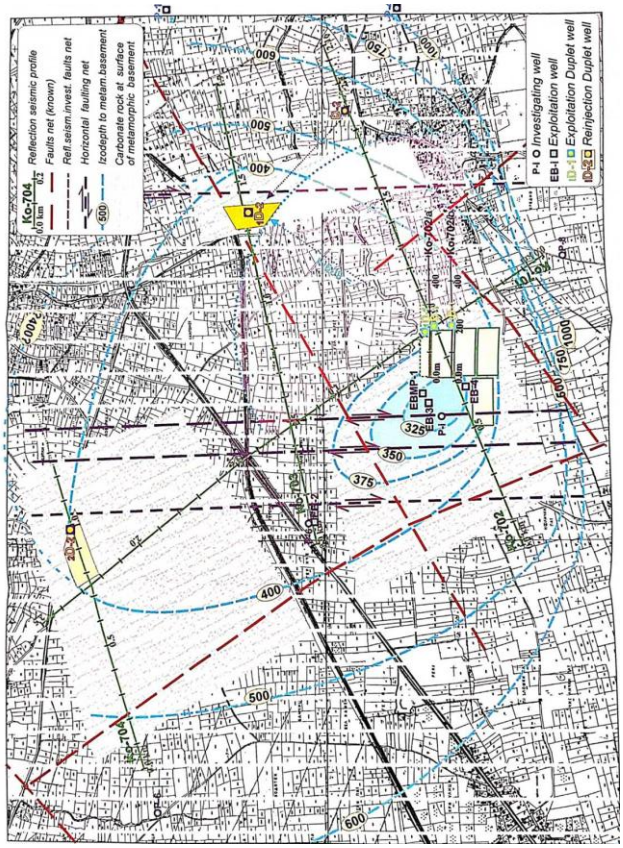


Fig. 6. Map with locations of douplet-system wells and faults net

2. The Basic geological map of the Republic of North Macedonia indicates the presence of several horizontal fault systems with north-south extension within the metamorphic basement of the geothermal field in the Plackovica mountain.

Discussion

The reflection seismic investigations performed in the "Podlog–Banja" geothermal field demonstrated both the potential and the limitations of applying seismic reflection methods in complex metamorphic terrains. Unlike sedimentary basins characterised by nearly horizontal layers and strong seismic impedance contrasts, the investigated area contains inclined lithological contacts, heterogeneous metamorphic rocks, and relatively small differences in seismic velocities between litho-units. These geological conditions significantly reduce the clarity and continuity of seismic reflections.

Despite these limitations, the processed seismic sections enabled identification of several important structural features relevant for geothermal exploitation. The interpreted fault systems and fractured carbonate zones indicate potential pathways for geothermal fluid circulation and represent favourable targets for locating geothermal production and reinjection wells.

The increased amplitudes observed in parts of profile Ko-702 are interpreted as indicators of fractured and potentially karstified carbonate rocks. However, such amplitude anomalies cannot be considered as a definitive proof of karstification because seismic amplitudes may also be influenced by lithological heterogeneity, structural discontinuities, and local velocity variations. Therefore, interpretation uncertainty remains significant and should be considered during planning of future drilling activities.

An important limitation of the study is the absence of dense borehole control data within all interpreted seismic sections. Because of this, parts of the lithological interpretation remain extrapolative in nature. The integration of future drilling data, well logging, and additional 3D seismic investigations would substantially improve the reliability of structural and hydrogeological interpretations.

The identified fault systems with NW-SE, E-W, and N-S orientations suggest a structurally complex geothermal reservoir controlled by multiple tectonic phases. These structures likely influence permeability distribution and geothermal fluid migration within the reservoir. Such structural interpretation is important for optimising the positioning of geothermal doublet wells and minimising thermal breakthrough during long-term exploitation.

Overall, the study confirms that reflection seismic investigations, despite their limitations in metamorphic environments, can provide valuable structural information for geothermal reservoir assessment when integrated with geological and hydrogeological data.

Conclusions

The conducted reflection seismic investigations provided important structural and geological information regarding the "Podlog–Banja" geothermal field and its suitability for future geothermal doublet-system development.

The interpreted seismic sections enabled identification of major lithological units, including Quaternary sediments, Oligocene deposits, volcanic units, Eocene sediments, and the Paleozoic metamorphic basement. Special attention was focused on fractured and potentially karstified carbonate zones within the metamorphic basement, which represent the most favourable environments for geothermal fluid circulation.

The investigation confirmed that fault systems with different orientations play a significant role in controlling the structural framework and permeability conditions of the geothermal reservoir. These tectonic structures are considered important factors for determining optimal locations of production and reinjection wells.

The study also demonstrated the limitations of applying reflection seismic methods in metamorphic terrains characterised by inclined geological structures and low contrasts in seismic velocities. Because of these unfavourable geological conditions, interpretation uncertainties remain, especially regarding differentiation of lithological units within the metamorphic basement.

Nevertheless, by integrating seismic interpretation with available geological and hydrogeological information, the investigations provide a useful basis for planning future drilling activities and further geothermal development in the "Podlog–Banja" field.

Future work should include integration of borehole logging data, additional geophysical investigations, and preferably 3D seismic surveys in order to reduce interpretation uncertainty and improve characterization of the geothermal reservoir.

References

Babaei, M., & Nick, M. H. (2019). Performance of low-enthalpy geothermal systems: Interplay of spatially correlated

heterogeneity and well-doublet spacings. *Applied Energy, 253*, 113569. DOI: 10.1016/j.apenergy.2019.113569

Gascuel, V., Rivard, C., & Raymond, J. (2024). Deep geothermal doublets versus deep borehole heat exchangers: A comparative study for cold sedimentary basins. *Applied Energy*, *361*, 122826. DOI: 10.1016/j.apenergy.2024.122826

Mahbaz, B., Yaghoubi, A., Dehghani-Sanij, A., Sarvaramini, E., Leonenko, Y., & Dusseault, M. (2021). Well-Doublets: A First-Order Assessment of Geothermal SedHeat Systems. *Applied Sciences*, *11*(2), 697. DOI: 10.3390/app11020697

Mirakovski, G., & Aleksovski, D. (2008). *Geophysical investigation work by using seismic reflexion method in the area of the geothermal waters bed "Podlog–Banja". Final report of the Project: Ecological sanitation and energetic rationalization of geothermal system "Geoterma" – Kocani*.

Rakikevik, T., Dumurdzanov, N., & Pekovski, P. (1965 – 1968). *Basic geological map of SFRJ, sheet Stip, 1 : 100000. Geological institute Skopje*.

Satman, A., Sustainability of geothermal doublets. Thirty-Sixth Workshop on Geothermal Reservoir Engineering, Stanford University, Stanford, California, January 31 - February 2, 2011, SGP-TR-191. chrome-extension://efaidnbmnnnibpcajpcglclefindmkaj/https://gondwana.stanford.edu/ERE/pdf/IGAstandard/SGW/2011/satman.pdf

Torres, L. (2019). *Technical and economic evaluation of geothermal doublet systems designs and configurations for heat production from low enthalpy sedimentary aquifers*. Master thesis. Politecnico di Torino. Danish Hydrocarbon Research and Technology Center - Denmark Technical University.

Vardon, P. B. (2020). *A Geothermal Well Doublet for Research and Heat Supply of the TU Delft Campus*. Delft, Netherland: 10.48550/arXiv.2003.11826.

Vizintin, G., Sporin, J., & Vukelic, Z. (2024). Geothermal potential of pumping–injecting doublet wells. *Energies, 17*(5), 980. https://doi.org/10.3390/en17050980

Wang, J., Zhihong, Z., Guihong, L., & Haoran, X. (2022). A robust optimization approach of well placement for doublet in heterogeneous geothermal reservoirs using random forest technique and genetic algorithm. *Energy*, *254*, 124427. DOI: 10.1016/j.energy.2022.124427

Wu, X., Yonghong, J., Hongyuan, M., Jing, K., Xiao, L., & Chao, J. (2021). Well spacing optimization of hydrothermal doublet. *IOP Conference Series: Earth and Environmental Science: 651* 032046. DOI: 10.1088/1755-1315/651/3/032046

Xia, Y., Plummer, M., Mattson, E., Podgorney, R., & Ghassemi, A. (2017). Design, modeling, and evaluation of a doublet heat extraction model in enhanced geothermal systems. *Renewable Energy*, *105*, 232-247. DOI: 10.1016/j.renene.2016.12.064

Sustainable Extraction and Processing of Raw Materials, 2026

DEVELOPMENT OF A NON-LINEAR LEAST-SQUARES KINETIC MODEL FOR HEAP LEACH CHEMICAL EXTRACTION USING COLUMN LEACH DATA

Naci Umut Duru

University of Nevada Reno, USA; E-mail: nduru@nevada.unr.edu

ABSTRACT. Mathematical modelling plays a central role in the interpretation of hydrometallurgical extraction processes. Laboratory experiments generate valuable information regarding the dissolution behaviour of minerals; however, meaningful interpretation of experimental results requires quantitative models capable of describing extraction kinetics. In this study, a non-linear kinetic model describing gold extraction by cyanide was developed using experimental column recovery data and parameter estimation through least-squares regression. Experimental recovery measurements obtained from column leach tests were fitted to an exponential extraction model expressed as, $F(t) = K_2 * [1 – \exp(K_1 * t)]$, where F represents fractional extraction, K_1 is the kinetic rate constant, K_2 represents the asymptotic maximum extraction, and t denotes time. Model parameters were estimated by minimising the sum of squared differences between experimental observations and model predictions using spreadsheet-based optimisation. The resulting model successfully reproduces the non-linear extraction behaviour observed in the experimental dataset and demonstrates the capability of exponential kinetic models to represent the rapid initial dissolution and subsequent asymptotic recovery typical of hydrometallurgical systems. Statistical validation of the fitted model gave squared correlation coefficient (R^2) as 0.9904 and root mean square error (RMSE) as 0.0168 in fractional extraction units. Direct comparison with reaction-control and diffusion-control shrinking-core alternatives showed that the selected single-exponential model gave the lowest RMSE for this dataset, and residual analysis showed no persistent bias after the initial ore wetting period.

Key words: heap leach, column test work, reaction kinetics, process simulation.

Introduction

Hydrometallurgical extraction processes involve complex interactions between chemical reactions, mass transfer, and mineralogical characteristics of the ore (Petersen, 2016). Laboratory column leaching experiments are commonly used to evaluate the dissolution behaviour of mineral samples under controlled conditions. These tests generate time-dependent recovery data that reflect the combined effects of reaction kinetics and transport phenomena within the column (Dixon and Hendrix, 1993).

Although experimental data provides important insights into the extraction process, interpretation of such data requires mathematical models capable of describing the observed trends. Kinetic models allow extraction behaviour to be represented using a small set of parameters that describe the rate and extent of metal dissolution. These parameters can then be used to predict recovery behaviour under different conditions and assist in the design and optimisation of metallurgical processes (Sohn and Wadsworth, 1979; Fogler, 2006).

Among the various kinetic models proposed for hydrometallurgical systems, exponential extraction models have proven particularly useful because they capture the characteristic recovery behaviour observed in many leaching experiments: rapid initial dissolution followed by a gradual decrease in reaction rate as the process approaches equilibrium (Crundwell, 2011).

The objective of the present work is to develop a kinetic model describing chemical extraction behaviour using experimental column recovery data. The model parameters are determined using non-linear least-squares regression and implemented in spreadsheet software.

Materials and methods

Experimental Conditions and Procedures

The dataset analysed in this study consists of experimental extraction values obtained from oxide gold ore laboratory column leach tests. These measurements represent the percentage of metal recovered from the column under controlled experimental conditions.

In the present study, the available experimental information consisted of cumulative extraction versus time data obtained from the laboratory column test. The original dataset used for regression did not include complete operating descriptors such as column diameter and height, particle size distribution, irrigation rate, or leach solution composition. Therefore, the present paper should be regarded as a kinetic fitting study based on time–extraction data, and these variables should be reported in future work to improve reproducibility and plant-scale interpretation.

A 55 kg charge of sample with P_{80} = 7.7 mm and 2.36 ppm average gold (Au) containing crushed ore sample was placed in a 0.15 m diameter Plexiglas column. Feed material particle size distribution is presented on Figure 1.

Ore bed height in the column was measured before and after leaching. The change in height was used to determine slump during leaching and to calculate the final apparent bulk density of the material in the column. Column slump provides an indication of possible permeability issues in operating heaps. Slump values greater than 10% are accepted as high. The test column showed low slump. The initial and final ore bed heights were 1.951 and 1.932 m, respectively, corresponding to a final apparent dry bulk density of 1.58 t/m³. The column was operated as a continuously drained drip leach test. This test configuration provides a close laboratory representation of heap leach conditions and is commonly used

when the ore contains sufficient fines to limit solution channelling along individual rock surfaces.

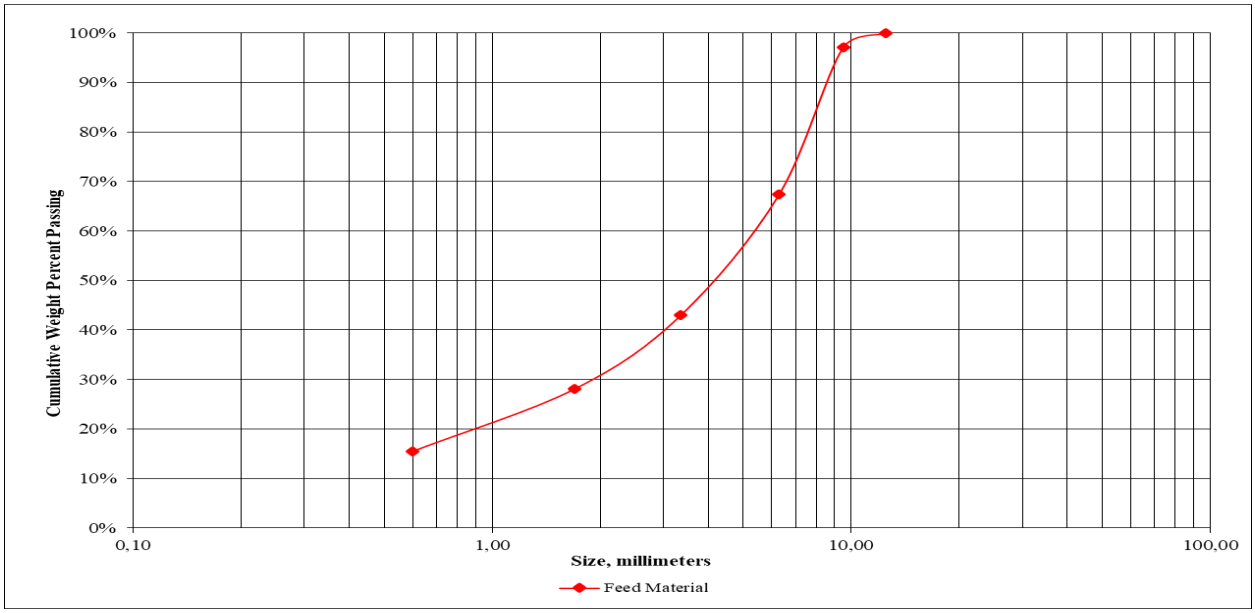


Fig. 1. Feed material particle size distribution

Solution was applied as a continuously drained drip leach at 11 L/(h m) using an initial 1.0 g/L sodium cyanide solution; on-flow solution was maintained at 0.5 g/L sodium cyanide and hydrated lime was used to control pH at a target of 10.5.

Protective alkalinity was provided by the initial addition of hydrated lime, and the leach solution was monitored to maintain pH in the range of 10 to 11.

Both sodium cyanide consumption and hydrated lime addition were elevated in this test. Sodium cyanide consumption was 1.04 kg per metric tonne of ore. Total lime addition was 2.7 kg per metric tonne of ore.

Effluent from the column was collected in the bottom floor pregnant leach solution (PLS) tank. During each cycle, the leach solution was analysed for pH, NaCN and Au. The solution was then passed for 24 hours through a bottle of activated carbon to recover dissolved gold. After carbon contact, the solution was re-analysed for pH, NaCN and Au. Sodium cyanide was added as needed to maintain a target concentration of 0.5 g/L NaCN, and the solution was recycled to the ore for another 24-hour leach cycle. Two solution batches were used so that one batch could be applied to the column while the other was treated through carbon. The cumulative extraction increased from 5.63% on day 1 to 67.14% on day 37 of column leaching.

The recovery values of the column leaching experiments are affected by ore mineralogy, permeability differences, and variations in mineral accessibility (Sohn and Wadsworth, 1979; Levenspiel, 1999). Despite the variability observed in individual measurements, the dataset exhibits an overall extraction trend that can be described using a continuous kinetic model. The supporting laboratory test ran for 53 days, but the regression dataset retained in this paper extends through day 37. Column set-up is presented in Figure 2.

Mineralogy influences extraction because gangue composition, oxidation state and the mode of gold occurrence determine how readily reactive surfaces are exposed to the lixiviant. Permeability controls solution distribution and residence time within the packed ore bed; reduced



Fig. 2. Column set-up (front-left)

permeability promotes channelling, perched solution, or incomplete wetting. Mineral accessibility represents the fraction of valuable metal that is exposed through pore space, fractures, or liberated surfaces, and limited accessibility contributes directly to the asymptotic approach to the recovery limit.

Initial and final effluent colour and clarity were observed and noted during the column test. The colour and clarity of initial and final column effluent was light yellow / clear and colourless / clear, respectively. A colourless, clear effluent from the column indicates that fines did not migrate through the ore bed. Significant metal accumulation is generally reflected by a noticeable change in solution colour. The lack of colour indicated that metal buildup did not occur during leaching.

Assaying procedures

Head assays gold content was performed by fire assaying technique.

Activated carbon used to recover the gold from solution was dried and weighed to analyse the gold content loaded in the carbon. Two samples were split and submitted for assay, and the remaining carbon was retained for reference. The assay samples were roasted to ash and then analysed by conventional fire assay.

Solution assays were completed during each cycle using an atomic absorption spectrophotometer and gold standards. These solution assays were used to monitor column test progress and leaching kinetics presented on the paper.

Sodium cyanide in leach solutions was determined by colorimetric titration using silver nitrate titrant and 5-[p-(Dimethylamino)-benzylidene]-rhodanine indicator. Free cyanide was determined by titrating 25 mL of leach solution to the colorimetric endpoint. Drops of 1N sodium hydroxide were then added to dissociate base-metal cyanide complexes, and titration continued to the final endpoint to determine total cyanide in solution.

Mathematical Model

The extraction observed in the experimental dataset was modelled using the exponential kinetic equation (Levenspiel, 1999; Fogler, 2006).

$$F(t) = K_2 * [1 - \exp(K_1 * t)] \quad (1)$$

where,

$F(t)$ = fractional extraction

K_1 = kinetic rate constant

K_2 = maximum extraction parameter

t = leaching time

For clarity, $F(t)$ is the fractional extraction at time t, K_2 is the asymptotic extraction limit, and K_1 is the first-order kinetic constant written in sign-convention form.

This model describes a system in which extraction increases rapidly during early reaction stages and gradually approaches an asymptotic recovery limit.

At the start of the reaction ($t = 0$), the model predicts $F(0) = 0$. As time increases, the exponential term decreases and extraction approaches the maximum value K_2.

Accordingly, the model predicts,

$$dF/dt = - K_1 * K_2 * \exp (K_1 * t) \quad (2)$$

So, the initial extraction rate is controlled jointly by the magnitude of K_1 and the asymptotic extraction level K_2.

Least-squares parameter estimation

To determine the kinetic parameters K_1 and K_2, a non-linear least-squares regression method was used. The objective of this method is to minimise the difference between experimental measurements and model predictions. The objective function minimised during the regression process is

$$S = \Sigma_{i=1}^{n} [F_{exp,i} - F_{model,i}]^2 \quad (3)$$

where, n is the number of experimental observations, $F_{exp,i}$ is the measured fractional extraction, and $F_{model,i}$ is the corresponding model prediction.

The spreadsheet model calculates predicted extraction values for each experimental point and then computes the squared residual error. The sum of these squared errors represents the total deviation between the model and the experimental dataset.

Excel Solver was used to iteratively adjust the kinetic parameters until the sum of squared residuals reached a minimum value.

In addition to minimising the sum of squared residuals, the fitted model was evaluated using the squared correlation coefficient, root mean square error, and approximate parameter confidence intervals (CI).

For the spreadsheet fit,

$R^2 = 0.9904$,

$RMSE = \sqrt{[\Sigma(F_{exp} - F_{cal})^2 / n]} = 0.0168$.

Based on the local sensitivity of the fitted equation, the 95% confidence intervals are,

$K_1 = -0.12398\ d^{-1}$ (95% CI: -0.13139 to $-0.11656\ d^{-1}$),

$K_2 = 0.67735$ (95% CI: 0.66579 to 0.68890).

Results

The regression procedure produced a kinetic model capable of reproducing the general extraction trend observed in the experimental dataset.

The data comparison between experimental extraction values and model predictions is presented in Table 1.

A non-linear least-squares kinetic model was developed from the spreadsheet calculations for the analysed column leach dataset. Equation (3) presents the fitted model for the recovery expression. The fitted relation is a single-exponential recovery model.

$$F(t) = 0.67735 * [1 - \exp(-0.12398 * t)] \quad (4)$$

The predicted values follow the overall trend of the experimental data and reproduce the non-linear behaviour observed in the extraction measurements.

Equation (3) indicates that the model asymptotically approaches an ultimate extraction of 67.7% under the test conditions.

The magnitude of the kinetic term, $k = 0.12398\ d^{-1}$, governs how rapidly the system approaches this limit and represents a lumped effect of dissolution kinetics, wetting behaviour, and internal mass-transfer resistance.

For the selected model,

$k = 0.12398\ d^{-1}$ gives a leaching half-time of $t_{1/2} = \ln(2)/k =$ 5.6 days.

The calculated times to reach 90% and 95% of the fitted asymptotic recovery are 18.6 and 24.2 days, respectively.

These values show that K_1 quantifies the apparent speed at which the column approaches K_2 under the stated test conditions.

Graphical Model

The relationship between experimental extraction values and model predictions is illustrated in Figure 3. Extraction vs time curve showed exponential recovery behaviour.

The figure illustrates that extraction increases rapidly during the early stages of the reaction and then gradually approaches a limiting value. This behaviour is typical of hydrometallurgical dissolution systems where the reaction rate decreases as reactive mineral surfaces become depleted.

In this plot, the modelled values closely follow the experimental data, indicating that the exponential kinetic model provides a reasonable representation of the extraction process.

The kinetic model developed in this study successfully reproduces the extraction behaviour observed in the column leach experiments. The exponential form of the model captures the characteristic recovery trend commonly observed in hydrometallurgical systems that is the rapid initial extraction followed by a gradual decrease in reaction rate as the system approaches equilibrium.

Relative to alternative heap-leach modelling approaches reported in the recent literature, the present formulation is deliberately simple. Its advantage is that only time and extraction data are required for calibration; its limitation is that it does not explicitly represent lift height, solution holdup, preferential flow, climatic effects, or downstream inventory delays (Ghorbani et al., 2015; Marsden and Botz, 2017; Botz and Marsden, 2019).

The column labelled as K_1 on Table 1 contains pointwise back-calculated rate constants obtained from

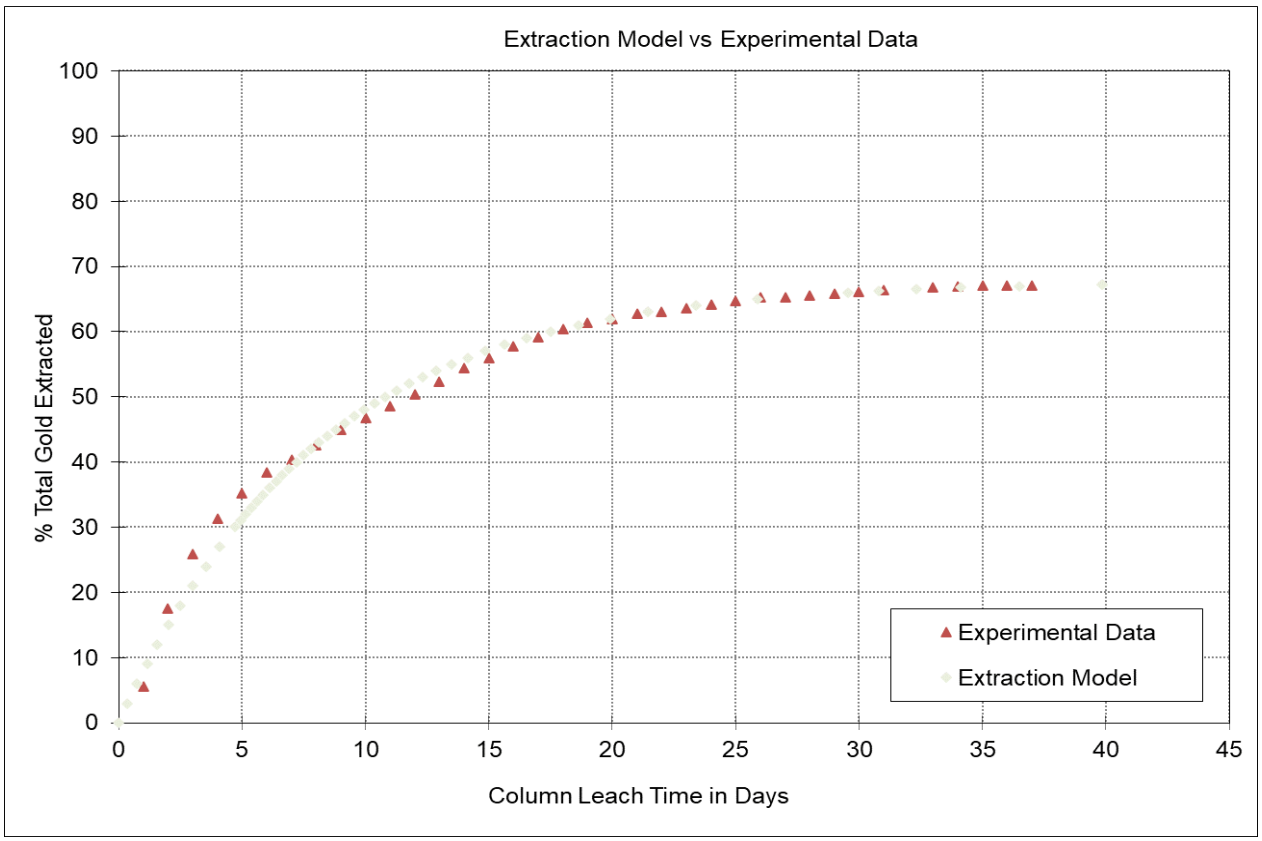


Fig. 3. Comparison of experimental and modelled extraction values

$$K_1 = \ln (1 - F / K_2) / t, \quad (5)$$

and these values are negative because the exponential term is written using, $K_1 < 0$.

The term, $\Sigma(K_1 - K_{1avg})^2$ gives the contribution of each point to the spreadsheet objective used to stabilise the average rate constant. The column "t given F" is the inverse-model solution for time at a specified extraction level, whereas "F estimated" and "F calculated" are model-predicted fractional extractions generated for prescribed times and for the actual experimental times, respectively (day 32 is absent because no experimental observation was available for that day in the original dataset). The R^2 value reported in the table refers to the goodness of fit between experimental and model-calculated extraction values in the spreadsheet regression.

Kinetic model comparison

A comparison with higher-complexity models was prepared as part of this study. In the tiered heap-leach framework, the present equation is closest to a Level 1–2 empirical description because it uses column extraction data directly and does not include explicit in-heap solution inventory, heap geometry, or downstream process constraints. By contrast, Level 3 spreadsheet models adjust production for solution holdup and recovery delays within the heap, which becomes increasingly important in multi-lift systems as inventory grows with heap height (Ghorbani et al., 2015; Botz and Marsden, 2019).

Table 1. *Experimental and modelled extraction data*

Rate of Chemical Extraction Model Equations:										R^2 = 0.9904
			$F = K_2 (1-e^{k1t})$							
F= 0.677 -0.124			$t\ (days) = (Ln(1-F)/K_2) / K_{1avg}$							
			$K_1 = (Ln(1-F) / K_2) / t_{days}$							
Column recovery (%)	Time (t) days	K_1	K_2	$(\bar{K_1}-K_1)^2$	Solve for t given F	Chemical extraction model F estimated		Solve for F given t	Chemical extraction model F calculated	$(F_{act}-F_{cal})^2$
5.629	1	-0.08676	0.677348	0.00138498	0.000	0.000	0.0	1.0	0.079	0.00051475
17.581	2	-0.1502517	0.677348	0.00069045	0.365	0.030	3.0	2.0	0.149	0.00073236
25.868	3	-0.1603664	0.677348	0.00132431	0.748	0.060	6.0	3.0	0.210	0.00233251
31.344	4	-0.1553176	0.677348	0.00098234	1.150	0.090	9.0	4.0	0.265	0.00236262
35.216	5	-0.1467575	0.677348	0.00051903	1.573	0.120	12.0	5.0	0.313	0.00153935
38.418	6	-0.1395747	0.677348	0.00024334	2.019	0.150	15.0	6.0	0.355	0.00082738
40.335	7	-0.1292942	0.677348	0.00002829	2.492	0.180	18.0	7.0	0.393	0.00010803
42.559	8	-0.1237131	0.677348	0.00000007	2.993	0.210	21.0	8.0	0.426	0.00000028
44.933	9	-0.1209756	0.677348	0.00000900	3.529	0.240	24.0	9.0	0.455	0.00003689
46.827	10	-0.1175481	0.677348	0.00004131	4.102	0.270	27.0	10.0	0.481	0.00016939
48.515	11	-0.1145158	0.677348	0.00008948	4.719	0.300	30.0	11.0	0.504	0.00036075
50.431	12	-0.1137242	0.677348	0.00010509	4.935	0.310	31.0	12.0	0.524	0.00040114
52.350	13	-0.1140167	0.677348	0.00009917	5.158	0.320	32.0	13.0	0.542	0.00034902
54.467	14	-0.1164465	0.677348	0.00005668	5.387	0.330	33.0	14.0	0.558	0.00017617
55.928	15	-0.1164643	0.677348	0.00005642	5.623	0.340	34.0	15.0	0.572	0.00015825
57.765	16	-0.1197508	0.677348	0.00001785	5.865	0.350	35.0	16.0	0.584	0.00004246
59.170	17	-0.1216459	0.677348	0.00000543	6.116	0.360	36.0	17.0	0.595	0.00001106
60.428	18	-0.1237084	0.677348	0.00000007	6.374	0.370	37.0	18.0	0.605	0.00000012
61.352	19	-0.1243143	0.677348	0.00000011	6.641	0.380	38.0	19.0	0.613	0.00000017
61.992	20	-0.1233796	0.677348	0.00000035	6.917	0.390	39.0	20.0	0.621	0.00000046
62.732	21	-0.1240792	0.677348	0.00000001	7.202	0.400	40.0	21.0	0.627	0.00000001
63.053	22	-0.1214518	0.677348	0.00000637	7.499	0.410	41.0	22.0	0.633	0.00000639
63.675	23	-0.1223688	0.677348	0.00000258	7.806	0.420	42.0	23.0	0.638	0.00000217
64.193	24	-0.1229519	0.677348	0.00000105	8.126	0.430	43.0	24.0	0.643	0.00000074
64.676	25	-0.1239085	0.677348	0.00000000	8.459	0.440	44.0	25.0	0.647	0.00000000
65.256	26	-0.1272228	0.677348	0.00001055	8.806	0.450	45.0	26.0	0.650	0.00000477
65.295	27	-0.1230925	0.677348	0.00000078	9.169	0.460	46.0	27.0	0.654	0.00000033
65.614	28	-0.1237155	0.677348	0.00000007	9.549	0.470	47.0	28.0	0.656	0.00000002
65.834	29	-0.1232145	0.677348	0.00000058	9.947	0.480	48.0	29.0	0.659	0.00000017
66.137	30	-0.1248939	0.677348	0.00000084	10.367	0.490	49.0	30.0	0.661	0.00000020
66.337	31	-0.1251877	0.677348	0.00000147	10.809	0.500	50.0	31.0	0.663	0.00000029
66.762	33	-0.1285868	0.677348	0.00002127	11.277	0.510	51.0	32.0	0.665	0.00000957
66.936	34	-0.1305798	0.677348	0.00004362	11.774	0.520	52.0	33.0	0.666	0.00001111
67.138	35	-0.1351754	0.677348	0.00012544	12.304	0.530	53.0	34.0	0.667	0.00001626
67.138	36	-0.1314205	0.677348	0.00005543	12.871	0.540	54.0	35.0	0.669	0.00000821
67.138	37	-0.1278686	0.677348	0.00001516	13.481	0.550	55.0	36.0	0.670	0.00000337

Dynamic flowsheet models go further by linking ore stacking, solution storage, recycle, and plant limitations in a time-dependent mass balance, allowing evaluation of PLS tenor, make-up water demand, and downstream bottlenecks (Muller and Newton, 2008).

To address model selection quantitatively, the same extraction dataset was also fitted with chemical reaction-control and diffusion-control shrinking-core formulations - equations (6 - 8).

The reaction-control form was evaluated as,

$$F(t) = F\infty \{1 - [1 - k_r t]^3\} \quad (6)$$

where k_r - intrinsic chemical reaction rate at the surface of the unreacted core, $F\infty$ - the fractional extraction at infinite time.

The diffusion-control form was evaluated as,

$$F(t) = F\infty X \quad (7)$$

where,

$$k_d t = 1 - 3 (1 - X)^{(2/3)} + 2 (1 - X) \quad (8)$$

where k_d - the overall rate constant that accounts for the diffusion in the product layer, X - the fractional conversion of the solid particle, i.e., the reacted fraction.

These equations represent idealised spherical-particle controls and are used here as comparison models rather than as complete heap simulators.

The model comparison was carried out using the same experimental column-leach extraction dataset for all three kinetic expressions. For each model, calculated extraction values were generated at the same leach times as the measured data, and the residual for each point was calculated as the difference between the experimental extraction and the model-predicted extraction

For the two alternative models, the shrinking-core reaction-control model and the shrinking-core diffusion-control model (SCM diffusion) the data were expressed in terms of reacted fraction, (X), and then converted to predicted extraction by $F(t) = F\infty X$, so that all three models were compared on the same fractional extraction basis.

For the shrinking-core reaction-control model (SCM reaction) case, the relationship (6) was rearranged to calculate (X) directly at each time step.

For the diffusion-control case, the relationship (8) was solved numerically for (X), because this expression is not conveniently rearranged into an explicit form for (X). The fitted constants were selected by minimising the sum of squared errors between measured and calculated extraction values.

For a direct quantitative comparison, the shrinking-core alternatives were fitted to the same fractional extraction dataset by minimising the sum of squared errors. To isolate the effect of the kinetic form, $F\infty$ was fixed at 0.677348 for the two shrinking-core alternatives.

The selected single-exponential model was evaluated using

$$F(t) = F\infty [1 - \exp(-k t)] \quad (9)$$

where F∞ represents the fitted ultimate extraction and (k) is the apparent first-order rate constant.

Model performance was then compared using the squared correlation coefficient R^2, root mean square error, mean absolute error, sum of squared errors, and maximum absolute residual. This procedure allowed the single-exponential model to be evaluated against two mechanistically based alternatives using identical experimental data and identical error criteria.

The comparison (Table 2) shows that the selected single-exponential equation has the best statistical performance for this dataset (the highest R^2 and lowest RMSE among the tested alternative models); however, the alternative shrinking-core models remain useful for mechanistic interpretation when additional particle-scale data are available.

The model reliability also depends on the defining ore type, particle-size distribution, leach kinetics, and solution hydrodynamics.

Table 1. *Quantitative comparison of kinetic models fitted to the same fractional extraction dataset*

Model	Model expression / fitting basis	Fitted or fixed parameters	R^2	RMSE	Selection comment
Single exponential model	$F(t) = F\infty\ [1 - \exp(-k\ t)]$	$F\infty = 0.677348$ $k = 0.12398\ d^{-1}$	0.9905	0.0168	Best fit; lowest RMSE and highest R^2 among the tested models.
Shrinking core -Diffusion controlled model	$F(t) = F\infty X$ $k_d * t = 1 - 3\ (1 - X)^{(2/3)} + 2\ (1 - X)$ Product-layer diffusion control X was capped at 1	$F\infty$ fixed = 0.677348 $k_d = 0.02599\ d^{-1}$	0.9879	0.0265	Intermediate fit; better than reaction-control SCM but still less accurate than the single-exponential model.
Shrinking core - Reaction controlled model	$F(t) = F\infty X$ $F(t) = F\infty\ \{1 - [1 - k_r\ t]^3\}$ Surface reaction at the shrinking interface control X was solved by Newton iterations	$F\infty$ fixed = 0.677348 $k_r = 0.03302\ d^{-1}$	0.9823	0.0329	Poorest of the three tested fits; the curve reaches completion too sharply for the observed gradual asymptote.

The fitted kinetic parameters provide quantitative insight into the extraction system. In this dataset, K_1 should be interpreted as an apparent first-order leaching-rate parameter rather than a pure intrinsic reaction constant.

Because the fitted response is based on solution recovered from the column, K_1 includes the effects of chemical dissolution at exposed mineral surfaces, diffusion through partially reacted particles, wetting and percolation through the packed ore bed, and solution transport to the effluent. Under the fixed test conditions summarised above, it is best described as an apparent or lumped rate constant. Separating the individual contributions of reaction control, diffusion control, permeability, and solution transport would require additional tests at multiple particle sizes, irrigation rates, column heights, or reagent concentrations.

One of the main advantages of the modelling approach used in this work is its simplicity. The exponential extraction model requires only two parameters yet can describe a wide range of extraction behaviours. This simplicity allows the model to be implemented easily using spreadsheet software and makes it suitable for rapid analysis of experimental datasets.

However, it should be noted that the model represents an empirical approximation rather than a fully mechanistic description of the extraction process. In real hydrometallurgical systems, additional factors such as diffusion limitations, surface passivation, changes in reagent concentration, and in-heap solution inventory may influence reaction kinetics and recovery behaviour (Habashi, 1999).

More complex shrinking-core, diffusion-controlled, or inventory-adjusted heap models can incorporate these effects when mineralogical, hydraulic, and operating data are available (Muller and T. Newton, 2008; Ghorbani et al., 2015; Botz and Marsden, 2019).

Mechanistic or phenomenological models are also more complex than the present formulation. These approaches may couple unsaturated flow, diffusion, and reaction kinetics and, in advanced cases, represent gas and liquid flow, reagent balance, bacterial effects, and thermodynamic or temperature responses (Muller and T. Newton, 2008). The shrinking-core type treatment is therefore more physically explicit for heterogeneous ore particles than the single-exponential equation used here, but it also requires more detailed characterisation and calibration (Dixon and Hendrix, 1993). The fitted relation in Equation (4) should therefore be interpreted as an empirical kinetic baseline for the present column data rather than as a complete mechanistic heap-leach simulator.

The contribution of the present work is therefore not the proposal of a new kinetic law, but the demonstration that a transparent spreadsheet-based nonlinear least-squares workflow can be used to fit column-leach extraction data, quantify model error, and interpret the fitted parameters in a way that is useful for preliminary metallurgical screening.

Accordingly, the scientific contribution of the present paper is not the development of a more comprehensive heap simulator, but the demonstration that the single-exponential fit

can provide a practical first-pass kinetic interpretation of column leach data and can serve as an initial benchmark against which more complex models may later be tested

Proposed model residuals plot

Residuals were calculated as experimental extraction minus calculated extraction. The largest residuals occur during the first four days, which is consistent with initial wetting and rapid early dissolution effects that are not explicitly represented by the single-exponential empirical model. After approximately day 8, residuals remain small and show no persistent directional bias.

The residual plot in Figure 4 should be read as a signed model-error plot. Points above the zero-residual line mean that the experimental extraction was higher than the calculated value, so the model underpredicted recovery at those times. Points below the zero-residual line mean that the calculated value was higher than the experimental extraction, so the model overpredicted recovery. Therefore, Figure 4 is a diagnostic plot used to evaluate whether the fitted equation (4) leaves systematic error, not a separate recovery model.

The residual pattern shows the largest positive deviations during the early leaching period and the largest negative deviations during the transition toward the asymptotic region. This indicates that the single-exponential equation slightly underpredicts part of the rapid early extraction stage and then slightly overpredicts the mid-test approach to the recovery limit. After approximately day 18, the residuals cluster close to zero, indicating that the later portion of the column-leach response is described without persistent positive or negative bias.

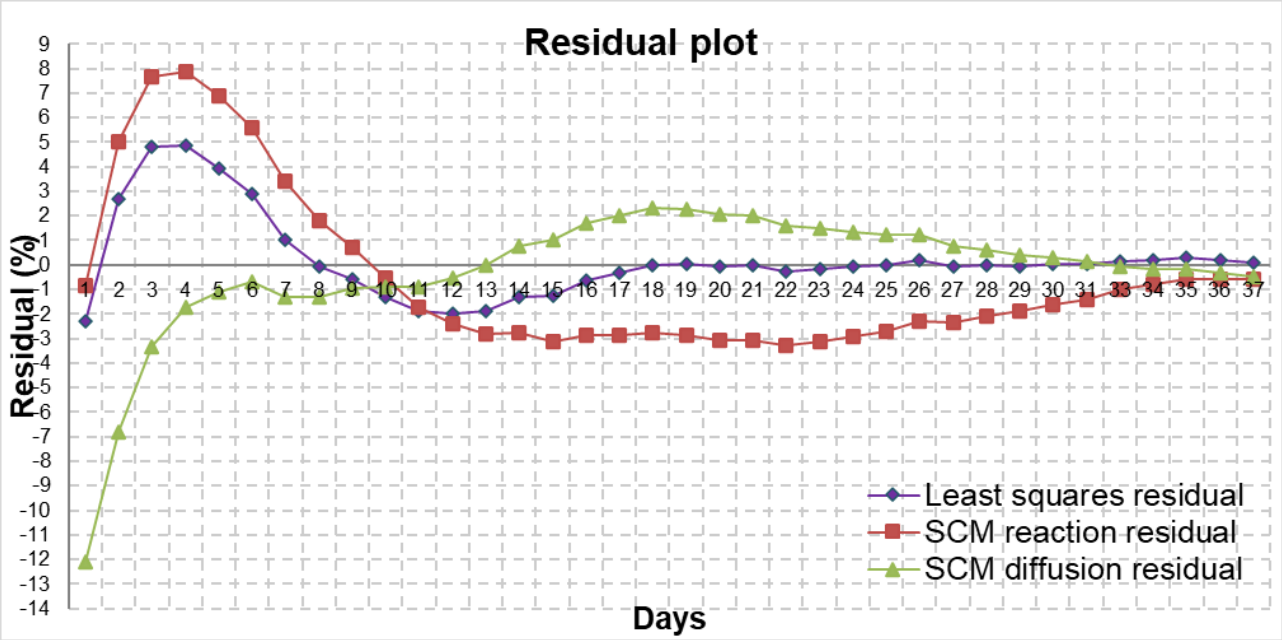


Fig. 4. Residual plots of the kinetic models

Conclusion

A non-linear kinetic model describing chemical extraction behaviour was developed using experimental column recovery data and least-squares regression.

The results demonstrate that

- The exponential extraction model successfully describes the non-linear recovery behaviour observed in the experimental dataset.
- Least-squares regression provides an effective method for estimating kinetic parameters from laboratory extraction data.
- Spreadsheet-based optimisation tools provide a convenient platform for performing kinetic modelling and parameter estimation.
- The resulting model can be used to predict extraction behaviour and assist in the interpretation of hydrometallurgical experiments.

The model is best suited for preliminary kinetic description of column-leach behaviour rather than direct prediction of full-scale heap performance.

This model comparison with shrinking core reaction and diffusion-controlled approach also addresses effectiveness and precision of the least squares model. The model presented in this paper produced explicit, reproducible translation of experimental column extraction data into fitted kinetic parameters and statistical error measures. It can be used as an interpretable baseline model that is simple enough for rapid metallurgical screening.

The comparison showed that the selected single-exponential model provided the best overall statistical fit to the column-leach data. The single-exponential model gave the highest coefficient of determination and the lowest error terms, with (R^2) of approximately 0.9905 and RMSE of approximately 0.0168. The shrinking-core diffusion-control model gave the next closest fit, while the shrinking-core reaction-control model showed larger deviations, particularly in the early-to-intermediate leaching period. These results indicate that the

observed extraction trend is better represented by a smooth asymptotic first-order recovery form than by the sharper reacted-core progression predicted by the reaction-control shrinking-core model. The comparison therefore supports the use of the exponential model as a practical empirical representation of the column-leach extraction data, while recognising that the shrinking-core models provide useful mechanistic alternatives for systems where particle-scale reaction or diffusion control can be independently demonstrated.

The novelty claim of the model presented in the paper is limited. The work does not claim a new leaching law, but it provides a reproducible spreadsheet-based workflow that,

- Fits the extraction curve.
- Reports confidence intervals and residual statistics.
- Compares the selected model against shrinking core model reaction and diffusion control alternatives.
- Identifies the fitted model as a practical baseline for preliminary column-leach screening.

Furthermore, the developed kinetic model provides a useful tool for interpreting and predicting extraction behaviour in column leach hydrometallurgical systems.

By determining the kinetic parameters K_1 and K_2, the model allows estimation of both the apparent extraction rate and the ultimate extraction achievable under the stated column conditions. Such information is valuable for evaluating metallurgical performance, comparing the leachability of different materials, and estimating the time required to reach a target recovery.

References

Botz, M., & Marsden, J. (2019). Heap leach production modeling: a spreadsheet-based technique. *Mining, Metallurgy & Exploration*, *36*, 1041 - 1052. DOI https://doi.org/10.1007/s42461-019-00129-0

Crundwell, F. (2011). *Extractive metallurgy of nickel, cobalt and platinum group metals*. Elsevier. Amsterdam.

Dixon, D. G., & Hendrix, J. L. (1993). A mathematical model for heap leaching of one or more solid reactants from porous ore pellets. *Metallurgical Transactions*, *24*, 1087 – 1102. DOI https://doi.org/10.1007/BF02661000

Fogler, H. S. (2006). *Elements of chemical reaction engineering*. Prentice Hall.

Ghorbani, Y., Franzidis, J. P., & Petersen, J. (2015). Heap leaching technology - current state, innovations, and future directions: A review. *Mineral Processing and Extractive Metallurgy Review*, *37*(2), 73-119. doi https://doi.org/10.1080/08827508.2015.1115990

Habashi, F. (1999). *Textbook of hydrometallurgy*. Metallurgie Extractive Québec.

Levenspiel, O. (1999). *Chemical reaction engineering*, John Wiley & Sons.

Marsden, J. O., & Botz, M. M. (2017). Heap leach modeling – A review of approaches to metal production forecasting. *Minerals & Metallurgical Processing*, *34*(2), 53-64. DOI https://doi.org/10.19150/mmp.7505

Muller, B., & Newton, T., Look Before You Leach: Dynamic Simulation of Heap Leach Flowsheets, ALTA Copper Conference," ALTA Metallurgical Services, 2008, Perth, Australia.

Petersen, J. (2016). Heap leaching as a key technology for recovery of values from low-grade ores - A brief overview. *Hydrometallurgy, 165*, 206–212. doi https://doi.org/10.1016/j.hydromet.2015.09.001

Sohn, H. Y., & Wadsworth, M. E. (1979). *Rate processes of extractive metallurgy*. Plenum Press.

Sustainable Extraction and Processing of Raw Materials, 2026

EFFICIENCY AND SELECTIVITY OF COPPER PRECIPITATION AS COPPER OXALATE FROM SOLUTIONS FROM THE MINING INDUSTRY

Plamen Georgiev, Marina Nicolova

University of Mining and Geology "St. Ivan Rilski", 1700 Sofia; E-mail: ps_georgiev@mgu.bg
Corresponding author: ps_georgiev@mgu.bg

ABSTRACT. The aim of this study was to investigate the effect of calcium and ferrous iron ions on the removal of copper-to-copper oxalate from a model solution containing 0.0069 M Cu^{2+}. Copper oxalate was synthesised under optimal experimental conditions (solution pH of approximately 2.5, temperature of 50 °C, and a stirring rate of 250 rpm). This was an effective process for removing copper from the model solution, and the resulting particles were larger than 200 µm and exhibited excellent filtration characteristics. In contrast, higher concentrations of calcium ions (0.036 M) and ferrous iron ions (0.045 M) decreased the selectivity and efficiency of copper removal, respectively.

Key words: copper, pregnant solutions, copper oxalate, selectivity

Introduction

Hydrometallurgy is widely applied to recover base metals from low-grade raw materials and industrial wastes, whose chemical composition and mineralogy make classical processing methods inefficient. In that case, the base metal leaches from the mineral structure and accumulates in the pregnant leach solution. That process is usually nonselective, and the leaching and accumulation of calcium, iron, aluminium, and silicon in solution accompany it. Therefore, processing the pregnant leach solution, the final step in the relevant hydrometallurgical method, aims to obtain a product with higher base-metal content. The most common approaches for separating and concentrating the base metal from the leach solution and transforming it into a higher-purity market product are solvent extraction, stripping, and electrowinning (Shlesinger et al., 2021). However, chemical reduction using scrap remains a suitable method for recovering copper ions from mining solutions in some cases (Li et al., 2024).

Oxalic acid is a natural product of the metabolism of a wide range of heterotrophic microorganisms (bacteria and fungi), plants and animals. Its role is to enhance acidolysis of minerals within their microenvironment and, in turn, to support and regulate the mineral nutrition of organisms (Palmieri et al., 2019).

Oxalic acid has attracted the attention of hydrometallurgists for many years as an efficient and selective agent for recovering base metals from various types of pregnant solutions (Gyliene et al., 1997; Gylliene & Saulkaskas, 1994). Based on its unique chemical properties, oxalic acid is used as a leaching and recovery agent for a wide range of primary raw materials such as lithium-bearing sediments (Tita et al., 2025), slag (Cheng et al., 2026), coal (Zeng et al., 2026), hydroxysulphate and silicate (Krajanova & Lalinska-Volekova, 2025) or spent products, such as spent ion batteries (Martins et al., 2023; Botta et al., 2025), diodes (Mustafa et al., 2025), spent catalysts (Verma et al., 2019), as well as to recover zinc (Lee et al., 2017), some critical elements such as cobalt (Aref et al., 2026), nickel (Yang et al., 2020), and rare earth elements (Wen et al., 2025).

To study the effect of calcium and ferrous iron ions concentration on the removal of copper-to-copper oxalate from a model solution containing 0.0069 M Cu^{2+} was the main aim of this study.

Materials and methods

Precipitation of copper ions to copper oxalate

The reagent-grade salts of $CuSO_4.5H_2O$, $CaCl_2$, and $FeSO_4.7H_2O$ were used in the experiments to prepare a model solution with a composition similar to that of waste or pregnant solutions from the mining industry or biohydrometallurgy. The concentration of Cu^{2+} in all experiments was 440 mg/ L (0.0069 M), while the concentration of Ca^{2+} and Fe^{2+} varied between 275 mg/ L – 1440 mg/ L (0.0069 M – 0.036 M) and 500 mg/ L – 2500 mg/ L (0.0089 M – 0.045 M), respectively. The amounts of the salts needed for the relevant experiment were dissolved in distilled water acidified with sulphuric acid. pH of the prepared solutions ranged from 2.38 to 2.59.

The amount of oxalate ions, $[C_2O_4^{2-}]$, needed to precipitate Cu^{2+} as oxalate was calculated according to the relevant equation:

$$[C_2O_4^{2-}] = (K_{spCuC2O4.H2O})/[Cu^{2+}] \quad (1)$$

where K_{sp} is the solubility product of copper oxalate (Table 1), while $[Cu^{2+}]$ is the copper concentration in solution, M.

Table 1. *K_{sp} values of some oxalates (Rumble, 2018)*

Compound	K_{sp} value at 25 °C
$CuC_2O_4.H_2O$	$4.43.10^{-10}$
CaC_2O_4	$2.3.10^{-9}$
$FeC_2O_4.2H_2O$	$2.1.10^{-7}$

The selective precipitation of cupric ions to copper oxalate was carried out on a magnetic stirrer at 250 rpm and at a constant temperature of 50 °C. After reaching the temperature, the initial pH was measured. The required amount of oxalic acid for the precipitation of cupric ions was divided into five portions and added to the solution at 10-minute intervals. The entire experiment lasted 60 minutes. The pH of the suspension was

measured at 50 °C and at 9.8 °C after the suspension was cooled in an ice bath.

The particles formed at the end of the experiment were separated by vacuum filtration through Blue Ribbon filter paper with a pore size of 2-3 µm. The filtrate was passed through a 0.45 µm membrane filter. The residual concentrations of Cu^{2+}, Ca^{2+}, and Fe^{2+} in the second filtrate were determined by AAS (Perkin Elmer 5000).

Characterisation of the precipitates obtained from the experiments

The efficiency of copper ions removal to copper oxalate ($E_{Cu,\ \%}$) was calculated according to the following formula:

$$Ecu = \frac{C1-C2}{C1} \times 100, \% \quad (2)$$

where C_2-copper ions concentration in the filtrate obtained after membrane filtration, mg/ L; C_1-copper ions concentration in the model solution, mg/ L.

The precipitate deposited on the filter paper was washed with distilled water, dried at 105 °C for 2 hours, and weighed on a precise balance.

The mineralogical composition of the obtained precipitates was determined using a Phillips PW 1050 X-ray Diffraction analyser with Cu anode, operated at 112 kV and 31 mA. The chemical analysis of the obtained precipitates and their surface morphology were carried out using an electron microscope, JEOL JSM-6010 PLUS/LA.

Selectivity of copper precipitation as copper oxalate (S, %) was calculated according to the following formula:

$$\boldsymbol{S} = \frac{Ccu2}{Ccu1} \times 100 \quad (3)$$

where C_{Cu2} – average copper content in the precipitate, determined by the EDS analysis, in the presence of other cations (calcium or ferrous iron) in the solutions; C_{Cu1} – average copper content in the precipitate, determined by the EDS analysis, in the absence of other cations in the solution.

Results and discussion

The rate of copper precipitation to copper oxalate is a pH-dependent. At a pH around 2.5, oxalic acid exists mainly in the non-protonated form, with about 2.0% of the added oxalic acid present as oxalate anions (Verma et al., 2019). Therefore, to maintain the higher rate of copper precipitation, the process was carried out at 50 °C in one hour:

$$Cu^{2+} + (COO)_2^{-} \rightarrow CuC_2O_4 \quad (4)$$

Removal of the oxalate anions from the solution enhances further dissociation of oxalic acid into the relevant anions:

$$(COOH.COOH) \leftrightarrow (COOH.COO^{-}) + H^{+}$$

$$(COOH.COO^{-}) \leftrightarrow (COO^{-}.COO^{-}) + H^{+} \quad (5)$$

Characteristics of copper oxalate

Oxalate anions react with copper ions in the model solution at a higher rate and with almost 100% efficiency (Table 2), forming a readily separable slurry consisting of a light blue, easily filterable precipitate. The electron microscope revealed the formation of irregularly shaped particles with a flat surface, with a predominance of sizes larger than 200 µm (Figure 1). The XRD pattern showed the presence only of the moolooite, copper oxalate ($CuC_2O_4.H_2O$), a mineral consisting of orthorhombic crystals. It forms distinctive peaks at 23, 38-39, 52, 60, 72-78 °Theta positions (Figure 2).

Table 2. *Efficiency of copper ions precipitation under relevant experimental conditions*

Composition of the model solution	Final pH (at 9.8 °C)	Yield of precipitate, g/ L	Residual $[Cu^{2+}]$ after a membrane filtration, mg/ L	$E_{Cu,\ \%}$
0.0069 M Cu^{2+}	1.56	1.15	< 1.5	99.6
0.0069 M Cu^{2+} + 0.0069 M Ca^{2+}	1.62	1.01	42.2	90.4
0.0069 M Cu^{2+} + 0.023 M Ca^{2+}	1.68	0.85	90.2	79.5
0.0069 M Cu^{2+} + 0.036 M Ca^{2+}	1.64	0.68	129.4	70.6
0.0069 M Cu^{2+} + 0.0069 M Fe^{2+}	1.47	0.35	218	50.4
0.0069 M Cu^{2+} + 0.01 M Fe^{2+}	1.58	0.24	295	32.9
0.0069 M Cu^{2+} + 0.045 M Fe^{2+}	1.64	0.11	350	20.4

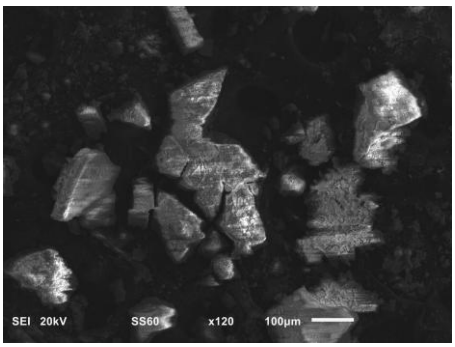


Fig. 1. SEM morphology of copper oxalate obtained from a solution containing 0.0069 M copper

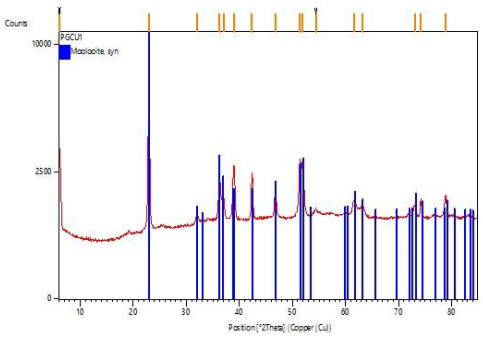
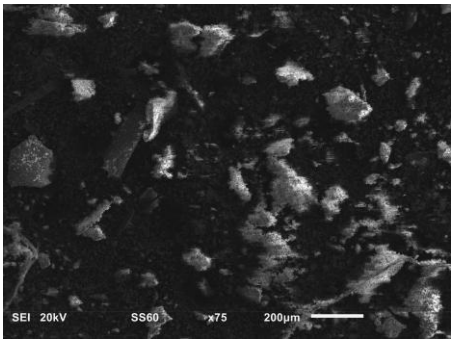
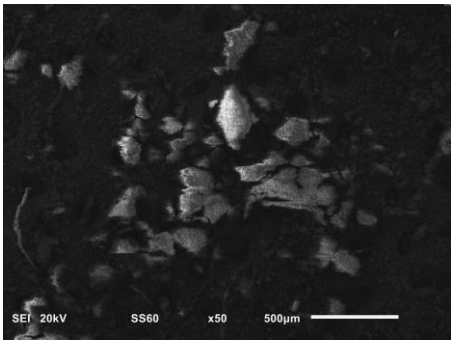


Fig. 2. XRD pattern of precipitates obtained from a solution containing 0.0069 M copper



(a)



(b)

Fig. 3. SEM morphology of precipitates obtained from a solution containing: 0.0069 M copper and 0.023 M calcium (a); 0.0069 M copper and 0.036 M calcium (b)

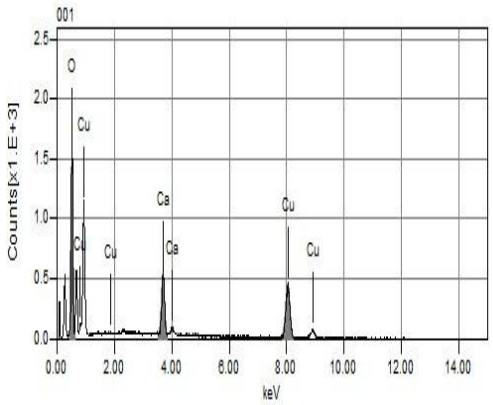


Fig. 4. EDS analysis of the precipitate from a solution containing 0.0069 M copper and 0.036 M calcium

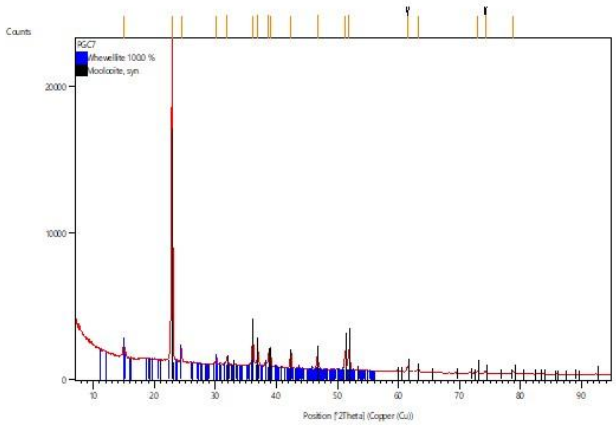


Fig. 5. XRD pattern of precipitates obtained from a solution containing 0.0069 M copper and 0.036 M calcium

The average copper content of copper oxalate, produced from a solution containing only copper, determined by EDS analysis, was 82.3%.

Copper oxalate could be used as a precursor for obtaining high-purity metallic copper, copper oxide, or advanced ceramics such as $CaCu_3Ti_4O_{12}$, which are applied in electronics and energy storage (Chen et al., 2018), or as a protective layer on historical bronze statues (Joseph et al., 20212).

Effect of calcium ions on the copper oxalate formation

Calcium ions in wastewater from the mining industry or biohydrometallurgy result from the chemical neutralisation of sulphuric acid generated or added to the raw material being processed with carbonates. The deposition of gypsum ($CaSO_4 \cdot 2H_2O$) is a key process that prevents the accumulation of high concentrations of calcium ions in waters.

A study (Werner et al., 2021) showed that calcium ions affected primary aggregation and crystallisation pathways of copper oxalate. Therefore, calcium oxalate formation could be minimised by precise control of the addition of oxalate anions. Due to the close K_{sp} values of both oxalates (Table 1), oxalic acid was added to the model solution serially at even intervals of time. It allowed initiating the copper precipitation process without exceeding the oxalate anion concentration required to initiate calcium oxalate formation. However, the experiment carried out at equimolar concentrations of copper and calcium showed a decrease of approximately 10% in the yield of precipitate and in the process efficiency (Table 2).

The precipitation of 0.0069 M Cu^{2+} as copper oxalate in the presence of 0.023 M or 0.036 M Ca^{2+} also resulted in the formation of light-blue particles, which filtered at a higher rate through Blue-Ribbon filter paper. Electron microscopy revealed that the particles still had an irregular shape but now also had a grainy surface. In the presence of 0.023 M Ca^{2+}, the size of deposited particles remained near to 200 µm (Figure 3a). In comparison, in the presence of 0.036 M Ca^{2+}, a significant proportion of the synthesised particles had a size close to 100 µm (Figure 3b). However, the yield of copper oxalate steadily decreased compared to the yield obtained from the experiment in the absence of calcium ions. It reached 59.1% in the presence of 0.036 M Ca^{2+} (Table 2). The fine particles smaller than 2-3 µm formed under these conditions accounted for about 12.7% from the initial copper concentration.

EDS analysis on three distinctive dots on the surface of analysed particles obtained from a model solution containing 0.036 M Ca^{2+}, showed that the average calcium content in precipitates was 9.3% (Figure 4, Table 3). It is evident that, due to their similar ionic radii, calcium ions co-precipitate to some extent with copper ions during the formation and growth of copper oxalate nuclei despite the applied experimental approach.

Notwithstanding a single order-of-magnitude difference in the K_{sp} values of copper and calcium oxalates and the applied experimental conditions, when the calcium concentration in the model solution was five times higher than the copper concentration, the selectivity of copper precipitation was 71.7% (Table 4).

The XRD pattern showed the presence of the moolooite, copper oxalate (CuC_2O_4 H_2O) and whewellite (CaC_2O_4 $2H_2O$) (Figure 5), the most common form of calcium oxalate (Werner et al., 2021). It has a monoclinic crystal structure and exhibits distinctive peaks at 14.9, 24.4, and 30.1 °2θ. However, the peak heights were distinctly lower than those of moolooite.

Table 3. *Chemical composition of the precipitate obtained from the solution containing 0.0069 M copper and 0.036 M calcium ions in three selected points (based on EDS analysis)*

Element	Content, %			Average value	Deviation
	1	2	3		
Cu	45.1	69.0	62.8	59.0	10.1
Ca	8.1	10.3	9.4	9.3	0.9
O	46.8	20.7	27.8	31.7	11.0

Table 4. *Effect of the calcium and ferrous iron ions on the selectivity of copper precipitation as copper oxalate*

Cation	Concentration, M	Selectivity coefficient, %
Ca^{2+}	0.036	71.7
Fe^{2+}	0.045	98.5

Bohner et al. (2014) showed that the selectivity of copper synthesis in the presence of calcium ions depends on the mixing rate, which enhances the complexation and precipitation kinetics of copper ions.

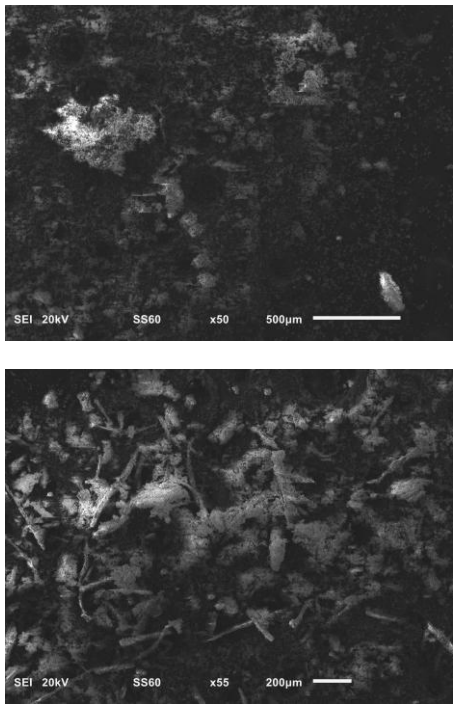
Effect of ferrous iron ions concentration on the copper oxalate formation

Acidic leaching of ferric iron oxyhydroxides and oxidation of sulphides are the main sources of iron ions (Fe^{2+} and Fe^{3+}) in wastewater from the mining industry and in pregnant leach solutions from biohydrometallurgy. Iron, compared to calcium, can build significant concentrations in the above-mentioned streams, requiring a separate stage for iron removal as part of the flowsheet for their processing. Ferrous and ferric iron ions behave differently in the presence of oxalate ions, as ferrous form precipitate to ferrous oxalate (mineral humboldtine, $FeC_2O_4.2H_2O$), while ferric ions form soluble complexes with the organic anions such as $[Fe(C_2O_4)_3]^{3-}$. Therefore, ferric ions must be removed from the mining solutions using suitable methods (precipitation, solvent extraction, reduction, etc.) before precipitating the raw materials as oxalates. In that case, the highly acidic pH of the solution suppressed chemical oxidation of ferrous iron to the ferric state.

The removal of copper as copper oxalate in the presence of ferrous iron ions could be possible due to the three orders of magnitude difference of their K_{sp} values (Table 1). Therefore, the process was carried out under experimental conditions similar to those used for copper removal in the presence of calcium ions.

The precipitation of 0.0069 M Cu^{2+} as copper oxalate in the tested concentrations of ferrous iron ions resulted in the formation of fine, light-blue particles with no yellow-lemon spots (distinctive appearance of $FeC_2O_4.2H_2O$). These particles filtered more slowly than the precipitates obtained from all other experiments. The yield of precipitate and efficiency of copper removal determined at equimolar concentrations of copper and ferrous iron ions dropped to 30.4 % and 50.4%, respectively, with the lowest values observed in the presence of 0.045 M Fe^{2+} (Table 2). It is well known that cation concentrations directly affect the rate of precipitation and the size of crystals at the next stage (Lee et al., 2022). Therefore, the initial higher concentration of ferrous iron ions resulted in rapid nucleation and a higher population of smaller particles on the one hand, and structural disorder due to their inhibitory effect on polymerisation and the long-range growth of already formed crystals on the other hand (Cismasu et al., 2011).

In this case, electron microscopy showed that the particles were not irregular in shape but were elongated and had a distinctly granular surface, especially particles formed in the presence of 0.045 M Fe^{2+}. In the presence of 0.01 M Fe^{2+}, the dominant size of deposited particles was below 100 μ (Figure 6a). In contrast, in the presence of a higher ferrous ion concentration, the particles deposited on the surface of filter paper formed a layer consisting of fine particles non-separable from each other (Figure 6b). However, despite the low efficiency of copper removal and the low value of copper oxalate yield, the collected precipitate contented minimal amount of iron which resulted in very high process selectivity (Table 5, Figure 7).



(a)

(b)

Fig. 6. SEM morphology of the precipitates obtained from a solution containing: 0.0069 M copper and 0.01 M ferrous iron (a); 0.0069 M copper and 0.045 M ferrous iron (b)

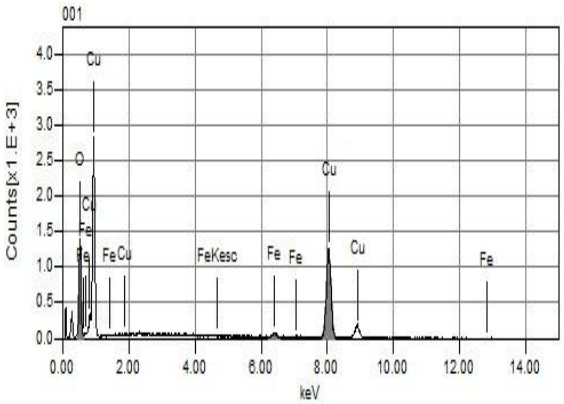


Fig. 7. EDS analysis of the precipitate obtained from a solution containing 0.0069 M copper and 0.045 M ferrous iron

Table 5. *Chemical composition of the precipitate obtained from the solution containing 0.0069 M copper and 0.045 M ferrous iron ions in three selected points (based on EDS analysis)*

Element	Content, %			Average value	Deviation
	1	2	3		
Cu	78.0	83.6	81.9	81.2	2.34
Fe	1.6	1.5	0.6	1.2	0.45
O	20.4	14.9	17.5	17.6	2.25

Mass balance of the copper content in the liquids obtained after sequential filtration through blue ribbon filter paper and a membrane filter with a pore size of 0.45 μm revealed that about 11.4% of the initial base metal content was present in fine particles smaller than 2-3 μm. Several approaches could be applied to increase the yield of larger copper oxalate particles in the presence of ferrous iron ions. Firstly, to increase reaction time and, in this way, enhance the agglomeration of fine particles into larger structures. Secondly, to change the scheme of oxalic acid addition to the solution, combined with maintaining a rate of agitation higher than 240 rpm, to decrease the number of the initially formed nuclei around which growth formed particles with a distinctive structure later.

The XR diffraction pattern revealed the presence of only moolooite, copper oxalate ($CuC_2O_4 \cdot H_2O$), but not humboldtine ($FeC_2O_4 \cdot 2H_2O$) in the precipitate obtained in the experiment (Figure 8). This is likely due to its content below the detection limit of the used diffractometer (2.0 %), or to the formation of crystals with a disordered structure, which makes it difficult to detect using this method (Korneev et al., 2022).

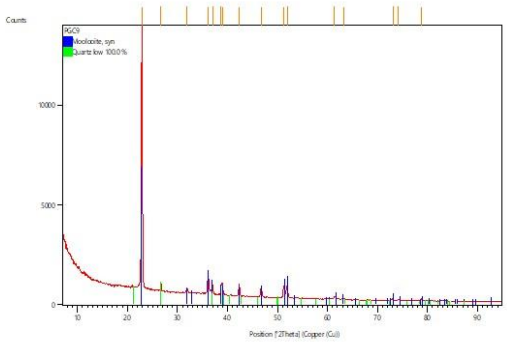


Fig. 8. XRD pattern of precipitates obtained from a solution containing 0.0069 M copper ions and 0.045 M ferrous iron

Conclusion

Calcium content in the model solution, exceeding the equimolar copper content negatively affected the efficiency and selectivity of copper removal as copper oxalate. However, the oxalate obtained from the process consisted of particles larger than 200 μm, which accounted for the high filtration rate. Ferrous iron ion content higher than the equimolar copper content significantly affected copper oxalate synthesis, resulting in particles smaller than 100 μm and reducing the filtration rate. Therefore, the iron content in the mining solution should be removed by suitable methods (oxidation, precipitation, solvent extraction, etc.) before the copper removal to copper oxalate.

Acknowledgements

The authors would like to express their gratitude to the National Science Programme "*Critical and Strategic Raw Materials for a Green Transition and Sustainable Development*", approved by the Resolution of the Council of Ministers № 508/18.07.2024 and funded by the Ministry of Education and Science (MES) of the Republic of Bulgaria, and the Scientific Research and International Partnership Unit of the University of Mining and Geology "St. Ivan Rilski", Sofia (under GPF-260/ 2026 project) for supporting this study.

References

Aref, R., Jantunen, N., & Virolainen, S. (2026). Recovery of high-purity cobalt oxalate from acidic effluents with solvent extraction technology. *Chemical Engineering Science*, *330,* 23878. https://doi.org/10.1016/j.ces.2026.123878

Bohner, B., Schuszter, G., Berkesi, O., Horváth, D., & Tóth, Á. (2014). Self-organization of calcium oxalate by flow-driven precipitation. *Chemical Communications*, *50*(33), 4289–4291. https://doi.org/10.1039/c4cc00205a

Botta, M. P., Attina, B., Ravera, M., & Gabano, E. (2025). Becoming aware of endangered and critical elements: spent batteries as metal mines. *Journal of Chemical Education, 0102 (5), 2103-211.* https://doi.org/10.1021/acs.jchemed.4c01535

Chen, X., Huang, K., & Wang, C. (2018). Facile synthesis of monodispersed copper oxalate flaky particles in the presence of EDTA. *International Journal of Minerals, Metallurgy, and Materials*, *25*(7), 762–769. https://doi.org/10.1007/s12613-018-1624-5

Cheng, S., Vaughan, J., Wang, G., Ma, X., Lyu, X., & Peng, H. (2026). Slag to product: Unlocking titanium-bearing slag value via selective leaching of amorphous titanium phase. *Minerals Engineering, 235*, 109846. https://doi.org/10.1016/j.mineng.2025.109846

Cismasu, A. C., Michel, F. M., Tcaciuc, A. P., Tyliszczak, T., & Brown, J. G. E. (2011). Composition and structural aspects of naturally occurring ferrihydrite. *Comptes Rendus. Géoscience*, *343*(2-3), 210–218. https://doi.org/10.1016/j.crte.2010.11.001

Gylliene, O., & Saulkaskas, M. (1995). Metal recovery from spent electroless plating solutions by oxalate precipitation. *Plating & Surface Finishing*, 61-63.

Gyliene, O., Saulkaskas, M., & Juskenas, R. (1997). The use of organic acids as precipitants for metal recovery from galvanic solutions. *Journal of Chemical Technology & Biotechnology 70*(1), 111-115. https://doi.org/10.1002/(SICI)1097-4660(199709)70:1<111::AID-JCTB691>3.0.CO;2-9

Joseph, E., Cario, S., Simon, A., Wörle, M., Mazzeo, R., Junier, P., & Job, D. (2012). Protection of metal artefacts with the formation of metal–oxalates complexes by Beauveria bassiana. *Frontiers in Microbiology*, *2*. https://doi.org/10.3389/fmicb.2011.00270

Krajanova, V., & Lalinska-Volekova, B. (2025). Hydrometallurgical leaching experiments on selected minerals and materials by oxalic acid. Proceedings of 25 SGEM International Multidisciplinary Scientific GeoConference 2025, 29 June – 06 July 2025 - Albena, Bulgaria, pp. 319-324. https://doi.org/10.5593/sgem2025/1.1/s03.39

Korneev, A. V., Izatulina, A. R., Kuz'mina, M. A., & Frank-Kamenetskaya, O. V. (2022). Solid Solutions of Lindbergite–Glushinskite Series: Synthesis, Ionic Substitutions, Phase Transformation and Crystal Morphology. *International Journal of Molecular Sciences*, *23*(23), 14734. https://doi.org/10.3390/ijms232314734

Lee, K. R., Kim, J., & Jang, J. G. (2017). Recovery of zinc in spent pickling solution with oxalic acid. *Korean Chemical Engineering Research 55*(6), 785-790. DOI:10.9713/kcer.2017.55.6.785

Lee, S. I., Kim, H. R., Park, J. K., J.K., Oh, W., Kim, J., Kim, C., Lee, J., Kim, K.-C., & Lee, B.-C. (2022). Precipitation of ferrous oxalate from ferrous ammonium sulphate in oxalic acid solution. *Processes*, *10*(11), 2420. https://doi.org/10.3390/pr10112420

Li, X., Ma, B., Wang, C., & Chen, Y. (2024). Sustainable recovery and recycling of scrap copper and alloy resources: a review. *Sustainable Materials & Technologies, 41*, e01026. doi.org:1016/j.susmat.2024/e01026

Martins, L. S., Rovani, S., Botelho, A. B. J., & Espinosa, D. C. R. (2023). Sustainable approach for critical metals recovery through hydrometallurgical processing of spent batteries using organic acids. *Industrial & Engineering Chemistry Research*, *62*(44), 18672-18682. https://doi.org/10.1021/acs.iecr.3c03048

Mustafa, L., Usman, M., Ali, S., Ali, A., & Naveed, A. (2025). Recycling technologies for extracting gallium from light-emitting diodes. *Photonics, 12* (8), 808. https://doi.org/10.3390/photonics12080808

Palmieri, F., Estoppey, A., House, G. L., Lohberger, A., Bindschedler, S., Chain, P.S.G., & Junier, P. (2019). Oxalic acid, a molecule, at the crossroads of bacterial-fungal interactions. *Advanced Applied Microbiology,* 106, 49-77. DOI: 10.1016/bs.aambs.2018.10.001

Roy, J. J., Srinivasan, M., & Cao, B. (2021). Bioleaching as an eco-friendly approach for metal recovery from spent NMC-based lithium-ion batteries at a high pulp density. *ACS Sustainable Chemistry & Engineering*, *9*(8), 3060-3069. https://doi.org/10.1021/acssuschemeng.0c06573

Rumble, J. (2018). *CRC Handbook of Chemistry and Physics* (99 ed.). CRC Press. pp. 5–188. ISBN 978-1138561632

Shlesinger, M.E., Sole, K.C., Davenport, W.G., & Alvear Flores, G.R.F. (2021). Extractive metallurgy of copper. (6th ed.). Elsevier. ISBN-13: 978-0128219034

Tita, A.M., Mends, E.A., Kar, U., Hussaini, S., & Chu, P. (2025). Leaching of Li-bearing sedimentary claystones using organic acids. *Green and Smart Mining Engineering*, *2(*2), 156-167. https://doi.org/10.1016/j.gsme.2025.06.002

Verma, A., Kore, R., Corbin, D.R., & Shiflett, M.B. (2019). Metal recovery using oxalate chemistry: a technical review. *Industrial & Engineering Chemistry Research, 58*(34), 15381-15393 https://pubs.acs.org/doi/10.1021/acs.iecr.9b02598#

Wen, Y., Tribby, E.L., & Tang, Y. (2025). Intensified and selective recovery of critical metals from aqueous extracts: Fundamentals and system design. *Chemical Engineering Journal*, *512*, 162661. https://doi.org/10.1016/j.cej.2025.162661

Werner, H., Bapat, S., Schobesberger, M., Segets, D., & Schwaminger, S. P. (2021). Calcium oxalate crystallisation: Influence of pH, energy input, and supersaturation ratio on the synthesis of artificial kidney stones. *ACS Omega*, *6*(39), 26566–26574. https://doi.org/10.1021/acsomega.1c03938

Yang, Y., Song, W., Ferrier, J., Liu, F., Csetenyl, L., & Gadd, G.M. (2020). Biorecovery of cobalt and nickel using biomass-free supernatants from *Aspergillus niger*. *Applied Microbiology & Biotechnology*, *104*, 417-425. DOI: 10.1007/s00253-019-10241-2

Ye, C., Wang, Z., & Shen, Y. (2022). Preparation of iron-copper oxalates and oxides for the oxygen evolution reaction. *Journal of the Electrochemical Society*, *169*, 064503. DOI: 10.1149/1945-7111/ac7259

Zeng, L., Deng, S., Yang, X., & Zhang, W. (2026). Valorisation of pyrite in coal refuse into battery-grade ferrous oxalate: A sustainable pathway. *Chemical Engineering Journal, 534,* 174699. https://doi.org/10.1016/j.cej.2026.174699

NON-FERROUS METAL BIOLEACHING FROM COPPER SLAG WITH A SPENT MEDIUM OF *SPOROSARCINA UREAE*

Plamen Georgiev, Marina Nicolova, Irena Spasova

University of Mining and Geology "St. Ivan Rilski", 1700 Sofia; E-mail: ps_georgiev@mgu.bg
Corresponding author: ps_georgiev@mgu.bg

ABSTRACT. The aim of this study is the indirect bioleaching of non-ferrous metals from pyrometallurgical copper slag containing 0.36% Cu, 1.93% Zn, and 0.09% Co using a spent culture medium from the bacterial strain *Sporosarcina ureae* CCM 981 with a pH of 9.43. Bioleaching was performed using the flask shaking technique at 150 rpm for 72 hours, yielding the best results for the extraction of copper (21.5%), zinc (21.2%), and cobalt (41.3%) at 55 °C and a pulp density of 7.5%. Iron and silicon co-leached, resulting in selectivity values of 0.307 and 0.98, respectively, for non-ferrous metal extraction from the copper slag sample under these experimental conditions.

Key words: bioleaching, non-ferrous metal, copper slag, selectivity

Introduction

The higher demand for base metals and some critical raw materials over the past few decades, driven by sectors such as IT and green transition technologies, has led to annual growth of 2.6% in copper pyrometallurgy and to worldwide annual copper slag generation of 37.7 million tons (Phiri et al., 2022). Apart from copper, copper slags also contain valuable metals, such as cobalt and nickel. Therefore, copper slag is regarded as a raw material whose processing and extraction are tools in the circular economy (Whitworth et al., 2022).

Base metals occur in different phases in copper slag, including sulphides, zero-valence states, oxides, and those absorbed or encapsulated in the crystal lattices of main minerals, such as fayalite, silicates, or magnetite (Deng & Ling, 2007; Prince et al, 2016; Dzinomwa et al., 2023). Therefore, classical methods of mineral processing, such as flotation and pyrometallurgy, are insufficient due to copper recovery of around 50% of the total copper content, the loss of cobalt and nickel in the generated flotation tailings, and higher operational costs for energy and reagents.

Another approach to recover base metals from copper is (bio)hydrometallurgy, which offers the main advantages of operating at ambient temperature and pressure and of generating / recycling lixiviants for the leaching process through microbial growth (Weng et al., 2025; Abraham and Shopf, 2026). A suitable group is the chemolithotrophic bacteria with sulphur-oxidising/ ferrous-oxidising abilities, related to the species *Acidithiobacillus thiooxidans*, *A. ferrooxidans*, and *Leptospirillum ferrooxidans*, which grow at highly acidic pH levels, thereby enhancing efficient copper and other base metal extraction (Mikoda et al., 2018; Watkin et al., 2024), as well as intensive co-leaching of silicon and iron, as the main drawback.

Heterotrophic microorganisms also participate in mineral transformations, especially at pH levels ranging from slightly acidic to alkaline. In that case, several bioleaching mechanisms, including acidolysis, complexolysis, redoxolysis, biosorption, bioaccumulation, and alkalolysis, driven by heterotrophic microorganisms, participate in the bioleaching of base metals (Kumar et al., 2023). Each microbial species with heterotrophic metabolism utilises a narrow range of the mechanisms mentioned above.

This study aims to recover base metals from a copper slag sample containing 0.36% Cu, 1.93% Zn, and 0.09% Co via indirect bioleaching using the spent medium of the bacterial strain *Sporosarcina ureae* CCM 981 at a slightly alkaline pH.

Materials and methods

Pyrometallurgical copper slag

The copper slag sample containing 1.93 % Zn, 0.36 % Cu, and 0.09 % Co as valuable elements and 27.2 % iron and 15.9 % Si (Table 1) was subjected to grinding to particle size – 75 μm to + 25 μm. In that form, the copper slag was used in bioleaching experiments.

Table 1. *Chemical content of the copper slag sample used in this study*

Chemical element, %	Value
Fe	27.2
Si	15.9
Ca	6.9
Al	2.78
Cu	0.36
Zn	1.93
Co	0.09
Mn	0.8
P	0.08
S	0.91
pH (H_2O)	7.95

Characterisation of the copper slag

The mineralogical composition of copper slag, which was carried out by X-ray Diffraction analyser EMPYREAN using Cu-Kα radiation and operated at 40 kV and 30 Ma, revealed the presence of compounds with the phase structures of protomangano-ferroanthophyllite ($H_2Fe_{4.48}Mg_{1.08}Mn_{1.44}O_{24}Si_8$), fayalite ($Fe_2SiO_4$) and an unidentified type of pyroxene ($Ca_{0.949}Fe_1Na_{0.051}O_6Si_2$) with content of 56.8 %, 33.2 %, and 10.0 %, respectively. The pH of the copper slag was determined

in distilled water after 1 hour of agitation with an overhead mixer at 150 rpm.

The chemical leaching of non-ferrous metals was studied over a pH range from slightly acidic to alkaline by adding sulphuric acid or ammonia solution to the prepared pulp, with agitation at 300 rpm and 25 °C. The acid/ base addition stopped when the pulp's pH reached the targeted value (6.0, 5.0, or 9.0, 10.0) and remained constant for 6 hours. The pulp sample was collected and centrifuged, and by AAS-ICP methods, the concentration of the elements in the transparent solution was determined.

Bacterial culture and maintenance

Sporosarcina ureae CCM 981 (hereinafter referred to as *S. ureae*) was obtained from the Czech Collection of Microorganisms at the Department of Experimental Biology at Masaryk University. The strain was maintained in a medium suitable for *Sporosarcina* spp. and stored at 4 °C as needed. The medium was inoculated with 1 mL bacterial suspension/ 100 ml and incubated for 7 days at 35 °C under continuous shaking (150 rpm). The duration was the only variable; all other parameters were constant across experiments.

Indirect biological leaching of copper slag

The indirect technique was carried out in two steps. The first step was initiated by inoculating the nutrient medium with the following content: peptone (20 g/ L), K_2HPO_4 (0.75 g/ L), $MgSO_4.7H_2O$ (0.3 g/ L), urea (20.0 g/ L), yeast extract (2.0 g/ L), with 1 mL of bacterial suspension. The flasks were incubated for 7 days at 35 °C under continuous shaking at 150 rpm. Water loss due to evaporation was compensated for by adding distilled water. After the 7th day, the bacterial biomass was separated from the spent medium by centrifugation at 10,000 rpm for 15 minutes. The second step of indirect bioleaching of non-ferrous metals from copper slag was carried out using a transparent, microbial-free spent medium produced under continuous shaking at 150 rpm for 3 days.

Alkalinity, the concentration of NH_4^+ and TOC of the obtained spent medium of *Sporosarcina ureae* were determined by standard analytical methods (APHA, 1995), such as acidic titration with 0.1 N HCl to a pH of 8.3, salicylate colourimetric method, and standard method 5310D (at a temperature of 200°C in a highly acidic pH and in the presence of strong chemical oxidants such as P_2O_5 and CrO_3), respectively.

The effect of leaching duration (1-4 days), pulp density (7.5, 10.0, or 12.5 %), and temperature (35 °C, 55 °C, or 75 °C) on the efficiency and selectivity of copper, zinc, and cobalt recovery was studied. Monitoring of pH and leaching of non-ferrous metals was carried out daily.

All experiments were performed in triplicate, and the results are reported as mean values.

The efficiency of metals (non-ferrous metals and iron) and silicon extraction from the copper slag sample under relevant experimental conditions (Er) was calculated according to the following formula:

$$Er = \frac{C1 - C2}{C1} \times 100, \% \quad (1)$$

where Er-element recovery, %; C_2-metal concentration in the copper slag residue, mg/ kg; C_1-metal concentration in the raw copper slag, mg/ kg.

Selectivity coefficient (S) of the non-ferrous leaching from the copper slag sample at the relevant experimental conditions was calculated according to the following formula:

$$\boldsymbol{S} = \frac{\sum(CCu + CZn + CCo)}{(\mathrm{Cse})} \quad (2)$$

where S – selectivity coefficient; $\sum$ (C_{Cu} +C_{Zn} + C_{Co}) - sum of copper, zinc, and cobalt concentrations in the pregnant leach solution, mg/L; C_{SE} - concentration of structural element (iron or silicon) in the pregnant leach solution, mg/ L.

Results and discussion

Non-ferrous metal chemical leaching from copper slag

The studied copper slag sample had a slightly alkaline pH of 7.95 (Table 1). The chemical leaching of non-ferrous metals at slightly acidic/slightly alkaline pH was chosen due to the higher content of silicate minerals in the raw material and the significant effect of certain microbial groups on the microenvironmental pH in the presence of suitable substrates for their growth (Rezza et al., 2001).

The chemical leaching of non-ferrous metals from the copper slag sample with ammonia was studied at a slightly alkaline pH (8-11). Biological processes, such as the bio-oxidation of organic acids and the ammonification of nitrogen-enriched organic compounds, carried out by heterotrophic microorganisms, consume free hydrogen ions, thereby shifting the pulp's pH toward alkalinity. It enhances the degradation of silicate minerals and the recovery of valuable elements from copper slag by liberating their cations and forming soluble complexes with ammonia ions (Rezza et al., 2001). Under such conditions, the amount of non-ferrous metals recovered by chemical leaching with ammonium ions ranges from 2.5 % for cobalt to 0.5 % for copper, which is insignificant compared to the results of chemical leaching at a slightly acidic pH (4-6) (Figure 1).

Biological processes of sulphide oxidation and oxidation of suitable organic compounds (monosaccharides/ alcohol), carried out by chemolithotrophic and heterotrophic bacteria, respectively, produce sulphuric acid or weak organic acids. Those compounds are sources of free hydrogen ions, turning the pH from slightly alkaline to acidic. Non-ferrous metal leaching from the copper slag sample under these conditions was simulated using sulphuric acid leaching. In that case, the minimum amount of sulphuric acid was needed to drop the native pH of the raw copper slag sample to a slightly acidic pH of 5.0 (Figure 1).

This results in the substantial leaching of non-ferrous metals, which varies between 19.8 % recovery for zinc and 14.2 % of copper, as well as substantial co-leaching of silicon and iron; 13.2% and 19.3 %, respectively. The higher content of protomangano-ferroanthophyllite in the copper slag sample indicated that weathering occurred during storage of the slag on the dump for more than sixty years. Weathering involves the sequential alteration of the initially deposited copper slag mass from larger grains with lower surface area to smaller grains with higher surface area, and changes in their chemical content due to leaching, co-precipitation, and adsorption. Therefore, non-ferrous metal leaching strongly depended on the leaching of iron and silicon, the main structural elements in the raw sample and in the minerals that contain them.

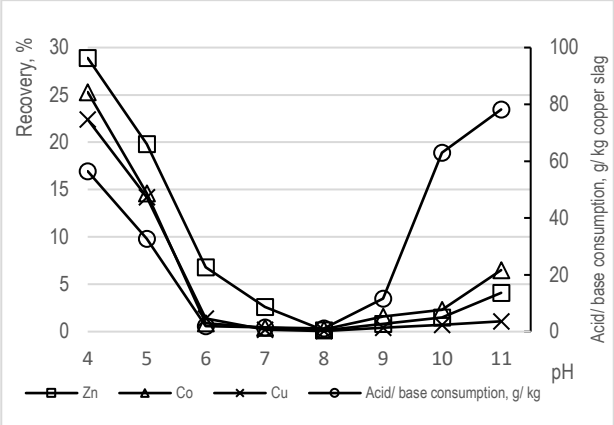


Figure 1. Acid/ base consumption of the copper slag sample and its effect on the non-ferrous metal recovery in dependence on the target pH

Characteristics of the spent medium of *Sporosarcina ureae*

S. ureae is a heterotrophic and mesophilic bacterium which gains energy using oxygen as a final acceptor of electrons. It is typical in soil and manure, biotopes enriched with nitrogen-containing organic compounds (Coelho et al., 2022). The *S. ureae* strain used in this study was chosen for its ability to produce the enzyme urease, converting urea into ammonia and carbon dioxide at a higher rate according to the following reaction:

$$(NH_2)_2CO + H_2O \rightarrow 2NH_3 + CO_2 \quad (3)$$

Urease is an inducible type of enzyme whose synthesis and regulation are strongly dependent on the urea content in the nutrient medium. Its synthesis results in faster microbial growth, a more negative surface charge, and higher biomineralisation ability (Ma et al., 2020).

Ammonia is a compound that dissolves easily in water and transforms into an ammonia ion:

$$NH_3 + H_2O \rightarrow NH_4^+ + OH^- \quad (4)$$

Because of its low toxicity and cost, ease of recovery, and higher selectivity, ammonium has been recognised as an effective leaching agent in hydrometallurgy. Therefore, it is highly used in the recovery of copper from a wide range of raw materials such as ore and concentrate (Radmehr et al., 2014), fly ash (Chiang et al., 2013; Ramanathan and Peng, 2016), slag (Wilcher and Bosecker, 2003; Chiang et al., 2013), sulphide tailings (Yin et al., 2018), and sewage sludge (Wang et al., 2024).

The spent medium obtained after a week of cultivation of *S. ureae* on the nutrient media, is characterised by a slightly alkaline pH, higher alkalinity, and ammonia ions and low-molecular-weight organic compounds, mainly organic anions, with contents exceeding 1.0 g/L (Table 2). Therefore, the chemical composition of the spent medium is more complex than that of the ammonia-based solution used for chemical leaching of copper slag at alkaline pH. Their effect on base metal recovery from raw materials is well recognised (Chiang et al., 2013). *S. ureae* has been widely studied recently because of its role in the microbial-induced carbonate precipitation process (MICP).

Table 2. *Spent medium of Sporosarcina ureae obtained after a week of cultivation*

Index	Value
pH	9.43
Alkalinity, g/ L	11.7
NH_4^+, g/ L	1.05
Total organic carbon, g/ L	1.73

This process could be applied to the practice for bioremediation of ecosystems situated around the abandoned mine sites and affected by acidic effluents and heavy metal ions, such as Cu, Cd, Cr(III), or Zn (Kang et al., 2016; Duarte-Nass et al., 2020; Huang et al., 2022), as well as to enhance the recovery of some critical metals, as lithium, due to the removal of alkaline earth metals, such as calcium and magnesium (Rehmanji et al., 2025). The concentration of carbonate ions produced, as well as the architecture and surface charge of the microbial biofilm, determined the efficiency of heavy metal ion removal via carbonate precipitation and reduced the biotope's ecotoxicity towards typical soil inhabitants (Yee and Fein, 2001; Ma et al., 2020).

Indirect bioleaching of copper slag with the spent medium of *Sporosarcina ureae*

Effect of the duration of the leaching process

The indirect leaching of copper slag at 7.5 % pulp density using the spent medium of *S. ureae* was a promising technique for the recovery of the easily leachable fractions of non-ferrous metal. The experiment revealed that the optimal duration of the process was three days, with recovered amounts of zinc, copper, and cobalt reaching 19.9%, 15.1%, and 39.6%, respectively. The higher cobalt extraction was due to the relatively low content of the critical element and its tendency to accumulate in micro-zones between copper slag particles, thereby enhancing its recovery through desorption (Deng and Ling, 2007).

The formation of soluble copper-ammonium complexes at alkaline pH enhanced the base metal recovery:

$$Cu^{2+} + 4(NH_4)^+ \rightarrow [Cu(NH_3)_4]^{2+} + 4H^+ \quad (5)$$

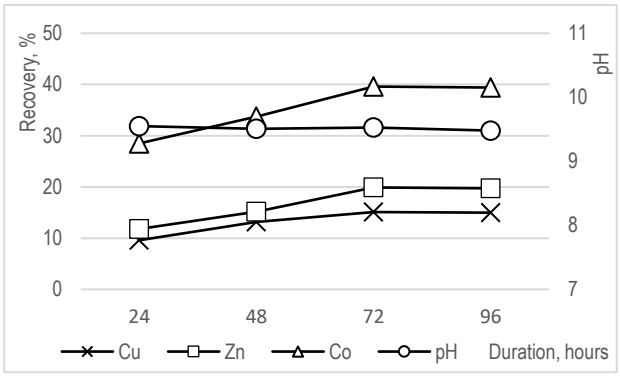


Figure 2. Effect of duration of experiment on the indirect bioleaching of non-ferrous metals from copper slag with spent medium of *S. ureae* at 7.5 % pulp density and at 35 °C

However, the higher base metal content and the fact that approximately 25% of that content remained as a phase-leachable fraction only after an oxidising process significantly

limited the recovery of copper (Georgiev et al., 2025a). Due to sorption, the concentration of base metals in the pregnant solution slightly declined after the third day of leaching.

The main processes involved in base metal leaching were acidolysis, desorption of the metals from the mineral surface, complexolysis of released cations with suitable ligands (organic anions and ammonium cations) in the spent medium, and alteration of the mineral surface due to enhanced co-leaching (Whitworth et al., 2022).

The indirect bioleaching of non-ferrous metals is carried out in two phases, each with its own recovery efficiency (Figure 2). The first phase began at the start of leaching and lasted for the first 24 hours. During that period, approximately 70% of the total leached amounts of copper, zinc, and cobalt were leached efficiently under these conditions. It relates to the amounts of base metals that desorb easily from mineral surfaces into the pregnant solution. However, the recovered amounts of non-ferrous metals for the first 24 hours were more than 10 times higher than the amounts recovered by chemical leaching at alkaline pH. This demonstrated the positive effect of dissolved organic compounds, particularly organic acids and their respective anions in the spent medium, on enhancing the extraction of non-ferrous metals by facilitating their desorption from the mineral surface and promoting the formation of soluble complexes.

The second phase of indirect leaching lasted from the second day until the end of the experiment, with the extraction of non-ferrous metals increasing by an additional 20–30%. It relates to the amounts of base metals leached due to iron and silicon co-leaching and weathering of the minerals` structure. Therefore, the copper slag decreased in weight by 2.7% at the end of the experiment.

The efficiency of microbial leaching of non-ferrous metals from copper slag depends directly on the type and concentration of microbial metabolites produced, as well as on each strain's adaptation to environmental conditions. For example, acidophilic chemoautotrophic bacteria not only oxidise and dissolve the sulphides of non-ferrous metals but also produce sulphuric acid, which, through acidolysis, dissolves their oxide minerals in the mineral feedstock. For this reason, as well as due to this group of bacteria's adaptations to highly acidic pH and high concentrations of non-ferrous metals in the pregnant solution, the efficiency of non-ferrous metal recovery usually exceeds 65% (Georgiev et al., 2017). This is why this group of microorganisms has been used for decades in the copper recovery from low-grade ores. A major drawback of this approach is the low selectivity of sulphuric acid as a leaching agent, leading to high concentrations of iron and, in some cases, silicon and calcium in the leachate.

Fungi, particularly strains of *Aspergillus niger*, are the most promising among heterotrophic microorganisms. The reason for this is that they are natural producers of citric acid, a natural organic compound with the strongest acidic properties and excellent complex-forming ability. For example, indirect biological leaching using spent culture medium of *Aspergillus niger* occurred at a slightly acidic pH (4.4), with non-ferrous metal recovery ranging from 22.5 to 44.4% (Georgiev et al., 2025a).

Heterotrophic bacteria play a role in the leaching of non-ferrous metals at neutral pH. For example, the indirect leaching of non-ferrous metals from copper slag using a production solution formed by the growth of the silicate bacterium *Bacillus megatherium* in a nitrogen-free medium but with nitrogen-fixing ability ranged from 11.8 to 16.4% (Georgiev et al., 2025b).

Effect of pulp density

The recovery of non-ferrous metals from raw material above a certain pulp density drops significantly, regardless of the leaching technique used. Factors, such as higher concentration of toxic metals in solutions, which resulted in the increased toxicity to microorganisms used in bioleaching; accumulation of ions in the pregnant leach solution, which hinders their further mass transfer from the solid sample; inadequate pulp mixing and insufficient oxygen transfer from the atmosphere into solution; increased shear stress on the microbial cell wall, which increases at higher values of agitation rate, either individually or in combination, have a negative effect on the recovery of non-ferrous metals when a direct leaching technique is applied (Gu et al., 2018).

The effect of pulp density during the indirect bioleaching of a copper slag sample using the spent medium from *S. ureae* showed that the extraction of copper, zinc, and cobalt decreases significantly when the pulp density is increased from 7.5% to 12.5% (Figure 3). For example, the extraction of copper and cobalt decreased from 15.1% to 9.9% and from 39.6% to 26.1%, respectively. However, the mass balance analysis showed that the concentrations of non-ferrous metals extracted remained nearly constant across different pulp densities. This revealed that the main factor limiting the improved non-ferrous metal recovery under the applied experimental conditions is the initial lixiviant concentration in the spent medium of *S. ureae*.

This process drawback can be overcome by applying two distinct approaches. One option is to increase the initial concentrations of lixiviants (such as ammonium and organic anions) by adding suitable reagents to the freshly obtained spent medium. Another option is to apply a multi-stage indirect bioleaching process, in which recovery of non-ferrous metals from the raw material is carried out in a series of reactors, with different batches of spent medium solution used in each reactor. However, the better recovery of non-ferrous metals will undoubtedly come at higher capital and operating costs.

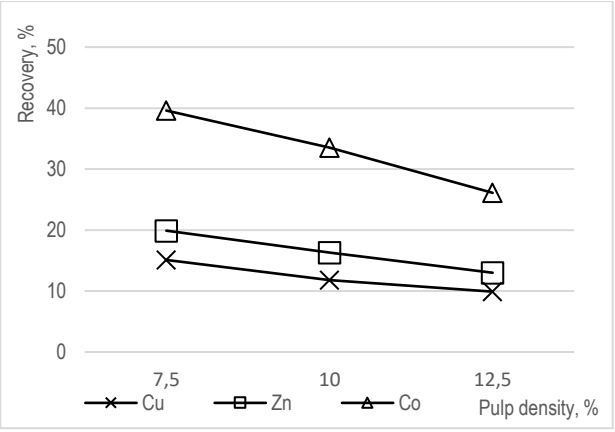


Figure 3. Effect of pulp density on the indirect bioleaching of non-ferrous metals from copper slag with spent medium of *S. ureae* for 72 hours and at 35 °C

Effect of the temperature

The main advantage of the indirect method of raw material leaching is that it is a microbial cell-free approach that can be applied at temperatures significantly above the optimal growth temperature of the relevant microbial strain. Therefore,

increasing the leaching temperature from 35 °C to 55 °C resulted in a slight increase by 1.3-1.7 % in the recovery of zinc and cobalt (Figure 4). The higher temperature had a more pronounced positive effect on copper leaching, with recovery increasing by 6.4%. However, a further increase in temperature during indirect leaching to 75 °C resulted in a significant drop in the recovery of non-ferrous metals (reaching 13.7% for zinc and 27.4% for cobalt) due to partial chemical oxidation, iron precipitation, and secondary sorption of already leached base metals.

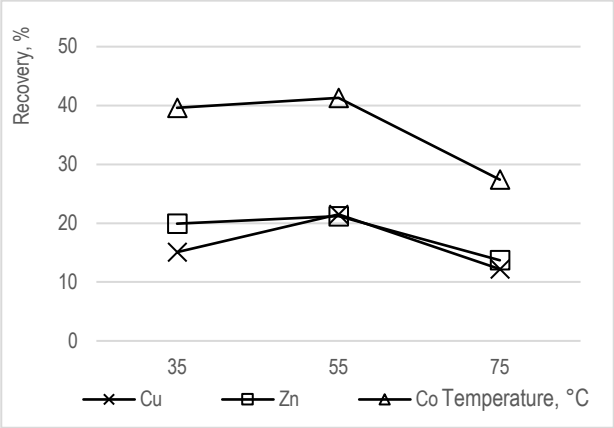


Figure 4. Effect of temperature on the indirect bioleaching of non-ferrous metals from copper slag with spent medium of *S. ureae* for 72 hours and at 7.5 % pulp density

Effect of the temperature on the selectivity of base metals leaching

The effect of temperature on the leaching of base metals from the studied copper slag sample was closely related to the leaching of silicon and iron, the main structural elements of the raw sample, and to changes in their concentrations in the pregnant leach solutions. Interrelations between those processes were characterised by the calculated selectivity coefficient values under relevant experimental conditions. Graphs presented in Figure 5 show that the indirect leaching of non-ferrous metals from copper slag with a spent medium of *S. ureae* was more selective than their alternative leaching with a spent medium generated from fungal cultivation and enriched with organic acids, such as citric and oxalic (Georgiev et al., 2025a).

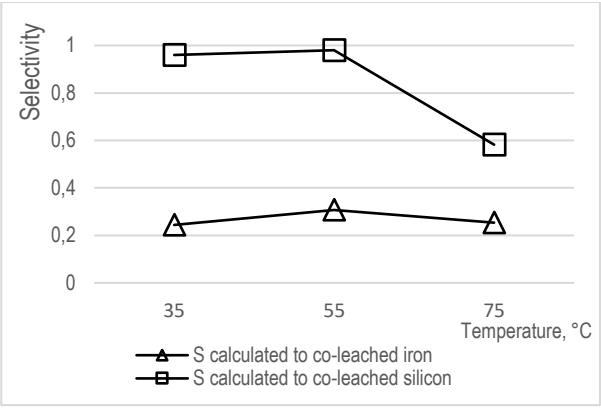


Figure 5. Effect of temperature on the selectivity of non-ferrous metals, indirect bioleaching with the spent medium of *S. ureae* from copper slag at 7.5 % pulp density

Despite the slightly alkaline pH at which the process occurred, a significant concentration of ferrous iron accumulated in the pregnant leach solution. It resulted in an S value of 0.244 at 35 °C. Despite the better leachability of silicon at slightly alkaline pH than at slightly acidic pH, the value of the relevant selectivity coefficient for base metal recovery changed only slightly at temperatures ranging from 35° to 55° C.

Indirect leaching of copper slag at 75 °C showed that higher temperatures negatively affected the recovery of base metals. Therefore, the values of both selectivity coefficients decreased due to pronounced chemical oxidation and hydrolysis of iron, as well as enhanced silicon leaching. Therefore, silicon leaching and calculated selectivity factor were not sensitive indicators of the selectivity of non-ferrous metal leaching from copper slag compared with those of iron co-leaching.

Conclusions

Sporosarcina ureae growth in media enriched in nitrogen organic compounds resulted in a spent medium with slightly alkaline pH and a significant concentration of ammonium ions. Indirect leaching of copper slag with the spent leaching solution obtained for 3 days at 35 °C resulted in recoveries of 15.1%, 19.1 and 39.6% for copper, zinc, and cobalt; the selectivity coefficient calculated with respect to the co-leached iron better characterises the non-ferrous metals recovery than selectivity calculated with respect to the co-leached silicon and the effect of temperature on the entire process. The constant concentration of the lixiviants in the spent medium, as well as the presence of 25% copper in phases leachable only under oxidising conditions, limited the further recovery of base metals.

Acknowledgements

This research has been funded by the Bulgarian "Scientific Research" Fund, Ministry of Education and Science, Bulgaria (Grant number KP-06-D002/6), ERAMIN-3 Call 2023, Project "Innovative copper slag processing for raw materials supply".

References

Abraham, A. P., & Shopf, S. (2026). Bioleaching as a biotechnological tool for metal recovery: from sewage to space mining. *Frontiers in Bioengineering and Biotechnology, 13,* 01-23. https://doi.org/10.3389/fbioe.2025.1712157

APHA. 1995. Standard methods for the examination of water and wastewater. (19th ed.). American Public Health Association, Washington, D.C

Chiang, Y. W., Santos, R.M., Monballiu, A., Ghyselbrecht, K., Martnes, J. A., Mattos, M. L. T., Gerven, T. V., & Meeschaert, B. (2013). Effects of bioleaching on the chemical, mineralogical, and morphological properties of natural and waste-derived alkaline materials. *Minerals Engineering, 48,* 116-125. doi:10.1016/j.mineng.2012.09.004

Coelho, M.A., Mesquita, A., Fusconi, R., Fernando, L., Roesch, W., & Ferreira, A. (2022). Ammonia volatilization and *Sporosarcina* genus abundance in an Oxisol enriched with urea, compost and biochar. *Applied Soil Ecology*, *176,* 104494. https://doi.org/10.1016/j.apsoil.2022.104494

Deng, T., & Ling, Y. (2007). Processing of copper converter slag for metals reclamation. Part I: Extraction and recovery

of copper and cobalt. *Waste Management & Research*, *25*(5), 440-448. doi: 10.1177/0734242X07077613

Duarte-Nass, C., Rebolledo, K., Valenzela, T., Kopp, M., Jeison, D., Rivas, M., Azocar, L., Torres-Aravena, A., & Ciudad, G. (2020). Application of microbe-induced carbonate precipitation for copper removal from copper-enriched waters: challenges to future industrial application. *Journal of Environmental Management, 256*, 109938. https://doi.org/10.1016/j.jenvman.2019.109938

Dzinomwa, G., Mapani, B., Nghipulile, T., Maweja, K., Kurasha, J. T., Amwaama, M., & Chigayo, K. (2023). Mineralogical characterization of historic copper slag to guide the recovery of valuable metals: A Namibian case study. *Materials, 16*, 6126. https://doi.org/10.20944/preprints202307.2016.v1

Georgiev, P., Spasova, I., Groudeva, V., Nicolova, M., Lazarova, A., Iliev, M., Ilieva, R., & Groudev, S. (2017). Bioleaching of valuable components from a pyrometallurgical final slag. *Solid State Phenomena, 262*, 696 – 699. DOI: 10.4028/www.scientific.net/SSP.262.696

Georgiev, P., Nicolova, M., Spasova, M., Iliev, M., & Ilieva, R. (2025a). Non-ferrous metal bioleaching from pyrometallurgical copper slag using spent medium of different fungal species. *Metals, 15*(12), 1359. https://doi.org/10.3390/met15121359

Georgiev, P., Nicolova, M., & Spasova, I. (2025b). Biological leaching of non-ferrous metals from copper slag using a strain of silicate-solubilising bacteria. *Sustainable Extraction and Processing of Raw Materials, 6*, 19-24. DOI: https://doi.org/10.58903/dw18920762

Gu, T., Rastegar, S.O., Mousavi, S.M., L,i M., & Zhou, M. (2018). Advances in bioleaching for recovery of metals and bioremediation of fuel ash and sewage sludge. *Bioresource Technology*, *261*, 428-440. doi: 10.1016/j.biortech.2018.04.033

Huang, X., Zhang, R., Cui, M., & Lai, H. (2022). Experimental investigation on bioremediation of heavy metal contaminated solution by *Sporosarcina pasteurii* under some complex conditions. *Water, 14,* 595. https://doi.org/10.3390/w14040595

Kang, C.-H., Shin, Y., Anbu, P., Nam, I.-H., & So, J.-S. (2016). Biosequestration of copper by bacteria isolated from an abandoned mine using microbial induced calcite precipitation. *Journal of General and Applied Microbiology, 62,* 206–212. doi 10.2323/jgam.2016.03.001

Kumar, V., Singh, G. & Dwivedi, S.K. (2023). Application of bioleaching for metal recovery. In Sillanpää, M.K.., Khadir, A., & Gurung, K. (Eds.), *Resource Recovery in Industrial Waste Waters*, 1st ed.; Publisher: Elsevier, 2023, pp. 295-318. https://doi.org/10.1016/B978-0-323-95327-6.00033-6

Ma, L., Pang, A-. P., Luo, X., & Lin, F. (2020). Beneficial factors for biomineralization by ureolytic bacterium *Sporosarcina pasteurii. Microbial Cell Factories, 19,* 12. https://doi.org/10.1186/s12934-020-1281-z

Mikoda, B., Potysz, A., & Kmiecik, E. (2019). Bacterial leaching of critical metal values from Polish copper metallurgical slags using *Acidithiobacillus thiooxidans*. *Journal of Environmental Management, 236*, 436-445. https://doi.org/10.1016/j.*jenvman*.2019.02.032

Phiri, T., Singh, P., & Nikoloski, A.N. (2022). The potential for copper slag waste as a resource for a circular economy. A review – part I. *Minerals Engineering, 180*, 107474. https://doi.org/10.1016/j.mineng.2022.107474

Prince, S., Young, J., Ma, G., & Young, C. (2016). Characterization and recovery of valuables from waste copper smelting slag. *Advances in Molten Slags, Fluxes, and Salts: Proceedings of the 10th International Conference on Molten Slags, Fluxes and Salts 2016*, 889-898.

Radmehr, V., Koleini, S. M. J., Khalesi, M. R., & Mohammadi, M. R. T. (2014). Ammonia leaching: a new approach of copper industry in hydrometallurgical processes. *Journal of The Institution of Engineers (India): Series D, 94*(2), 95–104. doi: 10.1007/s40033-013-0029-x

Ramanathan, T., & Peng, Y.-T. (2016). Alkaline bioleaching of municipal solid waste incineration fly ash by autochthonous extremophiles. *Chemosphere*, *160,* 54-61. https://doi.org/10.1016/j.chemosphere.2016.06.055

Rehmanji, M., Sceffington, A., Hudson-Edwards, K.A., & Newsome, L. (2025). Circular economy approaches to microbially-induced carbonate precipitation for bioprocessing of geothermal brine for lithium recovery. *RSC Advances, 15,* 43263-43.274. doi: https://doi.org/10.1039/D5RA06824J

Rezza, I., Salinas, E., Elorza, M., de Tosetti, M. S., & Donatti, E. (2001). Mechanisms involved in bioleaching of an aluminosilicate by heterotrophic microorganisms. *Process Biochemistry, 36,* 495-500. doi:10.1016/S0032-9592(00)00164-3

Wang, Z., Lu, X., Zhang, X., Yuan, Z., Zheng, M., & Hu, S. (2024). Ammonium-based bioleaching of toxic metals from sewage sludge in a continuous bioreactor. *Water Research*, *256*, 121651. https://doi.org/10.1016/j.watres.2024.121651

Watkin E.L.J., Nancucheo, I., & Schippers, A. (2024). Editorial: Acidophile microbiology: from extreme environments to biotechnological applications. *Frontiers in Microbiology*, *15,* 1454559. doi: 10.3389/fmicb.2024.1454559

Weng, W., Lan, Y., Tang, D., Chen, H., Xia, J., Chen J., & Zhong, S. (2025). Acid leaching of copper from copper slag based on machine leaching analysis. *Separation and Purification Technology, 379*(3), 135025. https://doi.org/10.1016/j.seppur.2025.135025

Willcher, S., & K. Bosecker (2003). Studies on the leaching behaviour of heterotrophic microorganisms isolated from an alkaline slag dump. *Hydrometallurgy, 71*(1), 257-264. doi: 10.1016/S0304-386X(03)00164-6

Whitworth, A. J., Vaughan, J., Southam, G., van der Ent, A., Nkrumah, P. N., Ma, X., & Parbhakar-Fox, A. (2022).Review on metal extraction technologies suitable for critical metal recovery from mining and processing wastes. *Minerals Engineering*, *182,* 107537-107537. doi: 10.1016/j.mineng.2022.107537

Yee, N., & Fein, J. (2001). Cd adsorption onto bacterial surfaces: a universal adsorption edge? *Geochimica et. Cosmochimica Acta, 65*(11), 2037-2042. https://doi.org/10.1016/S0016-7037(01)00587-7

Yin, S., Wang, L., Wu, A., Kabwe, E., Chen, X.,& Yan, R. (2018). Copper recycle from sulphide tailings using combined leaching of ammonia solution and alkaline bacteria. *Journal of Cleaner Production, 189*, 746–753. https://doi.org/10.1016/j.jclepro.2018.04.116

Sustainable Extraction and Processing of Raw Materials, 2026

INFLUELNCE OF THE CONSTRUCTION OF A BIOSENSOR BASED ON SEDIMENT MICROBIAL FUEL CELLS ON ITS SENSITIVITY TO WATERS CONTAMINATED WITH HEAVY METALS

Rosen Ivanov

University of Mining and Geology "St. Ivan Rilski", 1700 Sofia
Corresponding author: r.ivanov@mgu.bg

ABSTRACT. Sediment microbial fuel cells (SMFC) based biosensors can be a simpler and cheaper alternative to traditional methods for monitoring and early warning of water pollution with heavy metals. However, to make the transition from the laboratory to application in the environment, more research is needed on the influence, durability, and cost-effectiveness of their constructive elements. In the present study, three types of SMFC-based biosensors were constructed - with stainless steel electrodes without a separator, with graphite electrodes without a separator, and with graphite electrodes and a bentonite separator placed in the sediment. The last variant showed the highest sensitivity to the investigated pollutants - copper, chromium, nickel and zinc, as well as the highest correlation coefficient R^2 - over 0.99.

Key words: sediment microbial fuel cells, biosensor, real time monitoring, heavy metals

Introduction

With the rapid development of the industry, wastewater monitoring has become an extremely important issue worldwide. Traditional detection methods, such as spectrophotometry and atomic absorption spectrometry (AAS), have high selectivity and sensitivity, but cannot be used for in situ monitoring due to their high cost and complex sample pretreatment requirements (Turker and Yakar, 2025).

Among various emerging solutions, in recent years, microbial fuel cell (MFC)-based sensors have been envisioned as a promising low-cost and energy-efficient tool for online monitoring of water and soil contaminants. For most MFC-based sensors, exoelectric bacteria are inoculated and acclimated in the anode chamber to determine pollutant toxicity. If a pollutant inhibits the metabolic activity of exoelectric bacteria, the electrical signals (voltage or current) of these sensors weaken. This is considered the basic principle of sensors based on microbial fuel cells (Chauhan et al., 2025). However, the use of exoelectric bacteria for pollutant detection has serious drawbacks, as the sensors cannot monitor repeated fouling unless exoelectric bacteria are reconstituted or re-inoculated and acclimatized after each fouling event. Unfortunately, recovery from toxic shock or acclimatization usually takes several days to several weeks. To overcome these drawbacks, a new type of sediment microbial fuel cell (SMFC)-based sensors is being developed for monitoring water pollution events (Wang et al., 2023a). The main advantages of the sensor include a cathode instead of exoelectric bacteria in the sediment detecting pollution in the waters; the sediment adsorbs a large part of the contaminants, thus the exoelectric bacteria remain protected from inhibition and the sensor can work normally after a shock; the sensor uses naturally occurring exoelectric bacteria in the sediment to generate a base voltage; therefore, the inoculation process can be omitted; the sensor components are assembled into an integrated system, thus monitoring is conveniently started by placing the sensor in the monitored water (Li et al., 2024).

SMFCs are characterised by simplicity, low cost and maintenance, which facilitate the transfer of the technology from the laboratory to the environment (Sun et al., 2024). Sediment microbial fuel cells have great potential as cost-effective and sustainable sensors. The technology relies on endogenous electroactive microorganisms that convert chemical energy stored in biodegradable matter in the soil directly into electricity (Bose et al., 2026). Organic compounds in the sediment serve as a source of renewable fuel. Electrons are generated from the oxidation of organic matter near the anode by natural microorganisms present in the sediment. These electrons are transferred to the cathode where they reduce oxygen (Danhassan et al., 2023).

Recently, SMFCs have attracted the attention of many researchers due to the possibility of their use as biosensors for heavy metals (Abbas et al., 2026), soil toxicity, BOD (Abbas et al., 2022), oil spills (Dai et al., 2021), sediment bulking (Wang and Jiang, 2019), dissolved oxygen - DO (Azri et al., 2026), hexavalent chromium (Zhao et al., 2018) and others. However, a number of factors must be addressed before SMFC technologies can be applied on a larger scale. Previous research has focused on environmental factors, long-term stability, and other factors affecting peak voltage generation and scaling of SMFCs. Long start-up times are also one of the limitations that slow down their industrialisation. SMFC start-up refers to reaching a stable base voltage and generating electricity (Song and Jiang, 2018). Previous studies have made significant efforts to reduce the internal resistance of the cell and improve the performance of SMFCs at the laboratory scale by modifying anode surfaces, changing the anode configuration, using multiple anodes, optimising the depth and orientation of the anode in the sediment and increasing the oxygen supply to the cathode. Earlier investigations have shown that anode configuration and distribution could significantly affect SMFC performance. For example, increasing the area of a single anode will lead to higher electricity production, but it is challenging to accommodate large electrodes in cells (Wang et al., 2023b). Over the years, researchers have worked on the development of a variety of SMFCs. Many researchers have focused on increasing the current by modifying electrode materials (Wang et al., 2019) and investigating the effect of the distance between the electrodes (Simeon and Freitag, 2022).

Despite the development of platinum electrodes and other expensive materials, ultimately a major goal is to keep SMFC-based biosensors cheap and simple to operate devices so that they can gain widespread application in pollution monitoring and early warning (Nandy et al., 2023).

In the present study, the influence of two relatively low-cost stainless steel and graphite electrodes on the sensitivity and performance of SMFC-based biosensors for monitoring and early warning of water pollution with heavy metals was investigated. Also, for the first time, the influence of a separating layer of bentonite located in the sediment on the performance of a SMFC-based biosensor for monitoring water contaminated with heavy metals was investigated.

Materials and methods

Soil sampling

The river sediment used in the study was taken from Ivanyanska river, Bulgaria (23°11'46.4"E 42°42'27.1"N), from a depth of 20-30 cm. After taking the sediment, pieces larger than 2 mm were removed by sieving. For the purpose of physicochemical analyses, part of the sieved soil was air-dried. Soil pH was determined by pH-meter HANNA HI-9021 measured at 1:2.5 (soil : water). Soil electrical conductivity (EC) was determined by WTW LF 197-S measured at 1:5 (soil : water). The main physicochemical parameters of the soil were as follows: pH 6.68, EC 154.45 μS/cm. The soil was classified as sandy clay loam, the Kjeldahl-N content was 0.21% and the dissolved organic carbon 66.14 mg/ kg. The amount of copper measured was 59.5 mg/ kg, chromium – 20.2 mg/ kg, nickel – 13.0 mg/ kg, and zinc – 105 mg/ kg. The sediment microbial fuel cells-based biosensors were filled in with the soil prepared in the above-mentioned way.

Description of the laboratory installation

A scheme of the laboratory installation of a sediment microbial fuel cell-based biosensors is shown in Figure 1.

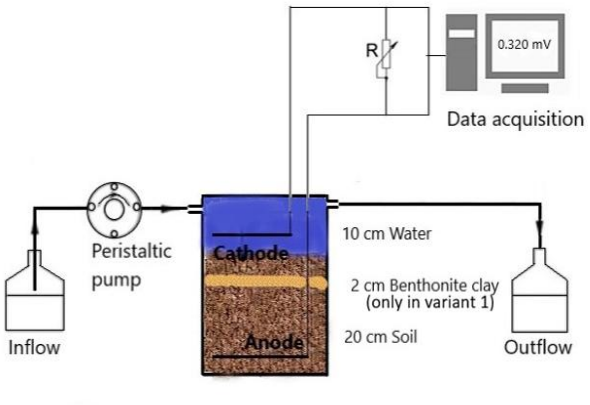


Fig. 1. Scheme of the laboratory installation of SMFC-based biosensors with different electrodes

For the purpose of the study 12 sediment microbial fuel cell-based biosensors were prepared in three variants. The sediment microbial fuel cell is a plastic container with a volume of 800 cm^3. In the first variant at the bottom of the vessel is a stainless-steel electrode AISI 304 (18% Cr, 10% Ni) with an area of 32 cm^2. The vessel was filled with river sediment with a volume of 550 cm^3. The cell was then filled with pure water and a second 32 cm^2 stainless steel electrode AISI 304 was placed in the surface layer of the water. In the second variant, graphite electrodes, also with an area of 32 cm^2, are placed in the sediment and in the surface layer of the water. The third variant is a plastic container with a volume of 800 cm^3. There is a graphite electrode with an area of 32 cm^2 at the bottom of the vessel. The cathode was made of graphite with the same area. The vessel was filled with river sediment with a volume of 510 cm^3. There is a layer of bentonite with a thickness of 2 cm in the middle of the sediment layer. The bentonite plays the role of a kind of membrane between the anode and cathode areas, which is aimed at achieving a better separation of the processes in the two areas.

The physicochemical characteristics of water were pH 7.06, Eh 213 mV and EC 58 μS/ cm measured by Vernier LabQuest Mini.

The heavy metal solutions pass through the cathode zone, where heavy metal ions play the role of an additional electron acceptor and increase the voltage of the cell by changing the electrochemical parameters. Initially, clean water was supplied to the cells until a constant base voltage was reached. The anode and cathode of each of the biosensors were connected with an external 1000Ω resistor using copper wire. Then they had been acclimated for 14 days, until the base voltage is reached and the electroactive microorganisms acclimatize. *Geobacter*, *Clostridium, Anaeromyxobacter*, and *Bacillus* were the most abundant in the sediment. *Pseudomonas*, *Desulfolobus* and *Desulfovibrio* were also isolated. The abundance of electroactive microorganisms was quantified by 16S rRNA gene.

After that, the heavy metal solutions were passed to the individual cells and the change in cell voltage was continuously recorded. Based on the correlation between voltage change and heavy metal concentration, standard curves were drawn.

Heavy metals pollution

For the purposes of the study, synthetic solutions containing copper ($CuSO_4.5H_2O$), chromium ($K_2Cr_2O_7$), zinc ($ZnSO_4.7H_2O$) and nickel ($NiSO_4.7H_2O$) with different concentrations were prepared. Solutions were prepared in eight concentrations – 0.5, 1, 2.5, 5, 10, 25, 50 and 100 mg/L.

Electrochemical analysis

To determine the response of voltage signals to heavy metals shock, the biosensors` voltage was measured and recorded with Vernier LabQuest Mini and Logger Lite software.

Results and discussion

In order to determine the influence of various design features on the performance of the SMFC-based biosensors, after stabilization of the base voltage, the passage of a synthetic copper solution through the three sensor variants began. The change in the voltage of the sensors during the passage of the solutions with different concentration was recorded, after which standard curves were drawn based on the obtained results. The graphs are presented in Figure 2. In the case of the cell with graphite electrodes and a separator placed in the sediment, the greatest change in voltages ΔU was observed as a function of Cu^{2+} ions concentration when passing the solutions of different concentration, which shows that this variant is the most sensitive to copper contamination.

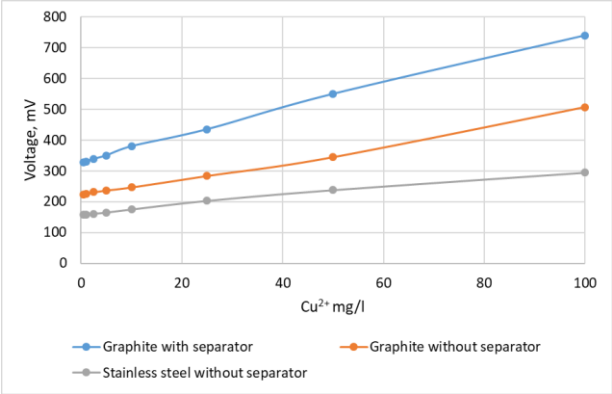


Fig. 2. Standard curves of three variants SMFC-based biosensor for copper contamination

From the presented graph, it can be seen that the biosensor with a stainless-steel electrode without a separator has the lowest baseline voltage, as well as the smallest voltage change ΔU relative to the concentration of copper ions. Nevertheless, both parameters are significantly higher compared to studies of other authors (Liu et al., 2020) on the sensitivity of SMFC-based biosensors to copper ions.

The next part of the experiment aimed to establish the influence of the design features of the SMFC-based biosensor in monitoring chromium-contaminated waters. Figure 3 shows the standard curves obtained when the chromium solutions were passed through the different variants of the sensor.

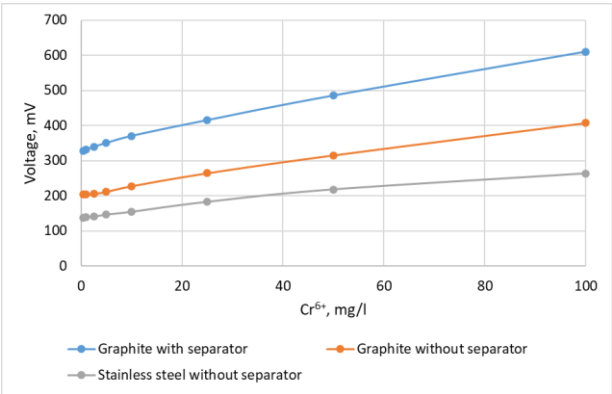


Fig. 3. Standard curves of three variants SMFC-based biosensor for chromium contamination

Again, the sensor with graphite electrodes and separator exhibits the largest change in voltages relative to the concentration of the investigated metal, corresponding to a high sensitivity to chromium ions. In this case, ΔU for a concentration of 100 mg/L Cr^{6+} ions reaches 412 mV. By comparison, when studying the sensitivity of SMFC-based biosensors to Cr^{6+} ions, this parameter varied between 25 and 150 mV (Zhao et al., 2018; Li et al., 2024).

The results from studies carried out to establish the sensitivity of SMFC-based biosensors to nickel-contaminated waters are presented in Figure 4.

The variant with graphite electrodes and separator has the highest base voltage and voltage change to different nickel ions concentrations.

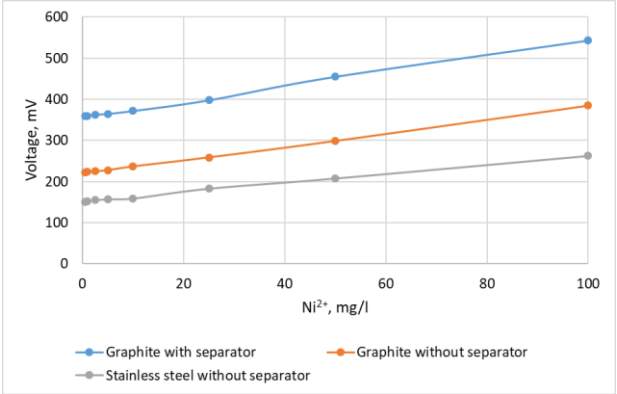


Fig. 4. Standard curves of three variants SMFC-based biosensor for nickel contamination

The last part of the experiment was aimed at establishing the influence of the structural features of the SMFC-based biosensors on their sensitivity to zinc-contaminated waters. The results obtained from the study are presented in Figure 5.

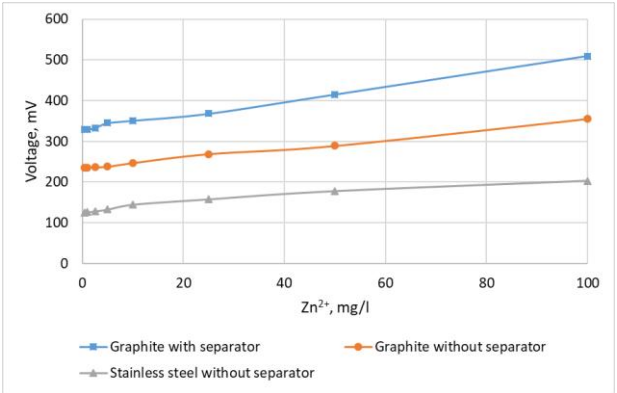


Fig. 5. Standard curves of three variants SMFC-based biosensor for zinc contamination

Smaller changes in the voltage of the sensor are observed during the passage of solutions with different concentrations of zinc ions, compared to the ions of other metals. The SMFC-based biosensor with graphite electrodes and separator again showed the highest sensitivity to zinc-contaminated waters.

From the presented graphs, it can be seen that heavy metal solutions with concentrations of 0.5 and 1 mg/L do not lead to a significant change in the biosensor`s voltage. ΔU for these concentrations varies between 1 and 4 mV, which may be attributed to side factors and cannot be indicative of heavy metal pollution.

From the obtained graphs, it can also be seen that the placement of a separator significantly increases both the baseline voltage and the sensitivity of the biosensor, expressed through ΔU. Placing a separator between the anodic and cathodic zone implies several key benefits, such as optimising ion transport, reducing oxygen penetration into the anodic zone, controlling chemical processes in the anodic and cathodic zones, and others (Bose et al., 2026). This resulted in more stable electrochemical parameters of the cell, and thus to improved sensitivity of the SMFC-based biosensor.

In order to provide better comparability of the obtained results, Table 1 presents the parameters of the linear regression and the correlation coefficient of the investigated SMFC-based biosensors.

Table 1. *Linear regression parameters and correlation coefficient of the SMFC-based biosensors*

Variant	Slope	Intercept	R^2
Cu^{2+}			
Graphite with separator	4.15	330.88	0.9981
Graphite without separator	2.79	219.7	0.9949
Stainless steel without separator	1.41	159.83	0.989
Cr^{6+}			
Graphite with separator	2.82	335.06	0.9943
Graphite without separator	2.08	203.98	0.9952
Stainless steel without separator	1.29	141.45	0.9768
Ni^{2+}			
Graphite with separator	1.87	356.43	0.9976
Graphite without separator	1.62	220.61	0.999
Stainless steel without separator	1.13	150.99	0.9972
Zn^{2+}			
Graphite with separator	1.77	329.55	0.9959
Graphite without separator	1.19	234.3	0.9954
Stainless steel without separator	0.79	130.49	0.9489

From the data presented in Table 1, high correlation coefficients are determined for all investigated variants. Nevertheless, for all four studied metals, the lowest R^2 value is obtained for the SMFC-based biosensor variant with stainless steel electrodes without a separator. Similar correlation coefficients have been reported by other authors when studying the sensitivity of SMFC-based biosensors towards copper and chromium (Liu et al., 2020; Li et al., 2024). The same trend is observed for the other two presented parameters – slope and intercept. These are highest for the SMFC-based biosensor variant with graphite electrodes and a separator, and lowest for the variant with stainless steel electrodes without a separator. The presented data further indicate that the constructed SMFC-based biosensors exhibit greater sensitivity to copper and chromium ions. This is evident from the obtained parameters for slope and intercept, which are significantly lower when investigating the sensitivity towards nickel and zinc ions. This is largely due to the nature of the studied metals and their standard reduction potentials.

Conclusion

Real-time monitoring and early warning of water pollution with heavy metals is extremely important for environmental protection. The construction of cheap and simple sensors will allow their widespread use and the timely detection and treatment of contaminated water. The present study aimed to determine the influence of construction of SMFC-based biosensors on their performance and sensitivity to waters contaminated with heavy metals. For this purpose, three variants of SMFC-based biosensors were constructed and investigated - with stainless steel electrodes without a separator, with graphite electrodes without a separator, and with graphite electrodes and a bentonite separator placed in the sediment. The sensitivity of the biosensors to four types of pollutants - copper, chromium, nickel and zinc - was investigated. The obtained results showed a high efficiency of the constructed biosensors to the investigated pollutants. A high correlation coefficient was achieved with all three biosensors variants. The most sensitive to the investigated pollutants was the SMFC-based biosensor with graphite electrodes and a separator placed in the sediment. For this variant, the highest values of the linear regression parameters – slope and intercept – were also established. The effect of a separator on the performance of a SMFC-based biosensor was investigated for the first time, and the results showed an increase in the base voltage of the sensor and an increase in the sensitivity of the biosensor to heavy metal water contamination. The studied SMFC-based biosensors display greater sensitivity to copper and chromium ions compared to nickel and zinc ions. The obtained results will contribute to a better understanding of SMFC-based biosensors and the construction of cheap and simple sensors for environmental application.

Acknowledgements

This research was financially supported by the Bulgarian National Science Fund, Grant КП-06-М57/1 from 16.11.2021.

References

Abbas, S. Z., Choi, S. H., Bruck, W. M., Samannan, B., Jang, J. K,. & Kim, T. (2026). Basswood-anode soil microbial fuel cell-based biosensor for self-sustained and wide-ranged heavy metal detection, *Bioresource Technology*, *444,* 134013. https://doi.org/10.1016/j.biortech.2026.134013

Abbas, S., Wang, J., Wang, H., Wang, J., Wang, Y., & Yong, Y. (2022). Recent advances in soil microbial fuel cells based self-powered biosensor. *Chemosphere*, *303*, 135036. https://doi.org/10.1016/j.chemosphere.2022.135036

Azri, Y. M., Sadi, M., Tou, I., Mehareb, F., Berouaken, A., & Tebbouche, L. (2026). Development of an eco-friendly and cost-effective biosensor for monitoring dissolved oxygen based on a ceramic-sediment microbial fuel cell, *Journal of Water Process Engineering*, *81,* 109312. https://doi.org/10.1016/j.jwpe.2025.109312

Bose, D., Bhattacharya, R., Pillai, M., Ray, A., Kaur, T., Mondal, S., & Mondal, A. (2026). State-of-the-art review on sediment microbial fuel cells: evolution, innovations, challenges, scalability, and policy implications for sustainable development, *Water-Energy Nexus*, *9,* 30–45. https://doi.org/10.1016/j.wen.2025.12.005

Chauhan, N., Sah, N., Saxena, K., & Jain, U. (2025). A review on biosensor approaches for the detection of hazardous elements in water, *Talanta Open*, *12,* 100536. https://doi.org/10.1016/j.talo.2025.100536

Dai, Z., Yu, R., Zha, X., Xu, Z., Zhu, G., & Lu, X. (2021). On-line monitoring of minor oil spills in natural waters using sediment microbial fuel cell sensors equipped with vertical floating cathodes. *Science of the Total Environment*, *782,* 146549. https://doi.org/10.1016/j.scitotenv.2021.146549

Danhassan, U. A., Lin, H., Lawan, I., Zhang, X., Ali, M., Muhammad, A., & Sheng, K. (2023). Critical insight into sediment microbial fuel cell: Fundamentals, challenges, and perspectives as a barrier to black-odour water formation. *Journal of Environmental Chemical Engineering*, *11*, 109098. https://doi.org/10.1016/j.jece.2022.109098

Li, C., Li, X., Li, T., Su, Y., Zhong, W., Han, C., Jiang, Y., & Deng, H. (2024). Sediment microbial fuel cell monitoring repeated Cr(VI) shocks in different wetlands for a year: Performance

and mechanism, *Journal of Cleaner Production*, *452*, 142147. https://doi.org/10.1016/j.jclepro.2024.142147

Liu, L., Lu, Y., Zhong, W., Meng, L., & Deng., H. (2020). On-line monitoring of repeated copper pollutions using sediment microbial fuel cell based sensors in the field environment, *Science of the Total Environment, 748,* 141544. https://doi.org/10.1016/j.scitotenv.2020.141544

Nandy, A., Farkas, D., Pepio-Tarrega, B., Martinez-Crespiera, S., Borras, E., Avignone-Rossa, C., & Di Lorenzo, M. (2023). Influence of carbon-based cathodes on biofilm composition and electrochemical performance in soil microbial fuel cells. *Environmental Science and Ecotechnology*, *16,* 100276. https://doi.org/10.1016/j.ese.2023.100276

Simeon, M., & Freitag, R. (2022). Influence of electrode spacing and fed-batch operation on the maximum performance trend of a soil microbial fuel cell, *International Journal of Hydrogen Energy*, *47,* 12304-123016. https://doi.org/10.1016/j.ijhydene.2021.11.110

Song, N., & Jiang, H. (2018). Effects of initial sediment properties on start-up times for sediment microbial fuel cells, *International Journal of Hydrogen Energy*, *43,* 10082-10093. https://doi.org/10.1016/j.ijhydene.2018.04.082

Sun, F., Chen, J., Tang, M., & Yang, Y. (2024). Recent research progress, challenges and future directions of sediment microbial fuel cell: A comprehensive review, *International Journal of Hydrogen Energy*, *50,* 870-886. https://doi.org/10.1016/j.ijhydene.2023.09.112

Turker, O. C., & Yakar, A. (2025). Sediment-based microbial fuel cell sensor for detecting boron mine effluent pollution in aquatic habitats, *Microchemical Journal*, *218,* 115355. https://doi.org/10.1016/j.microc.2025.115355

Wang, C., & Jiang, H. (2019). Real-time monitoring of sediment bulking through a multi-anode sediment microbial fuel cell as reliable biosensor, *Science of the Total Environment*, *697,* 134009. https://doi.org/10.1016/j.scitotenv.2019.134009

Wang, G., Yu, M., Xie, K., Zhao, R., Fu, Y., & Chen, T. (2019). Graphene modified polyacrylonitrile fibre as high-performance cathode for marine sediment microbial fuel cells, *Journal of Power Sources*, *438,* 227002. https://doi.org/10.1016/j.jpowsour.2019.227002

Wang, H., Ye, Y., Zhang, J., Ning, H., Xiang, Y., Song, X., Zhao, W., & Guo, F. (2023a). Power performance improvement in sediment microbial fuel cells: Recent advances and future challenges, *International Journal of Hydrogen Energy*, *48,* 24426-24446. https://doi.org/10.1016/j.ijhydene.2023.03.291

Wang, S., Wang, J., Zhao, L., Abbas, S., Yang, Z., & Yong, Y., (2023b). Soil microbial fuel cell based self-powered cathodic biosensor for sensitive detection of heavy metals, *Biosensors*, *13,* 145. https://doi.org/10.3390/ bios13010145

Zhao, S., Liu, P., Niu, Y., Chen, Z., Khan, A., Zhang, P., & Li, X. (2018). A novel early warning system based on a sediment microbial fuel cell for in situ and real time hexavalent chromium detection in industrial wastewater, *Sensors*, *18,* 642. https://doi.org/10.3390/s18020642

Sustainable Extraction and Processing of Raw Materials, 2026

STUDY OF STRENGTH REDUCTION IN NATURAL STONE UNDER REPEATED NON-DESTRUCTIVE DYNAMIC LOADING

Valentyn Korobiichuk[1], Sergii Iskov[1], Vasyl Mamrai[1,2], Volodymyr Shamrai[1], Dmytro Bilobrov[1]

[1]Zhytomyr Polytechnic State University, 10005 Zhytomyr, Ukraine; E-mail: korobiichykv@gmail.com, serga.iskov@ztu.edu.ua, vmamray@ztu.edu.ua, kgt_shvi@ztu.edu.ua, dimabelobrov86@gmail.com
[2] Kütahya Dumlupınar University, 43100 Kütahya; E-mail: vmamray@gmail.com
Corresponding author: korobiichykv@gmail.com

ABSTRACT. This paper investigates the reduction of strength in natural stone under repeated non-destructive dynamic loading, which is essential for assessing the suitability of deposits for selective extraction of block stone in crushed stone quarries. A laboratory testing methodology is proposed based on repeated impacts of a spherical striker on stone samples, simulating the development of tensile stresses and accumulation of microcracks in the rock mass. Numerical modelling using Ansys AUTODYN was applied to establish relationships between the impact kinetic energy and induced tensile stresses. Experimental studies were carried out on granite, gabbro, and labradorite samples from more than ten deposits in Ukraine. Strength degradation was evaluated using an ultrasonic method by measuring the propagation velocity of surface waves after each loading cycle. The results indicate that most rocks fail when their strength decreases by 11% to 41.5%. Based on the obtained data, natural stone was classified into three groups according to resistance to repeated dynamic loading: high, medium, and low durability. It was found that fatigue strength is significantly influenced by quartz content and rock structure. Coarse-grained rocks and those with a high content of accessory minerals exhibit lower resistance to cyclic loading. The practical significance of the study lies in predicting disturbed zones within quarry rock masses, which enables optimisation of block stone extraction.

Key words: natural stone, dynamic loading, fatigue strength, ultrasonic testing, selective extraction.

Introduction

During mass blasting at crushed stone quarries, repeated dynamic loads of varying energy and frequency induce intensive microcrack development throughout the rock mass. Since rocks are substantially weaker in tension than in compression, strength degradation under explosive loading is driven predominantly by tensile stresses – making tensile strength the most appropriate criterion for assessing rock damage in quarry conditions.

Information on the reduction in the strength of natural stone in certain areas of the quarry is essential for effective selective extraction of natural stone blocks at crushed stone quarries. A preliminary assessment of the suitability of a building stone deposit for selective extraction can be performed by conducting laboratory tests. Under laboratory conditions, it is possible to assess the weakening of rock strength under the action of cyclic dynamic loads using non-destructive methods. Analysis of the intensity of blasting operations and the resistance of rocks to cyclic dynamic loads will allow zoning of the quarry, where damaged and undamaged areas of the rock mass can be identified for each deposit.

Currently, the nature of dynamic rock destruction remains not fully understood, especially under conditions of cyclic loading (Xiao et al., 2010). During cyclic loading, some materials become stronger and more plastic, while others become weaker and more brittle (Bagde and Petros, 2005). For rocks, a decrease in strength during cyclic dynamic loading is characteristic, particularly during blasting operations, which is why there is a need to predict the strength characteristics of the rock (Stavrogin and Tarasov, 2001).

The effect of cyclic loads on the fatigue properties of rocks has been studied by various researchers. Bagde and Petroš (2009), based on the results of a study of fatigue and dynamic energy change in sandstone and conglomerate, established that the microstructure, texture of the stone, and quartz content affect the weakening of rock strength under cyclic dynamic loads, and that microcracks were the main cause of fatigue. Laboratory studies have shown that the behaviour of rock under dynamic cyclic loading is significantly influenced by the frequency and amplitude of the load, with the dynamic fatigue strength and dynamic axial stiffness of the rock decreasing with increasing frequency and amplitude (Vaneghi et al., 2018). Momeni et al. (2015), based on the results of a study of the behaviour of Alvand granite under different maximum loads with variable frequency and amplitude, concluded that with an increase in the cyclicity of loading, the level of resistance to destruction decreases and plastic behaviour becomes dominant in each cycle. However, due to the brittleness of the rock and the low loading rate at low frequencies, it was not possible to trace the process of accumulative damage of the granite. Singh (1989) and Momeni et al. (2015) established that natural stone is destroyed after a small number of cycles and has a shorter service life with an increase in the energy of dynamic loading. More recently, Zhou et al. (2018) confirmed this pattern for granite under low-cycle repetitive compressive impacts using a split Hopkinson pressure bar, demonstrating that cumulative damage energy increases nonlinearly with impact number. Li et al. (2022) further showed that under repeated dynamic tension – the stress regime most directly relevant to blast-induced failure – granite exhibits fatigue thresholds of 0.49–0.71 times the critical impact stress, with peak strength decreasing progressively with each loading cycle. Physical and mechanical properties of granites can be determined by the ultrasonic method (Vasconcelos et al., 2008), and this also applies to strength characteristics and accumulative damage assessment (Korobiichuk, 2016). Yang et al. (2018) demonstrated that damage accumulation under cyclic loading is reliably tracked by changes in ultrasonic wave velocity and elastic modulus, confirming the suitability of ultrasonic monitoring as a non-destructive tool for fatigue assessment in brittle geomaterials.

The presented studies demonstrate that rock texture and quartz content influence strength degradation under cyclic dynamic loading. However, the existing data remain contradictory, which is attributable to the unique texture and structural characteristics of natural stone at each individual deposit. Crucially, previous investigations have focused predominantly on uniaxial cyclic compressive loading under controlled laboratory conditions, whereas the response of rocks to repeated low-energy impact loading – directly analogous to the stress regime induced by blasting in quarries – has received considerably less attention. Moreover, no systematic classification of natural stones from Ukrainian deposits according to their resistance to repeated dynamic loading has been proposed to date. Consequently, the available data are insufficient for solving the practical problem of predicting granite strength degradation within crushed stone quarries and optimising the selective extraction of block stone.

The aim of the present study is to establish quantitative patterns of strength degradation in natural stone samples from more than ten Ukrainian deposits under repeated non-destructive dynamic loading, to develop a classification of rocks according to their fatigue resistance, and to provide a practical basis for predicting disturbed zones in quarry rock masses for the purposes of selective block stone extraction.

Materials and methods

Studies on the reduction of natural stone strength under repeated non-destructive loading were carried out in order to establish quantitative patterns of the development of damage and reduction of natural stone strength depending on the number of loadings.

Theoretical model of stress distribution under impact

To assess the magnitude of the stress that occurs in a rock piece when an impactor is dropped onto it, a theoretical problem of the destruction of a piece located on a sandy base under impact by an impactor was considered. Let a sample with mass m_1 lie on an elastic base, onto which an impactor with mass m_2 falls with the velocity of the centre of mass V_2. It is assumed that the impact of the impactor is carried out on a flat section of the piece surface along a straight line across its width C (Figure 1). The interaction between the piece and the impactor occurs at a certain point A.

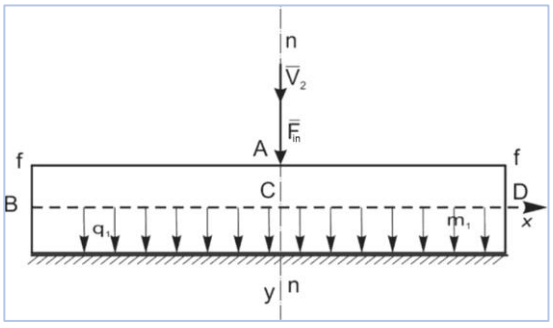


Fig. 1. Scheme of load distribution in a rock piece when an impactor is dropped onto it

Upon impact at point A, interaction forces will arise that act for a short time t_1. The influence of the displacement of the pieces on the process of their collision and motion during this process will be neglected. The collision occurs in two stages. During the first stage, maximum convergence of the contacting areas takes place with an increase in the interaction force to its maximum value, while in the second stage, unloading of the stressed state of the collided pieces occurs and the interaction force decreases to zero. In the initial period of collision, elastic waves will begin to propagate in both pieces, which will quite quickly transform into shear waves.

Therefore, the first (in time) possible variant of piece destruction will occur when the shear stresses that arise in the pieces in the shear waves reach their limiting values τ_{sh}.

$$\tau_{sh} = \rho c_2 V_{2y}, \quad (1)$$

where τ_{sh} – limiting shear stress in the rock piece (MPa);
ρ – density of the rock (kg/m³);
c_2 – velocity of propagation of transverse (shear) waves (m/s), defined as $c_2 = \sqrt{(G/\rho)} = \sqrt{\frac{E}{2\rho(1+\nu)}}$, where G is the shear modulus (Pa), E is the elastic modulus (Pa), and ν is Poisson's ratio (dimensionless);
V_{2y} – component of the impactor velocity normal to the sample surface at the moment of impact (m/s).

As the interaction of the pieces intensifies and after several superpositions of elastic waves in the pieces, a certain stress-strain state arises that reaches its extreme value at the end of the first stage of collision of the pieces at the maximum interaction force. The interaction force F_{in} is balanced according to d'Alembert by inertia forces continuously distributed throughout the entire piece. Under the action of this force and the moment that arises, bending of the piece occurs.

The value of the bending moment *M* will be equal to:

$$M = \frac{F_{in} x^2}{a} \quad (2)$$

where *M* – bending moment in the cross-section of the piece (N·m); F_{in} – interaction force between the impactor and the piece, balanced by d'Alembert inertia forces distributed continuously along the piece (N); x – coordinate of the cross-section where the bending moment reaches its maximum value (m); a – length of the rock piece along the impact axis (m).

The stress state in the piece is equal to:

$$\sigma = \frac{MY}{l_1}, \quad (3)$$

where σ – normal (tensile) stress at the outermost fibre of the cross-section (MPa); M – bending moment at the critical cross-section, determined from equation (2) (N·m); Y – distance from the neutral axis to the outermost point of the cross-section (m); l_1 – second moment of area (moment of inertia) of the cross-section about the neutral axis (m⁴), defined as $l_1 = a \cdot b^3/12$, where b is the thickness of the piece (m).

Since $V_2 \sim F_{in}$, $F_{in} \sim M$, and $M \sim \sigma$, it follows that $V_2 \sim \sigma$, that is, the destruction stresses of the pieces are directly proportional to the velocity of dropping the impactor onto them.

Physical analogue of tensile failure under impact loading

The repeated impact of a spherical striker on the upper surface of a rock sample resting on a sand base was adopted as a physical analogue of tensile failure for the following reasons. When the striker contacts the sample surface, a

compressive stress pulse propagates downward through the sample thickness. Upon reflection from the lower free surface, this pulse undergoes a phase inversion and re-enters the sample as a tensile wave. The resulting tensile stresses act transversely to the sample midplane, replicating the stress regime responsible for rock failure under blast loading in a quarry rock mass, where tensile waves generated by explosive detonation propagate radially outward and interact with free surfaces and pre-existing discontinuities. Furthermore, the bending mechanism induced by the impact – in which the interaction force F_{in} (Figure 1) is balanced by distributed inertia forces along the sample length, generating a bending moment M with maximum tensile stress at the outermost fibre of the critical cross-section (equation 3) – is physically equivalent to Brazilian disc splitting, a widely accepted indirect tensile test for brittle geomaterials (Stavrogin and Tarasov, 2001). The blast-induced damage context is further supported by Shadabfar et al. (2021), whose review of analytical, numerical, and experimental models of single-hole blasting damage confirms that tensile stress waves radiating from the blast epicentre govern the extent of the fractured zone – directly supporting the choice of tensile strength as the failure criterion in the present study. It is acknowledged that this analogy has inherent limitations: the stress field under impact is three-dimensional and transient, whereas classical tensile tests assume quasi-static uniaxial loading. Nevertheless, the proportionality $V_2 \sim \sigma$ (derived from equations 1–3) confirms that the impactor drop velocity controls the magnitude of induced tensile stress, providing a controllable and reproducible experimental parameter for fatigue testing under repeated sub-failure loading.

The multiple non-destructive loading of granite pieces by dropping a spherical impactor onto them served as an analogue of the process of multiple loading of natural stone samples. In this process, both the drop height of the impactor and the number of load applications were varied.

Numerical modelling using Ansys AUTODYN

To quantify the stress state induced in rock samples during impact loading, numerical simulations were performed using Ansys AUTODYN R16.0 (ANSYS Inc., Canonsburg, PA, USA). This software was selected for the following reasons: (1) it implements an explicit time-integration solver specifically designed for short-duration dynamic and impact events, which is essential for modelling high strain-rate loading with durations in the order of 10^{-4} s; (2) it supports the finite element method combined with Lagrangian mesh formulations, enabling accurate tracking of stress wave propagation and material deformation in brittle solids such as granite; (3) it allows direct computation of both compressive and tensile stress distributions throughout the sample volume, which is critical given that tensile failure governs rock degradation under blast-induced loading.

The numerical model reproduced the experimental geometry: a 200×200×30 mm rock sample resting on a sand base, impacted by a 1 kg spherical striker dropped from heights of 15 to 50 cm, corresponding to kinetic energies of 1.47 to 4.9 J. The dynamic analysis employed the explicit solver with a time step smaller than the Courant time step – defined as the time required for a stress wave to traverse one finite element – to ensure numerical stability. Nodal accelerations were resolved directly at each time step without iteration, with displacements and stresses updated sequentially. The simulation output confirmed a linear relationship between impactor drop velocity and induced tensile stress, validating the analytical proportionality $V_2 \sim \sigma$ derived from equations (1) – (3) and providing quantitative estimates of both compressive and tensile stress distributions along the sample length at each tested drop height (Figure 2).

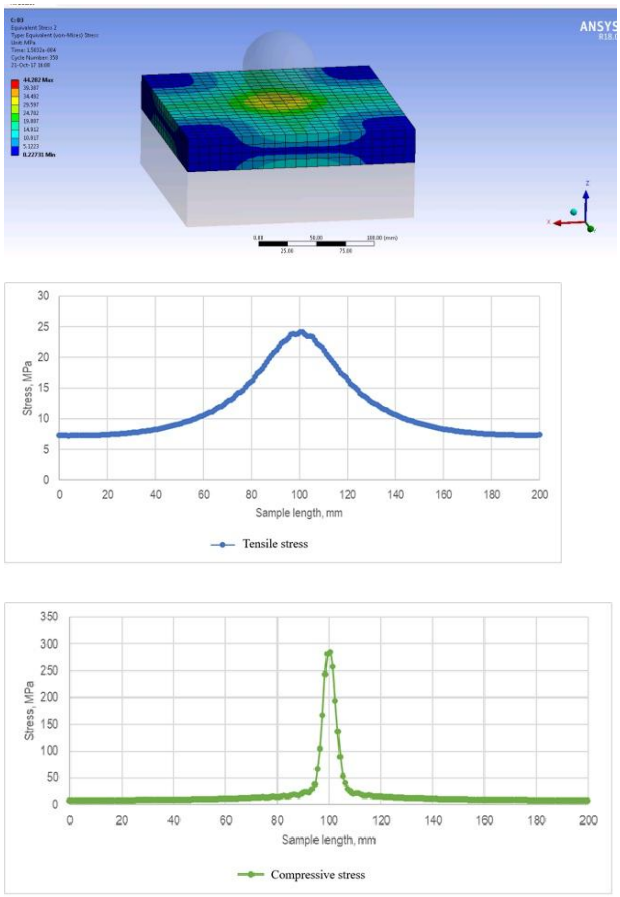


Fig. 2. Digital model of load distribution in rock fragment when an impactor is dropped onto it from a height of 15 cm

Laboratory testing programme

Laboratory studies were carried out to solve two main tasks: (1) to determine the impact velocity of rock fragments at which their failure occurs; (2) to establish quantitative relationships governing the development of damage and the reduction in strength of granite fragments depending on the velocity and the number of load applications.

The loading of natural stone samples was investigated using a special testing setup (Figure 3), consisting of: (1) a drop tower frame; (2) height markings; (3) a spherical steel impactor with a mass of 1 kg; (4) a sand cushion of at least 100 mm thickness; (5) the stone sample; (6) the base of the drop tower. Repeated non-destructive loading of granite fragments was performed by dropping the spherical impactor onto them, which is analogous to tensile testing of a granite specimen.

For each rock type, tests were conducted on four samples measuring 200×200×30 mm with a sawn surface texture. Each sample, in an air-dry state (natural moisture condition), was placed at the centre of a box on a levelled sand layer at least 100 mm thick. Impacts were then applied to the geometric centre of the sample using the falling weight of 1 kg. The first impact was applied from a height of 15 cm, and for each subsequent impact the height was increased by 5 cm. After each impact, the samples were inspected visually. Testing continued until visible cracks appeared in the sample or complete failure occurred.

During the tests, the underlying sand layer was continuously levelled. The indicator of rock resistance to impact loading was taken as the minimum drop height (in centimetres) at which cracks appeared in the sample or its destruction occurred. Rock resistance to impact loading was calculated as the arithmetic mean of the results obtained from four specimens.

The determination of rock resistance to repeated impact loading was carried out on similar samples; however, all impacts were applied from the same fixed height until sample failure occurred as a result of the accumulation of damage from previous loadings. The critical number of loadings *n* corresponded to the number of drops of the spherical impactor from the selected height that caused sample failure through accumulation of damage from preceding impacts.

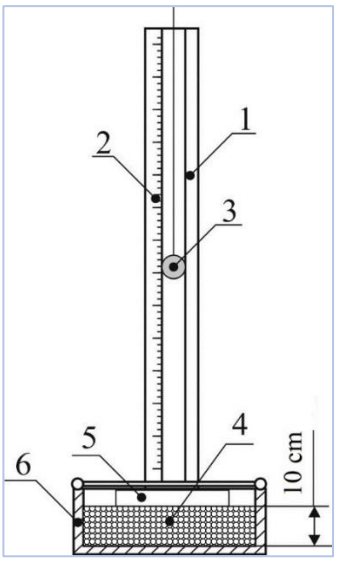


Fig. 3. Installation for testing the loading of natural stone samples:
1 – drop tower (impact rig frame); 2 – height markings; 3 – metal weight (ball) with a mass of 1 kg; 4 – sand cushion; 5 – stone sample; 6 – base of the drop tower (impact rig)

Ultrasonic monitoring

Before testing, the velocity of surface ultrasonic wave propagation in the stone sample was measured using a UK-14 MP ultrasonic device. After each drop of the weight, the velocity of the surface ultrasonic wave in the sample was measured in four directions, and the obtained data were averaged. The specific impact energy applied to the sample was calculated for each drop height, and the cumulative specific impact energy was accumulated across all loading cycles. The relationship between ultrasonic wave velocity and cumulative specific impact energy was used to monitor the progressive accumulation of internal damage in each sample. This approach is consistent with Yang et al. (2018), who demonstrated that ultrasonic wave velocity reliably tracks damage accumulation under cyclic loading in brittle geomaterials, and with Vasconcelos et al. (2008) and Korobiichuk (2016), who established robust correlations between ultrasonic velocity and the mechanical properties of granites.

Experimental studies were carried out on granite, gabbro, and labradorite samples from more than ten deposits in Ukraine - Table 1. The deposits tested included Tokivskyi, Koretskyi, Bukynske (gabbro), Maslavskyi, Leznikivskyi, Novodanylivskyi, Lukovetskyi, Vasylivskyi, Mezhyrichskyi, Kapustynskyi, Dobryn (labradorite), Didkovetskyi, and Zhezhelivskyi. Grain size ranged from fine-to-medium (Tokivskyi, Koretskyi, Bukynske gabbro) to coarse-grained (Lukovetskyi, Kapustynskyi, Dobryn labradorite), and quartz content varied from 0.6% (gabbro) to 30.4% (Tokivskyi granite), providing a representative range of mineralogical and textural characteristics for the classification of fatigue resistance.

Results and discussion

Rock resistance to single impact loading

Tests of rock resistance to single impact loading showed that the minimum drop height at which cracking or failure occurred varies from 35 to 55 cm across the tested deposits (Figure 4). Rock resistance to impact loading was calculated as the arithmetic mean of the results obtained from four specimens. The lowest values were observed for the red medium-grained granite of the Lezniki deposit (35 cm) and the Dobryn labradorite (35 cm), while the highest resistance was demonstrated by the grey medium-grained granite of the Zhezheliv deposit (55 cm). All remaining deposits showed approximately equal resistance to single impact loading, with values clustering around 40–45 cm.

These results indicate that single impact resistance alone is not a sufficient criterion for evaluating rock suitability for selective block stone extraction, since deposits with similar single-impact resistance (e.g., Tokivskyi and Vasylivskyi granite, both 45 cm) may differ dramatically in their response to repeated sub-failure loading, as demonstrated in the sections below.

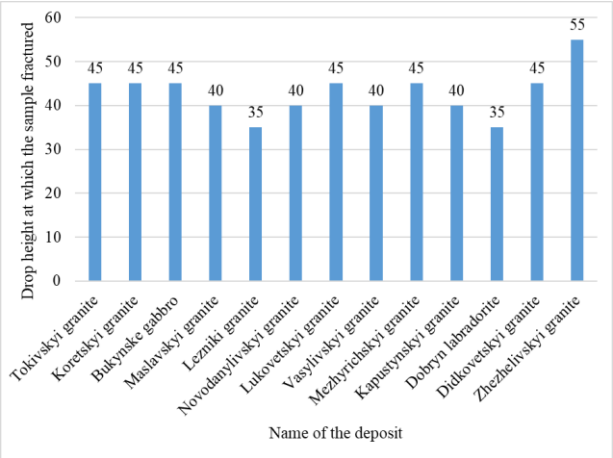


Fig. 4. Results of tests on rock resistance to impact loading

Strength reduction under repeated impact loading at low energy (drop height 15 cm, E = 1.47 J) showed significant differences in fatigue resistance among the tested rocks, with failure occurring after 25 to 1400 impacts.

In determining the reduction in strength of natural stone samples under repeated impact-induced loading, it was found that not all rock types can withstand repeated dynamic loading with low impact energy of 1.47 J (Figure 5, Table 1). The number of impacts sustained before failure at this energy level varied from 25 (Dobryn labradorite) to 1400 (Zhezhelivskyi granite), representing a 56-fold difference between the least and most resistant deposits.

The highest resistance at a specific energy of 1.47 kJ/m³ (Table 1) was observed in samples of granite from the Korets deposit (1000 impacts), Zhezheliv deposit (1400 impacts), Tokiv

deposit (1100 impacts), as well as gabbro from the Bukynske deposit (1350 impacts). Most of these rocks are medium-grained. The least resistant were granites from the Vasyliv deposit (54 impacts), Didkovychi deposit (36 impacts), Mezhyrich deposit (36 impacts), and Kapustyn deposit (47 impacts), as well as Dobryn labradorite (25 impacts). Most of these rocks are coarse-grained.

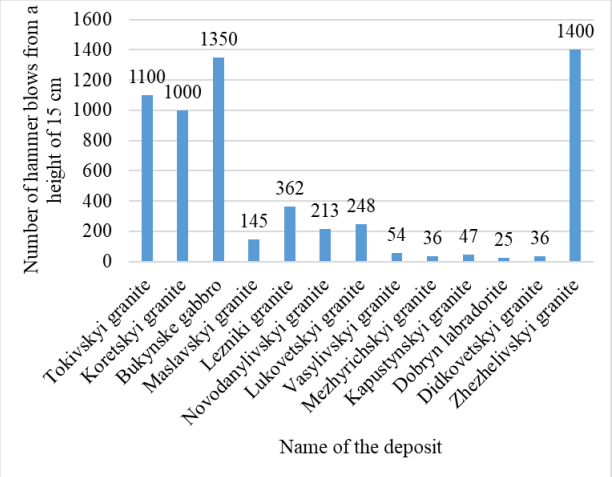


Fig 5. Results of dropping a weight from a height of 15 cm onto natural stone samples

After each drop, the velocity of ultrasonic wave propagation in the sample was measured in four directions and the obtained data were averaged. The relationship between ultrasonic wave velocity and cumulative specific impact energy at a drop height of 15 cm is shown in Figure 6.

Table 1. *Results of the study on the failure of stone samples under repeated dynamic loading*

Rock type	Number of impacts of the weight from a drop height, cm						
	15	25	30	35	40	45	50
Tokivskyi granite	1100	18	10	7	6	5	3
Koretskyi granite	1000	17	11	5	4	4	3
Bukynske gabbro	1350	107	6	-	-	-	-
Maslavskyi granite	145	7	6	4	4	2	2
Lezniki granite	362	8	6	3	2	2	2
Novodanylivskyi granite	213	13	7	6	4	3	3
Lukovetskyi granite	248	7	6	5	4	4	3
Vasylivskyi granite	54	7	3	-	-	-	-
Mezhyrichskyi granite	36	8	7	6	5	-	-
Kapustynskyi granite	47	6	5			-	-
Dobryn labradorite	25	3	3			-	-
Didkovetskyi granite	36	3	5			-	-
Zhezhelivskyi granite	1400	75	22	7	7	4	4

The curves reveal a characteristic three-phase pattern consistent with the fatigue failure model described by Xiao et al. (2010): an initial Phase I of stable ultrasonic velocity (microcrack closure and stable propagation), followed by a gradual Phase II decline (accelerated crack coalescence), and a rapid Phase III drop to zero immediately prior to macroscopic failure. The transition from Phase I to Phase II at a specific impact energy of 1.47 kJ/m³ occurred at cumulative specific energies of 500–800 kJ/m³ for high-resistance rocks, 130–150 kJ/m³ for medium-resistance rocks, and 25–90 kJ/m³ for low-resistance rocks – a threefold to twentyfold difference that underscores the practical significance of the proposed classification for quarry zoning.

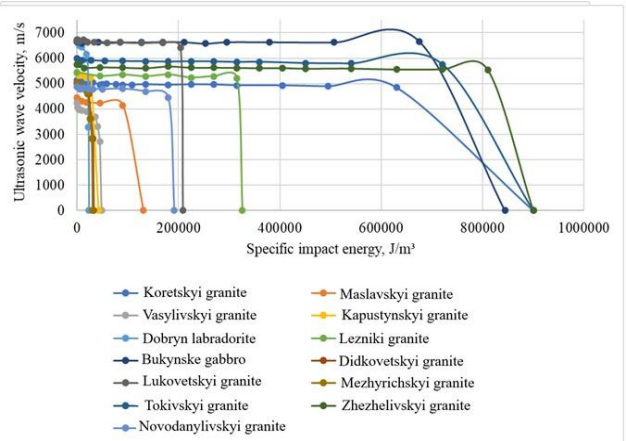


Fig. 6. Dependence of ultrasonic wave propagation velocity on cumulative specific impact energy at a drop height of 15 cm

Strength reduction at intermediate and high impact energies (drop heights 25–50 cm)

When the weight was dropped from a height of 25 cm (specific impact energy of 2.45 kJ/m³), the differences in the number of impacts sustained before failure narrowed considerably compared to the 15 cm results (Figure 5, Table 1). The most resistant to impact were granite from the Zhezheliv deposit (75 impacts) and gabbro from the Bukynske deposit (107 impacts), while the least resistant were granite from the Didkovychi deposit (3 impacts) and Dobryn labradorite (3 impacts).

At a specific impact energy of 2.94 kJ/m³ (drop height of 30 cm), a tendency toward further reduction in differences between sample properties was observed. The most resistant were granites from the Tokiv deposit (10 impacts), Korets deposit (11 impacts), Novodanyliv deposit (7 impacts), and Mezhyrich deposit (7 impacts), as well as Zhezheliv granite (22 impacts). However, it is notable that at low specific impact energy (15 cm), the Mezhyrich deposit showed relatively weak results and proved to be among the least impact-resistant deposits, whereas at 30 cm it performed comparably to high-resistance granites. This reversal suggests that the Mezhyrich granite possesses a relatively high threshold energy for crack initiation, but once microcracks are initiated, they propagate rapidly – a behaviour consistent with the brittle fracture mechanics framework described by Xiao et al. (2010), where rocks with lower initial crack density exhibit a compressed Phase II prior to failure.

At specific impact energies of 3.43 kJ/m³ (40 cm) and 3.92 kJ/m³ (45 cm), the differences in failure indicators between samples became negligible, with most deposits sustaining 2–7 impacts before failure. At the highest tested energy of 4.9 J (drop height 50 cm), the deposits that retained meaningful resistance were Zhezhelivskyi, Tokivskyi, Koretskyi, and Novodanylivskyi granites (medium-grained) and Lukovetskyi granite (coarse-grained), sustaining 2–4 impacts each.

With increasing impact energy from 1.47 J to 4.9 J, the fatigue strength of all tested granites decreased sharply, and the transition from Phase I to Phase II occurred at cumulative specific energies of only 10–30 kJ/m³ – an order of magnitude lower than at 1.47 J. This is consistent with the energy-

dependent failure model of Bagde and Petroš (2009), who demonstrated that dynamic fatigue life decreases nonlinearly with increasing load amplitude, and with Singh (1989), who established that natural stone is destroyed after fewer cycles as loading energy increases. Zhou et al. (2018) similarly confirmed for granite under low-cycle repetitive compressive impacts that cumulative damage energy increases nonlinearly with impact number, with fatigue life reducing sharply at higher impact stress levels.

Strength loss quantified by ultrasonic monitoring

The use of ultrasonic monitoring during impact strength testing of stone samples made it possible to establish the percentage of strength loss at the moment of macroscopic failure for each deposit (Figure 7). Samples from the Tokiv deposit and Korets deposit granites, as well as gabbro from the Bukynske deposit, failed with a relatively small loss of strength of 11.6 %, 11.7 %, and 14.2 %, respectively – indicating that these rocks maintain the vast majority of their original strength up to the point of sudden brittle failure. Overall, the stone samples failed at a strength loss ranging from 11 % to 41.5 %.

This range is broader than that reported by Momeni et al. (2015) for Alvand granite under uniaxial cyclic loading (approximately 15–30 % strength reduction prior to failure), which can be explained by the greater variability in mineralogical composition, grain size, and accessory mineral content among the thirteen rock types tested in the present study. The results of Singh (1989) for greywacke under cyclic loading are also consistent with the present findings in that rocks with higher initial stiffness – reflected in higher initial ultrasonic wave velocities – demonstrated greater resistance to fatigue-induced strength degradation. Li et al. (2022) further confirmed that under repeated dynamic tension, peak strength decreases progressively with each loading cycle and that total dissipated energy for fatigue failure increases linearly with fatigue life – a pattern reflected in the ultrasonic velocity curves obtained in the present study.

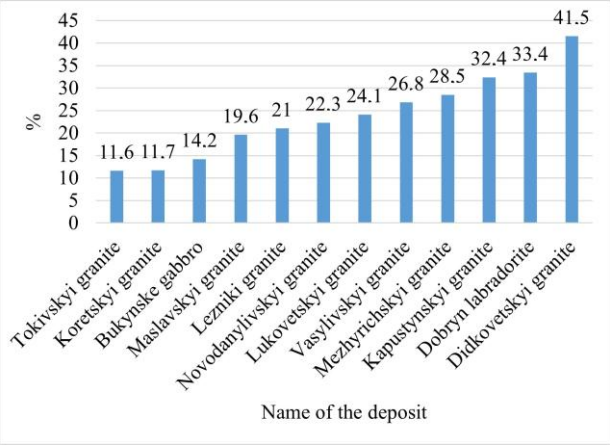


Fig. 7. Reduction in strength of natural stone samples during impact-induced failure

Factors governing fatigue resistance: mineralogical composition, grain size, and accessory minerals

The observed differences in fatigue resistance among the tested deposits can be attributed to three principal interacting factors: mineralogical composition, grain size, and accessory mineral content.

Mineralogical composition and quartz content. Granites with high resistance to repeated dynamic loading (Tokiv, Korets, Zhezheliv granites; Bukynske gabbro) contain 23–30 % quartz and 50–65 % feldspar and plagioclase and have a medium-grained structure. The elevated quartz content is consistent with findings by Bagde and Petroš (2009), who established that quartz content is a primary determinant of fatigue resistance in crystalline rocks, attributing this to the high hardness and strong covalent bonding of the SiO_2 lattice, which impedes microcrack initiation and propagation under cyclic loading. In the present study, granites with quartz content below 15 % (Maslavskyi, Leznikivskyi, Novodanylivskyi, Lukovetskyi granites) demonstrated medium resistance and failed with a strength loss of 19–24 %, confirming the positive correlation between quartz content and fatigue strength. Granites with medium resistance contain 10–15 % quartz and 55–80 % feldspar and plagioclase and also have a medium-grained structure.

Grain size effect. Coarse-grained rocks (Kapustyn granite, Dobryn labradorite) consistently exhibited lower resistance to cyclic loading compared to medium-grained rocks of similar mineralogical composition. This finding aligns with the theoretical framework of Griffith crack theory and is supported by Akesson et al. (2004), who demonstrated that cyclic loading in granite promotes the formation of new microcracks and extension of pre-existing ones within constituent minerals, with the rate of crack propagation proportional to grain boundary length – a parameter that increases directly with grain size. The greater the grain size, the lower the energy threshold required to propagate existing microcracks to a critical length, resulting in earlier macroscopic failure. Yu et al. (2020) confirmed through combined experimental and numerical modelling that under repeated dynamic loading, irreversible sliding between particles at crack tips generates concentrated lateral tensile stress which – once it exceeds the local strength limit – drives crack initiation and propagation independently of the applied bulk compressive load. This mechanism is amplified in coarse-grained rocks where longer grain boundaries provide more extensive sliding surfaces.

Accessory mineral content. Vasyliv granite represents a distinct case where accessory mineral content overrides the beneficial effect of relatively high quartz content. Despite containing 20–27 % quartz – comparable to high-resistance granites – Vasyliv granite exhibited low fatigue resistance and failed with a strength loss of 24.1 %, owing to its exceptionally high content of accessory minerals (up to 22 %). Accessory minerals – predominantly biotite and hornblende in the studied samples – are characterised by pronounced cleavage planes and lower elastic moduli compared to quartz and feldspar. Under cyclic loading, stress concentrations develop preferentially at the interfaces between accessory minerals and the surrounding matrix, accelerating microcrack coalescence and reducing the overall fatigue life of the rock (Momeni et al., 2015). A similar mechanism was reported by Vaneghi et al. (2018) for sandstone and granodiorite under uniaxial cyclic loading, where mineral interface boundaries served as dominant crack initiation sites.

Natural stone with low resistance to repeated dynamic loading contains 18–27 % quartz and 42–90 % feldspar and plagioclase and has either a medium-grained (Vasyliv granite) or coarse-grained (Kapustyn granite, Dobryn labradorite) structure. Samples in this group failed with a strength loss of 28–41.5 %.

Classification of natural stone by fatigue resistance

Depending on the energy capacity of failure at a specific impact energy of 1.47 kJ/m³, natural stone can be conditionally divided into three groups (Figure 8):

A. High resistance to repeated dynamic loading – energy capacity of failure 147 kJ/m³ and above. This group includes Zhezhelivskyi, Tokivskyi, and Koretskyi granites, as well as Bukynske gabbro. These rocks contain 23–30 % quartz, have a medium-grained structure, and failed with a relatively small strength loss of 11–14 %. Phase II of the fatigue test (stable crack propagation) is short in duration, resulting in fewer disturbances in the stone and sudden brittle failure with minimal preceding deformation.

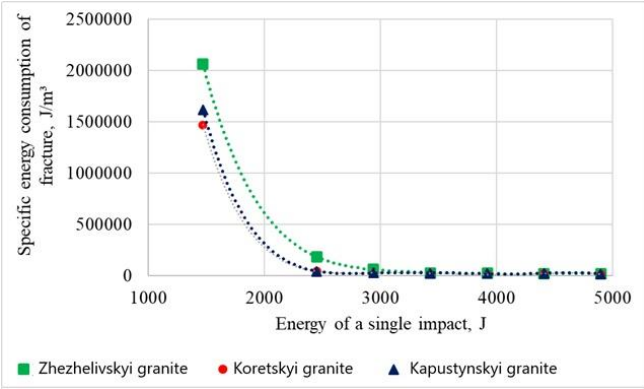


Fig. 8. Dependence of the energy capacity of failure of natural stone with high resistance to repeated dynamic loading on the energy of a single impact

B. Medium resistance to repeated dynamic loading – energy capacity of failure 15–147 kJ/m³. This group includes Leznikivskyi, Maslavskyi, Novodanylivskyi, and Lukovetskyi granites. These rocks contain 10–15 % quartz and 55–80% feldspar and plagioclase, have a medium-grained structure, and failed with a strength loss of 19–24 %.

C. Low resistance to repeated dynamic loading – energy capacity of failure below 15 kJ/m³. This group includes Vasylivskyi and Kapustynskyi granites and Dobryn labradorite. These rocks contain 18–27 % quartz and 42–90 % feldspar and plagioclase, have a medium-to-coarse-grained structure, and failed with a strength loss of 28–41.5 %.

The energy capacity of failure for individual deposits is described by quadratic regression equations, reflecting the nonlinear decrease in fatigue life with increasing single-impact energy. For Zhezheliv deposit granite:

$$E_r = 0{,}3624P_r^2 - 2703{,}2P_r + 5 \cdot 10^6, J. \quad (8)$$

where E_r is the specific energy capacity of failure of the rock sample (J/m³) and P_r^2 is the energy of a single impact (J). This nonlinear pattern is consistent across all three resistance groups and in agreement with the general fatigue behaviour of brittle geomaterials reported in the literature (Xiao et al., 2010; Vaneghi et al., 2018; Zhou et al., 2018).

Practical implications for selective block stone extraction

Although the conducted studies do not allow full modelling of natural stone disturbance in a rock mass – where more complex fracture mechanisms operate simultaneously – they provide a practical basis for assessing the suitability of strong rocks for the by-product extraction of monolithic blocks in crushed stone quarry conditions.

Granites from the Zhezheliv deposit, Tokiv deposit, and Korets deposit are capable of sustaining small repeated loads with minimal strength loss, which indicates that monolithic zones within these quarries can be developed for dimension stone extraction even in proximity to blast epicentres. On the other hand, at the Vasyliv deposit, Kapustyn deposit, Didkovychi deposit, Mezhyrich deposit, and Dobryn labradorite deposit, even the most remote monolithic zones from the explosion epicentre may be affected by technogenic fractures resulting from cumulative blast-induced damage. This finding is consistent with the blast damage review of Shadabfar et al. (2021), who confirmed that tensile stress wave attenuation with distance from the blast source is the primary factor governing the extent of the fractured zone in quarry rock masses.

The proposed method for assessing strength degradation of rocks under cyclic dynamic loading is more informative compared to the standard method for determining rock resistance to single impact loading (State Committee of Ukraine, 2004), since it captures the cumulative damage process and allows quantitative prediction of the fatigue life of each deposit under realistic quarry loading conditions. Based on these studies and the analysis of blasting intensity at a given quarry, it is possible to evaluate the degree of natural stone disturbance within a deposit and to delineate zones suitable for selective block stone extraction with sufficient confidence for practical application.

Conclusions

1. Although the conducted studies do not allow full modelling of natural stone disturbance in a rock mass, they provide an opportunity to assess the suitability of strong rocks for the by-product extraction of monolithic blocks in crushed-stone quarry conditions. For example, granites from the Zhezheliv deposit, Tokiv deposit, and Korets deposit are capable of sustaining small repeated loads, which makes it possible to develop their monolithic zones for dimension stone extraction. On the other hand, at the Vasyliv deposit, Kapustyn deposit, Didkovychi deposit, Mezhyrich deposit, and Dobryn deposit, even the most remote monolithic zones of natural stone from the explosion epicenter may be affected by technogenic fractures.

2. The proposed method for assessing strength degradation of rocks under cyclic dynamic loading is more informative compared to the standard method for determining rock resistance to impact loading. Based on these studies and the analysis of blasting intensity, it is possible to evaluate the degree of natural stone disturbance within a deposit.

3. The investigation describes the nature of strength reduction in natural stone samples with increasing impact energy and number of load cycles. Most of the studied rocks exhibit high resistance to repeated dynamic loading with low impact energy, which indicates high fatigue strength of the rocks.

4. The obtained data make it possible to distinguish three groups of natural stone at a specific impact energy of 1.47 kJ/m³, where the transition from the initial phase (Phase I) of the fatigue test to the steady-state phase (Phase II) occurs at cumulative specific energies of 500–800 kJ/m³, 130–150 kJ/m³, and 25–90 kJ/m³. In rocks with high fatigue resistance to low dynamic loads

(Figure 6), Phase II (stable crack propagation) is short in duration, resulting in fewer disturbances in the stone. With increasing impact energy (4.9 J), the fatigue strength of granites decreases sharply, and the transition from Phase I to Phase II occurs at a cumulative specific energy of 10–30 kJ/m³.

5. The results also show that the fatigue strength of granites is influenced by quartz content: with increasing quartz content, strength increases. However, granite texture has an equally important effect: with increasing grain size, despite a high quartz content, fatigue strength decreases. An increase in accessory minerals in granites leads to a reduction in fatigue strength.

References

Akesson, U., Stigh, J., Lindqvist, J. E., & Göransson, M. (2004). The influence of foliation on the fragility of granitic rocks, image analysis and quantitative microscopy. *Engineering Geology, 73*(3–4), 167–180. https://doi.org/10.1016/j.enggeo.2004.01.003

Bagde N., & Petros V. (2005). Fatigue properties of intact sandstone samples subjected to dynamic uniaxial cyclical loading. *International Journal of Rock Mechanics and Mining Sciences, 42*, 237–250. https://doi.org/10.1016/j.ijrmms.2004.08.008

Bagde, M. N., & Petroš, V. (2009). Fatigue and dynamic energy behaviour of rock subjected to cyclical loading. *International Journal of Rock Mechanics and Mining Sciences, 46*(1), 200–209. https://doi.org/10.1016/j.ijrmms.2008.05.002

Korobiichuk, V. (2016). Study of ultrasonic characteristics of Ukraine red granites at low temperatures. *International Conference on Systems, Control and Information Technologies*, 653–658. https://doi.org/10.1007/978-3-319-48923-0_69

Li, R., Zhu, J. B., Qu, H., Zhou, T., & Zhou, C. (2022). An experimental investigation on fatigue characteristics of granite under repeated dynamic tensions. *International Journal of Rock Mechanics and Mining Sciences, 158,* 105185. https://doi.org/10.1016/j.ijrmms.2022.105185

Momeni, A., Karakus, M., Khanlari, G.R., & Heidari, M. (2015). Effects of cyclic loading on the mechanical properties of a granite. *International Journal of Rock Mechanics and Mining Sciences, 77*, 89–96. https://doi.org/10.1016/j.ijrmms.2015.03.029

Shadabfar, M., Gokdemir, C., Zhou, M., Kordestani, H., & Muho, E. V. (2021). Estimation of damage induced by single-hole rock blasting: a review on analytical, numerical, and experimental solutions. *Energies, 14*(1), 29. https://doi.org/10.3390/en14010029

Singh, S.K. (1989). Fatigue and strain hardening behaviour of graywacke from the flagstaff formation. *New South Wales Engineering Geology*, *26*(2), 171–179. https://doi.org/10.1016/0013-7952(89)90005-7

State Committee of Ukraine for Technical Regulation and Consumer Policy Kyiv (2004) *Natural stone test methods – Determination of rupture energy* (DSTU EN 14158:2004).

Stavrogin, A. N., & Tarasov, B. G. (2001). Experimental physics and rock mechanics [Monograph]. *CRC Press*, 356.

Vaneghi, G. R., Ferdosi, B., Okoth, A. D., & Kuek, B. (2018). Strength degradation of sandstone and granodiorite under uniaxial cyclic loading. *Journal of Rock Mechanics and Geotechnical Engineering, 10*(1), 117–126. https://doi.org/10.1016/j.jrmge.2017.09.005

Vasconcelos, G., Lourenço, P. B., Alves, C. A. S., & Pamplona, J. (2008). Ultrasonic evaluation of the physical and mechanical properties of granites. *Ultrasonics*, *48*(5)*,* 453–466. https://doi.org/10.1016/j.ultras.2008.03.008

Xiao, J. Q., Ding, D. X., Jiang, F. L., & Xu, G. (2010). Fatigue damage variable and evolution of rock subjected to cyclic loading. *International Journal of Rock Mechanics and Mining Sciences, 47*, 461–468. https://doi.org/10.1016/j.ijrmms.2009.11.003

Yang, S., Nong, Z., Feng, X., Kan, J., Pan, D., & Qian, D. (2018). Experimental investigation of sandstone under cyclic loading: damage assessment using ultrasonic wave velocities and changes in elastic modulus. *Shock and Vibration, 2018,* 1–13. https://doi.org/10.1155/2018/7845143

Yu, Z., Zhao, D., Tang, Q., & Wang, M. (2020). Experimental and numerical investigation of the fatigue behaviour and crack evolution mechanism of granite under ultra-high-frequency loading. *Royal Society Open Science, 7*(4), 200091. https://doi.org/10.1098/rsos.200091

Zhou, T., Dong, S. L., Zhao, G. F., Zhang, R., Wu, S. Y., & Zhu, J. B. (2018). An experimental study of fatigue behaviour of granite under low-cycle repetitive compressive impacts. *Rock Mechanics and Rock Engineering, 51*(10), 3157–3166. https://doi.org/10.1007/s00603-018-1515-0

Sustainable Extraction and Processing of Raw Materials, 2026

SUSTAINABLE MATERIALS FOR URANIUM REMOVAL FROM MINE WATER: COMPARATIVE EVALUATION OF ZERO-VALENT IRON NANOPARTICLES, CONVENTIONAL SORBENTS, AND FUNCTIONALISED MAGNETIC NANOMATERIALS

Alexandre Loukanov[1,2]

[1]Laboratory of Engineering NanoBiotechnology, Department of Eng. Geoecology, University of Mining and Geology "St. Ivan Rilski", Sofia, Bulgaria, E-mail: a.loukanov@mgu.bg
[2]Department of Chemistry and Materials Science, National Institute of Technology, Gunma College, 580 Toriba, Maebashi, Gunma 371-8530 Japan, E-mail: loukanov@gunma-ct.ac.jp

ABSTRACT. Uranium contamination of mine water and groundwater represents a significant environmental challenge associated with mining activities, ore processing, and radioactive waste management. In this study, uranium removal from aqueous solutions was comparatively evaluated using zero-valent iron nanoparticles (ZVINs), ligand-functionalised magnetic nanoparticles, water works sludge (WWS), and apatite under near-neutral conditions. The results revealed substantial differences in uranium immobilisation behaviour among the investigated materials. Water works sludge and apatite exhibited rapid uranium removal and reached near-equilibrium within a relatively short period, whereas ZVINs demonstrated slower but sustained uranium uptake over extended reaction times. This behaviour suggests that uranium immobilisation in Fe^0 systems is influenced by progressive nanoparticle aging and the formation of iron corrosion products. The observed trends are consistent with uranium immobilisation mechanisms previously reported for Fe^0-based systems, including adsorption onto iron oxides and hydroxides, co-precipitation with corrosion products, and possible reductive transformation of U(VI). In addition, amino-functionalised magnetic nanoparticles coated with a silsesquioxane polymer exhibited effective uranium adsorption and enabled rapid magnetic separation from aqueous solutions. Treatment of a 0.040 M uranium solution reduced the uranium concentration to approximately 0.014 M after 24 h, corresponding to about 64–65% removal efficiency, whereas uncoated magnetic nanoparticles exhibited negligible adsorption. Equilibrium adsorption data analysed using the Langmuir model indicated adsorption behaviour consistent with a finite number of active binding sites and confirmed the affinity of the amino-functionalised surface toward uranyl species within the investigated concentration range. The comparative results demonstrate that iron-based nanomaterials, particularly magnetically recoverable systems, may provide useful approaches for uranium removal and recovery from contaminated water. Although the experiments were conducted under simplified laboratory conditions, the findings provide a basis for further investigations in more complex mine-water systems, including the effects of competing ions, pH variability, sorbent regeneration, and long-term stability of immobilised uranium species.

Key words: uranium removal; zero-valent iron nanoparticles; magnetic nanoparticles; uranium immobilisation; mine water remediation; iron corrosion products.

Introduction

The contamination of groundwater and mine water with uranium represents a significant environmental and public health concern associated with uranium mining, ore processing, radioactive waste disposal, and naturally occurring uranium-bearing geological formations (Loukanov et al., 2017; Abdessamed et al., 2023; Afrikaner et al., 2025). Soluble uranium species can migrate through aquatic systems and accumulate in groundwater resources, leading to long-term environmental risks and potential human exposure (Kairullova et al., 2026). Consequently, the development of efficient, economically viable, and environmentally sustainable methods for uranium removal and immobilisation remains a major challenge in environmental engineering and mine water remediation (Helal et al., 2025; Wu et al., 2026). Under oxidising conditions, uranium predominantly exists as hexavalent U(VI), typically forming soluble uranyl ions and carbonate complexes (Wazne et al., 2003). The mobility and persistence of uranium in groundwater are strongly influenced by pH, redox conditions, and the presence of competing ligands such as bicarbonate and phosphate ions (Skierszkan et al., 2021). Conventional treatment methods, including chemical precipitation, ion exchange, membrane filtration, coagulation, adsorption, and biological processes, are widely applied but often suffer from high operational costs, limited selectivity, formation of secondary waste, or insufficient long-term stability under complex environmental conditions (Akash et al., 2022; Lin et al., 2026). Iron-based materials have attracted increasing attention due to their low cost, high reactivity, and ability to immobilise inorganic contaminants and radionuclides (Zhao et al., 2020; Arahangelova et al., 2023; Fu et al., 2025; Loukanov et al., 2025). In particular, zero-valent iron nanoparticles (ZVINs) exhibit high specific surface area and strong reducing properties, enabling uranium removal through multiple mechanisms including adsorption onto iron corrosion products, reductive transformation of U(VI), and incorporation into iron oxide matrices (Riba et al., 2008; Sheng et al., 2014; Li et al., 2015; Gheju, 2025). During aqueous aging, Fe^0 nanoparticles undergo progressive transformation into ferrihydrite, FeOOH, maghemite and magnetite phases, which significantly influence uranium immobilisation behaviour (Wazne et al., 2003; Xiao et al., 2023; Gheju, 2025).

Although the fundamental mechanisms responsible for uranium removal by Fe^0-based systems are well established, several practical aspects relevant to environmental remediation remain insufficiently explored. In particular, comparatively limited attention has been devoted to the long-term evolution of uranium immobilisation during nanoparticle aging under near-neutral conditions representative of natural groundwater systems. Most previous studies have focused primarily on short-term removal efficiencies and mechanistic investigations, whereas the contribution of corrosion products generated during prolonged Fe^0 oxidation to sustained uranium stabilisation remains less clearly defined. Furthermore, direct comparisons between Fe^0 nanoparticles and alternative low-cost sorbents commonly considered for mine water treatment, such as apatite and water works sludge (WWS), are relatively scarce despite their practical relevance. Evaluations performed under comparable experimental conditions may therefore

provide useful information regarding the advantages and limitations of different uranium immobilisation strategies and their suitability for long-term environmental applications.

In parallel, magnetic nanomaterials functionalised with chelating ligands have emerged as promising candidates for uranium adsorption and recovery (Mahfouz et al., 2015). A key practical limitation of nanoscale adsorbents is their separation from treated water; magnetic nanoparticles address this challenge by enabling rapid recovery using an external magnetic field, thereby reducing the need for filtration and minimising secondary waste generation. Surface functionalisation with organosilane compounds introduces amino and chelating groups that enhance binding affinity toward uranyl ions while improving colloidal stability (Zhu et al., 2018). Such hybrid materials combine adsorption performance with magnetic recoverability and are increasingly investigated for environmental remediation applications (Ngerem et al., 2026).

While amino-functionalised magnetic adsorbents for uranium removal have been reported previously, studies integrating adsorption performance with practical considerations such as magnetic recovery, regeneration potential, and comparison with Fe^0-based immobilisation systems remain relatively limited. Consequently, further evaluation of these materials under conditions relevant to uranium-contaminated waters is warranted. In this context, the present study provides a comparative evaluation of uranium removal using zero-valent iron nanoparticles, apatite, and water works sludge under near-neutral conditions, with particular emphasis on the role of Fe^0 corrosion products in long-term uranium immobilisation. In addition, amino-functionalised magnetic nanoparticles coated with a silsesquioxane shell were investigated as magnetically recoverable adsorbents for uranium separation and recovery. Rather than proposing new uranium-removal mechanisms, the study aims to assess the relative performance, long-term behaviour, and practical advantages of different remediation approaches under comparable experimental conditions. Particular attention is given to sustained uranium stabilisation during Fe^0 aging and to the feasibility of combining adsorption with magnetic recovery. Comparative studies involving extended reaction times and multiple classes of remediation materials remain relatively limited in the literature, and the present work seeks to contribute to this area by providing a unified experimental evaluation under near-neutral aqueous conditions.

Experimental procedures

Synthesis of zero-valent iron nanoparticles

Zero-valent iron nanoparticles (ZVINs) were synthesised using a liquid-phase reduction method modified after the procedure reported by Sun et al. (2006), as shown on Figure 1A. Ferric chloride hexahydrate ($FeCl_3 \cdot 6H_2O$) was used as the iron precursor, while sodium borohydride ($NaBH_4$) served as the reducing agent. Briefly, 1.35 g of $FeCl_3 \cdot 6H_2O$ was dissolved in 50 mL of ultrapure Milli-Q water (18.2 MΩ·cm) under continuous magnetic stirring at ambient temperature. The pH of the precursor solution was adjusted to 6.8 using 4 M NaOH added dropwise in order to minimise premature hydrolysis and formation of ferric hydroxide species. Prior to reduction, the solution was purged with nitrogen to decrease dissolved oxygen concentration and minimise oxidation during nanoparticle synthesis. The reduction reaction was initiated by gradual addition of 2.0 g $NaBH_4$ dissolved in deoxygenated water under vigorous stirring. The immediate formation of black precipitates indicated the generation of nanoscale iron particles according to the following reaction:

$$2Fe^{3+} + 6BH_4^- + 18H_2O \rightarrow 2Fe^0 + 6B(OH)_3 + 21H_2$$

The reaction mixture was stirred for an additional 30 min to ensure complete reduction of ferric ions and homogeneous particle formation. The resulting nanoparticles were isolated by centrifugation at 6000 rpm and sequentially washed with deionised water, ethanol, and acetone (20 mL each) to remove residual salts, borates, and unreacted reagents. The purified nanoparticles were dried under reduced pressure (~10^{-2} mbar) for 48 h and subsequently stored in an oxygen-free nitrogen glovebox (Saffron Scientific) prior to use in uranium adsorption experiments. Based on the synthesis route employed and previous reports describing borohydride-reduced nZVI materials (Sun et al., 2006), the synthesised material is expected to consist predominantly of nanoscale Fe^0 particles that may form chain-like aggregates as a consequence of magnetic dipole interactions. However, detailed structural characterisation of the synthesised nanoparticles was beyond the scope of the present study. Therefore, all discussion regarding nanoparticle morphology and surface structure is based on the established characteristics of similar nZVI materials reported in the literature.

Surface functionalisation of magnetic nanoparticles with silsesquioxane polymer shell

Magnetically active iron oxide nanoparticles with an average particle size of 8–10 nm were functionalised using a silsesquioxane polymer shell containing ethylenediamine chelating groups capable of coordinating uranium ions and other heavy metals (Figure 1B). The synthesis strategy was designed to combine the magnetic separability of iron oxide nanoparticles with the selective adsorption properties of amine-containing organosilane ligands. Such hybrid nanomaterials have attracted increasing interest for environmental remediation applications due to their high surface area, tunable surface chemistry, and facile magnetic recovery from aqueous systems. The magnetic nanoparticles were coated through reaction with [N-(2-aminoethyl)-3-aminopropyl] trimethoxy-silane in toluene at 80 °C under continuous stirring. During the initial stage of the reaction, hydroxyl groups located on the nanoparticle surface reacted with methoxy groups of the silane molecules, resulting in formation of Fe–O–Si covalent bonds and methanol as a side product. Subsequent hydrolysis of residual alkoxy groups generated silanol functionalities that further condensed to produce an extended siloxane (Si–O–Si) network surrounding the magnetic nanoparticle core. Cross-linking reactions between adjacent silanol groups resulted in formation of a stable silsesquioxane polymer shell with a high density of accessible amino coordination sites. The overall coating process produced hybrid magnetic nanomaterials with improved colloidal stability and enhanced affinity toward uranyl ions through coordination interactions involving ethylenediamine functional groups. The polymer loading was estimated gravimetrically from the mass increase after the coating procedure and corresponded to approximately 22 wt.% relative to the initial nanoparticle mass. No additional spectroscopic or thermal analysis was performed to quantify the exact shell composition. Therefore, the proposed coating

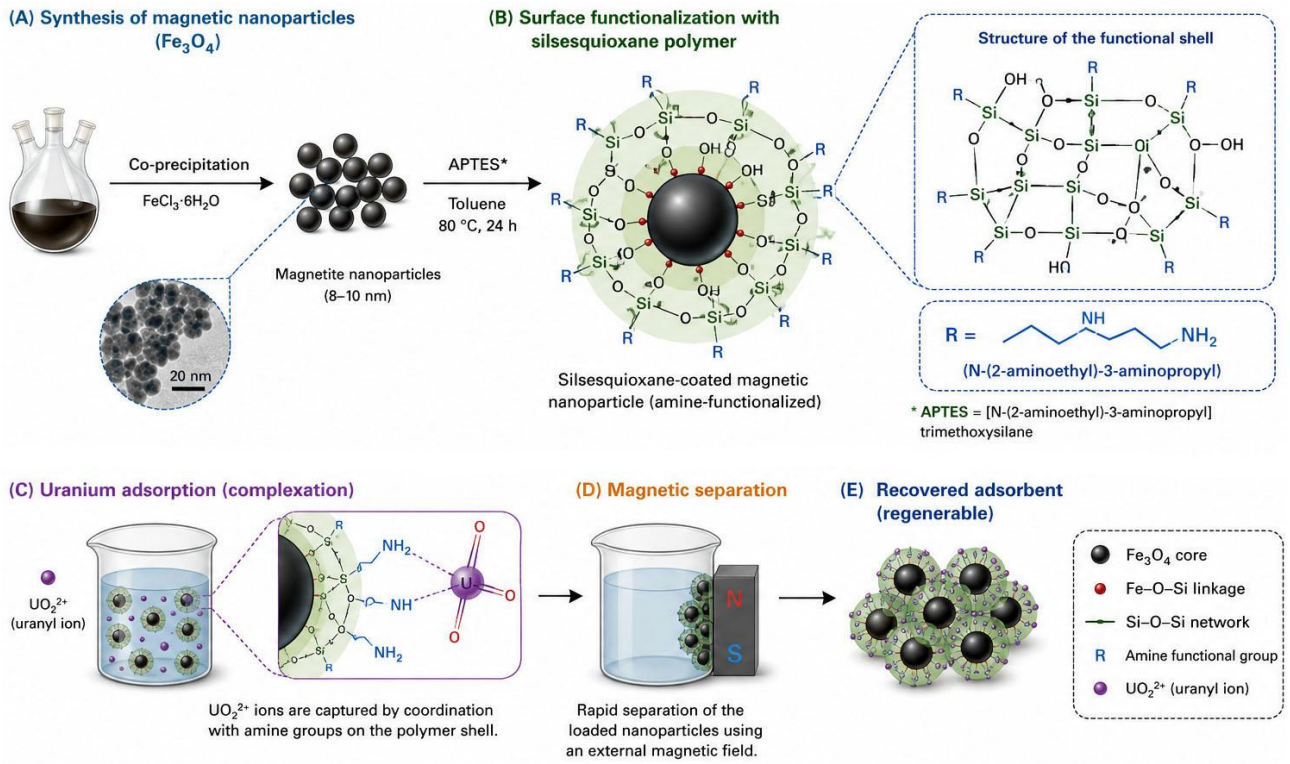


Figure 1. Schematic representation of the preparation, surface functionalisation, uranium coordination, and magnetic separation process of silsesquioxane-coated magnetic nanoparticles

structure should be regarded as a schematic representation based on the reaction chemistry of the silane precursor and literature reports describing similar silsesquioxane-coated magnetic nanoparticles. The resulting coating composition can be represented by the structural formula:

$$[(N-(2-aminoethyl)-3-aminopropyl)SiO_{1.5-x}(OH)_x]_n$$

The functionalised nanoparticles remained readily dispersible in aqueous media while preserving magnetic responsiveness, allowing rapid magnetic separation after uranium adsorption experiments. The presence of amino-functional groups is expected to promote uranium uptake through surface complexation and chelation mechanisms involving uranyl species (Figure 1C). The adsorption experiments reported in this study were conducted under near-neutral pH conditions (pH ≈ 7.2), and the observed adsorption behaviour should therefore be interpreted within this pH range only. Near-neutral pH was deliberately selected because one of the objectives of the study was to evaluate uranium removal and regeneration (Figure 1D,E) under environmentally relevant conditions that could potentially be applied without extensive chemical conditioning of contaminated waters. Such an approach is consistent with sustainable remediation strategies aimed at minimising reagent consumption and secondary waste generation. A systematic investigation of pH-dependent uranium speciation and adsorption behaviour was beyond the scope of the present work and should be addressed in future studies.

Batch adsorption experiments

Batch adsorption experiments were carried out to compare the uranium removal performance of zero-valent iron nanoparticles (ZVINs), apatite, water works sludge (WWS), and ligand-functionalised magnetic nanoparticles under near-neutral conditions. The apatite used in the experiments was laboratory-grade hydroxyapatite powder obtained from Sigma-Aldrich and used without additional purification. Water works sludge was collected from a local drinking water treatment facility following coagulation and sedimentation processes. Prior to use, the sludge was washed several times with deionised water, dried at 60 °C for 24 h, mechanically homogenised, and sieved to obtain particle sizes below 250 µm. Synthetic uranium-containing solutions were prepared by dissolving uranyl nitrate hexahydrate in deionised water. The initial uranium concentration for the batch experiments was adjusted to 20 mg/L unless otherwise stated. The experiments were intentionally performed using simplified synthetic uranium solutions to evaluate the intrinsic uranium removal performance of the investigated materials under controlled laboratory conditions.

The influence of competing ions commonly present in mine waters, including sulphate, carbonate, calcium, silica, and dissolved trace metals, was not investigated in the present study. Consequently, the reported results should be regarded as proof-of-concept laboratory data rather than a direct simulation of complex mine-water systems. The initial solution pH was adjusted to approximately 7.2 using diluted NaOH or HNO_3 solutions. Adsorption experiments were performed in 50 mL polypropylene centrifuge tubes containing 20 mL uranium solution and predetermined amounts of adsorbent material. The suspensions were continuously agitated using an orbital shaker operating at 150 rpm at room temperature (22 ± 2 °C). For kinetic experiments, independent replicate tubes were prepared for each sampling time in order to avoid changes in solution volume during the course of the experiment. At the designated contact time, the entire contents of a tube were centrifuged and the supernatant was collected for uranium analysis. In experiments involving magnetic nanoparticles, magnetic separation using an external permanent magnet was additionally applied. Residual uranium concentrations in the

supernatants were determined spectrophotometrically using the Arsenazo III method. Desorption and regeneration experiments were performed using uranium-loaded magnetic nanoparticles recovered after the adsorption step. Approximately 100 mg of the loaded adsorbent was contacted with 20 mL of 0.1 M Na_2CO_3 solution (solid-to-liquid ratio: 5 g/L) and agitated at 150 rpm for 2 h at room temperature (22 ± 2 °C). Following desorption, the nanoparticles were separated magnetically and the uranium concentration in the eluate was determined using the Arsenazo III method. Desorption efficiency was calculated as the percentage of previously adsorbed uranium released into the Na_2CO_3 solution. Regeneration experiments were conducted over three consecutive adsorption–desorption cycles under identical conditions. All experiments were conducted at least in duplicate, and the reported values represent average experimental results

Results and discussions

Time-dependent uranium removal by iron-based reactive materials

The uranium removal performance of water works sludge, apatite, and zero-valent iron nanoparticles (ZVINs) was evaluated under batch conditions at near-neutral pH. The time-dependent removal profiles are presented in Figure 2.

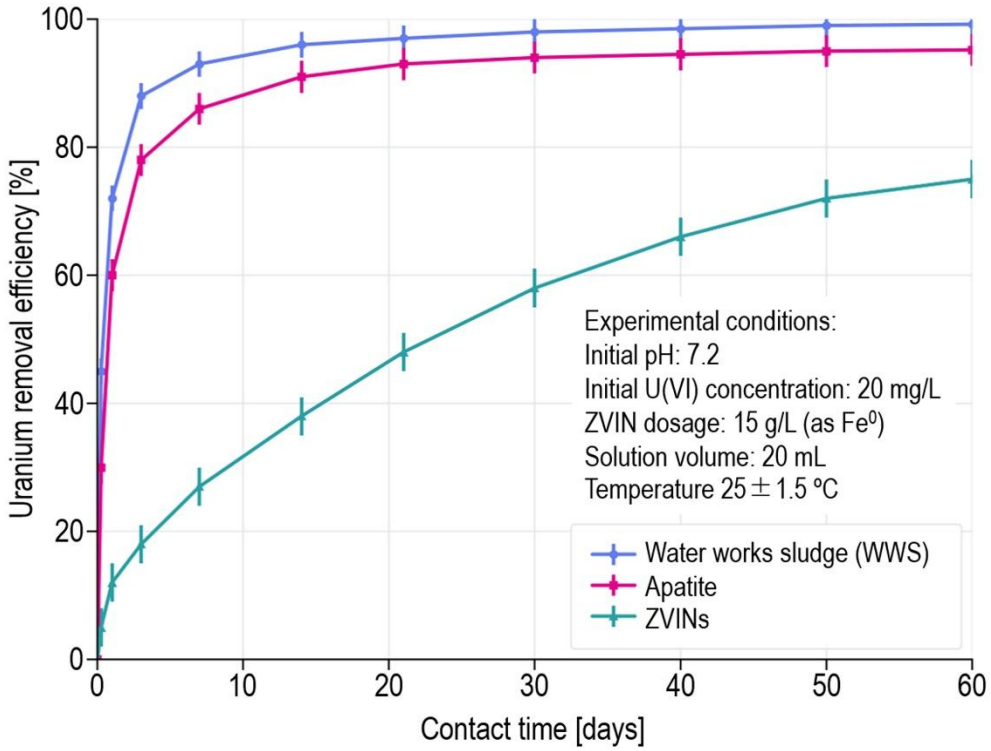


Figure 2. Time-dependent uranium removal efficiency by water works sludge (WWS), apatatite, and zero-valent iton nanoparticles (ZVINs). Error bars represents standard deviation (n=3).

The results demonstrated substantial differences in uranium immobilisation kinetics depending on the reactive material used. Adsorption onto WWS occurred rapidly during the initial contact period and reached near-equilibrium within approximately 72 h. Similar behaviour was observed for apatite, where uranium removal proceeded predominantly through adsorption and phosphate-assisted precipitation mechanisms.

In contrast, uranium removal by ZVINs proceeded more gradually and continued over extended reaction times exceeding 50 days. This behaviour indicates that uranium immobilisation by nanoscale iron systems is governed not only by initial surface adsorption but also by slower corrosion-mediated processes involving the progressive formation of iron hydroxides, oxides, and mixed Fe/U secondary phases. The gradual and continuously increasing uranium removal observed for ZVINs is consistent with previous studies reporting that nanoscale Fe^0 materials undergo dynamic surface evolution during aging in aqueous systems (Zhang et al., 2022). The progressive transformation of Fe^0 into ferrihydrite, FeOOH, maghemite, and magnetite phases generates additional reactive sites capable of uranium adsorption and co-precipitation. These differences in removal kinetics highlight that the mechanism of uranium immobilisation depends strongly on the physicochemical properties and reactivity of the material.

While WWS and apatite mainly act through relatively rapid adsorption and precipitation processes and reach near-equilibrium within a short time, ZVINs systems exhibit a slower but progressive removal trend without a clear equilibrium plateau within the investigated time frame. This observation suggests that surface transformation processes continue during nanoparticle aging, resulting in the gradual development of new reactive interfaces. Such prolonged reactivity may be advantageous for long-term groundwater remediation applications where sustained uranium immobilisation over extended periods is required, even if the overall removal efficiency remains lower than that achieved by WWS and apatite under the present experimental conditions. Recent investigations have demonstrated that uranium immobilisation by iron-based nanomaterials may involve several simultaneous mechanisms, including (Hua et al., 2023):

- surface complexation,
- reductive precipitation,
- incorporation into iron oxide lattices,
- adsorption onto corrosion products,
- and co-precipitation with secondary mineral phases.

The continuously increasing uranium removal observed for ZVINs over the 60-day experimental period therefore suggests that the progressive formation of iron corrosion products contributes to ongoing uranium immobilisation. Although the overall uranium removal efficiency remained lower than that obtained with WWS and apatite, the absence of a clear equilibrium plateau indicates that corrosion-mediated surface transformations continued throughout the experiment and may contribute to long-term uranium stabilisation. It should be noted that the present data do not directly identify the specific corrosion phases responsible for uranium fixation; therefore, the proposed interpretation should be regarded as consistent with the observed kinetic behaviour and previous mechanistic studies of Fe⁰-based remediation systems rather than as direct experimental proof (Anang et al., 2021).

Mechanistic evidence for U(VI) co-precipitation with aging corrosion products

The obtained results suggest that uranium immobilisation by ZVINs cannot be explained solely by direct interaction with metallic Fe⁰ surfaces. Instead, the data indicate that aging iron corrosion products likely play an important role in uranium fixation and long-term stabilisation. Based on the experimental conditions and approximate mass-balance considerations, a limited fraction of the initial Fe⁰ was assumed to undergo oxidation during the investigated reaction period. No direct phase-specific quantification of Fe⁰ oxidation products was performed in the present study. The partial oxidation of Fe⁰ resulted in the formation of substantial quantities of amorphous and poorly crystalline iron oxides and hydroxides. These secondary phases are known to possess strong affinity toward uranyl species and may act as efficient scavengers for dissolved uranium. Based on the experimental conditions and estimated extent of Fe⁰ oxidation, the Fe molar ratio associated with the resulting corrosion products was approximately 154 (Table 1).

Table 1. *Experimental conditions and estimated Fe : U molar ratio in corrosion products formed during uranium immobilisation experiments*

Initial pH	Fe^0 dosage mg/L	Initial U(VI) concn., mg/L	Solution volume, mL	Estimated Fe:U ratio
7.2	15	20	20	154

Such a high Fe ratio indicates that uranium represents only a minor component incorporated within a large excess of iron corrosion phases. Consequently, direct detection of uranium-bearing crystalline phases by conventional X-ray diffraction would be expected to be difficult. The obtained results are consistent with previous report indicating that uranium immobilisation in iron-based systems frequently occurs through mixed adsorption/co-precipitation pathways rather than through purely reductive precipitation mechanisms (Kong et al., 2016). In particular, the progressive transformation of Fe⁰ into magnetite and FeOOH phases may generate highly reactive surfaces capable of retaining uranyl ions through several pathways, including:

- incorporation within into magnetite lattices,
- formation of U–O–Fe surface complexes,
- and entrapment within amorphous iron hydroxide matrices.

The persistence of immobilised uranium in the ZVINs system, together with the continuously increasing removal observed during long-term aging, is consistent with the possibility of partial structural incorporation and co-precipitation within iron corrosion products rather than weak reversible adsorption alone (Figure 3). Visual observations during the experiments also indicated gradual darkening and aggregation of the nanoparticles, suggesting progressive surface oxidation and formation of mixed Fe(II)/Fe(III) phases.

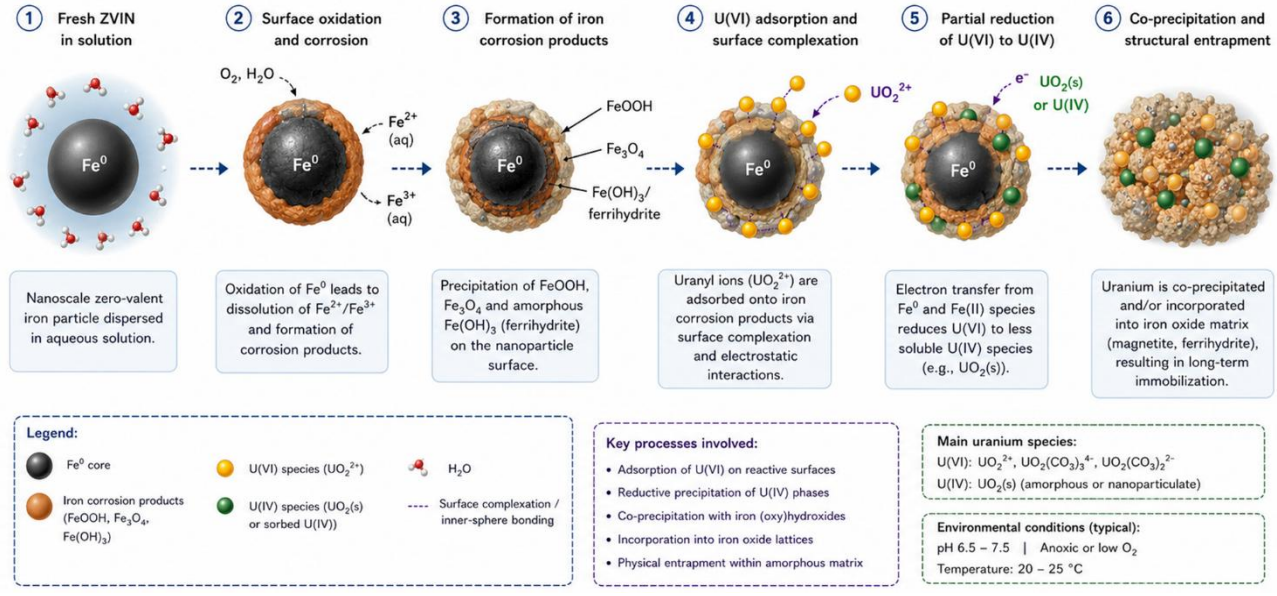


Figure 3. Schematic illustration of the proposed mechanisms responsible for uranium immobilisation by zero-valent iron nanoparticles. Multiple processes including adsorption, reduction, co-precipitation and structural incorporation contribute to the long term stabilisation of uranium

The proposed mechanism therefore suggests that uranium stabilisation is governed by coupled adsorption-corrosion processes rather than by direct reduction alone. Progressive oxidation of Fe^0 nanoparticles generates reactive iron oxide and hydroxide phases that provide additional adsorption and co-precipitation sites for dissolved uranium species. Simultaneously, electron transfer from Fe^0 and Fe(II)-containing corrosion products may promote partial reduction of soluble U(VI) species to less mobile forms. The combined action of surface complexation, co-precipitation, reductive transformation, and structural incorporation within aging iron corrosion matrices is therefore likely responsible for the long-term immobilisation and decreased mobility of uranium under the investigated experimental conditions. The inability to desorb a significant fraction of immobilised uranium using Na_2CO_3 further supports the hypothesis of partial structural incorporation rather than weak reversible adsorption. Moreover, visual observations during the experiments indicated gradual darkening and aggregation of the nanoparticles, suggesting progressive surface oxidation and formation of mixed Fe(II)/Fe(III) phases. Such transformations are widely recognized as critical factors controlling uranium stabilisation in iron-based remediation systems (Roberts et al., 2017).

Uranium separation by ligand-functionalised magnetic nanoparticles

The uranium adsorption properties of silsesquioxane-coated magnetic nanoparticles were investigated using aqueous uranyl nitrate solutions followed by magnetic separation. Treatment of 10 mL of a 0.040 M uranyl nitrate solution with 0.1 g of functionalised magnetic nanoparticles for 24 h resulted in a decrease in uranium concentration from 0.040 M to 0.0145 M, corresponding to approximately 64% uranium removal efficiency under the investigated conditions. In contrast, uncoated magnetic nanoparticles exhibited negligible uranium uptake, indicating that the ethylenediamine-functionalised silsesquioxane shell plays a dominant role in uranium coordination and adsorption. The enhanced adsorption performance can be attributed to the presence of amino donor groups capable of forming coordination complexes with uranyl ions according to the following interaction scheme:

$$Fe_3O_4{-}Si{-}(NH_2)_2 + UO_2^{2+} \rightarrow Fe_3O_4{-}Si{-}(NH_2)_2{\cdot}UO_2^{2+}$$

The magnetic properties of the developed nanomaterial enabled rapid separation of the uranium-loaded adsorbent from aqueous suspension within several minutes after application of an external magnetic field. This represents a significant practical advantage for the treatment of contaminated mine water, where separation of nanoscale adsorbents is often technically challenging.

Adsorption Isotherm study

To evaluate adsorption performance over a broader concentration range, equilibrium adsorption experiments were conducted using initial uranium concentrations between 0.005 and 0.150 M while maintaining a constant adsorbent dosage (0.1 g) and contact time (24 h). The obtained results are summarised in Table 2. The expanded dataset comprises nine equilibrium concentration points spanning more than one order of magnitude, providing a substantially improved basis for evaluation of equilibrium adsorption behaviour and isotherm analysis compared with the original dataset. The results demonstrate that the amino-functionalised silsesquioxane coating provides substantial uranium uptake under all investigated conditions. At lower uranium concentrations, removal efficiencies reached approximately 68–70%, indicating strong affinity of the chelating amino groups toward dissolved uranyl species. As the initial uranium concentration increased, the removal efficiency gradually decreased to approximately 37%, reflecting progressive occupation of available adsorption sites and the approach toward sorbent saturation. Despite this trend, significant uranium removal was maintained even at elevated concentrations, confirming the strong adsorption capability of the functionalised magnetic nanomaterial. The observed concentration-dependent behaviour is consistent with adsorption processes involving a finite number of energetically favourable binding sites.

Table 2. *Equilibrium adsorption data for uranium uptake by ligand-functionalised magnetic nanoparticles used for Langmuir isotherm analysis*

Initial U concn. (M)	Adsorbent dosage (g)	Contact time (h)	Final U concentration (M)	Removal efficiency (%)
0.005	0.1	24	0.0015	70
0.01	0.1	24	0.0032	68
0.02	0.1	24	0.0076	62
0.04	0.1	24	0.0145	64
0.05	0.1	24	0.018	64
0.06	0.1	24	0.0235	61
0.08	0.1	24	0.034	58
0.1	0.1	24	0.052	48
0.15	0.1	24	0.095	37

Langmuir isotherm analysis

The equilibrium adsorption data were analysed using the Langmuir adsorption model:

$$q_e = (q_{max}\, K_L C_e) / (1 + K_L\, C_e)$$

where q_e (mmol/g) is the equilibrium adsorption capacity, q_{max} (mmol/g) is the maximum monolayer adsorption capacity, K_L (L/mol) is the Langmuir affinity constant, C_e (mol/L) is the equilibrium uranium concentration in solution. The corresponding Langmuir isotherm is presented in Figure 4.

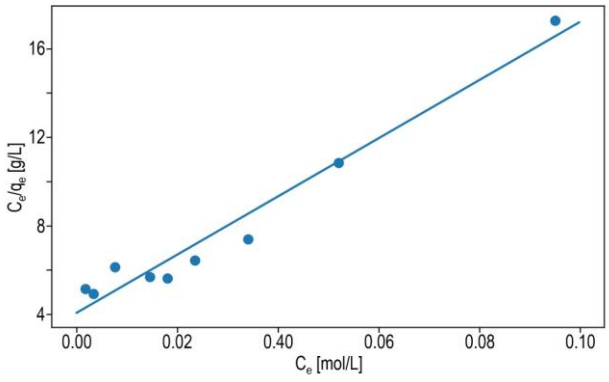


Figure 4. Langmuir isotherm for uranium adsorption onto ligand-functionalised magnetic nanoparticles

Linear regression analysis of the linearised Langmuir equation yielded a coefficient of determination (R^2) of 0.97, indicating satisfactory agreement between the experimental data and the Langmuir adsorption model. The estimated maximum adsorption capacity was approximately 5.8 mmol U/g. Although the investigated concentration range does not span multiple orders of magnitude, the expanded dataset provides a reasonable basis for preliminary Langmuir analysis and evaluation of adsorption performance. Therefore, the Langmuir model is used here as an empirical approximation of the adsorption behaviour rather than a definitive mechanistic description. The observed adsorption behaviour is consistent with coordination interactions between uranyl ions and amino-functional groups incorporated within the silsesquioxane coating. Nevertheless, additional factors such as surface heterogeneity, multilayer adsorption, or partial precipitation may also contribute to uranium uptake under certain conditions. The Langmuir model was selected as an initial approximation of the adsorption process. Evaluation of additional adsorption models such as Freundlich and Temkin could provide further mechanistic insight and will be considered in future investigations. Despite these limitations, the isotherm analysis confirms the substantial adsorption affinity of the functionalised magnetic nanomaterial toward uranium species. In combination with the rapid magnetic separation capability of the material, these results indicate that amino-functionalised magnetic nanoparticles represent promising candidates for uranium recovery and remediation applications in contaminated aqueous systems.

Desorption and regeneration

To further evaluate the regeneration potential of the developed nanomaterials, desorption experiments were performed using Na_2CO_3 solution as an eluent. Approximately 48 ± 5% of the adsorbed uranium was desorbed under the investigated conditions, indicating partial reversibility of the adsorption process (Table 3).

Table 3. *Regeneration cycles (magnetic nanoparticles)*

Cycle	Removal efficiency, %	Desorption efficiency, %
1	65 ± 2	48 ± 5
2	60 ± 3	45 ± 4
3	55 ± 3	42 ± 4

These results demonstrate that a substantial fraction of the adsorbed uranium can be recovered, while another fraction remains strongly immobilised on the adsorbent surface. The regeneration experiments should be considered preliminary and were included primarily to assess the feasibility of adsorbent reuse rather than to provide a comprehensive optimisation of regeneration conditions. The incomplete desorption suggests that a significant fraction of uranium is strongly bound to the nanoparticle surface or retained through more stable immobilisation mechanisms. Regeneration tests over three consecutive adsorption-desorption cycles showed that the removal efficiency decreased gradually from 65% to 55%, while desorption efficiency decreased from approximately 48% to 42%. These results indicate that the magnetic nanoparticles exhibit moderate regeneration capability, although partial loss of adsorption performance occurs during repeated use. This behaviour is consistent with a combination of reversible surface adsorption and stronger uranium immobilisation mechanisms.

An important practical advantage of the developed material is the possibility of rapid magnetic separation after adsorption, which simplifies recovery of the adsorbent from treated water and may reduce the need for additional solid-liquid separation processes. Together with the moderate regeneration capability demonstrated in the present study, this characteristic may facilitate repeated use of the adsorbent and improve process sustainability. Although the present study was conducted under controlled laboratory conditions using synthetic uranium solutions, the obtained results demonstrate that amino-functionalised magnetic nanoparticles possess substantial uranium adsorption capacity and can be readily recovered using an external magnetic field. Further investigations should focus on optimisation of regeneration efficiency, evaluation of adsorption performance in the presence of competing ions, and assessment of long-term material stability under environmentally relevant conditions. Nevertheless, the results indicate that functionalised magnetic nanomaterials represent promising candidates for uranium remediation technologies combining selective adsorption and magnetic recovery.

Conclusion

This study demonstrates that iron-based nanomaterials provide effective approaches for uranium removal and immobilisation under near-neutral aqueous conditions. Zero-valent iron nanoparticles (ZVINs) exhibited gradual but sustained uranium removal over extended reaction times, in contrast to the rapid but equilibrium-limited behaviour observed for water works sludge and apatite. The time-dependent removal profile suggests that uranium immobilisation in Fe^0 systems is governed by coupled adsorption and corrosion processes, with progressive formation of iron corrosion products likely contributing to continued uranium uptake. The experimental results are consistent with uranium immobilisation mechanisms reported in the literature for Fe^0-based systems, including surface complexation, co-precipitation, reductive transformation, and incorporation into aging iron corrosion products. Although these mechanisms were not directly resolved at the phase level, the observed kinetic behaviour and limited desorption support the role of corrosion products in long-term uranium stabilisation. Ligand-functionalised magnetic nanoparticles demonstrated substantial uranium adsorption capacity and enabled rapid magnetic separation from aqueous solutions. The adsorption behaviour is consistent with coordination interactions between uranyl ions and amino-functional groups, while regeneration experiments indicate moderate reusability with partial irreversible binding of uranium. These characteristics highlight the potential of such materials for applications where both adsorption efficiency and facile recovery are required. Overall, the results suggest that functionalising magnetically recoverable iron nanoparticles offers a versatile approach for uranium remediation. However, the present study was conducted under controlled laboratory conditions using simplified aqueous systems, and further investigations are required to evaluate performance in complex mine-water matrices, including the effects of competing ions, pH variability, and long-term stability. Future work should focus on detailed characterisation of corrosion products, validation under realistic

mine-water conditions, and optimisation of adsorption and regeneration processes.

References

Abdessamed, D., Jodar-Abellan, A., Ghoneim, S. S. M., Almaliki, A., Hussein, E. E., & Pardo, M. Á. (2023). Groundwater quality assessment for sustainable human consumption in arid areas based on GIS and water quality index in the watershed of Ain Sefra (SW of Algeria). *Environmental Earth Sciences, 82*(21), Article 510. https://doi.org/10.1007/s12665-023-11183-9

Afrikaner, L. C., Mapani, B., & Amwele, H. (2025). Groundwater in arid environments: A review of uranium occurrence and impacts. Journal of Hydrology*: Regional Studies, 62*, Article 102814. https://doi.org/10.1016/j.ejrh.2025.102814

Akash, S., Sivaprakash, B., Vadivel Raja, V. C., Rajamohan, N., & Muthusamy, G. (2022). Remediation techniques for uranium removal from polluted environment – Review on methods, mechanism and toxicology. *Environmental Pollution, 302*, Article 119068. https://doi.org/10.1016/j.envpol.2022.119068

Anang, E., Hong, L., Fan, X., & Asamoah, E. N. (2022). Attapulgite supported nanoscale zero-valent iron in wastewater treatment and groundwater remediation: synthesis, application, performance and limitation. *Environmental Technology Reviews, 11,* 1-17. https://doi.org/10.1080/21622515.2021.2010131

Arahangelova, V., & Loukanov, A. (2023). Phytoremediation and extraction of colloidal contaminants from mine effluents through legume plants. *Sustainable Extraction and Processing of Raw Materials Journal (SEPRM), 4,* 6–10. https://doi.org/10.58903/u17190823

Fu, W., Liu, Z., Yang, Z., Li, Y., & Pan, B. (2025). Confined iron-based nanomaterials for water decontamination: Fundamentals, applications, and challenges. *Fundamental Research, 5*(2), 612–623. https://doi.org/10.1016/j.fmre.2023.07.011

Gheju, M. (2025). Mechanisms of contaminant removal with metallic iron (Fe0): A comprehensive and critical review. *Separation and Purification Technology, 364*(Part 3), Article 132503. https://doi.org/10.1016/j.seppur.2025.132503

Helal, A. S., Hémadi, M., Lomas, J. S., Ammar, S., Abdelhafiz, A., El-Sheikh, S. M., Sheta, S. M., Galanek, M., Hassan, M. H., Chang, J.-K., & Li, J. (2025). Uranium removal from environmental water and nuclear waste: Nanomaterial solutions and their environmental sustainability. *Chemical Engineering Journal, 507,* Article 160298. https://doi.org/10.1016/j.cej.2025.160298

Hua, Y., Li, D., Zou, J., Wang, W., Wu, X., Zhang, X., Liu, Q., Zhao, G., Li, M., Zhang, W-x., & Yang, J. (2023). Evolutional solid phase and solid-liquid interface uranium immobilisation mechanisms by nanoscale zero-valent iron and enhanced uranium stability control strategy. *Chemical Engineering Journal, 453,* 139924. 10.1016/j.cej.2022.139924

Kairullova, M., Bakhtin, M., Ilbekova, K., & Ibrayeva, D. (2026). Migration and accumulation of uranium-associated heavy metals in mining-affected ecosystems (water, soil, and plants). *Biology, 15*(6), Article 502. https://doi.org/10.3390/biology15060502

Kong, L., Zhu, Y., Wang, M., Li, Z., Tan, Z., Xu, R., Tang, H., Chang, X., Xiong, Y., & Chen, D. (2016). Simultaneous reduction and adsorption for immobilisation of uranium from aqueous solution by nano-flake Fe-SC. *Journal of Hazardous Materials, 320,* 435–441. doi: 10.1016/j.jhazmat.2016.08.060

Li, Z.-J., Wang, L., Yuan, L.-Y., Xiao, C.-L., Mei, L., Zheng, L.-R., Zhang, J., et al. (2015). Efficient removal of uranium from aqueous solution by zero-valent iron nanoparticle and its graphene composite. *Journal of Hazardous Materials, 290*, 26–33. https://doi.org/10.1016/j.jhazmat.2015.02.028

Lin, K., Wan, Y., Chang, H., Yu, H., Yang, H., & Qu, F. (2026). Advances and challenges in remediation technologies for uranium/radium-contaminated groundwater. *Environmental Science: Water Research & Technology, 12*, 769–788. https://doi.org/10.1039/D5EW00910C

Loukanov, A. (2025). Magnetic nanoparticle-assisted remediation of petroleum-contaminated soils. Sustainable Extraction and Processing of Raw Materials Journal (SEPRM), 6, 51–59. https://doi.org/10.58903/dw18922073

Loukanov, A., Udono, H., Takakura, R., Mladenova, P., Kobayashi, N., Kawamura, R., & Nakabayashi, S. (2017). Monitoring and extraction of uranium in polluted acid mine drainage by super-paramagnetic nanoparticles coated with carbon nanodots. *Journal of Radioanalytical and Nuclear Chemistry, 314*, 1149–1159. https://doi.org/10.1007/s10967-017-5471-z

Mahfouz, M. G., Galhoum, A. A., Gomaa, N. A., Abdel-Rehem, S. S., Atia, A. A., Vincent, T., & Guibal, E. (2015). Uranium extraction using magnetic nano-based particles of diethylenetriamine-functionalised chitosan: Equilibrium and kinetic studies. *Chemical Engineering Journal, 262,* 198–209. https://doi.org/10.1016/j.cej.2014.09.061

Ngerem, E. C., Sanusi, I. A., Dalu, T., & Suinyuy, T. N. (2026). Sustainable acid mine drainage wastewater remediation: A comprehensive review and bibliometric analysis. *Environmental Science Advances, 5*(3), 681–710. https://doi.org/10.1039/d5va00266d

Riba, O., Scott, T. B., Ragnarsdottir, K. V., & Allen, G. C. (2008). Reaction mechanism of uranyl in the presence of zero-valent iron nanoparticles. *Geochimica et Cosmochimica Acta, 72*(16), 4047–4057. https://doi.org/10.1016/j.gca.2008.04.041

Roberts, H., Morris, K., Law, G., Mosselmans, J., Bots, P., Kvashnina, K., & Shaw, S. (2017). Uranium(V) Incorporation Mechanisms and Stability in Fe(II)/Fe(III) (oxyhydr)Oxides. *Environmental Science & Technology Letters, 4,* 421–426. https://doi.org/10.1021/acs.estlett.7b00348

Sheng, G., Shao, X., Li, Y., Li, J., Dong, H., Cheng, W., Gao, X., & Huang, Y. (2014). Enhanced removal of uranium(VI) by nanoscale zerovalent iron supported on Na–bentonite and an investigation of mechanism. *Journal of Physical Chemistry A, 118*(16), 2952–2958. https://doi.org/10.1021/jp412404w

Skierszkan, E. K., Dockrey, J. W., Helsen, J., Findlater, L.-L., Bataille, C. P., de Laplante, G., McBeth, J. M., Mayer, K. U., & Beckie, R. D. (2021). Persistence of uranium in old

and cold subpermafrost groundwater indicated by linking 234U-235U-238U, groundwater ages, and hydrogeochemistry. *ACS Earth and Space Chemistry, 5*(12), 3474–3487. https://doi.org/10.1021/acsearthspacechem.1c00307

Sun, Y.-P., Li, X.-Q., Cao, J., Zhang, W.-X., & Wang, H. P. (2006). Characterization of zero-valent iron nanoparticles. *Advances in Colloid and Interface Science, 120*(1–3), 47–56. https://doi.org/10.1016/j.cis.2006.03.001

Verma, Y., Verma, A., Bhaskaralingam, A., Dhiman, P., Wang, T., Kumar, A., & Sharma, G. (2025). Application of zero-valent iron and its derivatives in the removal of toxic metal ions from groundwater. *Water, 17*(10), Article 1524. https://doi.org/10.3390/w17101524

Wazne, M., Korfiatis, G. P., & Meng, X. (2003). Carbonate effects on hexavalent uranium adsorption by iron oxyhydroxide. *Environmental Science & Technology, 37*(16), 3619–3624. https://doi.org/10.1021/es034166m

Wu, R., Wang, X., He, S., Wu, M., Li, P., Show, P.-L., Han, P., Hamzah, M. H., Zhang, Y., & Chen, J. (2026). Robust immobilisation of uranium using biogenic FeS with lignocellulose from green plant waste. *Chemical Engineering Journal, 528*, Article 172352. https://doi.org/10.1016/j.cej.2025.172352

Xiao, Y., Helal, A. S., Mozario, E., Mayoral, A. et al. (2023). Functionalized maghemite nanoparticles for enhanced adsorption of uranium from simulated wastewater and magnetic harvesting. *Environmental Research, 216*(2), 114569. https://doi.org/10.1016/j.envres.2022.114569

Zhang, X., Liu, X., Peng, Y., Wu, X., Tan, Y., Zeng, Q., Song, Z. & Li, M. (2022). Controllable shell corrosion of coated nanoscale zero valent iron induces long-term potentiation of its reactivity for uranium removal. *Separation and Purification Technology, 287,* 120550. https://doi.org/10.1016/j.seppur.2022.120550

Zhao, X., Liu, W., Cai, Z., Fu, J., Duan, J., Zhao, D., Bozack, M.& Feng, Y. (2020). Reductive immobilisation of uranium by stabilised zero-valent iron nanoparticles: Effects of stabilisers, water chemistry and long-term stability. *Colloids and Surfaces A: Physicochemical and Engineering Aspects, 604,* 125315. 10.1016/j.colsurfa.2020.125315

Zhu, N., Ji, H., Yu, P., Niu, J., Farooq, M. U., Akram, M. W., Udego, I. O., Li, H., & Niu, X. (2018). Surface modification of magnetic iron oxide nanoparticles. *Nanomaterials, 8(*10), Article 810. https://doi.org/10.3390/nano8100810)

Sustainable Extraction and Processing of Raw Materials, 2026

REHABILITATION AND RECONVERSION OF COAL MINING SITES: SUSTAINABLE SOLUTIONS FOR ENERGY TRANSITION IN THE PERNIK REGION

Petar Petrov, Veneta Stefanova, Zhivko Vasilev, Stanimira Ivanova, Iva Stamenova-Yordanova, Elena Georgieva

University of Forestry, 10 Kliment Ohridski Blvd., 1797 Sofia, Bulgaria, petargpetrof@gmail.com, venistefanova3@gmail.com, zhivko.vasilev@mail.bg, ivanova.stanimiraa@gmail.com, ivastamenovaa@gmail.com, eli1307@abv.bg
Corresponding author: zhivko.vasilev@mail.bg

ABSTRACT. This study assesses the rehabilitation and reconversion potential of coal mining sites in the Pernik region, Bulgaria, within the context of the energy transition and post-mining land-use planning. An integrated multi-criteria framework was applied, combining site inventory, regulatory review, spatial interpretation and expert-based assessment. The framework evaluates post-mining land according to geotechnical stability, contamination-related suitability, infrastructure accessibility, ecological suitability and land-use constraints. The analysis identifies a heterogeneous post-mining landscape, including ash disposal sites, spoil heaps, residual mining areas, underground mining zones and former industrial platforms. The results show that stabilised technogenic landforms are most suitable for controlled renewable energy applications, particularly photovoltaic development combined with containment and monitoring. Former industrial platforms demonstrate potential for industrial and energy-related reuse, while underground mining zones affected by subsidence and hidden voids require restricted use and long-term control. Lower-risk or partially restored sites are suitable for ecological restoration and nature-based solutions. Notably, two site groups with identical aggregate suitability scores lead to fundamentally different reconversion pathways depending on their underlying criterion profile, indicating that the framework should be applied as a profile-based screening tool rather than as a one-dimensional ranking. The proposed suitability-based framework supports decision-oriented planning by linking site-specific constraints with feasible reconversion pathways and contributes to the sustainable transformation of coal regions under transition.

Key words: rehabilitation, mine closure, coal, Pernik.

Introduction

Coal mining has historically played a key role in the energy sector of Bulgaria, with the Pernik coal basin representing one of the country's earliest and most significant mining regions. Its development has included a long sequence of mine opening, operation, restructuring and closure, which has resulted in a heterogeneous post-mining landscape of disturbed terrains, mining waste facilities, spoil heaps, ash disposal areas and residual mining sites (State Archives Agency, 2023; EEA, 2026; Ministry of Energy, 2026). In this context, the systematic identification of mining sites, their operational status and concession framework is necessary for assessing their rehabilitation and reconversion potential (Subsurface Resources Act, 1999, Council of Ministers, 2026; Ministry of Energy, 2026; Kostadinova-Slaveva, 2026).

At present, coal mining activity in the Pernik region is significantly reduced, with most mining operations discontinued or undergoing closure-related transformation (Ministry of Energy, 2015; Ministry of Energy, 2026). This transition has generated environmental challenges, including degraded soils, altered terrain morphology, disturbed hydrological regimes and residual contamination, but also creates opportunities for rehabilitation and new land-use functions (ICMM, 2019; River Basin Directorate "West Aegean Region", 2024; Panayotov, 2024). The broader energy transition and the Just Transition framework further reinforce the need for sustainable pathways that combine environmental restoration, risk reduction and economic diversification (World Bank, 2018; European Commission, 2020; Regulation (EU) 2021/1056).

The present study aims to identify and characterise the mining objects in the Pernik region, analyse the existing regulatory and concession conditions, and assess the potential for rehabilitation and post-mining land-use transformation. Special attention is given to good practices and innovative solutions supporting sustainable regional development in the context of the energy transition (IGF, 2022; Pagouni et al., 2024).

Materials and methods

Study area

The study area covers the Pernik coal basin in Western Bulgaria — one of the country's oldest coal-mining regions, historically exploited for brown coal by both underground and open-pit methods. Long-term mining has formed a complex post-mining landscape of spoil heaps, ash disposal sites, open pits, subsidence-prone zones and disturbed industrial terrains near urban areas, infrastructure and energy facilities, making the region a relevant case for assessing rehabilitation and reconversion options.

Table 1 summarises the inventory of identified post-mining sites used in the analysis. The listed facilities represent only registered closed and abandoned mining waste facilities and do not cover the full spatial extent of mining-affected land in the region (open-pit areas, active concession areas, subsidence zones, industrial platforms, ash disposal sites).

According to the data from the Ministry of Energy and the register of active concessions for extraction of underground resources (updated as of 17.03.2026), a total of 16 valid concessions for coal extraction are currently in force in Bulgaria (Ministry of Energy, 2026).

Within the present study, only concessions located on the territory of Pernik region or partially overlapping it are considered.

Table 1. *Registered closed and abandoned mining waste facilities included in the inventory*

Site	Type	Period	Area (m²)	Location
Bela voda	MWF	1987–1998	41,626	Pernik
Teva	MWF	1986–2000	20,035	Lyulin
Teva	MWF	1975–2000	11,024	Lyulin
Garvanov	SH	1954–2001	21,719	Divotino
Garvanov	SH	1954–2007	1,298	Divotino
Shahta	MS	1925–2009	48,736	Pernik
Shahta	MS	1937–2007	3,209	Pernik
Shahta	MS	1938–2007	2,389	Pernik
Shahta	MS	1981–2006	5,160	Pernik
Shahta	MS	1971–2000	3,827	Pernik
Shahta	MS	1971–2000	700	Pernik
Shahta	MS	1975–2000	1,567	Pernik
Shahta	MS	1990–2004	27,952	Pernik
Shahta	MS	1957–2004	1,190	Pernik

Source: Compiled by the authors based on data from the Ministry of Energy (n.d.) and the EEA (n.d).

Note: MWF – mining waste facility; SH – spoil heap; MS – mining site / technogenic area; n.d. - no data. Total inventoried area: 190,432 m².

The identified active concessions are summarised and illustrated in Figure 1 (State Gazette, 2005; Ministry of Energy, 2016; Ministry of Energy, 2026).

Methods

The study employs a screening-level approach that integrates desk research, regulatory review, analysis of scientific and technical sources, and synthesis of administrative and geospatial data, following the general logic of mine-closure planning, risk-based assessment and post-mining land-use decision-making (ICMM, 2019; IGF, 2022; Pagouni et al., 2024). The objective of the present study is to provide a decision-support framework for the identification of rehabilitation and reconversion pathways for post-mining land in the Pernik region. It is important to note that the present study does not seek to conduct a full quantitative environmental or geotechnical investigation.

The analysis was conducted in three stages. Initially, post-mining sites within the Pernik coal basin were identified and classified according to site type and operational status. This classification included underground mining areas, open-pit areas, spoil heaps, mining waste facilities, ash disposal sites and former industrial platforms.

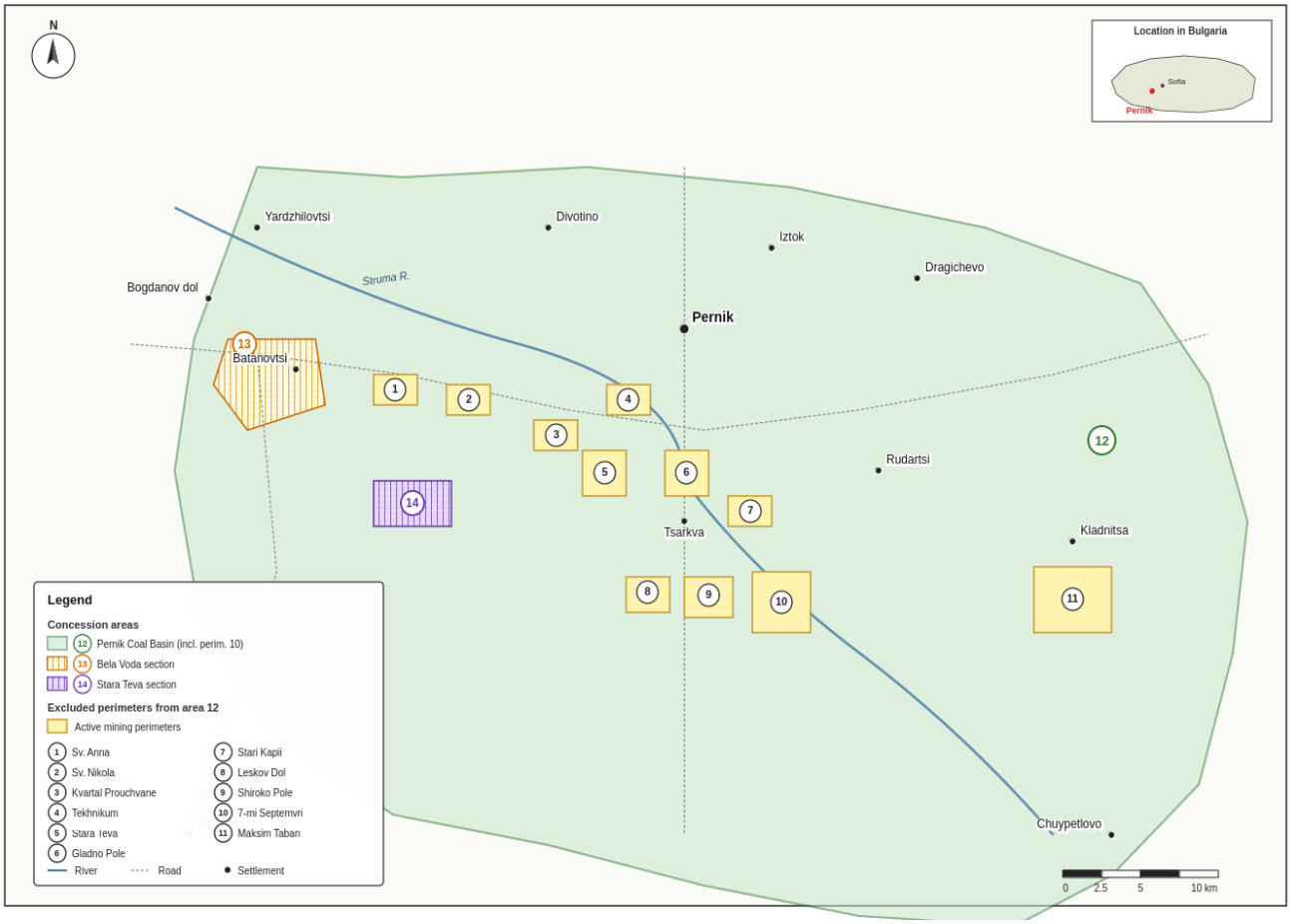


Fig. 1. Active coal mining concessions in the Pernik region

Legend: (1) “Sv. Anna”, (2) “Sv. Nikola”, (3) “Kvartal Prouchvane”, (4) “Tekhnikum”, (5) “Stara Teva”, (6) “Gladno Pole”, (7) “Stari Kapii”, (8) “Leskov Dol”, (9) “Shiroko Pole”, (10) “7-mi Septemvri” and (11) “Maksim Taban”; active mining perimeters excluded from the concession area of the “Pernik Coal Basin” deposit (12, green), including perimeter (10) “7-mi Septemvri”; (13) Concession area of the “Bela Voda” section; (14) Concession area of the “Stara Teva” section

Secondly, a review was conducted of the regulatory and concession framework, with particular attention paid to issues such as mine closure, mining waste management, environmental protection and land rehabilitation. The review covered the key national legislative and regulatory framework relevant to post-mining land rehabilitation, including the Subsurface Resources Act 1999, Ordinance No. 26 on the Reclamation of Disturbed Lands, Improvement of Low-Productivity Lands, and Removal and Utilisation of the Humus Layer (2002), and the Ordinance on the Management of Mining Waste (2016), complemented by the Global Industry Standard on Tailings Management - GISTM (2020), which provides internationally recognised principles and requirements for the safe management, closure and post-closure governance of mining waste facilities.

The third stage of the research applied a semi-quantitative multi-criteria suitability assessment based on five criteria: geotechnical stability (GS), contamination-related suitability (CR), infrastructure access (IA), ecological suitability (ES) and land-use constraints (LC) - Table 2. These criteria were selected for their direct influence on the feasibility of renewable energy, ecological restoration, industrial reuse and restricted-use management, reflecting commonly used dimensions in post-mining land-use assessment, including geotechnical stability, environmental risk, infrastructure availability, land-use constraints and closure-management requirements (World Bank, 2018; ICMM, 2019; Pagouni et al., 2024).

Table 2. *Criteria for assessment of post-mining land suitability*

Crit eria	Indicator	Low suitability (Score = 1)	Moderate suitability (Score = 2)	High suitability (Score = 3)
GS	Slope stability, subsidence risk	Unstable terrain	Partly stabilised	Stable terrain
CR	Heavy metals, ash, leaching	High risk	Moderate risk	Low/con-trolled risk
IA	Roads, grid, industrial access	Limited	Moderate	Well-develop-ed
ES	Protected areas, Natura 2000, habitats	High sensitivity	Buffer/con ditional zones	Low sensiti-vity
LC	Legal and safety restrictions	Severe	Condition-al	Minimal

To operationalise the assessment, it was necessary to evaluate each criterion using a three-level semi-quantitative scoring system. A score of 1 indicates low suitability, 2 indicates moderate suitability and 3 indicates high suitability for post-mining land reconversion. The scores were assigned as a screening-level interpretation of documented site characteristics, based on available administrative records, spatial information, published studies and environmental descriptions. In instances where uniform, site-specific quantitative data were not available for all facilities, a conservative typology-based assessment was applied.

No explicit weighting procedure was employed in the multicriteria assessment. Methods commonly used for criterion weighting, such as the Analytic Hierarchy Process (AHP) and Delphi technique, were not applied because the available evidence did not support a scientifically justified prioritisation of the geotechnical, environmental, spatial and planning-related criteria. Therefore, all criteria were assigned equal weights and the overall suitability index (SI) was computed as the arithmetic mean of the five criterion scores:

$$SI = \frac{(GS + CR + IA + ES + LC)}{5} \quad (1)$$

The assessment should therefore be interpreted as a screening-level suitability classification intended to support preliminary decision-making and prioritisation. The implementation of any reconversion pathway on a specific site would necessitate further field verification, encompassing geotechnical investigation, soil and waste characterisation, hydrogeological assessment, and, where pertinent, deformation monitoring.

Results and discussion

Spatial extent and typology of post-mining sites

The registered closed and abandoned mining waste facilities included in the inventory encompass a total area of 190, 432 m². It is important to note that these areas represent only a subset of the broader post-mining landscape. They exclude open-pit areas, active and former concession zones, subsidence-prone areas, ash disposal sites and former industrial platforms. According to regional land-cover and planning data, mining-related and technogenic land uses account for approximately 2% of the regional territory — a cumulative footprint that is not directly comparable with the inventory area in Table 1.

The post-mining landscape is characterised by a heterogeneous mosaic of disturbed terrains, which are concentrated in the central part of the basin and extend to cover Pernik city and adjacent settlements (Divotino, Lyulin, Batanovtsi). Representative sites include the "Bela voda" and "Teva" waste facilities, the "Garvanov" spoil heaps and the "Shahta" mining areas.

From a typological perspective, post-mining sites in the Pernik region can be grouped into six main categories, which are used consistently in the suitability assessment that follows. The initial three categories collectively denote large-scale technogenic landforms, which are characterised by the accumulation of mining and combustion residues, yet exhibit divergent geochemical and geotechnical profiles. Ash disposal sites (ADS) exemplified by the “7-mi Septemvri” site, developed on a former open pit mine, display altered geomorphology, low soil fertility and technogenic substrates with elevated contamination potential. Mining waste facilities (MWF), such as "Bela voda" and "Teva", exhibit a combination of substrate instability and residual contamination, with their reuse potential being contingent on the efficacy of prior technical rehabilitation. Spoil heaps (SH), as exemplified by the "Garvanov" site, are distinguished by slope instability, erosion processes and heterogeneous substrates.

A fourth category comprises underground mining zones (UMZ), where subsidence processes, underground voids and

surface deformation are observed. These zones are often located near urban areas, thereby increasing their environmental sensitivity and limiting their potential for redevelopment.

A fifth category is represented by former industrial platforms and associated infrastructure (IIP), characterised by relatively stable terrain conditions and existing access to transport and energy networks. Finally, a sixth group of partially restored or lower-risk sites (PRS) includes rehabilitated and semi-natural post-mining areas with reduced disturbance levels, whose constraints relate primarily to fragmentation and residual substrate limitations rather than active environmental risks.

The spatial configuration of post-mining sites in the Pernik region is characterised by fragmentation, significant interaction with urban structures, and the coexistence of multiple disturbance types. These factors directly impact the sites' suitability for rehabilitation and reconversion.

Suitability assessment of post-mining land for rehabilitation and future land-use conversion

The suitability of post-mining land for rehabilitation and future land-use conversion in the Pernik region was assessed using the multi-criteria framework described above and applied to six functional groups of sites identified through the typological analysis. The results are presented in two complementary forms: Table 3 summarises the qualitative characterisation of each group, including representative sites, dominant constraints, and recommended reuse pathways, while Figure 2 visualises the semi-quantitative scores for each criterion, together with the aggregate suitability index and the resulting suitability class.

The first group comprises sites designated for the disposal of ash (ADS). The implementation of photovoltaic technology on sites such as “7-mi Septemvri” necessitates the implementation of specific technical safeguards. These include surface stabilisation, the application of sealing cover layers, foundation systems that minimise the disturbance of contaminated material, and the control of wind erosion and ash dispersion during the construction phase (RIEW Sofia, 2021).

The second group is that of mining waste facilities (MWF). The reconversion potential of "Bela voda", "Teva" and analogous sites is contingent on the efficacy of prior technical rehabilitation, which exhibits considerable variation across the region and necessitates site-specific verification prior to any reuse decision.

The third group is characterised by the presence of spoil heaps (SH). Garvanov-type sites demonstrate a clear preference for ecological restoration over photovoltaic deployment, given that slope stabilisation and erosion control are prerequisites for any active land use. Unlike other site groups, SH display a uniformly moderate criterion profile (all scores = 2), reflecting the co-occurrence of multiple constraints of comparable severity rather than a single dominant axis. Geotechnical instability is the primary operational barrier, but contamination risks, limited access, ecological sensitivity and land-use restrictions are co-present at the same level. Ecological restoration is therefore the only reconversion pathway that does not require prior resolution of all constraint dimensions simultaneously, unlike photovoltaic or industrial reuse, which are contingent on demonstrated slope stability and acceptable contamination levels.

The fourth group is constituted by industrial platforms (IIP). In the Pernik case, this category is represented by former mining-related service areas, processing facilities and infrastructure platforms of the historical mining-energy complex, where access roads, grid proximity and industrial land-use context remain available — significantly reducing the cost of redevelopment.

Table 3. *Qualitative characterisation and reconversion pathways for post-mining site groups in the Pernik region*

Site group	Representative sites	Dominant constraints	Recommended use
ADS	7-mi Septemvri	Contamination, low fertility, dust generation, containment needs	Controlled photovoltaic (PV) use with cover layers, containment and long-term monitoring
MWF	Bela voda, Teva	Substrate stability, residual contamination, rehabilitation status	Conditional reuse depending on prior technical rehabilitation
SH	Garvanov	Slope instability, erosion, heterogeneous substrates	Ecological restoration; conditional PV only where stability is demonstrated
IIP	Former mining-related platforms and energy-related sites	Residual contamination, planning requirements, urban interface	Industrial reuse, energy systems, hybrid economic functions
UMZ	Central Pernik, Shahta-related areas	Subsidence, underground voids, urban proximity, deformation	Restricted use; risk management and continuous deformation monitoring
PRS	Rehabilitated and semi-natural post-mining areas	Fragmentation, residual substrate limitations	Ecological restoration; nature-based solutions; green infrastructure

The fifth group is comprised of underground mining zones (UMZ). The term "restricted use" is associated with two practical implications. Firstly, it necessitates precautionary planning. Secondly, it involves the continued deformation monitoring of existing built-up areas above former workings. Furthermore, it establishes a default presumption against new construction unless supported by site-specific stability investigations.

Group 6 is comprised of sites that have undergone partial restoration and are classified as lower risk (PRS). Beyond the realm of ecological recovery, nature-based solutions (NBS) interventions in such locations contribute to the integration of

landscapes and the enhancement of ecosystem services across the broader post-mining environment (Řehounková & Prach, 2008; Prach et al., 2011).

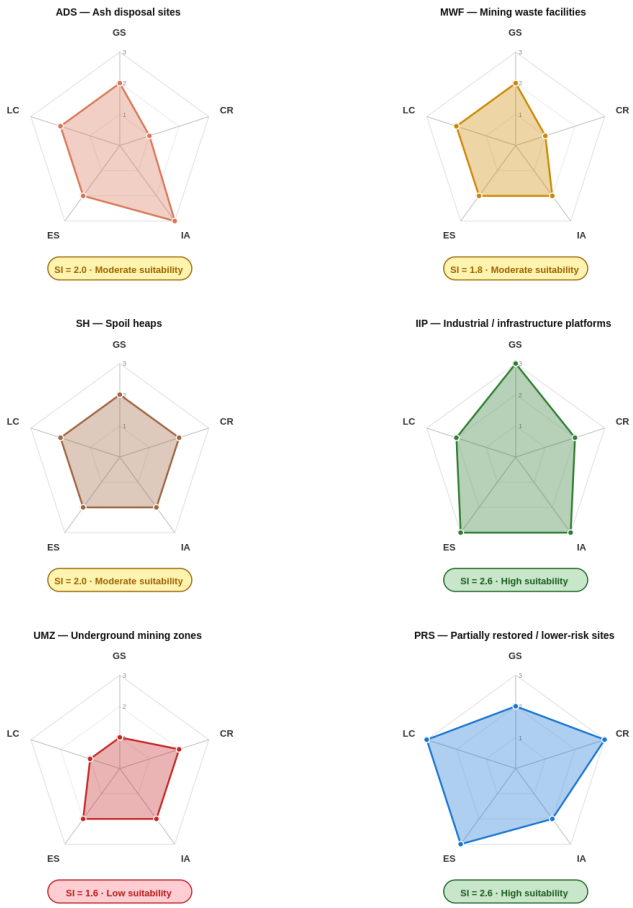


Fig. 2. Criterion profiles of post-mining site groups and their suitability for rehabilitation and reconversion pathways

Note: Scores: 1 – low; 2 – moderate; 3 – high. SI classes: low (SI < 1.67), moderate (1.67 ≤ SI < 2.34), high (SI ≥ 2.34). The suitability class intervals were derived mathematically through equal-interval partitioning of the theoretical SI range (1.00–3.00), obtained from the arithmetic mean of five equally weighted criteria evaluated on a three-level semi-quantitative scale. The resulting interval width (0.67) produced three suitability classes: low (1.00–1.66), moderate (1.67–2.33) and high (2.34–3.00). Equal-interval classification is widely applied in screening-level GIS-based and multi-criteria suitability assessments where empirically calibrated threshold values are unavailable (Eastman, 1995; Malczewski, 2004). The scoring was checked for internal consistency by comparing the assigned values with the documented site typology, known environmental constraints and expected land-use limitations.

Synthesis: from scores to differentiated reconversion pathways

Two methodological observations should be highlighted before discussing transferability. First, the aggregate suitability index alone is not sufficient to determine the reconversion pathway. Industrial platforms (IIP) and partially restored sites (PRS) both score SI = 2.6 (high), yet the underlying criterion profiles are essentially complementary — the former is anchored in geotechnical stability and infrastructure (GS = 3, IA = 3, ES = 3), the latter in low environmental constraints (CR = 3, ES = 3, LC = 3). The same overall score therefore translates into completely different recommended uses (industrial / energy reuse vs. nature-based restoration).

Similarly, ash disposal sites (ADS) and spoil heaps (SH) share SI = 2,0 (moderate) but require very different interventions: in the ADS case, the contamination axis is the operationally decisive factor, while SH display a uniformly moderate profile across all five criteria, reflecting the co-occurrence of multiple constraints of comparable severity rather than a single dominant axis.

Despite the identical aggregate score, this distinction confirms that ecological restoration is the only SH pathway that does not require prior resolution of all constraint dimensions simultaneously.

Second, a brief sensitivity check confirms that the high- and low-suitability classes are robust under reasonable reweighting: doubling the weight of geotechnical stability further reinforces the position of industrial platforms (IIP) and widens the gap with underground mining zones (UMZ) but does not change the class of any group. Within the moderate band, the relative ranking remains stable, although the narrow margins suggest that differences between moderate-class groups should be interpreted with caution.

Taken together, the results show that post-mining land in the Pernik region cannot be addressed through a single land-use model. The coexistence of ash disposal sites, mining waste facilities, spoil heaps, former industrial platforms, underground mining zones and partially restored sites creates a highly heterogeneous post-mining landscape, where each site type requires a different combination of engineering stabilisation, environmental risk control and future land-use planning.

Comparative perspective with European post-mining regions

The Pernik coal basin cannot be interpreted through the same logic as the large post-mining regions of Germany, the Czech Republic and Poland (Vráblík et al., 2019; Deshaies, 2020; LMBV, 2020) – Table 4. Unlike Lusatia and North Bohemia, where extensive lignite open pits have enabled large-scale hydrological rehabilitation, Pernik represents a more fragmented and constrained post-mining landscape. Its legacy combines underground workings, smaller open-pit areas, spoil heaps, ash disposal sites and former industrial platforms, many of which are located close to urban and peri-urban areas. This spatial structure is not a minor contextual difference; it fundamentally limits the direct application of lake-based or large-scale landscape redevelopment models.

The European examples are therefore useful mainly as comparative references, not as ready-made solutions for Pernik. Cottbuser Ostsee in Lusatia and Lake Most and Medard in North Bohemia demonstrate the potential of controlled flooding and long-term hydrological rehabilitation where large residual pits and favourable hydrogeological conditions exist (Council of Ministers, n.d.; Vráblík et al., 2019; LMBV, 2020; Mandausová, 2021). By contrast, Góra Kamieńsk in the Bełchatów region is more relevant for assessing the reuse potential of stable spoil heaps for energy or recreational functions (PGE GiEK, 2022). The Ruhr examples, including Zollverein and Duisburg-Nord, are particularly instructive for Pernik because they show how former industrial areas near urban centres can be converted through adaptive reuse and cultural-landscape transformation (UNESCO, 2001; Deshaies, 2020).

Table 4. *Comparative interpretation of post-mining reconversion models based on selected European reference cases*

Reference region (country) / case	Dominant model	Key condition	Relevance for Pernik
Lusatia (Germany) /Cottbuser Ostsee	Pit lake and landscape recreation	Large open-pit voids, controlled flooding	Limited — applicable only where hydrogeology allows
North Bohemia (Czech Republic) / Lake Most, Medard	Hydrological rehabilitation and recreation	Large residual pits, long-term stabilisation	Partial — useful as reference, not direct model
Bełchatów region (Poland) / Góra Kamieńsk	Spoil heap reuse for energy / recreation	Stable elevated technogenic landform	Moderate — relevant for spoil heaps and stabilised landforms
Ruhr region (Germany) /Zollverein, Duisburg-Nord	Industrial heritage and urban reuse	Urban industrial platforms and infrastructure	Moderate — relevant for urban-adjacent platforms
Pernik (Bulgaria) — study area	Mixed site-specific reconversion	Fragmented mining legacy, urban proximity	Combines PV, NBS, industrial reuse and monitoring

Note: The comparison has to be used as an interpretative reference, not as a direct transfer model, because the Pernik basin differs in scale, landform structure, urban proximity and legacy underground mining constraints.

This comparison suggests that the main lesson for Pernik is not to replicate a single European model, but to match each post-mining site type with a technically realistic and context-sensitive reconversion pathway. Pit lake development should be considered only where hydrogeological and geotechnical conditions clearly allow it. Stabilised ash disposal sites are more defensible candidates for controlled photovoltaic use, provided that containment, cover layers and monitoring are ensured. Spoil heaps should be prioritised for ecological restoration or restricted-access functions unless slope stability is demonstrated. Former industrial platforms and infrastructure-related areas offer the strongest potential for industrial or energy-related reuse because they already benefit from accessibility, grid proximity and an established land-use context (World Bank, 2018; Pagouni et al., 2024).

In this sense, the Pernik basin requires a selective and hybrid reconversion strategy rather than the transfer of large-scale post-mining models developed elsewhere. Its future redevelopment should be driven by site-specific constraints, not by the visual or symbolic appeal of well-known European examples. Within this differentiated approach, two operational implications merit particular emphasis. Firstly, the European reference cases provide a clear decision logic for matching disturbance type with feasible reuse: hydrological reconversion is appropriate where water balance and pit geometry permit, renewable energy where terrain stability and access are sufficient, ecological restoration where contamination and construction suitability are limiting factors, and industrial or recreational reuse where existing infrastructure and urban proximity create functional advantages.

Secondly, the implementation of this logic in relation to ash disposal sites – the most probable candidates for photovoltaic reuse in the basin – necessitates the introduction of supplementary technical safeguards. These include the verification of bearing capacity and differential settlement risk, the management of wind erosion and ash dispersion during the construction phase, the installation of protective or sealing cover layers, and the judicious selection of foundation systems that minimise the disturbance of contaminated material. Consequently, the development of PV energy on such sites should be regarded as a regulated form of reuse rather than a conventional land-use conversion.

Conclusion

The study confirms that post-mining land in the Pernik region cannot be addressed through a uniform rehabilitation model. Its fragmented structure and varying levels of geotechnical, environmental and land-use constraints require a differentiated, site-specific reconversion strategy.

The most appropriate pathways include controlled photovoltaic use on stabilised ash disposal sites, ecological restoration of spoil heaps and partially rehabilitated areas, conditional reuse of mining waste facilities, and industrial or energy-related redevelopment of former infrastructure platforms. In contrast, underground mining zones affected by subsidence and hidden voids should remain subject to restricted use and long-term monitoring.

A central conclusion is that the aggregate suitability index is useful for screening, but insufficient as a stand-alone decision tool. Sites with similar scores may require different interventions depending on their criterion profile. Therefore, the proposed framework should be applied as a profile-based planning instrument that links site-specific constraints with feasible reconversion options and supports the sustainable transformation of coal regions under energy transition conditions.

References

Council of Ministers (n.d.). *National Concession Register. (in Bulgarian) Centralised electronic information system*. https://nkr.government.bg/ (accessed on 08.06.2026)

Deshaies, M. (2020). Metamorphosis of mining landscapes in the Lower Lusatian lignite basin (Germany): New uses and new image of a mining region. *Les Cahiers de la recherche architecturale urbaine et paysagère, 7.* doi:10.4000/craup.4018

Eastman, J. R., Weigen, J., Kyem, P. A. K., & Toledano, J. (1995). Raster procedures for multi-criteria/multi-objective decisions. *Photogrammetric Engineering and Remote Sensing 61*(5), pp. 539–547

European Commission. (2020). *Toolkits for coal regions in transition. Platform for Coal Regions in Transition,* Directorate-General for Energy. https://ec.europa.eu/newsroom/ener/items/678083

European Parliament and Council (2006). Directive 2006/21/EC on the management of waste from extractive industries. *Official Journal of the European Union, L102*, 15–34.

Executive Environment Agency (EEA). (n.d.). *Inventory of closed mining waste facilities, inactive mines and quarries as part of the National Environmental Monitoring System* (in Bulgarian): https://eea.government.bg/bg/nsmos/soil/opis-na-zakriti-saorazheniya-za-minni-otpadatsi.html

Global Industry Standard on Tailings Management (GISTM). (2020). *Global Industry Standard on Tailings Management.* United Nations Environment Programme (UNEP), International Council on Mining and Metals (ICMM) and Principles for Responsible Investment (PRI). https://globaltailingsreview.org/wp-content/uploads/2020/08/global-industry-standard-on-tailings-management.pdf

ICMM (2019). *Integrated mine closure: Good practice guide* (2nd ed.). https://hub.icmm. com/website/publications/ pdfs/environmental-stewardship/2019/guidance_ integrated-mine-closure.pdf

IGF (2022). Mine closure: *A toolbox for governments. Intergovernmental Forum on Mining, Minerals, Metals and Sustainable Development.* https://www.igfmining.org/ resource/

Kostadinova-Slaveva, A. G. (2026). *Harakteristika na minnite otpadatsi ot vagledobivnata promishlenost i tyahnoto ekologosobrazno upravlenie [Characteristics of mining waste from the coal mining industry and their environmentally sound management].* Publishing House at the University of Forestry, Sofia (in Bulgarian).

LMBV (2020). *Post-mining landscape development in Lusatia*. Lausitzer und Mitteldeutsche Bergbau-Verwaltungsgesellschaft mbH.

Malczewski, J. (2004). GIS-based land-use suitability analysis: A critical overview. *Progress in Planning, 62*(1), 3–65. DOI: https://doi.org/10.1016/j.progress.2003.09.002

Mandausová, K. (2021). Místo dolu jezero, hotel a rodinné domy. Sokolovská uhelná představuje svou vizi [Instead of a mine: a lake, a hotel and family houses. Sokolovská uhelná presents its vision]. *Forbes Česko,* 26 August 2021. https://forbes.cz/misto-dolu-jezero-hotel-a-rodinne-domy-sokolovska-uhelna-predstavuje-svou-vizi/.

Ministry of Energy. (2016). *The concession agreement for the "Gladno pole" mining area in Pernik will not be extended* (in Bulgarian). https://www.me.government.bg/bg/news/ koncesionniyat-dogovor-za-plosht-gladno-pole-v-grad-pernik-nyama-da-bade-udaljen-2231.html.

Ministry of Energy. (2026). *Register of active concessions for extraction of underground resources (updated as of 17.03.2026)* (in Bulgarian). https://www.me.government. bg/themes/koncesii-za-dobiv-735-1613.html

Ministry of Energy. (n.d.). *List of closed and abandoned mining waste facilities under Article 22m(5) of the Subsurface Resources Act* (1999, in Bulgarian). Available at: https://www.me.government.bg/bg/themes/spisak-na-zakritite-vklyuchitelno-i-naizostavenite-saorajeniya-za-minni-otpadaci-2158-0.html.

Ordinance No. 26 on the Reclamation of Disturbed Lands, Improvement of Low-Productivity Lands, and Removal and Utilization of the Humus Layer (State Gazette No. 89/1996, amended State Gazette No. 30/2002).

Ordinance on the Management of Mining Waste (State Gazette No. 5/2016, amended and supplemented in State Gazette No. 58/2019).

Pagouni, C., Pavloudakis, F., Kapageridis, I., & Yiannakou, A. (2024). Transitional and Post-Mining Land Uses: A Global Review of Regulatory Frameworks, Decision-Making Criteria, and Methods. *Land 13,* 1051. https://doi.org/10.3390/land13071051

Panayotov, K. (2024). *Rekultivatsiya na Sgurootval „Sedmi Septemvri": Otsenka i Preporaki [Rehabilitation of the "Sedmi Septemvri" Ash Disposal Site: Assessment and Recommendations].* Expert report. AgroVar SS Ltd. https://www.zazemiata.org/resources/rekultivatsiya-na-sgurootval-sedmi-septemvri/

PGE Górnictwo i Energetyka Konwencjonalna (PGE GiEK). (2022). *Integrated Report 2021.* Warsaw: PGE Polska Grupa Energetyczna S.A. https://raportzintegrowany2021.gkpge.pl/en/.

Prach, K., Řehounková, K., Lencová, K., Jírová, A., Konvalinková, P., Mudrák, O., Študent, V., Vaněček, Z., Tichý, L., Petřík, P., Šmilauer, P., & Pyšek, P. (2011). Vegetation succession in restoration of disturbed sites in Central Europe: The direction of succession and species richness across 19 series. *Applied Vegetation Science, 14*(2), 193–200. doi:10.1111/j.1654-109X.2010.01110.x

Regional Inspectorate of Environment and Water – Sofia (RIEW Sofia) (2021). *Decision No. SO-97-PR/2021 concerning investment proposal for technical closure and rehabilitation of "7th September" ash disposal site* (in Bulgarian).

Řehounková, K., & Prach, K. (2008). Spontaneous vegetation succession in gravel-sand pits: A potential for restoration. *Ecological Engineering, 33*(3–4), 305–312. doi:10.1016/j.ecoleng.2008.05.006

River Basin Directorate "West Aegean Region". (2024). *Opinion on an investment proposal for "Technical liquidation and mitigation of the adverse impacts from the cessation of coal mining activities within the city of Pernik – Zone II, Klepalo district".* 16.09.2024. (in Bulgarian). https:// wabd.bg/content/ wp-content/uploads/2024/09/%D0%9F-01-312-1.pdf

State Archives Agency. (2023). *Archival records on mining activities in the Pernik coal basin* (in Bulgarian). https://archives.government.bg/51

State Gazette. (2005). *Decision No. 242 of 5 April 2005 for granting concession for coal extraction* (in Bulgarian).

Subsurface Resources Act. (1999). *Subsurface Resources Act* (State Gazette No. 23/1999, last amended and supplemented in State Gazette No. 95/2025).

UNESCO. (2001). *Zollverein Coal Mine Industrial Complex in Essen.* UNESCO World Heritage Centre. https://whc.unesco.org/en/list/975/

Vráblík, P., Vráblíková, J., & Wildová, E. (2019). Hydrological Mine Reclamations in the Anthropogenically Affected Landscape of North Bohemia. In M. Zelenakova, J. Fialová, & A. M. Negm (Eds.), *Assessment and Protection of Water Resources in the Czech Republic* (pp. 203–223). Cham: Springer. https://doi.org/10.1007/978-3-030-18363-9_9

World Bank. (2018). *Managing Coal Mine Closure: Achieving a Just Transition for All.* Washington, DC: World Bank. https://openknowledge.worldbank.org/handle/10986/31020.

Sustainable Extraction and Processing of Raw Materials, 2026

INVESTIGATION OF FACTORS AFFECTING UAV-BASED MINE SURVEYING ACCURACY

Dmytro Polischuk[1], Andrii Panasiuk[1], Vasyl Mamrai[1,2]

[1] Zhytomyr Polytechnic State University, 10005 Zhytomyr; E-mail: kgt_pds@ztu.edu.ua, kgt_pav@ztu.edu.ua, vmamray@gmail.com
[2] Kütahya Dumlupınar University, 43100 Kütahya; E-mail: vmamray@gmail.com
Corresponding author: kgt_pav@ztu.edu.ua

ABSTRACT. The adoption of unmanned aerial vehicles (UAVs) for mine surveying has increased significantly within the extractive industry due to their high operational efficiency, superior measurement accuracy, and reduced susceptibility to human error. The primary application of UAV-based surveying is the volumetric estimation of mined-out spaces and stockpile measurement at mining enterprises. The aim of this study is to evaluate the effects of flight altitude and weather conditions on the accuracy of UAV-assisted mine surveying, and to determine the optimal operational parameters for its implementation.
The study was conducted at an amber deposit in the Korosten district. Surveying of the extracted rock mass was performed using a DJI Phantom 4 quadcopter at different flight altitudes under two meteorological conditions. Three repetitive measurements were carried out for each combination of parameters, yielding a total of 30 observations. The reference volume was obtained using a Sokkia 550RXL total station, with subsequent processing in Civil 3D, while UAV data were processed in Agisoft Metashape. The analysis demonstrated that all investigated survey configurations produce deviations within the permissible error tolerance for mine surveying operations. The key factors affecting UAV-based surveying accuracy were identified, and the optimal flight altitude and meteorological conditions were established. The objectivity of the images obtained and the automation of processing ensure high quality results when using UAVs.

Keywords: mine surveying, UAV, photogrammetry, flight altitude, survey accuracy.

Introduction

Currently, open-pit mining accounts for more than two-thirds of all mineral extraction worldwide. The widespread adoption of this method is attributed to a range of advantages inherent to surface mining compared to underground operations. As technological progress advances, the requirements for mine surveying support are increasing accordingly — in terms of productivity, accuracy, and data currency.

Mine surveying operations in open-pit conditions are carried out in strict compliance with established safety requirements for mining activities. The execution of surveying work must ensure the completeness and accuracy of measurements and calculations sufficient for the rational use and protection of mineral resources, as well as the safe conduct of mining operations. To meet these requirements, a continuously expanding and modernizing range of surveying instruments is being employed.

In accordance with the Instruction on Mine Surveying Operations (Ministry of Energy and Coal Industry, 2018) and DSTU-N B A.2.2 Geodetic and Mine Surveying Works, the total error in volume determination must not exceed ±3–5%, depending on the accuracy class and volume magnitude. Consequently, considerable attention has been directed toward methods that can achieve error rates of 2–3% while significantly reducing time expenditure, which is a highly relevant objective.

Specific mine surveying tasks correspond to specific instruments, methods, and procedures for their execution. To reduce labour intensity and time expenditure in mine surveying operations, combined and hybrid measurement methods are employed, using various mine surveying instruments simultaneously (Hassanalian et al., 2017).

Aerial photogrammetry is the most cost-effective and consequently the most widely adopted method for monitoring large areas. Unmanned aerial vehicle (UAV) technology has firmly established itself as a tool for solving engineering problems traditionally performed through ground-based geodetic measurements.

Instruments used in classical surveying methods have their own developmental trajectories, characterised by significant advances in structural features and functional diversity, which undoubtedly lead to more relevant and accurate results in the execution of mine surveying tasks. Any measurements — regardless of the method applied — inevitably contain errors, which are classified by nature into gross, systematic, and random errors, and by origin into instrumental, environmental, and personal (subjective) errors. When using classical geodetic instruments, the role of personal errors is more pronounced, as the specialist is directly involved in the measurement process at each stage.

In recent years, Ukraine has witnessed a rapid increase in UAV deployment at open-pit mining operations, particularly at amber, granite, sand, and iron ore deposits, where traditional surveying methods become inefficient due to large areas and complex terrain. According to expert estimates, the transition to aerial photogrammetric surveying reduces mine surveying costs by 30–60% and significantly improves personnel safety. However, the accuracy of such measurements is strongly dependent on external conditions — flight altitude, image overlap parameters, meteorological factors, and object illumination. For this reason, detailed experimental studies are necessary to determine the optimal UAV operating regimes under the actual conditions of Ukrainian quarries. Incidents arising during field operations will negatively impact office-based data processing and may even go unnoticed by specialists (Lee, et al., 2016).

Preventing errors during mine surveying can be achieved by automating all operational processes. It is logical to assume that reducing the specialist's involvement in the mine surveying process, or delegating their tasks to the measuring instrument, is directly proportional to the number of potential errors attributable to the human factor over a given time interval. Thus, by reducing time, potential surveying errors are eliminated.

Reduction of errors in the mine surveying process — specifically during office-based data processing — is achieved through software products that visibly and proactively flag potential deviations from the correctness of completed work (Jarahizadeh et al., 2024).

Taking the foregoing into account, the application of UAVs will reduce the probability of human-factor errors during mine surveying operations. It is precisely for this purpose that the present study investigates the factors influencing measurement error in surveys conducted with UAVs.

There is a growing demand for UAVs with diverse capabilities for both civilian and military applications. There is also significant interest in developing new drones capable of autonomous flight across varied environments and locations, and able to perform diverse missions. Over the past decade, a broad spectrum of applications for these drones has attracted the greatest attention, leading to the development of various drone types with different sizes and weights (Hassanalian et al., 2017).

Recent literature has devoted particular attention to the influence of illumination and cloud cover on photogrammetric quality. Studies demonstrate that under overcast conditions (illuminance < 40,000–50,000 lux), reprojection error increases by 30–50%, owing to reduced image contrast and the associated difficulty in automated keypoint detection (Arroyo-Mora et al., 2021; Burdziakowski, 2021). Under clear sky conditions with uniform illumination (≥ 90,000 lux), minimum error is achieved, whereas moving clouds or shadows may cause localised model distortions. These effects are particularly pronounced at open quarries with homogeneous granular surfaces, where loss of detail directly affects the accuracy of volume calculations (Kozuba et al., 2025).

Zapico et al. (2021) noted that conducting topographic surveys at active mining enterprises is a complex task due to the constant dynamic movement of material masses and the associated hazards. This substantiates one of the key advantages of UAVs — the ability to collect data remotely without personnel in hazardous zones.

Shahmoradi et al. (2020) conducted a series of studies on the feasibility of applying UAVs in the mining industry, focusing specifically on their use in underground mines (including variants for installing additional remote sensing equipment) and on their deployment for rescue missions.

Ren et al. (2019) drew attention during their research to the influence of external factors on the quality of UAV-based surveying.

UAV-based surveying, particularly using multi-rotor quadcopters, is increasingly in demand in the mining industry. This trend is driven by the growing need for operational efficiency, completeness, and measurement accuracy sufficient for the rational use and protection of mineral resources, the safe conduct of mining operations, and rational, forward-looking solutions in mine surveying support for open-pit mining. However, at this stage, there is no clear understanding of the influence of various factors on the quality of quadcopter-based surveys, nor of the measurement error under specific instrument operating conditions.

The absence of clearly standardised UAV surveying parameters in Ukrainian regulatory documents — particularly in the updated Instructions for Mine Surveying Operations — leads to inconsistent results across different enterprises. At the same time, the method's economic efficiency — a manifold reduction in survey time and lower personnel costs — makes it particularly attractive for medium- and small-sized quarries. Hence, a quantitative assessment of the influence of flight altitude and weather conditions on measurement error represents a key step towards transition from experimental applications to the systematic integration of UAVs into open-pit mine surveying practice.

Therefore, determining the measurement error under varying operational conditions is of considerable practical relevance, as it enables the optimization and adjustment of instrument performance.

Methods

The principal methods employed in this study include literature review, factorial analysis, and analysis of the influence of factors on measurement error during mine surveying operations.

During the research, numerous flight experiments were conducted; the uncontrolled factors and their qualitative condition values were selected artificially — the timing of experiments was chosen and adjusted to correspond to desired weather quality values. The properties of local climatic conditions, i.e., the uncontrolled factors — designated as such under the condition of unplanned execution of an engineering task at open-pit mining operations during a mine surveying measurement — directly include:

- the weather regime during the execution of the mine surveying flight;
- the time of day at the moment of flight execution (this parameter is of research interest with respect to the degree of illumination of the object being measured during data acquisition).

The present study was conducted at an amber extraction deposit in the Korosten district, Ukraine, during which the volume of extracted mining mass at the enterprise was measured using a DJI Phantom 4 quadcopter and a Sokkia 550RXL total station. Quadcopter measurements were performed at five altitudes, under both sunny and overcast conditions at each altitude. Three measurements were performed for each variant, yielding a total of 30. Flight planning was performed using DroneLink software with Grid Mission settings over the site boundary polygon. The principal mission parameters were as follows: flight altitude — 60, 80, 100, 120, and 140 m (AGL); forward overlap — 80%; side overlap — 70%; flight speed — 7–10 m/s; camera tilt angle — 90° (nadir); shutter trigger mode — distance-based (Distance interval); route orientation — along the longer side of the site; automatic return-to-home (RTH) — triggered at battery level below 20%.

Following the field operations, data processing was performed using Agisoft Metashape (for the DJI Phantom 4) and Civil 3D (for the Sokkia 550RXL), after which volume calculations were carried out and the obtained results were analysed (Pomortseva et al., 2022; Polishchuk et al., 2025). During the survey, three illuminance measurements were taken using a lux meter under each weather condition — sunny and overcast — at the moment of quadcopter take-off, during the survey itself, and following landing.

The selection of flight altitudes (60–140 m) is justified by typical recommendations for the DJI Phantom 4 in mining photogrammetry: at altitudes of 50–80 m, a GSD of approximately 1.5–3 cm/pixel is achieved, which is sufficient for detailed modelling of granular waste dumps; at altitudes exceeding 100 m, GSD increases to 4–6 cm/pixel, resulting in

loss of fine detail and increased volume calculation error (Nguyen et al., 2020). The 80/70% overlap was selected as a compromise between strip-matching quality and flight duration (to avoid excessive battery consumption) (Kozuba et al., 2025).

The number of ground control points (GCPs) — 8 to 10 — provides a reliable geodetic reference framework: according to published data, 6–12 points achieve a model accuracy of 2–5 cm in plan and 5–10 cm in elevation without RTK.

During flights, the camera axis was oriented vertically (90° to the surface), which is standard practice for mine surveying of areal extents. Data processing was carried out in Agisoft Metashape in several sequential stages. Stage 1 — Image Alignment (Align Photos): quality — High; tie method — Reference (based on GPS coordinates and GCPs); pair pre-selection — Generic preselection enabled; number of keypoints per image — 40,000; number of tie points — 4,000; adaptive camera model fitting — enabled. Stage 2 — Camera Optimisation (Optimise Cameras): performed following the marking of ground control points (GCPs); distortion parameters optimised — f, cx, cy, k1, k2, k3, p1, p2; tie quality criterion — reprojection error less than 1 pixel. Stage 3 — Dense Point Cloud Construction (Build Dense Cloud): quality — High; depth filtering method — Mild, selected in order to preserve surface details of granular waste dumps; point cloud classification — automatic (via Metashape tools). Stage 4 — Digital Elevation Model Construction (Build DEM): data source — dense point cloud; surface type — DSM (Digital Surface Model); resolution — corresponding to the GSD of each flight (from 1.5 to 6 cm/pixel depending on altitude); interpolation — enabled; export format — GeoTIFF. Volume calculations were performed relative to the baseline surface (terrain level prior to commencement of site operations), with validation using a reference total station model constructed from Sokkia 550RXL data in Civil 3D (Polishchuk et al., 2025).

Results

Aerial photogrammetry is highly relevant at present, as this methodology can be applied to monitor and audit extracted and stockpiled mineral resources. However, the method is equally applicable in other domains for determining the volume and mass of any bulk raw material or product. The question of UAV deployment is particularly pertinent for small-scale enterprises (Polishchuk et al., 2025).

A key criterion by which the effectiveness of UAV-based surveying is evaluated relative to conventional surveying methods is the measurement error introduced during data acquisition. When examining the nature of errors — not merely as a surveying concept inherent to every measurement by a given instrument, but also as an unintentional deviation from a true value — it is necessary to identify the source of error associated with the highest degree of unpredictability and randomness: the human factor. The interaction within the complex "human–technology" system is a widespread and unavoidable phenomenon, whose contribution is directly linked to the specialist's condition, individual characteristics, and other personal variables.

The influence of the human factor on the final result is reduced when measurements are performed with robotic total stations and laser scanning systems that use autonomous coordinate determination. Nevertheless, the other aforementioned random influencing factors remain applicable.

Systematic and random errors, including the human factor, are inherent to all devices that perform measurement and quantification functions. Quadcopters are no exception, and the classical measurement methods used in open-pit mining are accompanied by instruments already familiar to specialists.

The quadcopter, as part of UAV technology more broadly, and its application in mining, represent a relatively new field; consequently, the scientific community has only recently begun systematically studying quadcopters, acknowledging the undeniable interest in their use in geodesy and related disciplines.

Controlled factors — so termed due to the specialist's ability to modify their magnitude — include the following parameters affecting measurement error, directly related to the technical and functional capabilities of the surveying quadcopter:

- flight altitude;
- flight speed;
- longitudinal and lateral image overlap — a photogrammetric factor governing image acquisition and inter-image connectivity (stereopairs), related to the functionality of the camera integrated into the quadcopter as an inseparable component of the entire surveying measurement process;
- number of ground control points — a controllable factor expressed as the numerical quantity of reference markers with defined coordinates, exerting a significant influence on the configuration of all photogrammetric derivatives of the mine survey.

Uncontrolled factors affecting the error of a quadcopter mine surveying flight, and consequently the final measurement value, are environmental parameters, specifically the weather conditions prevailing at the time of measurement.

To evaluate measurement error in UAV-based surveying, the volume of the mined area of the deposit was measured and calculated, as illustrated in Figure 1.

Surveying of the mined mass was carried out at flight altitudes of 60, 80, 100, 120, and 140 m under both sunny and overcast conditions, using the DJI Phantom 4 quadcopter and the Sokkia 550RXL total station. Three illuminance measurements were taken with a lux meter for each weather condition, yielding the following results: 101,000, 99,000, and 102,000 lux (sunny conditions); and 32,000, 34,000, and 31,000 lux (overcast conditions).

To assess the influence of these parameters on surveying accuracy, the obtained results were compared against the reference values presented in Table 1.

Based on the results presented in Table 1, the deviations (%) from the reference value were calculated and are presented in Table 2.

The results presented in Table 2 indicate that all experimental variants yield deviations below the permissible error threshold established for mine surveying operations. Based on the data in Table 2, a comparative analysis by flight altitude was performed, the results of which are illustrated in Figures 2 and 3. Based on the data presented in Figures 2 and 3, it can be concluded that the minimum error is observed at flight altitudes of 60 and 80 m under any weather condition, while an increase in altitude to 100 m results in a substantial growth of measurement error. Taking this into account, it is recommended that surveying be conducted at flight altitudes of 60–80 m.

Based on the results of Table 2, the mean error values were calculated for each flight altitude variant; these are presented in Table 3.



Fig. 1. Boundary contour of the study area

Table 1. *Comparison of obtained results for mined mass volume calculation*

Weather condition	Volume, m³					
	Flight altitude, m					Civil 3D (total station survey)
	60	80	100	120	140	
Sunny	6477	6515	6691	6743	6854	6350
	6462	6524	6713	6682	6792	
	6453	6534	6708	6831	6824	
Overcast	6512	6535	6914	6984	7084	
	6534	6548	7001	6991	7091	
	6610	6539	6905	6999	7053	

Table 2. *Deviations from the reference value*

Weather condition	Deviation, %				
	Flight altitude, m				
	60	80	100	120	140
Sunny	2.0	2.6	5.4	6.2	7.9
	1.8	2.7	5.7	5.2	7.0
	1.6	2.9	5.6	7.6	7.5
Overcast	2.6	2.9	8.9	10.0	11.6
	2.9	3.1	10.3	10.1	11.7
	4.1	3.0	8.7	10.2	11.1

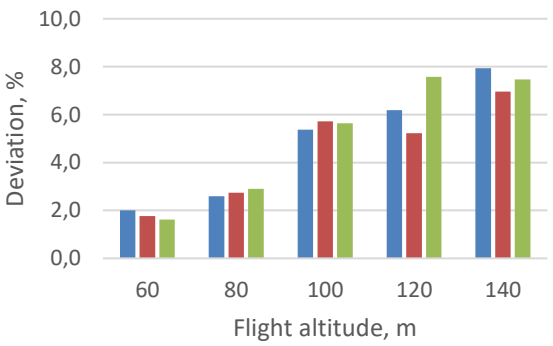


Fig. 2. Comparison of measurement errors under sunny weather conditions

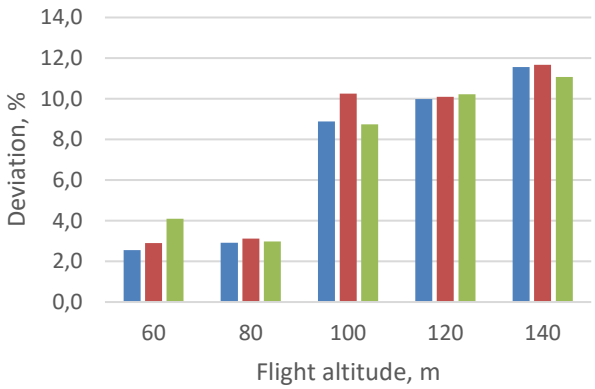


Fig. 3. Comparison of measurement errors under overcast weather conditions

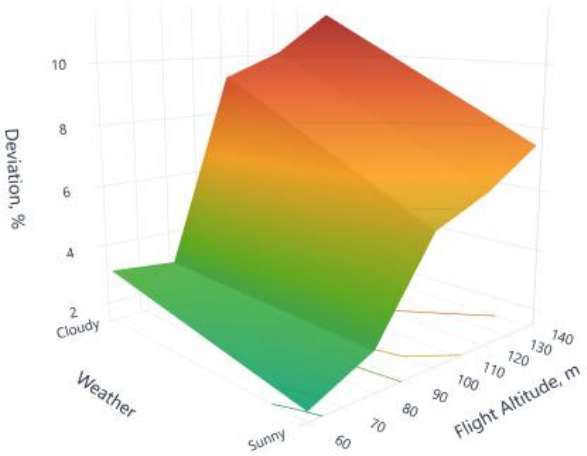


Fig. 4. 3D surface of mean deviations under varying meteorological conditions and flight altitudes

The 3D surface in Figure 4 illustrates the mean volume deviation from the reference value as a function of UAV flight altitude (X-axis, m) and weather regime (sunny/overcast). The colour scale represents the magnitude of error as a percentage, from a minimum of 1.8% (altitude 60 m, sunny conditions) to a maximum of 11.4% (altitude 140 m, overcast conditions). The surface clearly demonstrates the non-linear increase in error with increasing altitude, as well as the substantial influence of cloud cover on photogrammetric surveying accuracy.

Based on the data presented in Table 3, a graph was constructed - Figure 5.

As illustrated in Figure 5, the relationship between mean error and flight altitude exhibits a non-linear character and is substantially dependent on weather conditions.

The minimum error values (1.8% under sunny conditions and 3.0–3.2% under overcast conditions) are observed at altitudes of 60 m and 80 m. Within this range, the error remains within or close to the normatively permissible threshold (±3%).

From 100 m altitude onward, the error increases sharply: under sunny conditions it reaches 5.6%, while under overcast conditions it rises to 9.3%. At altitudes of 120 m and 140 m, the error exceeds 6–7% under clear-sky conditions and 10–11.4% under overcast conditions, rendering such flight modes unsuitable for accurate mine surveying volume calculations.

Table 3. *Mean error values for the determination of extracted mining mass volume as a function of UAV flight altitude and meteorological conditions*

Weather condition	Deviation, %				
	Flight altitude, m				
	60	80	100	120	140
Sunny	1.8	2.7	5.6	6.3	7.5
Overcast	3.2	3.0	9.3	10.1	11.4
Difference (Overcast – Sunny), %	+1.4	+0.3	+3.7	+3.8	+3.9

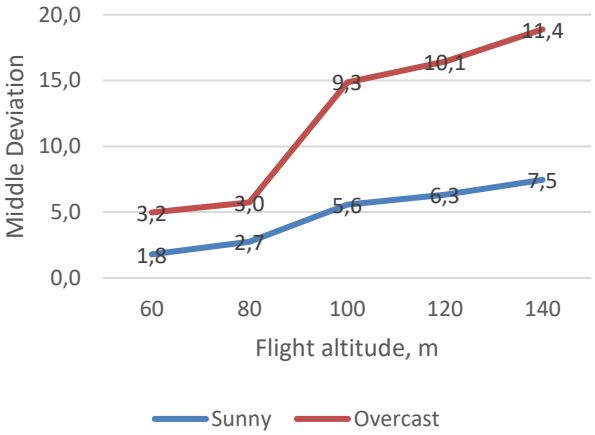


Fig. 5. Relationship between mean volumetric determination error and UAV flight altitude under varying meteorological conditions

The difference between sunny and overcast conditions is most pronounced at altitudes above 100 m (3.7–3.9%), which indicates a significant adverse effect of reduced illuminance on the quality of photogrammetric reconstruction — manifested as decreased texture contrast, difficulties in automated keypoint matching, and increased image stitching error.

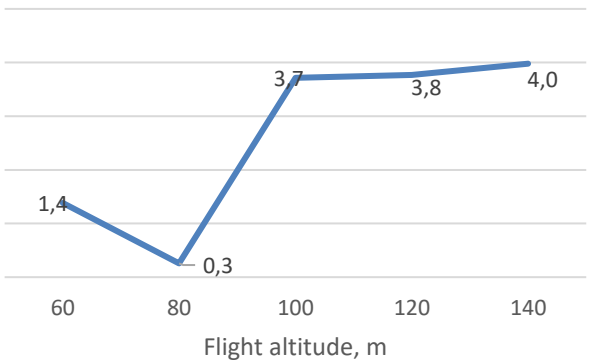


Fig. 6. Difference in measurement errors at various UAV flight altitudes as a function of meteorological conditions

Analysis of Figure 6 demonstrates that overcast weather conditions have virtually no effect on survey accuracy at flight altitudes of 60–80 m (a delta of 0.3–1.4%). However, at an altitude of 100 m the difference already reaches 3.7%, while at 120–140 m it consistently amounts to approximately 3.8–3.9%. It should be noted that the difference in deviations between overcast and sunny conditions is exclusively positive (overcast weather yields greater error) across all investigated flight altitudes. This is attributable to the physical nature of illuminance effects on the photogrammetric process: low illuminance (32,000–34,000 lux under overcast conditions versus 99,000–102,000 lux under sunny conditions) reduces surface texture contrast. It impedes automated keypoint detection during image alignment, thereby systematically increasing error regardless of flight altitude (Hajjaret al., 2025).

Conclusion

The present study accounted for both UAV flight altitude (60, 80, 100, 120, and 140 m AGL) and specific meteorological conditions — sunny weather with illuminance of 99,000–102,000 lux and overcast weather with illuminance of 31,000–34,000 lux. It was established that the combined effect of these two parameters determines the final measurement error: at altitudes of 60–80 m, the difference between weather regimes does not exceed 1.4%, whereas at altitudes above 100 m it increases to 3.7–3.9%, which confirms that meteorological conditions cannot be considered independently of flight altitude. Accordingly, for practical application it is recommended that mine surveying using UAVs be conducted at altitudes of 60–80 m under sunny conditions (illuminance no less than 90,000 lux), which ensures minimum volume determination error — within the range of 1.6–2.9% — and complies with the normative accuracy requirements for mine surveying operations. The assessment of the influence of flight altitude and meteorological conditions (in particular, illuminance level) on volume measurement error represents a step towards transitioning from experimental application to the systematic implementation of UAV technology in the mine surveying practice of open-pit operations, as well as towards updating the Instructions for Mine Surveying Operations in Ukraine.

The results of the present study are broadly consistent with the findings of Arroyo-Mora et al. (2021), Szypuła (2024) and Kozuba, et al. (2025): a reduction in illuminance under overcast conditions substantially increases volume determination error, particularly at altitudes exceeding 100 m. At the same time, the data obtained allow for refining existing models. At an altitude of 80 m, the difference in errors between sunny and overcast conditions was only 0.3%, the minimum among all investigated altitudes. This indicates that the influence of meteorological conditions on survey accuracy cannot be considered in isolation from flight altitude — it is their combined effect that determines the final measurement error. Thus, the results of the study validate existing models for conditions characteristic of open quarries with homogeneous granular surfaces, while also identifying flight altitude as a key modifier of the effect of illuminance on survey accuracy.

References

Arroyo-Mora, J. P., Kalacska, M., Løke, T., Schläpfer, D., Coops, N. C., Lucanus, O., & Leblanc, G. (2021). Assessing the impact of illumination on UAV pushbroom hyperspectral imagery collected under various cloud cover conditions. *Remote Sensing of Environment, 261,* 112480. https://doi.org/10.1016/j.rse.2021.112396

Burdziakowski, P. (2021). UAV photogrammetry under poor lighting conditions — Accuracy considerations. *Sensors, 21*(10), 3531. https://doi.org/10.3390/s21103531

Hajjar, M., Zappa, E., & Bolzon, G. (2025). The state of the art and potentialities of UAV-based 3D measurement solutions in the monitoring and fault diagnosis of quasi-brittle structures. *Sensors, 25*(16), 5134. https://doi.org/10.3390/s25165134

Hassanalian, M., & Abdelkefi, A. (2017). Classifications, applications, and design challenges of drones: A review. *Progress in Aerospace Sciences, 91,* 99–131. https://doi.org/10.1016/j.paerosci.2017.04.003

Jarahizadeh, S., & Salehi, B. (2024). A comparative analysis of UAV photogrammetric software performance for forest 3D modelling: A case study using AgiSoft Photoscan, PIX4DMapper, and DJI Terra. *Sensors, 24*(1), 286. https://doi.org/10.3390/s24010286

Kozuba, J., Marcisz, M., & Maliszewski, Ł. (2025). Influence of cloud cover and light intensity on the quality of photographic material obtained during nadir photogrammetric flights. *Transport Problems, 20*(1), 47–58. https://doi.org/10.20858/tp.2025.20.1.04

Lee, S., & Choi, Y. (2016). Reviews of unmanned aerial vehicle (drone) technology trends and its applications in the mining industry. *Geosystem Engineering, 19*(4), 197–204. https://doi.org/10.1080/12269328.2016.1162115

Ministry of Energy and Coal Industry (2018) Order No. 604, Ukraine.

Nguyen, Q. L., Goyal, R., Bui, K. L., Le, V. C., Cao, X. C., Pham, V. C., Bui, N. Q., & Bui, X.-N. (2020). Influence of flight height on the accuracy of UAV-derived digital elevation model at complex terrain. *Inżynieria Mineralna, 1,* 101–127. https://doi.org/10.29227/IM-2020-01-27

Polishchuk, D. S., Panasyuk, A. V., & Kalchuk, S. V. (2025). Optymizatsiia marshrutiv polotiv pry obrobtsi danykh za dopomohoiu prohramnoho zabezpechennia Agisoft Metashape [Optimisation of flight routes in data processing using Agisoft Metashape software]. *Tekhnichna Inzheneriia, 1*(95), 206–211. https://doi.org/10.26642/ten-2025-1(95)-206-211

Pomortseva, O., Kobzan, S., & Steshenko, P. (2022). Processing of geodesic data obtained with the help of UAVs. *Collection of Scientific Papers ΛΌГОΣ,* 162–165. https://doi.org/10.36074/logos-16.09.2022.47

Ren, H., Zhao, Y., Xiao, W., & Hu, Z. (2019). A review of UAV monitoring in mining areas: Current status and future perspectives. *International Journal of Coal Science & Technology, 6*(3), 320–333. https://doi.org/10.1007/s40789-019-00264-5

Shahmoradi, J., Talebi, E., Roghanchi, P., & Hassanalian, M. (2020). A comprehensive review of applications of drone technology in the mining industry. *Drones, 4*(3), 34. https://doi.org/10.3390/drones4030034

Szypuła, B. (2024). Accuracy of UAV-based DEMs without ground control points. *GeoInformatica, 28,* 1–28. https://doi.org/10.1007/s10707-023-00498-1

Zapico, I., Laronne, J. B., Sánchez Castillo, L., & Martín Duque, J. F. (2021). Improvement of workflow for topographic surveys in long highwalls of open pit mines with an unmanned aerial vehicle and structure from motion. *Remote Sensing, 13*(17), 3353. https://doi.org/10.3390/rs13173353

Sustainable Extraction and Processing of Raw Materials, 2026

INTENSIFICATION OF THE PROCESS OF BENEFICIATION OF MINERALS BY VIBRATION-IMPACT ACTIVATION

O. Yu. Svietkina, O. V. Fedoskina

Dnipro University of Technology, Dnipro, Ukraine
Emails: svietkina.o.y@nmu.one, fedoskina.ev@gmail.com
Corresponding author: svietkina.o.y@nmu.one

ABSTRACT. Experimental data are presented on the use of vertical vibrating mills (MVV) for the preparation of mineral feedstock for the beneficiation process. The influence of optimising the vibro-impact loading process on the parameters of the mineral beneficiation process is examined. Galena (PbS) was selected as the experimental sample. This is because the surface energy characteristics of PbS depend on the number and nature of defects in the crystal lattice, which is a key feature of material activation in MVV. The relationship between the degree of liberation (f) and the technological parameters of grinding in the vibro-mill (vibro-impact loading dose (D) and collision velocity (V_{imp})) is demonstrated. It has been found that even a slight change in the interplanar distances between atoms in the crystal lattice and the presence of a small number of impurity atoms of a foreign element significantly affect the chemical and adsorption activity of this mineral particle with respect to the components of the pulp's liquid phase and, ultimately, — the flotation activity.

Key words: *mechanochemistry, beneficiation, vertical vibrating mill, galena*

Introduction and theoretical background

When preparing ores for beneficiation, various types of grinding and classification equipment are used to break up the mineral grains. Broadly speaking, ore comminution is divided into batch processes carried out in crushing machines and continuous processes in grinding units.

In practice, the disintegration of mineral raw materials is carried out in machines using various crushing principles, with ball mills being the most commonly used.

The technological and chemical stages involved in preparing ore for processing are determined by factors such as particle size and shape, the presence of impurities, and defects in the crystal structure.

Until recently, the selection of grinding equipment was carried out using F. Bond's method, which is based on determining the grinding of material using the work index W_i (Bond, 1961). The Bond grinding index is the specific energy (in kilowatt-hours per metric tonne) required to grind material from an infinite particle size down to a specific fraction, 80% of which passes through a 100-micron sieve (Stamboliadis et al., 2011). W_i is a mathematical indicator of the hardness and grindability of a specific ore or rock – equation (1):

$$W_i = 44{,}5/a^{0,23} q_n^{0,820}\, 10\left(1/\sqrt{P} - 1/\sqrt{F}\right), \qquad (1)$$

where a is the mesh size of the sieve used to separate the final product, in μm; q_n is the quantity of the newly formed product «-a» per drum revolution, in kilograms per revolution; F and P are the 80% particle sizes of the feedstock and the final product, respectively, in μm.

This index serves as an industry standard for calculating the energy required to grind materials in the mining and cement industries (Malyarov et al., 2008).

Its calculation is based on the «size-energy» relationship

$$e_{1,2} = C\left(\frac{1}{x_2^n} - \frac{1}{x_1^n}\right), \qquad (2)$$

where n = 0.5, $x_1 = \infty$ and $x_2 = 100$, C is a constant, $e_{1,2}$ is the specific energy required to grind a particulate material from initial size x_1 to final size x_2.

By definition

$$e_{\infty,100} = W_i \qquad (3)$$

and, as a result,

$$C = 10W_i. \qquad (4)$$

In theory, for any material ground in a mill, the value of W_i found should be constant regardless of the measured dimensions x_1 and x_2 used to calculate the constant C by measuring the energy $e_{1,2}$. In practice, this is not the case because $n \neq 0.5$, and so a number of correction factors have been proposed to overcome this inaccuracy arising from assuming n = 0.5. Stamboliadis et al. (2011) proposed a simple method for calculating n using conventional grinding methods. The same calculation can be used to determine the true value of W_i and to define the potential energy state of the material at any size.

It is well known that grinding mills are characterised by low energy efficiency. This is because the energy required to create new surfaces accounts for less than 1% of the electricity consumed by ball mills. The remaining 99% is presumably dissipated as noise, vibration and heat; it is also possible that energy is lost to the atmosphere or used to heat the pulp. Bouchard et al., (2017) present the results of a study aimed, on the one hand, at characterising energy outputs in industrial grinding plants and, on the other, at identifying the potential for energy recovery from grinding plants. Agnico-Eagle Goldex Division, the Canadian Malartic mine and the New Gold New Afton mine participated in the studies. The results showed that, on average, 79% of the supplied electrical energy is converted into heat absorbed by the pulp, 8% is lost through the drive system, and around 2% of the energy is transferred to the surrounding air. The analysis showed that 91% of the energy consumed is lost as heat. The authors suggested that energy could be recovered using appropriate technologies or integrated

energy management systems; however, this topic requires further study.

To date, sufficient experience has been gained worldwide in the operation of various types of disintegration equipment in mineral processing, and this is taken into account in the design of crushing machinery.

One of the main indicators of grinding efficiency in ball mills is the specific throughput q_d (t/(m³·h)) for the newly formed nominal particle size class (– d):

$$q_d = (Q/V)(\beta_d - \alpha_d) = q_o \Delta\beta_d = q_o{}^{+}\Delta\beta, \qquad (5)$$

where q_d is the specific capacity of the mill or grinding plant for the newly formed design particle size class d, t/(m³·h); Q is the mill capacity based on the feed rate, t/h; V is the working volume of the mill or mills in the grinding plant, m³; q_0 – specific load based on the feed material (feed rate of fresh feed material per unit volume of the mill), t/(m³·h); $q_0{}^{+} = q_0 (1 – \alpha_d)$ – specific load for the coarse fraction (+d) in the feed material, t/(m³·h); $\Delta\beta = \beta_d – \alpha_d$ – increase in the content of the design particle size class, in units; β_d – relative proportion of the design particle size class in the ground products, in units; α_d – the same in the feed (Malyarov et al., 2012).

The q_d index presented above is a technical parameter that merely assesses the formation of the target particle size class and is not related to energy consumption. Furthermore, it does not take into account the formation of other, larger particle size classes that appear simultaneously with it. A very important characteristic of the grinding process is the grinding energy efficiency e_d for the newly formed particle size class (-d):

$$e_d = Q(\beta_d - \alpha_d)/N = q_d V/N = q_d/N_V, \qquad (6)$$

where e_d is the energy efficiency of grinding, tonnes/(kWh); N is the total power consumed by the mill's motor (kW), N_v is the specific power consumption of the mill motor, kW/m³.

A research article (Wentao et al., 2020) focuses on predicting particle size during grinding, which is an effective method for optimising the grinding process. Cassiterite polymetallic sulphide ore and lead-zinc ore were selected as the subjects of the study. The authors investigated the mechanism for predicting particle size based on the falling weight method and experimental data on batch grinding, taking into account the theory law of media motion in a ball mill and the population balance model. The results obtained show that the particle size distribution of the ground products at various energies and ore particle sizes was determined using the falling-weight method, whilst the grinding parameters ~~A~~ and ~~b~~ were calculated using a regression approximation method. A correlation was then established between the data from the falling-weight experiments. It was found that this correlation can also be applied to the correlation obtained for grinding products during media movement in a ball mill. This allows the tasks of determining the grinding function and the classification function to be solved effectively using MATLAB computing platform. The reliability of applying the particle size prediction model during grinding has been demonstrated. All the results obtained have been confirmed by experiments on periodic grinding.

In the paper of Kondratets et al. (2019), an equation was derived analytically that links the operational parameters of the ball mill and the material being ground to the parameters of the primary rod mill, which determine the energy efficiency of ore grinding.

A mathematical model has been analytically derived for energy-efficient ore grinding in a ball mill with three-phase movement of the grinding media, which remains invariant to changes in the length of the grinding media due to wear. The model enables the energy efficiency of grinding large ore chunks to be assessed on the basis of the volume of ground material obtained. The mathematical model includes such constant parameters as the cross-sectional areas of the rod-type primary transducers, the initial length of the rod-type primary transducers, the length of the base section where the strain gauges are located, the Young's modulus of the material of the primary transducers, as well as variable constants determined by the material being ground. Furthermore, a relationship for determining the length of the main rod-type primary transducer has been derived analytically, on the basis of which the height can be estimated.

Research (Ma et al. 2022 a), which focused on polymetallic complex ores from Tongken and Gaofen, revealed that the particle size of the ground products significantly influences the technical and economic performance of subsequent separation operations. Tests were conducted using the JK falling-weight method, periodic grinding, and a kinetic population balance model of grinding on the Simulink platform. The grinding characteristics of the two ore types and methods for predicting the particle size of the ground products were investigated. The results showed that the impact crushability of the ores from Tongken and Gaofen corresponds to 'medium' and 'soft' degrees, respectively. To improve the accuracy of the methods used in the study, the PSO–BP method was proposed, which offers high prediction accuracy and high model processing speed; however, it should be noted that the accuracy and speed of the iterative results depend on parameters such as the threshold value. The process of solving parametric problems for each forecasting method is based on various simplifications and assumptions. Therefore, for practical application, appropriate hypothetical theoretical models should be selected depending on the properties of the ore.

In another study of the same research group (Ma et al. 2022, b), again the Tongkeng and Gaofeng polymetallic complex ores were used as the subjects of investigation, and the effects of grinding patterns were examined using a single-factor experiment, whilst the grinding parameters were optimised using the response surface method for the two ore types. The results show that grinding time is a significant factor influencing particle size distribution. The optimal grinding concentration for Tongken and Gaofeng ores is 70% and 75%, respectively. The effect of the mill loading ratio on the Gaofeng ore is negligible. Rotational speed has a negligible effect on the technical efficiency of grinding. The regression model equations obtained using the response surface method are highly significant, and the relative prediction errors are within 1%, indicating the high reliability of the approximation equations. Optimal grinding conditions were determined for the ores: for Tongkeng ore, a grinding time of 5.4 minutes, a grinding concentration of 67% and a filling ratio of 35%; and for Gaofeng ore, a grinding time of 3.8 minutes, a grinding concentration of 73% and a filling ratio of 34%.

Fine grinding in a ball mill equipped with an agitator, which on the one hand improves ore liberation but on the other is associated with high energy consumption, is examined by Elbendari et al. (2025). According to the authors, energy consumption can be minimised by optimising operating conditions. This study investigated the influence of key

operating parameters, such as grinding time, agitator tip rotation speed, solid phase concentration and feed size, on grinding efficiency. Grinding efficiency was assessed based on specific energy consumption during the grinding of Egyptian copper ore in a mixer mill. Experimental data showed a linear correlation between the natural logarithm of the cumulative retained fraction and particle size (μm). As a result of the research, a model was proposed that accurately describes the particle size distribution (PSD) at various solid concentrations and grinding durations.

On the other hand, mechanochemical transformations occur during the grinding of materials. The dynamics of mechanochemical transformations are expressed by the relationship between the formation of a particular product and the excitation dose. Under real-world conditions, a dependence on the duration of mechanochemical treatment is most commonly observed. The activation dose (*D*) is determined by the formula (Butyagin et al., 1986):

$$D = N_v \cdot t \tag{7}$$

where *D* is the dose of vibro-impact excitation, N_v is the specific power consumed by the mill motor, kW/m³; t is the processing time, s.

The relationship between the vibro-impact activation of the material and the energy yield is determined using the formula:

$$G = W / N_v \tag{8}$$

where *G* is the energy output, mol/MJ; *W* is the specific reaction rate per unit mass of the material being ground, mol/(kg·s); N_v is the specific power density, representing the amount of mechanical power supplied per unit mass of the material being processed. In this system of units, N_v has the dimension MJ/(kg·s) (which is equivalent to MW/kg). If power is measured in the more familiar units of W/kg, a factor of 10^{-6} is usually introduced into the formula to convert to MJ.

It has been confirmed that mechanical activation of aluminium oxide – the grinding of material (Andrić et al., 1999) – alters the size and structure of its particles; this results in an increase in the system's potential energy, as well as in the material's chemical activity, due to an increase in surface area and the concentration of crystal lattice defects. Studies show that the properties of the processed materials change. Control of the mechanical activation process and the properties of activated materials is utilised in various technologies (sintering, chemical synthesis, hydrometallurgy, etc.).

Mañosa J. et al. (2024) investigated the mechanical activation of kaolin as a supplementary cementitious material with the aim of optimising grinding parameters using the response surface methodology. The study employed the Ritveld method to assess the influence of rotation speed and grinding time on the amorphous phase content, the reduction of crystalline kaolinite, and the incorporation of impurities into the activated clay. The results showed that regulating the grinding parameters effectively enhances the activation of the clay, allowing its use in low-carbon cements.

An article (Vugrin et al., 2023) discusses the optimisation of mechanochemical reactions through the energy generated by inelastic collisions between balls in a mill; it was found that chemical transformations occur during the grinding of the reaction mixture. The motion of the grinding media leads to physical mixing of the reactants, resulting in a chemical reaction. It was found that the energy input increases with the mass of the ball, its average velocity and the frequency of impacts, but decreases with the hardness of the grinding media due to more elastic collisions.

A study investigated the synthesis and filling of crystallographic sites in $MgAl_2O_4$ - with and without mechanochemical activation (Corlett et al., 2022). Without mechanochemical activation, heating to 1200 °C and above leads to the formation of a single spinel phase, regardless of whether the powders were mechanically activated or not. Neutron diffraction analysis was used to determine the filling of cation sites and showed that mechanical activation leads to a lower degree of cation site inversion compared to non-activated materials, indicating that the powders were closer to thermodynamic equilibrium. This is the first study in which neutron diffraction has been used to characterise the effect of mechanical activation on the filling of crystallographic sites in magnesium-aluminium spinel.

A number of studies (Bakil et al., 2025, Loudari et al., 2025, Korkmaz and Kayıran, 2025) have focused on improving the efficiency of grinding processes whilst reducing energy consumption. Őze et al. (2023) investigated the influence of various grinding parameters (ball-to-powder ratio (BPR), material of grinding media and grinding chambers, rotation speed and mill type) on minimising energy consumption during the mechanochemical activation of kaolinite. X-ray diffraction, Fourier-transform infrared spectroscopy, inductively coupled plasma optical emission spectroscopy, scanning electron microscopy and specific surface area measurements were used to investigate the influence of grinding parameters. It was found that the addition of just 25% (by mass) of trass reduces the specific energy requirement for complete amorphisation of kaolinite by 56%. The use of steel grinding media (instead of ZrO_2 media) had a negligible effect on the kinetics of kaolinite amorphisation, but allowed 30% more samples to be mechanochemically activated at the same BPR ratio and specific energy requirement. The use of four-chamber grinding instead of single-chamber grinding significantly reduced the specific energy requirement for complete and incomplete (α = 0.9) amorphisation of kaolinite. Overall, using steel grinding media, a BPR ratio of 14:1, four-chamber grinding and incomplete amorphisation of kaolinite, it was possible to reduce the specific energy requirement by 94%.

Shan et al. (2022) used measurements of specific surface area (using the BET method), X-ray diffraction (XRD), scanning electron microscopy (SEM), energy-dispersive X-ray analysis (EDX) and laser particle size analysis to investigate the mechanism of mechanical activation of titanium-containing domain slag. The results showed that the specific surface area of the slag increases upon activation compared to the unactivated sample. A decrease in the intensity of the diffraction peaks corresponding to perovskite ($CaTiO_3$) is observed, which is mainly due to an increase in lattice distortion and a decrease in the unit cell volume. With an increase in the mass ratio of the beads to the mass of the material, the mechanical activation time and the rotation speed during mechanical activation, the activated titanium-containing blast furnace slag underwent intensive agglomeration and sintering. Based on the results obtained, the authors concluded that the optimal parameters for the mechanical activation process are a ball-to-material mass ratio of 20:1, an activation time of 170 min and a rotation speed during activation of 400 rpm, respectively.

It is well known that higher grinding speeds and greater powder fineness are achieved in mills with higher ball energy – namely, vibratory and planetary mills.

In global practice, the most widely used design is that of a vibrating mill with a horizontally positioned grinding chamber and an inertial vibrator, the housing of which performs oscillatory movements along a trajectory close to a circular one. In this case, the material is ground as a result of impact and abrasion, with the grinding media acting on the surface layers of the particles.

For many years, research has been conducted at the Dnipro University of Technology into the mechanochemical activation of solids under vibro-impact loading in a vertical vibratory mill (MVV). A distinctive feature of these mills compared to other types is that the grinding chambers perform oscillatory movements along a straight-line trajectory in a vertical plane. Such parameters ensure a predominantly vibro-impact effect on the material being ground, with the deformation zone penetrating the entire volume of the particle. Ball wear is minimal and occurs uniformly across the entire surface, whilst maintaining the spherical shape. This means that, in many cases, there is no need to use surfactants (Franchuk, 2010).

The process parameters for the dispersion of various materials were presented by Svetkina (2008). It has been experimentally demonstrated that the grinding process of ore and non-ore materials can be optimised using process parameters (the size of the process gap in the grinding chamber between the upper layer of grinding media and its cover (in static conditions), and the maximum collision velocity of the grinding media). It was found that grinding results in a directed change in physicochemical properties.

In view of the above, the use of a vibro-impact mill would be appropriate for flotation processes, in which the interaction of reagents with activated minerals is crucial.

Therefore, the aim of this study was to determine the relationship between the degree of liberation (*f*) and changes in the technological parameters of the vibro-impact mill.

Methods and materials

The experimental study was conducted on a laboratory prototype of MVV with a rigid eccentric drive, the schematic of which is shown in Figure 1.

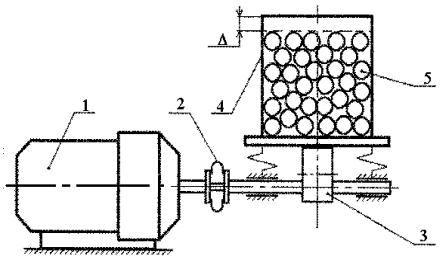


Fig. 1. Experimental setup diagram:
1 – electric motor; 2 – coupling; 3 – rigid eccentric vibration exciter; 4 – grinding chamber; 5 – grinding media

Electric motor 1 transmits rotation to vibration exciter 3 via petal clutch 2. This exciter imparts harmonic oscillations along the vertical axis to grinding chamber 4. The chamber oscillation amplitude (*a*) was 0.007 m, and the frequency (ω) was 16 Hz. The gap size Δ in the grinding chamber between the upper layer of grinding media 5 and its cover (in static conditions) was selected experimentally and was such that, at the specified oscillation parameters, it ensured, according to calculations (Anciferov et al., 2011) the maximum impact velocity and intensity of interaction between the grinding media and the grinding chamber. The computational model represents the process feed (grinding media), which is treated as a reduced unit mass interacting with the grinding chamber housing, without taking into account the impact time. The authors include dimensionless load coordinates in the mathematical models, as well as the clearance ratio between the grinding media and the chamber cover, and the maximum collision velocity (V_{imp}, m/s) and intensity of interaction between the grinding media and the grinding chamber. V_{imp} was calculated using the following formula:

$$V_{imp} = a \cdot \omega + \sqrt{2g\Delta}\,, \tag{9}$$

where *a* is the amplitude, m, ω – is the angular frequency, Hz, *g*=9.81 m/s^2, Δ is the gap in the grinding chamber between the upper layer of grinding media, mm.

Based on the experimental data, the starting point was chosen to be the technological gap Δ in the grinding chamber between the upper layer of grinding media and its cover (in static conditions) equal to $2.5 \cdot 10^{-2}$ m.

Therefore, experiments were conducted at various gaps (Δ). The process gap was varied by increasing or decreasing the volume of the grinding media. The dependences on changes in Δ are shown in Table 1.

Table 1 presents the process gap values established during vibro-impact activation of minerals and the corresponding impact velocities, calculated using formula (9).

Table 1. *Technological gap sizes and impact speeds*

Technological gap Δ, m	0.010	0.015	0.020	0.025	0.030
Collision velocity, V_{imp}, m/s	0.555	0.654	0.738	0.812	0.879

Further increasing the gap is undesirable, as it will disrupt the relationship between the grinding media and the mass of the material being ground, and could also result in the grinding media only impacting the bottom of the grinding chamber.

A laboratory (MVV) sample with a specific power of N_v = 394.7 kW/m^3 was used in the mechanical activation experiments.

Galenite (PbS) – a mineral prone to over-grinding – was selected as the subject of the study. The experiments involved the preliminary vibro-impact activation of the ore prior to the beneficiation process, comprising grinding in a ball mill, the determination of interplanar distances, and subsequent flotation.

For this purpose, an X-ray diffractometer (XRD) with a copper anode was used. The Bragg–Wolff formula was used to process the experimental data:

$$2d \sin\theta = n\lambda \tag{10}$$

where d is the interplanar spacing, in Å; θ is the angle of reflection, in degrees; λ is the wavelength of the emitter (1.5393 Å for copper); n is the order number of the line on the Debye diagram.

The angle of reflection was calculated using the following formula:

$$\theta = \frac{L}{4R} \quad (11)$$

where L is the distance between pairs of lines on the Debye diagram, m; R is the radius of the chambers ($5.7 \cdot 10^{-2}$ m). For the analysis, we used the concentrate from the first minute of the run and the galena flotation tailings with a particle size of −40 ± 15 μm.

To confirm the difference in the chemical activity of galena, we leached these products in 5% nitric acid and in a 5% solution of ammonium acetate. The galena sample weight for leaching was 0.1 g. The dissolution time of the mineral was 3 minutes.

For the flotation test, galena was used which had been activated by vibro-impact treatment (ground in a ball mill under the following operating conditions: Δ=25 mm and D=130.3) in a dry state and strictly classified within the following ranges: - 150 + 100 μm; - 100 + 74 μm; - 74 + 40 μm and - 40 + 15 μm. The latter fraction was prepared by separating the - 15 μm fraction through washing. A mixture containing 25% of each fraction was prepared for the experiments. The concentration of potassium butyl xanthate was 12 mg/L, 50 g/t of pine oil was added, and the pH was 8. The foam was skimmed off in fractions; after drying, each fraction was separated into the +74 and –74 μm classes using sieves. The –74 μm fraction was subjected to particle size analysis using a photometric method, which yields highly reproducible results. The +74 μm fraction was separated into narrower fractions using appropriate sieves.

In addition to factors determined by the conditions of interaction with reagents, the transition to foam is influenced by statistical factors that determine the conditions under which particles of different sizes attach to bubbles and partially detach from them as they fall back out of the foam layer; this is not the subject of this study.

Results and discussion

The strength of the chemisorption bond between the collector and the sulphide surface depends on the energy state of the cationic and anionic lattice sites, which determines the adsorption behaviour of the mineral surface. The energy characteristics of the sulphide surface depend on the number and nature of the disruptions to the strict periodicity of the crystal lattice.

As demonstrated in previous studies (Svietkina, et al., 2020), vibro-activation of minerals leads not only to surface ionisation but also to bulk ionisation. Consequently, the proportion of the covalent component of the bond between the metal and sulphur in galena may increase, which will weaken the interaction of water molecules with the mineral surface. This leads to the formation of surface areas with hydrophobic properties. From this perspective, it is of interest to perform X-ray structural analysis of the flotation products of the same mineral using the Debye–Scherrer method following activation in a high-pressure, high-temperature (HPHT) environment.

Table 2 presents experimental data on interplanar distances for the most intense lines in galena following its activation in MVV. The data presented in Table 2 show that the interplanar distances in galena following activation of the chamber product exceed those of the concentrate from the first minute of leaching. This indicates an increase in the ionic component of the chemical bond in the lattice of the activated mineral, as a result of which this galena particle will possess increased adsorption and chemical activity with respect to the ions and molecules of the liquid phase of the flotation pulp.

Table 2. *Values of interplanar distances for the most intense lines of the galena Debayagram following activation in the MVV*

№	Chamber product, d_1, Å	Concentrate, d_2, Å	$\Delta d=d_1-d_2$, Å
1	3.4964	3.4301	+0.0663
2	2.8861	2.8800	+0.0001
3	2.0531	2.0502	+0.0029
4	1.9047	1.8886	+0.0161
5	1.8223	1.8201	+0.0022
6	1.7159	1.7149	+0.0010
7	1.4259	1.4233	+0.0026
8	1.1103	1.1100	+0.0003

Leaching was carried out to confirm the changes in chemical activity. The leaching results are presented in Table 3.

Table 3. *Results of experiments on the dissolution of flotation products from galena particles of various particle size classes (initial sample weight 0.1 g)*

Class, μm	Vibration impact dose D (at Δ=25 mm)	Impact velocity V_{imp}, m/s	Amount of dissolved substance, g	
			HNO_3	CH_3COONH_3
—40+15	0	0	0.0045	0.0022
	67.1	0.812	0.0108	0.0074
—74+40	0	0	0.0019	0.0015
	67.1	0.812	0.0089	0.0053
—100+74	0	0	0.0015	0.0009
	67.1	0.654	0.0047	0.0019
	67.1	0.738	0.0059	0.0023
	67.1	0.812	0.0066	0.0025
	130.3	0.812	0.0086	0.0027
	197.4	0.812	0.0092	0.0029
150+100	0	0	0.0009	0.0005
	67.1	0.812	0.0023	0.0016

Table 3 presents the results of our experiments, which show that the dissolution rate of activated galena is higher in all cases than that of non-activated galena. Consequently, the galena particles that will pass into the concentrate first are those with a higher proportion of covalent bonding, i.e. those activated by vibrational impact.

Since the flotation process involves the continuous extraction of the mineral into the froth product, it is to be expected that the mineral particles will be distributed in the froth over time according to their surface properties, and vibro-impact activation allows the adsorption properties of the minerals to be altered.

Figures 2 and 3 show the results of experiments to determine the flotation rate of galena in individual size classes during both individual and combined flotation, as well as the distribution of individual size classes in each fractionated

product. Analysis of these data shows that the –40+15 μm class has a higher flotation rate compared to the –150+100 μm class. The remaining classes have an intermediate flotation rate.

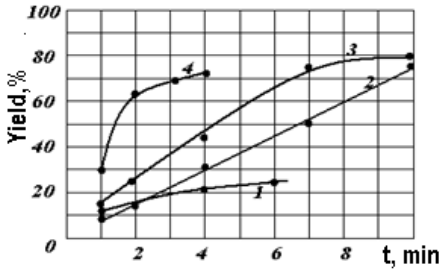


Fig. 2. Change in the flotation rate of galena of different sizes during separate flotation: 1 – -150…+100 μm; 2 – -100…+74 μm; 3 – -74…+40 μm; 4 – -40…+15 μm

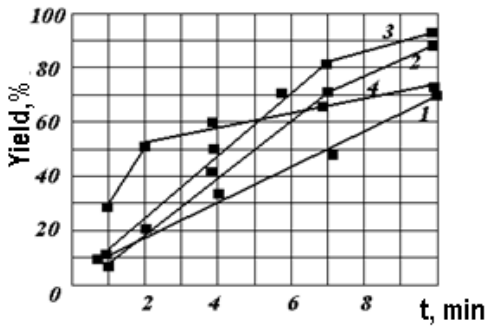


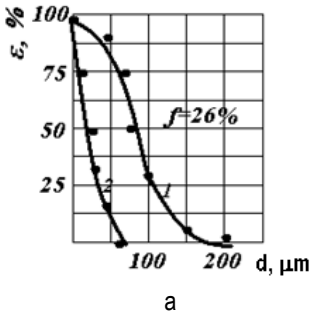
Fig. 3. Change in the flotation rate of galena of different sizes during combined flotation: 1 – -150+100 μm; 2 – -100+74 μm; 2 – -74+40 μm; 4 – -40+15 μm

The high yield of the –40 to +15 μm particle size class in the foam during the initial minutes indicates that this size class is more flotation-active. The increased flotability of the fine fraction is likely determined by two factors: an increase in the adsorption activity of particles as their size decreases, and the fact that larger particles are heavier and, all other things being equal, detach more easily from air bubbles. In addition, a certain quantity of the -40…+15 μm and -150…+100 μm classes remains in the tailings. The presence of the -40…+15 μm class in the flotation tailings can be explained by the distribution of particles according to their chemical bonds over the course of flotation. In this case, the activated galena in the tailings is characterised by a large interplanar distance and a higher value of the ionic component of the bond. The presence of galena particles of -150…+100 μm in the tailings is likely due to their high detachment force and insufficient density of the collector coating on the surface.

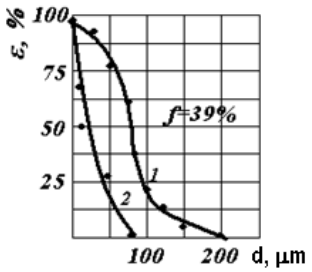
We determined the quantity of the mineral in the form of free particles, its total quantity and the degree of fragmentation using a graphical method, by plotting the size distribution curves for the mineral as a whole and for its free grains.

Figure 4 shows the size distribution curves for galena (curve 1) and its free grains (curve 2) before (a) and after vibro-impact loading (b). The experimental data shown in Fig. 4a and 4b indicate that vibration activation increases the degree of liberation for galena by 13%.

The grinding process in the vibrating impact mill depends on the process parameters under which the vibro-impact activation is carried out; consequently, the mineral liberation factor will also depend on these parameters.



a



b

Fig. 4. Characteristics of the size of galena (curve 1) and its free grains (curve 2) before (a) and after vibro-impact loading (b)

Figures 5 and 6 show the relationships between the degree of liberation (*f*) and the impact loading dose (*D*) and the collision velocity (V_{imp}).

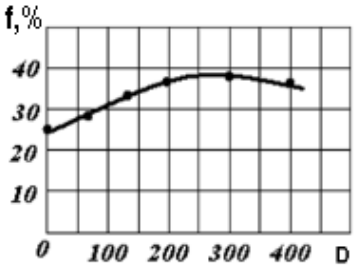


Fig. 5. Relationship between the degree of liberation (*f*) and the dose of vibro-impact loading, D, J/kg

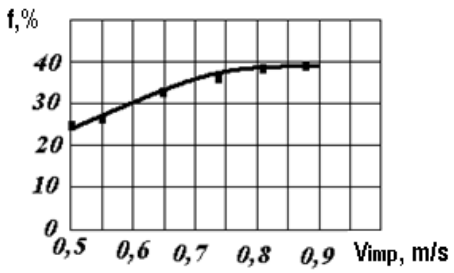


Fig. 6. Relationship between the degree of liberation (*f*) and the collision velocity V_{imp}, m/s

The relationships presented show that, during vibro-impact activation, there is a steady-state region in which the energy yield remains constant. The inhibition observed at high doses may be attributed to two factors: on the one hand, impurity

atoms within the mineral may cause the covalent component of the galena bond to become unstable; its proportion will vary in one direction or another, thereby causing varying degrees of interaction with the flotation reagents among galena particles of the same size; and, on the other hand, the predominance of ionic bonding makes the particles more chemically active towards the components of the pulp's liquid phase, which hinders their release into the froth. Nor can one rule out differences in the chemical activity of galena particles of varying sizes during the flotation process, which affects the rate of release into the froth, thereby determining the distribution of particles according to their surface properties across the flotation front. In addition, a study of the distribution of mineral particles along the flotation front (Nkadimeng et al., 2023) identifies additional technological factors regulating flotation by altering the feed particle size, time of conditioning with the collector and flotation water quality.

Conclusions

1. During vibro-impact treatment, a slight change is observed in the interplanar distances between atoms in the galena crystal lattice. These changes affect the chemical and adsorption activity of this mineral with respect to the components of the pulp's liquid phase, i.e. its flotation activity. This leads to an increase in the flotation rate.

2. It has been found that grinding the mineral in the MVV increases the degree of liberation *f* (for galena) from 26% to 39%.

3. Dependencies of the degree of liberation (*f*) on the technological parameters of the MVV have been obtained: on the vibrating impact loading dose (*D*) and on the collision velocity (V_{imp}), in which there is a steady-state region at constant energy output. As the vibrating load is increased, a decrease in the value of *f* is observed, which is attributed to changes in particle size and the presence of impurities in the mineral.

References

Anciferov, A., & Draban, D. (2011). Raschet tehnologicheskih rezhimov vertikalnoj vibracionnoj melnicy [Calculation of operating parameters for a vertical vibrating mill]. *Vibracii v tehnike i tehnologiyah*, *2* (62), 59 – 60 (in Russ.).

Andrić, L., Živanović, D., & Milošević, S. (1999). Change of the physical — chemical characteristics of the materials by mechanical activation. In: Stojanović, B.D., Skorokhod, V.V., & Nikolić, M.V. (eds) *Advanced Science and Technology of Sintering. Springer, Boston, MA.* https://doi.org/10.1007/978-1-4419-8666-5_27

Bakil, S.N.A., Dibrova, S., Breitung-Faes, S., & Mucsi, G. (2025). Optimizing coal gangue reactivity for geopolymer applications: A comprehensive study on high-energy grinding parameters, *Powder Technology*, *466,* 121441, https://doi.org/10.1016/j.powtec.2025.121441

Bond, F. C. (1961). Crushing and Grinding Calculations, *British Chemical Engineering, 6,* 378-385. https://www.911metallurgist.com/wp-content/uploads/2015/11/Bond-F-C-1961-Crushing-and-Grinding-Calculations.pdf

Bouchard, J., LeBlanc, G., Levesque, M., Radziszewski, P., & George-Filteau, D. (2017). Breaking down energy consumption in industrial grinding mills. Canadian Mineral Processors Conference. 17-19 January 2017, Ottawa, Canada. https:// www.researchgate.net/publication/315148304_Breaking_down_energy_consumption_in_industrial_grinding_mills

Butyagin, P., & Pavlichev, I. (1986) Determination of energy yield of mechanochemical reactions. *Reactivity of Solids*, *1, Issue 4*, *361-372, ISSN 0168-7336*. doi: https://doi.org/10.1016/0168-7336(86)80027-4

Corlett, C.A., Frontzek, M.D., Obradovic, N., Watts, J.L. & Fahrenholtz, W.G. (2022). Mechanical activation and cation site disorder in $MgAl_2O_4$. *Materials, 15*(18), 6422. https://doi.org/10.3390/ma15186422

Elbendari, A.M., & Ibrahim, S.S. (2025). Optimizing key parameters for grinding energy efficiency and modelling of particle size distribution in a stirred ball mill. *Scientific Reports, 15,* 3374. https://doi.org/10.1038/s41598-025-87229-8

Franchuk, V. P. (2010). Vybratsyonnaia tekhnyka v malykh proyzvodstvakh [Vibration technology in small industries]. *Geo-Technical Mechanics, 85,* 290-296 (in Russ.).

Kondratets, V., Matsui, A., Yatsun, V., & Lichuk, M. (2019). Identification of energy efficiency of ore grinding and the liner wear by a three-phase motion of balls in a mill. *Eastern-European Journal of Enterprise Technologies*, *3*(5 (99), 21–28. https://doi.org/10.15587/1729-4061.2019.167046

Korkmaz, A.V., & Kayıran, H.F. (2022). Investigation of mechanical activation effect on high-volume natural pozzolanic cements. *Open Chemistry*, *20*(1), 1029-1044. https://doi.org/10.1515/chem-2022-0217

Loudari, C., Cherkaoui, M., Harraki, I. E., Bennani, R., Adnani, M. E., Abdelwahed, L. H., Benzakour, I., Bourzeix, F., & Baina, K. (2025). Optimization of grinding mill parameters using genetic algorithms for energy efficiency in mining industry. *Journal of Mining and Environment (JME) 16* (6), *1867-1879* https://doi.org/10.22044/jme.2025.15869.3095

Ma, S., Li, H., Shuai, Z., Yang, J., Deng, X., & Xu, W. (2022b) Research on grinding law and grinding parameters optimization of polymetallic complex ores. *Minerals*, *12* (10), 1283. *https://doi.org/10.3390/min12101283*

Ma, S., Li, H., Shuai, Z., Yang, J., Xu, W., & Deng, X. (2022a) Research on grinding characteristics and comparison of particle-size composition prediction of rich and poor ores. *Minerals*, *12*(11), 1354. https://doi.org/10.3390/min12111354

Malyarov, P., & Kuzminyh, A. (2008). Otsenka-effektivnosti-izmelcheniya-i-raspredeleniya-potreblyaemoy-energii-mezhdu-stadiyami-izmelcheniya [Efficiency assessment of the grinding process and distribution of energy consumption across the grinding stages]. *Izvestiya vuzov. Severo-Kavkazskij region. Seriya: Tehnicheskie nauki. 2.* URL: https://cyberleninka.ru/article/n/otsenka-effektivnosti-izmelcheniya-i-raspredeleniya-potreblyaemoy-energii-mezhdu-stadiyami-izmelcheniya (in Russ.)

Malyarov, P., Sysoev, N., Manaka, V., Mironova, S., & Braginec, I. (2012). Sovremennoe sostoyanie i perspektivy razvitiya tehniki i tehnologii v izmelchitelnyh otdeleniyah obogatitelnyh fabric [The modern state and prospects for the development of machinery and technology in the crushing departments of mineral processing plants]. *Izvestiya vysshih uchebnyh zavedenij. Severo-Kavkazskij region. Tehnicheskie nauki, (2), 96-101*. (in Russ.). https://cyberleninka.ru/article/n/sovremennoe-sostoyanie-i-perspektivy-razvitiya-tehniki-i-tehnologii-v-izmelchitelnyh-otdeleniyah-obogatitelnyh-fabrik

Mañosa, J., Alvarez-Coscojuela, A., Maldonado-Alameda, A., & Chimenos, J.M. (2024). A lab-scale evaluation of parameters influencing the mechanical activation of kaolin using the design of experiments. *Materials*, *17*(18), 4651. https://doi.org/10.3390/ma17184651

Nkadimeng, M., Manono, M.S., & Corin, K.C. (2023). Developing a relationship between ore feed grade and flotation performance. *Engineering Proceedings, 37*, 101. https://doi.org/10.3390/ECP2023-14651

Őze, C, & Makó, É. (2023). Optimization of grinding parameters for the mechanochemical activation of kaolin with the addition of trass. *Minerals*, *13*(7), 915. https://doi.org/10.3390/min13070915

Shan, Z., Jiugang, H., Chenhu, Z, Song, L., & Na, A. (2022). Study on optimization and mechanism of mechanical activation process of titanium-bearing blast furnace slag, *Journal of Materials Research and Technology, 19*, 3130-3144, ISSN 2238-7854. https://doi.org/10.1016/j.jmrt.2022.06.038.

Stamboliadis, E., Emmanouilidis, S., & Petrakis, E. (2011). A new approach to the calculation of work index and the potential energy of a particulate material. *Geomaterials, 1(2),* 28-32. DOI: 10.4236/gm.2011.12005

Svetkina, E. (2008). Parametry optimizacii processa vibroudarnoj aktivacii [Optimization parameters for the vibro-impact activation process] *Naukovyi visnyk Natsionalnoho hirnychoho universytetu, 11,* 58 – 60 (in Russ.).

Svietkina, O., Bas K., Haddad, J., Ziborov, K., Olishevska, V. (2020). Mechanochemical Activation of Polymetallic Ore and Further Selective Floatation, *Key Engineering Materials, 844,* 65-76. Trans Tech Publications Ltd, Switzerland. https://www.scientific.net/Paper/Preview/548983

Vugrin, L., Carta, M., Lukin, S., Meštrović, E., Delogu, F., & Halasz, I. (2023). Mechanochemical reaction kinetics scales linearly with impact energy. *Faraday Discussions*, *241*, 217-229. DOI https://doi.org/10.1039/D2FD00083K

Wentao, Z., Yuexin, H., Yanjun, L., Jinlin, Y., Shaojian, M., & Yongsheng, S. (2020). Research on prediction model of ore grinding particle size distribution. *Journal of Dispersion Science and Technology*, *41*(4), 537–546. https://doi.org/10.1080/01932691.2019.1592688

INSTRUCTION FOR AUTHORS

General

Manuscripts submitted to the journal have to adhere to its scope and fields. Research papers are expected to be complete and sound description of significant work, presented clearly and concisely. Critical reviews are commissioned by the Editor-in-Chief. Authors intending to offer critical reviews are asked first to contact the Editor-in-Chief. Paper will not be accepted if plagiarism (https://www.plagiarism.org/article/what-is-plagiarism; Strikeplagiarism.com) and / or redundant / overlapping text recycling are detected. (Text recycling, also known as self-plagiarism, is the case when sections of the same text appear in more than one of an author's own publications - https://textrecycling.org).

The authors are fully responsible for the content of their publications and the opinions expressed in them. The publication of a manuscript does not mean that the views and position of the author are shared by the Editorial Board.

Authors of manuscripts have to strictly follow the SEPRM Template that can be downloaded from seprm.com.

Generally, the work has to contain the following items:

Title of the work and authors, including their affiliation, corresponding author. Authors' ORCIDs may be added;

Abstract – not longer than 300 words, focused on the most important issues, discussed in the paper;

Introduction **–** adequate references to previous work of other scientists have to be given and clear statement of the aim of the work, presented in the manuscript;

Concise but sufficient description of the theoretical basis (if necessary);

Materials and methods used;

Results and discussion, including comparison of experimental results with the findings of other authors;

Conclusions – not repeating the abstract and reflecting the corresponding research results;

Acknowledgements – optional;

References - for the exact requirements, please consult the journal template.

Please, strictly follow the SEPRM template!

Submission of manuscripts

Manuscripts should be submitted to the Editor-in-Chief together with a covering letter briefly describing the work proposed. A statement in this letter that (i) all the authors agree with the submission, (ii) the paper results from their own work and (iii) the paper has not been published somewhere and is not sent to another journal represents a good practice and is welcomed. We do not view the following prior uses of a work as prior publication: publication in the form of an abstract, publication as an academic thesis and publication as an electronic preprint *without* a doi assigned. However, we notice the authors that since we use a double-blind review process, the availability of a preprint could compromise the authors' anonymity.

Manuscripts can be submitted:

– *By post at the following address:* University of Mining and Geology "St. Ivan Rilski" 1700 Sofia, Bulgaria, Prof. Boyan Kamenov Str., No 1 (for SEPRM);

– *Electronically* (*preferable*) to e-mails: m_panayotova@mgu.bg, journal@seprm.com, or using the form on journal site.

The average number of weeks between article final submission and publication is 12. If necessary, the Editor-in-chief can issue a document that the paper has been accepted for publication.

For inquiries, comments, suggestions, please use the e-mail m_panayotova@mgu.bg or contact form.

All articles accepted for publication in the SEPRM journal after double-blind peer-review by 2 rewires will be published at open access, free of charge for authors, no any author-facing fees.



UNIVERSITY OF
MINING AND GEOLOGY
"ST. IVAN RILSKI"

www.mgu.bg

www.seprm.bg